CORA Cork Open Research Archive
Cartlann Taighde Oscailte Chorcaí

Title	Studies of ferrite, borosilicate and intercalation materials
Authors	Herlihy, Emmet A.
Publication date	1999
Original Citation	Herlihy, E. A. 1999. Studies of ferrite, borosilicate and intercalation materials. PhD Thesis, University College Cork.
Type of publication	Doctoral thesis
Link to publisher's version	http://library.ucc.ie/record=b1301530~S0
Rights	© 1999, Emmet A. Herlihy - http://creativecommons.org/licenses/by-nc-nd/3.0/
Download date	2026-10-31 04:02:23
Item downloaded from	https://hdl.handle.net/10468/1621

UCC
University College Cork, Ireland
Coláiste na hOllscoile Corcaigh

DP1999 HERL

STUDIES OF FERRITE, BOROSILICATE AND INTERCALATION MATERIALS

By

Emmet Anthony Herlihy, B.Sc.



Being a thesis submitted for the degree of

DOCTOR OF PHILOSOPHY

to

THE NATIONAL UNIVERSITY OF IRELAND

Based on research carried out under the direction of

Professor T. R. Spalding
Department of Chemistry
University College
Cork

September 1999

UNIVERSITY COLLEGE
Library
CORK

ABSTRACT

This thesis is concerned with several aspects of the chemistry of iron compounds.

Chapter 1 gives a brief introduction on the magnetic properties of ferrites. The preparation (with particular emphasis on coprecipitation and sol-gel techniques) and processing of ferrites are discussed.

Chapter 2 describes the synthesis of Ni-Zn ferrites with various compositions by three methods. These methods included coprecipitation and sol-gel techniques. The Ni-Zn ferrites were characterised by powder X-ray diffactometry (PXRD), scanning electron microscopy (SEM), vibrating sample magnetometry (VSM), Mössbauer spectroscopy and resistivity measurements. The results for the corresponding ferrites prepared by each method are compared.

Chapter 3 reports the sol-gel preparation of a lead borosilicate glass and its addition to Ni-Zn ferrites prepared by the sol-gel method in **Chapter 2**. The glass-ferrites formed were analysed by the same techniques employed in **Chapter 2**. Alterations in the microstructure, magnetic and electronic properties of the ferrites due to glass addition are described.

Chapter 4 introduces compounds containing Fe-O-B, Fe-O-Si or B-O-Si linkages. The synthesis and characterisation of compounds containing Fe-O-B units are described. The structure of $[Fe(SALEN)]_2O.CH_2Cl_2$ **(17)**, used in attempts to prepare compounds with Fe-O-Si bonds, was determined by X-ray crystallography. **Chapter 4** also details the synthesis of three new borosilicate compounds containing ferrocenyl groups, i.e. $[FcBO)_2(OSiBu^t_2)_2]$ **(19)**, $[(FcBO)_2(OSiPh_2)_2]$ **(20)** and $[FcBOSiPh_3]$ **(21)**. The structure of **(19)** was determined by X-ray crystallographic analysis.

Chapter 5 reviews the intercalation properties of the layered host compound iron oxychloride (FeOCl). Intercalation compounds prepared with the microwave dielectric heating technique are also discussed. The syntheses of intercalation compounds by the microwave method with FeOCl as host and ferrocene, ferrocenylboronic acid and 4-aminopyridine as guest species are described. Characterisation of these compounds by powder X-ray diffractometry (PXRD) and Mössbauer spectroscopy is reported. The attempted synthesis of an intercalation compound with the borosilicate compound **(19)** as guest species is discussed.

Appendices A-E describe the theory and instrumentation involved in powder X-ray diffractometry (PXRD), scanning electron microscopy (SEM), vibrating sample magnetometry (VSM), Mössbauer spectroscopy and electrical resistivity measurements, respectively. **Appendix F** details the attempted syntheses of compounds with Fe-O-B and Fe-O-Si linkages.

ACKNOWLEDGEMENTS

I would like to express my sincerest thanks to my supervisor, Prof. Trevor Spalding for his guidance and encouragement throughout the course of this work. I would also like to mention my research director Prof. W.B. Jennings.

I am grateful to Dr. F.A. Deeney for the work on the Mössbauer spectroscopy (and his conversations on the immoralities of academic life), to Dr. Simon Lawrence for solving the crystal structures and to Dr. Mick Morris for his expertise on PXRD patterns.

Thanks are also due to the technical staff of U.C.C. chemistry department, especially to Sean Downey (Douglas Dynamo), Pat O' Connell (the bearded one), Jim Allen, Chrissie O' Flaherty, Derry Kearney, Katie, Agnes, Deirdre and Karen. Thanks to Mick and Mattias for the mass spectra, Helen and Barry for the microanalysis and Donal for the NMR spectra.

To all the postgrads I have ever initiated or ended a chemical conversation with: Lorraine, Maria, Donogh (the man who "trended" a thinner me), Ger, Trish, Brian, Karen, Anna, Andy, Anne-Marie, Maureen, Yvonne, Dave, Susan, Eamonn, Mark, Cathal, Gillian, George and Donnacha.

College life would have been unbearable (but probably more profitable) only for the regular bombardment of the local with "the lads". This bunch of unsavoury characters included: John, Dave, Derek, Declan, Ed, Eoin, Kevin, Vicki, Tom, Stewart, Colm and Niall.

I would also like to thank Breeda for all her understanding, love and putting up with my constant "whinging" for more years that I'm afraid to recall. Thanks Girl!! A special mention to Peggy whose hospitality and cooking has sustained me through the long hours.

Finally, I wish to thank my family, Tim, Marian, Sandra, Brendan, Nigel, Eithne, John, Peter, Eric and especially to my parents, Timothy and Ellen, for all their support, love and encouragement without which this thesis would not have been possible.

To my parents

TABLE OF CONTENTS

CHAPTER 1: INTRODUCTION TO SYNTHESIS AND MAGNETIC PROPERTIES OF FERRITE MATERIALS

1.1	**Introduction**	**1**
1.2	**History of Ferrites**	**1**
1.3	**Origin of Ferrite Magnetism in Electrons and Atoms**	**2**
	1.3.1 Paramagnetism and Diamagnetism	**2**
	1.3.2 Ferromagnetism	**4**
	1.3.3 Antiferromagnetism	**5**
	1.3.4 Ferrimagnetism	**6**
1.4	**Crystal Structure of Ferrites**	**9**
	1.4.1 Spinel Chemistry	**9**
	1.4.2 Interaction between Magnetic Moments on Lattice Sites	**11**
	1.4.3 Normal and Inverse Spinels	**12**
	1.4.4 Mixed Zinc Ferrites	**14**
1.5	**Magnetism in Ferrite Domains and Bulk Materials**	**16**
	1.5.1 Dynamic Behaviour of Domains	**17**
1.6	**Properties of "Soft" Ferrites (such as Mn-Zn and Ni-Zn Ferrites)**	**20**
1.7	**Preparation of Ferrites**	**22**
	1.7.1 Coprecipitation Technique	**24**
	1.7.2 Sol-Gel Technique	**25**
1.8	**Processing of Ferrite Powders**	**29**
1.9	**Summary**	**32**

CHAPTER 2: SYNTHESIS AND CHARACTERISATION OF Ni-Zn FERRITE MATERIALS

2.1	**Introduction**	**33**
	2.1.1 Synthesis of Ni-Zn Ferrites	**33**
	2.1.2 Characterisation of Ni-Zn Ferrites	**33**

2.1.2.1 PXRD Analysis 33
2.1.2.2 SEM Analysis 35
2.1.2.3 VSM Analysis 35
2.1.2.4 Mössbauer Spectroscopy 35
2.1.2.5 Electrical Resistivity Analysis 41
2.2 Results and Discussion 41
2.2.1 Synthesis of Ni-Zn Ferrites 41
2.2.2 PXRD Analysis 46
2.2.3 Magnetic (VSM) Measurements 64
2.2.4 Mössbauer Spectroscopy 74
2.2.5 Resistivity Measurements 81
2.3 Summary and Conclusions 86
2.4 Experimental Details 91
2.4.1 Instrumentation 91
2.4.2 Starting Materials 92
2.4.3 Preparation of Ni-Zn Ferrites 92
2.4.3.1 Coprecipitation Method 92
2.4.3.2 Sol-Gel Method 94
2.4.3.3 MNCD Method 95

CHAPTER 3: SYNTHESIS AND PROPERTIES OF Ni-Zn FERRITE MATERIALS WITH LEAD BOROSILICATE GLASS ADDITIVES

3.1 Introduction 98
3.1.1 Definition of Glass 98
3.1.2 Structure of Glass 100
3.1.3 Lead Borosilicate Glass: Preparation and Properties 101
3.1.4 Glass Additives for Ferrites 102
3.1.5 Summary 105
3.2 Results and Discussion 106
3.2.1 Preparation and Analysis of Lead Borosilicate Glass 106

3.2.2 Preparation of Ni-Zn Ferrite with Lead Borosilicate Glass Additives 108
3.2.3 Characterisation of Glass-Ferrite Compounds 112
3.2.4 Infrared Spectroscopy 112
3.2.5 PXRD Analysis 113
3.2.6 SEM Analysis 122
3.2.7 VSM Analysis 125
3.2.8 Mössbauer Spectroscopy 128
3.2.9 Electrical Resistivity Analysis 131
3.3 Summary and Conclusions 135
3.4 Experimental Details 137
3.4.1 Instrumentation 137
3.4.2 Starting Materials 137
3.4.3 Preparation of Lead bis(dodecanoate), $Pb(O_2CC_{11}H_{23})_2$ 137
3.4.4 Preparation of Standard Lead Borosilicate Glass 138
3.4.5 Method A: Preparation of Cogelled Glass-Ferrite 138
3.4.6 Method B: Preparation of Heterogeneous Mixed Glass-Ferrite 140

CHAPTER 4: A STUDY OF COMPOUNDS CONTAINING Fe-O-B, Fe-O-Si AND B-O-Si LINKAGES

4.1 Introduction 141
4.1.1 General Considerations of Systems Containing Fe-O-B Linkages 141
4.1.1.1 Synthesis of Compounds with Fe-O-B Units 141
4.1.1.2 Structural Studies of Compounds Containing Fe-O-B Linkages 146
4.1.2 General Considerations on Systems Containing Fe-O-Si Linkages 148
4.1.3 General Considerations of Borosilicate Compounds 153
4.1.3.1 Structural Studies of Compounds Containing B-O-Si Linkages 155
4.1.4 Summary 156
4.2 Results and Discussion 157

4.2.1 Synthesis and Characterisation of Compounds Containing Fe-O-B Linkages, (6), (27), (28) and (29) 157
4.2.1.1 Synthesis of (6), (27), (28) and (29) 157
4.2.1.2 Infrared Spectra 158
4.2.1.3 Mössbauer Analysis 159
4.2.2 Synthesis and Characterisation of $[Fe(SALEN)]_2O.CH_2Cl_2$ (17) 160
4.2.2.1 Synthesis of $[Fe(SALEN)]_2O.CH_2Cl_2$ (17) 161
4.2.2.2 Mössbauer Analysis of $[Fe(SALEN)]_2O.CH_2Cl_2$ (17) 161
4.2.2.3 Structural Study of $[Fe(SALEN)]_2O.CH_2Cl_2$ (17) 162
4.2.3 Synthesis and Characterisation of Three Novel Borosilicate Compounds which also Contain Iron 169
4.2.3.1 Synthesis of (19), (20) and (21) 169
4.2.3.2 Infrared Spectra 170
4.2.3.3 Mass Spectra 170
4.2.3.4 Mössbauer Spectra 171
4.2.4 Structural Study of $[(FcBO)_2(Bu^t_2SiO)_2]$ (19) 173
4.3 Summary and Conclusions 179
4.4 Experimental Details 180
4.4.1 Instrumentation 180
4.4.2 Starting Reagents 181
4.4.3 Synthesis of Boron Oxygen-Bridged Iron Compounds 181
4.4.3.1 Synthesis of $[Fe_2(C_{30}H_{29}B_2N_6O_6)Cl_3]$, (6) 181
4.4.3.2 Synthesis of $[Fe_2(C_{30}H_{27}B_2Br_2N_6O_6)Cl_3]$, (27) 181
4.4.3.3 Synthesis of $[Fe_2(C_{32}H_{29}B_2N_6O_8)Cl_3]$, (28) 182
4.4.3.4 Synthesis of $[Fe_2(C_{34}H_{33}B_2N_6O_6)Cl_3]$, (29) 182
4.4.4 Synthesis of μ-Oxo-bis-[NN'-ethylenebis(salicylideneiminato)iron(III)], $[Fe(SALEN)_2O$ 183
4.4.5 Synthesis of Borosilicate Compounds from Ferrocenylboronic Acid 184
4.4.5.1 Preparation of di-*tert*-butylsilanediol, $Bu^t_2Si(OH)_2$ 184
4.4.5.2 Synthesis of $[(FcBO)_2(OSiBu^t_2)_2]$, (19) 184
4.4.5.3 Synthesis of $[(FcBO)_2(OSiPh_2)_2]$, (20) 185
4.4.5.4 Synthesis of $[FcB(OSiPh_3)_2]$, (21) 186

CHAPTER 5: MICROWAVE-ASSISTED SYNTHESIS OF INTERCALATION COMPOUNDS DERIVED FROM IRON OXYCHLORIDE

5.1 Introduction **187**

5.1.1 Definition of Intercalation **187**

5.1.2 Mechanism of Intercalation **191**

5.1.3 Synthetic Methods **193**

5.1.4 Methods of Analysis **194**

5.1.5 Iron(III) Oxychloride: Host Structure and Intercalation Properties **198**

5.1.6 Intercalation Reactions of FeOCl **199**

5.1.7 Microwave Dielectric Heating and its Application to Intercalation Reactions **205**

5.1.8 Interaction of Microwaves with Matter **206**

5.1.9 Microwave Dielectric Heating at High Pressure Conditions **208**

5.1.10 Microwave Dielectric heating in Synthesising Intercalation Compounds **211**

5.1.11 Summary **213**

5.2 Results and Discussion **214**

5.2.1 Preparation of Intercalation Compounds **214**

5.2.2 Infrared Spectroscopy **217**

5.2.3 Intercalation of Ferrocene into FeOCl **218**

5.2.3.1 PXRD Analysis **218**

5.2.3.1.1 Reaction in Acetone **218**

5.2.3.1.2 Reaction in Dichloromethane **220**

5.2.3.2 Mössbauer Spectroscopy **223**

5.2.3.2.1 Reaction in Acetone **223**

5.2.3.2.2 Reaction in Dichloromethane **226**

5.2.4 Intercalation of Ferrocenylboronic Acid into FeOCl **228**

5.2.4.1 PXRD Analysis **228**

5.2.4.2 Mössbauer Spectroscopy **231**

5.2.5 Intercalation of 4-Aminopyridine (Apy) into FeOCl **234**

5.2.5.1 PXRD Analysis **234**

5.2.5.2 Mössbauer Spectroscopy 235
5.2.6 Attempted Intercalation of $[(FcBO)_2(Bu^t_2SiO)_2]$ (19) into FeOCl 237
5.3 Summary and Conclusions 238
5.4 Experimental Details 240
5.4.1 Instrumentation 240
5.4.2 Starting Reagents 241
5.4.3 General Methodology 241
5.4.4 Intercalation of Ferrocene into FeOCl 241
5.4.4.1 Conventional Thermal Method 241
5.4.4.2 Microwave Method 241
5.4.5 Intercalation of Ferrocenylboronic Acid into FeOCl (Microwave Method) 243
5.4.6 Intercalation of 4-Aminopyridine (Apy) into FeOCl 244
5.4.6.1 Conventional Reflux Method 244
5.4.6.2 Microwave Method 244
5.2.7 Attempted Intercalation of $[(FcBO)_2(Bu^t_2SiO)_2]$ (19) into FeOCl 244

APPENDICES:

Appendix A: Powder X-ray Diffraction (PXRD). Technique, Theory and Equipment 245
Appendix B: The Scanning Electron Microscope (SEM) 247
Appendix C: Vibrating Sample Magnetometry (VSM) 248
Appendix D: Mössbauer Spectroscopy 249
Appendix E: Electrical Resistivity Method 251
Appendix F: Attempted Syntheses of Compounds Containing Fe-O-B and Fe-O-Si Linkages 253

REFERENCES 257

CHAPTER 1

INTRODUCTION TO SYNTHESIS AND MAGNETIC PROPERTIES OF FERRITE MATERIALS

1.1 Introduction

This thesis is divided into three sections. The first section (**Chapters 1 to 3**) is concerned with the synthesis and characterisation of Ni-Zn ferrites, with and without lead borosilicate glass additives. The second section (**Chapter 4**) is concerned with the synthesis and characterisation of molecular compounds with iron-oxygen-boron or iron-oxygen-silicon linkages. The third section (**Chapter5**) discusses intercalation reactions of the layer compound iron oxychloride (FeOCl).

Chapter 1 introduces ferrites with an account of their structural and magnetic properties and also reviews the synthesis and processing of ferrite materials. In **Chapter 2**, Ni-Zn ferrites, prepared by coprecipitation and sol-gel techniques, are characterised structurally, magnetically and electronically. In **Chapter 3**, the effect of the addition of lead borosilicate glass to the Ni-Zn ferrites synthesised by the sol-gel technique in **Chapter 2** is described.

Chapter 4 is a continuation of **Chapter 3** in that it investigates the Fe-O-B, Fe-O-Si and B-O-Si linkages that are formed in the reaction between the ferrite material and the lead borosilicate glass. **Chapter 4** reviews the structures of compounds with these linkages and details attempted syntheses of novel related compounds.

The link between magnetic materials and the intercalation compounds discussed in **Chapter 5** may at first appear tentative but FeOCl is a potential ferrite precursor through the intermediate γ-FeOOH which is formed by the hydrolysis of iron oxychloride. **Chapter 5** is directly connected to **Chapter 4** by the attempted use of one of the borosilicate compounds synthesised in **Chapter 4** as a guest in the intercalation process.

1.2 History of Ferrites

Ferrites may be defined[1] as "magnetic materials composed of oxides containing ferric ions as the main constituent". Magnetite, or ferrous ferrite, is a naturally-occurring ferrite and was used in the form of lodestone for navigating in ancient times. Hilpert[2] published the first study of the relation between the chemical and magnetic properties

of several binary iron oxides in 1909. Forestier[3] in France reported quantitative studies into the relation between chemical composition, saturation magnetisation and the Curie temperature of ferrites in 1928. However it was Snoek[4] in 1948 who laid the foundations of the physics and technology of practical ferrites and a new industry was born. For a more detailed account of the history of ferrite development the reader is referred to the article by Wijn.[5]

The work described in **Chapter 2** of this thesis attempted to prepare one ferrite of practical importance, namely, nickel-zinc ferrite (Ni-Zn ferrite), in various compositions, by different chemical means. Physical, chemical, electrical and magnetic properties were investigated and are discussed in detail. However, an account of the origins of magnetism in ferrites and their crystal structures will be given first as well as a review of established methods of preparation and processing ferrite materials.

1.3 Origin of Ferrite Magnetism in Electrons and Atoms

The postulation of the "rotating electron" spinning on its own axis around the nucleus of an atom led to an explanation of magnetism in materials early in the 20th century.[6-9] A material's magnetism arises from the sum of the individual spin moments of the electrons in the atom's outer shell. For an atom with complete filled electron shells, or subshells, there is a total cancellation of the spin moments and the material is known as diamagnetic. If an atom contains unpaired electrons, then the material gives rise to a net magnetic moment and is termed paramagnetic. A paramagnetic material that displays some long-range ordering between the atomic spins may be classed as ferromagnetic (positive interaction), antiferromagnetic (negative interaction) or ferrimagnetic (uncompensated negative interaction). A fuller explanation of these five different magnetic types is detailed below.

1.3.1 Paramagnetism and Diamagnetism

Paramagnetism refers to a system in which each atom has a net magnetic moment due to its unpaired electrons. However, the atomic moments point in all directions due to

thermal agitation thus generating no net magnetisation. A large magnetic field is necessary to achieve even a small degree of alignment.

In many paramagnetic materials as the temperature is raised, the increased thermal agitation of the spins reduces further any amount of alignment. Curie[10] showed that in such cases the susceptibility, χ, which is unitless, follows the Curie Law given by:

$$\chi = C/T \qquad [1]$$

where C = Curie constant (K) and T = temperature (K). This implies that $1/\chi = T/C$. **Figure 1.1** shows the temperature dependence of the inverse of the susceptibility in a paramagnetic material. The slope of the line is then 1/C.

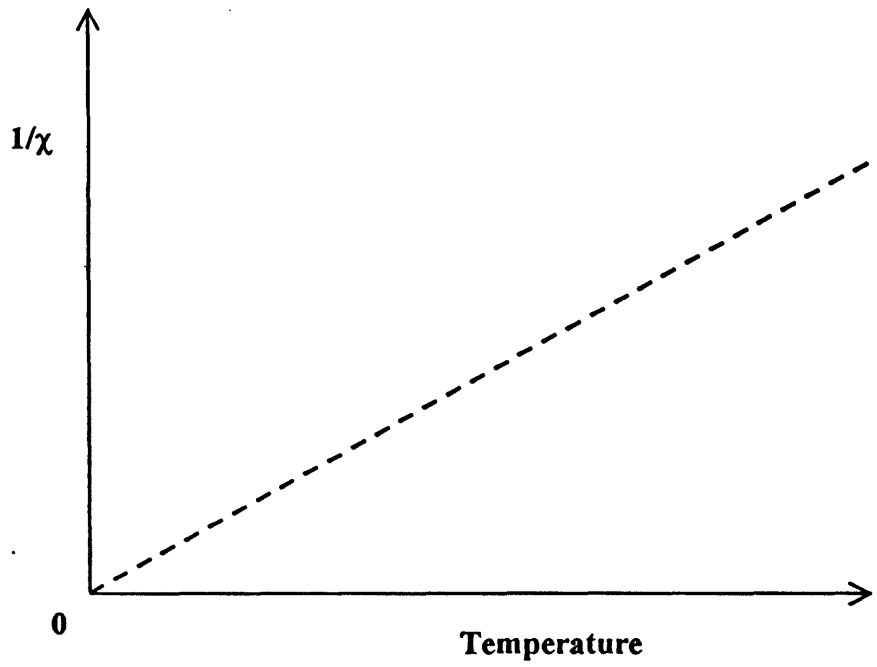


Figure 1.1 Variation of reciprocal of susceptibility of a paramagnetic material with temperature.[11]

The susceptibility of a material, χ, may be defined as:

$$\chi = H/M \qquad [2]$$

where **M** is the magnetisation per unit density with units $JT^{-1}kg^{-1}$ (where J = joules and T = tesla) and **H** is the applied magnetic field strength per unit density with units $JT^{-1}kg^{-1}$. For later considerations, the magnetic flux density of a material (magnetic induction), **B** (tesla), is defined as:

$$B = \mu_o\rho(M + H) \qquad [3]$$

where μ_o = vacuum permeability = $4\pi \times 10^{-7}$ Hm^{-1} (where H = henry = $VA^{-1}s$, V = volt, A = ampere) and ρ = density of material (kg m^{-3}).

Diamagnetic materials possess no net permanent atomic moment as in the case of the two electrons in the same orbit rotating in opposite senses. However, in an applied magnetic field, the orbital motion sets up a field opposite to the applied field in a manner similar to the back emf (electromotive force) of Lenz's law. This effect leads to a negative susceptibility. Diamagnetism is a weak effect and a small paramagnetic impurity can often mask a diamagnetic effect.

1.3.2 Ferromagnetism

Large-scale magnetic effects resulting in commercially important materials occur in atoms (and ions) of only a few metallic elements (Fe, Co and Ni) and some of the rare earths. These elements possess a magnetic moment at a relatively low temperature, even in the absence of an applied magnetic field. This phenomenon occurs because of the co-operative interaction of large numbers (10^{13} - 10^{14}) of the atomic spins producing a region where all atomic spins are essentially aligned parallel (positive exchange interaction). This property of spontaneous magnetism is known as ferromagnetism.

The regions of materials in which the co-operative effect extends are known as "magnetic domains". These were first postulated by Weiss[12] and have been confirmed by several techniques.

As in paramagnetic materials, the alignment of magnetic moments of a ferromagnetic substance in a magnetic field decreases as the temperature is raised. With further temperature increases, the thermal agitation will exceed the exchange forces and at a critical temperature (Curie point, T_C), ferromagnetism disappears and the material becomes paramagnetic, and follows the Curie law as stated above. The Curie-Weiss law (equation [4]) can express ferromagnetic behaviour, which simplifies to the Curie law for $T \geq T_C$.

$$1/\chi = (T - T_C)/C \qquad [4]$$

where T = temperature (K), T_c = Curie point (K) and C = Curie constant (K).

1.3.3 Antiferromagnetism

In ferromagnetism, the interaction of atomic spin moments was a positive one, which means neighbouring spins align themselves parallel to one another in a magnetic domain. However, in his studies of paramagnetic susceptibilities of certain alloys, Néel[13] noticed that they did not follow the Curie law at low temperatures. However, they did obey the Curie-Weiss law at high temperatures i.e.,

$$1/\chi = (T - T_N)/C \qquad [5]$$

where T = temperature (K), T_N = Néel temperature (K) and C = Curie constant (K).

The $1/\chi$ versus T curve for this behaviour is shown in **Figure 1.2** and the extrapolation of the high temperature section of the graph results in a negative value for the Curie point (T_C').

Néel proposed a negative exchange interaction that aligned the neighbouring spins antiparallel to accommodate his findings. At very low temperatures, the negative exchange force prevented the normal paramagnetic alignment in a field so that the

susceptibility was low (i.e. $1/\chi$ was large). As the temperature was increased, the exchange interaction weakened, thus increasing the susceptibility until a point (Néel point) where the negative interaction disappears. The material then behaved as a paramagnetic one with the expected Curie-Weiss law dependence. The negative exchange behaviour of material of this type is called antiferromagnetism.

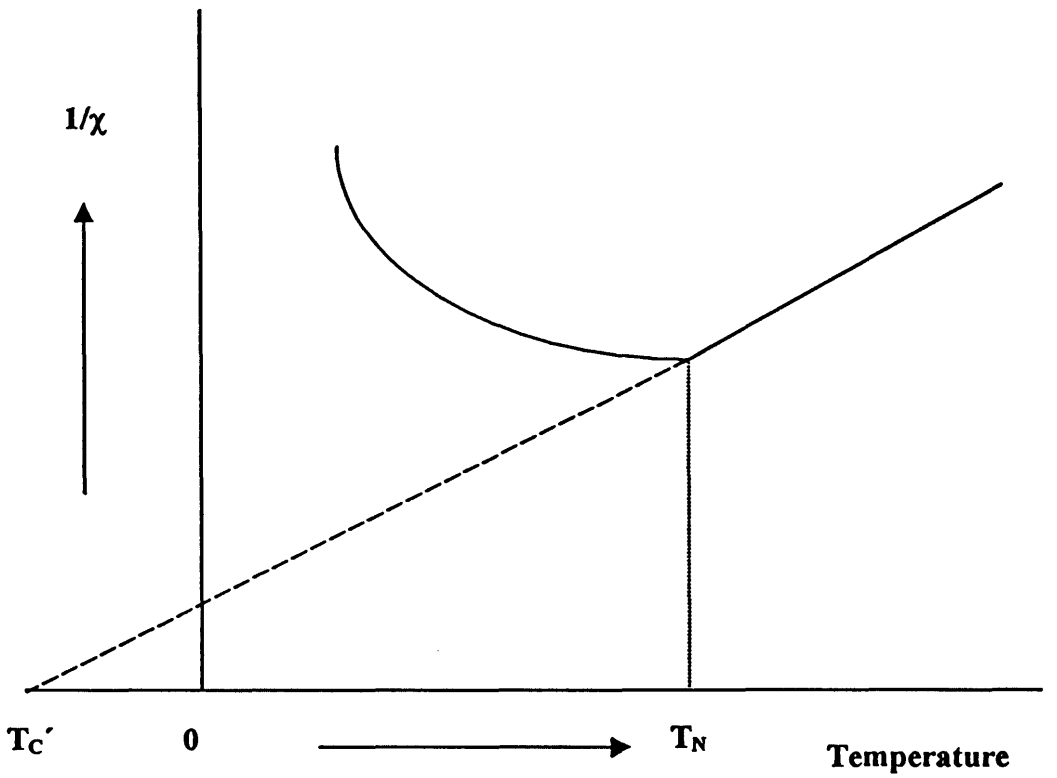


Figure 1.2 Variation of reciprocal of the susceptibility of an antiferromagnetic material with temperature showing the discontinuity at the Néel temperature T_N and the extrapolation of the linear potion to a "negative" Curie temperature T_C'.[14]

1.3.4 Ferrimagnetism

In 1948, Snoek[4] reported a number of interesting properties of a class of oxide materials called ferrites. Taking as an example, magnetite, Fe_3O_4 or $FeO.Fe_2O_3$, the theoretical number of unpaired electrons for that formula is 14, i.e. 5 each for each Fe^{3+} ion and 4 for the Fe^{2+} ion. Therefore the effective moment (μ_{eff}) should be 7.8 B.M. (B.M. = Bohr-Magneton) as calculated from equation [6].

$$\mu_{eff} = 2(2S + 1)^{1/2} \quad [6]$$

where S = number of unpaired electrons x 0.5.

However, the experimental value (μ_{eff}) is only 4.5 B.M. per formula unit. The observed μ_{eff} value necessitates a configuration in which the spins of the Fe^{3+} ions are evenly split and coupled antiferromagnetically, whereas the spins of the Fe^{2+} ions are coupled ferromagnetically as shown in **Figure 1.3**. Néel called this phenomenon ferrimagnetism or uncompensated antiferromagnetism.[15] The ferrous ions are the sole contributors to the net magnetisation. Such a complex spin configuration is possible because the Fe^{3+} ions are divided into two equal parts, each occupying the tetrahedral and half the octahedral sites in the inverse-spinel lattice system (see **Section 1.4**).

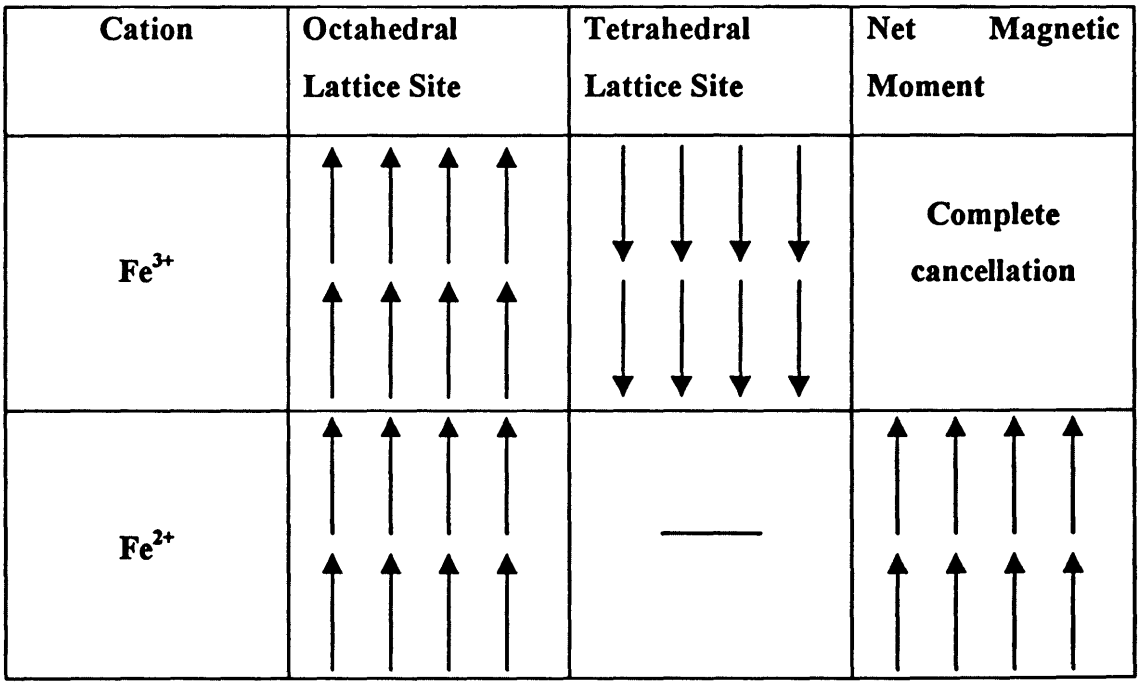


Figure 1.3 Distribution of spin magnetic moments for Fe^{2+} and Fe^{3+} ions in a unit cell of Fe_3O_4.

The interactions of the net moments are continuous throughout the rest of the crystal and so domains can form in a similar manner. Ferrimagnets also have a Curie point and paramagnetic behaviour would expect to be observed above the Curie

temperature. But, due to the negative interaction, the curve $1/\chi$ versus T is concave as shown in Figure 1.4. This behaviour is confirmation of Néel's theory.

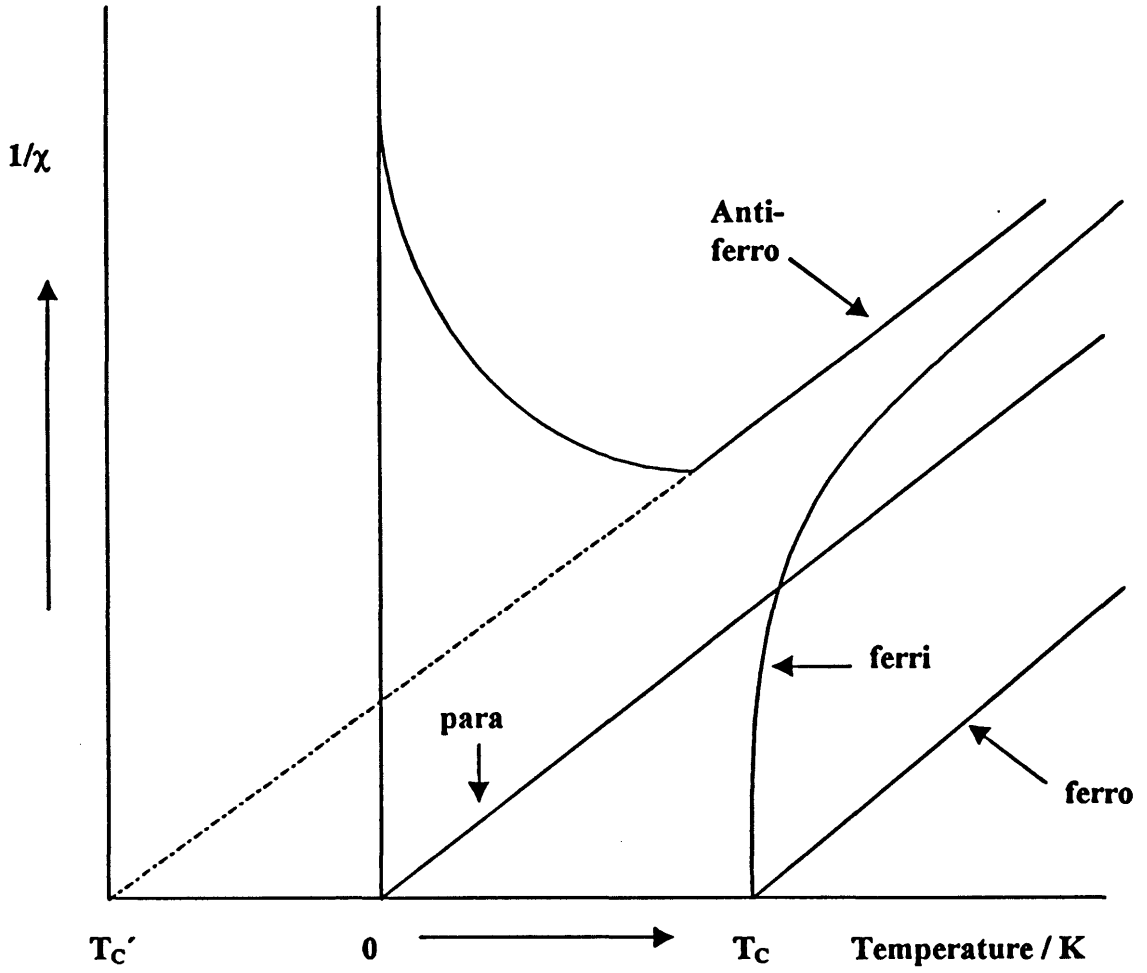


Figure 1.4 Comparison of the temperature dependencies of the reciprocal susceptibilities of paramagnetic, ferromagnetic, antiferromagnetic and ferrimagnetic materials. T_C= Curie temperature for ferromagnetic and ferrimagnetic materials. T_C' = extrapolated negative Curie temperature for antiferromagnetic materials.[11]

1.4 Crystal Structure of Ferrites

The crystal structure of a ferrite can be regarded as an interlocking network of positively charged metal ions (Fe^{3+}, M^{2+}) and negatively charged oxide ions (O^{2-}). The crystal structure of the ferrite plays an important role in determining the magnetic interactions and thus, the magnetic properties. Ferrites crystallise in three different crystal types, namely, spinel, garnet and magnetoplumbite and so they can be classified into these groups (see **Table 1.1**). Only the crystal structure of the spinel ferrite will be dealt with in detail since this is the only one of relevance to this thesis. The crystal structure of the magnetic garnets was elucidated by Geller and Gilleo[22] and the structure consists of tetrahedral, octahedral and dodecahedral sites. The magnetoplumbite structure is hexagonal with all the magnetic moments aligned along one preferred axis.[16] These materials are largely used as ceramic-type permanent magnets.

Table 1.1 Crystal types of ferrites

Type	Structure	General formula	Example
Spinel	Cubic	$A^{II}Fe_2O_4$	A^{II} = Cd, Co, Mg, Ni, Mn and Zn
Garnet	Cubic	$Ln_3^{III}Fe_2O_{12}$	Ln^{III} = Y, Sm, Eu, Gd, Tb, Ho, Er, Tm, and Lu
Magneto-plumbite	Hexagonal	$A^{II}Fe_{12}O_{19}$	A^{II} = Ba and Pb

1.4.1 Spinel Chemistry

The spinel structure is derived from the mineral spinel [$MgAl_2O_4$ or ($MgO.Al_2O_3$)]. The spinel lattice is composed of a cubic close-packed arrangement (abcabc) in which 32 oxide ions form a unit cell. Between the layers of oxide ions are interstices that

may accommodate the metal ions. One type of site (A site) is co-ordinated with four nearest neighbour oxide ions in the form of a tetrahedron. These sites are called tetrahedral sites. The second type of site (B site) is co-ordinated with six nearest neighbour oxide ions which describe an octahedron. These B sites are called octahedral sites. In the unit cell of 32 oxide ions there are 64 tetrahedral sites and 32 octahedral sites. If, as in the mineral spinel, the tetrahedral sites are occupied by divalent ions and the octahedral sites are occupied by trivalent ions, then only one eighth of the tetrahedral sites and one half of the octahedral sites can be occupied in order to obtain a balance of the overall charges. Therefore, the unit cell would consist of eight units of AB_2O_4. A spinel unit cell contains two types of subcells as shown in **Figure 1.5**. These subcells alternate in a three-dimensional array, so that each fully repeating unit cell requires eight subcells.

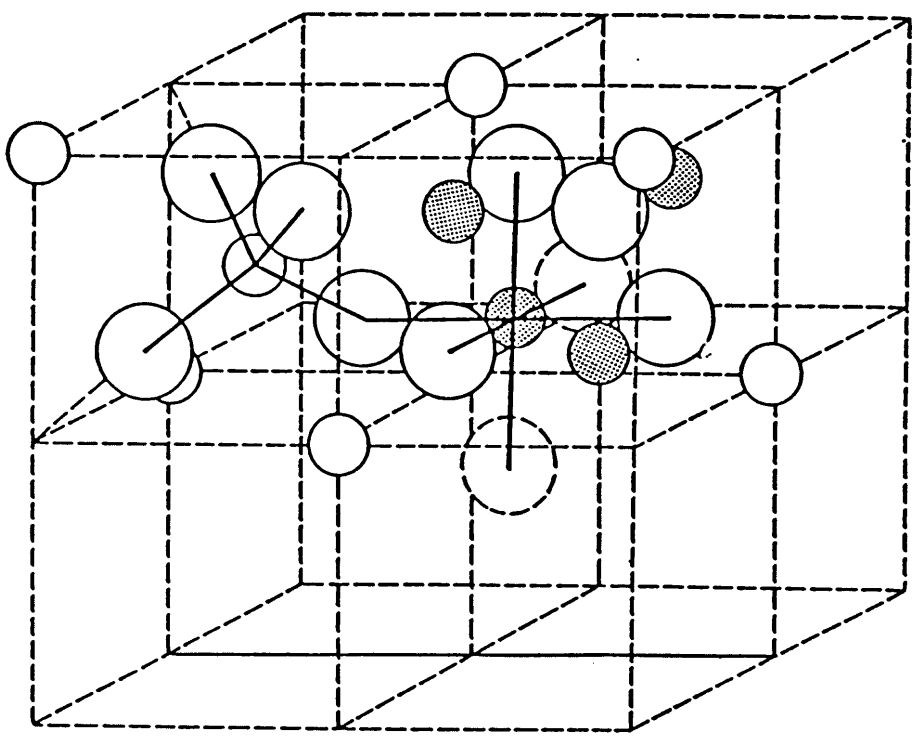


Figure 1.5 Two subcells of a unit cell of the spinel structure.[16]

The mechanism of ferrimagnetism in spinel structured compounds involves the negative exchange interaction of atomic moments of ions on two different lattice sites.

Many properties of ferrites can be predicted by gaining an understanding of these interactions and the site preferences of the metallic ions.

In general, for ions of one element, octahedral sites require larger radii than tetrahedral sites and hence should accommodate divalent ions in preference to trivalent ions since divalent ions have generally larger radii than trivalent ions. Therefore, it would be reasonable to assume that the Fe^{3+} ions occupy the tetrahedral sites in preference to the divalent cations and this is what normally occurs. However, in Zn-containing ferrites, the Zn^{2+} ions have preference for tetrahedral sites because their structural chemistry favours tetrahedral interactions. Thus, Zn^{2+} ions replace some of the Fe^{3+} ions in the tetrahedral sites with a consequential change in magnetic properties.

1.4.2 Interaction between Magnetic Moments on Lattice Sites

As already mentioned, the metallic ions in ferrites occupy two crystallographically different sites i.e. tetrahedral (A) sites and octahedral (B) sites. Three kinds of magnetic interactions are possible between the metallic ions through the oxide ions by a superexchange mechanism, namely; A-A interactions, B-B interactions and A-B interactions.

The superexchange mechanism proposes that one of the electrons on the oxide ion could interact with, or exchange with, the unpaired electrons in one of the metal ions on a lattice site (A or B). To do this, the oxide-based spin would have to be opposite to that of the metal ion. This leaves the second spin of the oxide ion suborbital (which is opposite to the first) to couple with an unpaired spin of another metal ion preferably located opposite to the original metal ion. This leads to an antiparallel alignment (negative interaction) of the two metal ions adjacent to the oxide ion.

The strength of interactions between magnetic moments of two metal ions on different sites depends on the distances between these ions and the oxide ions that link them as well as on the angle between the three ions. An angle of 180° will give rise to the greatest interaction energy. The energy would decrease very rapidly with increasing distance apart.

Figure 1.6 shows the interatomic distances and the angles between the ions for the different types of interactions. The large open circles represent oxide ions; the smaller

circles are cations. The interionic angles φ are calculated from an analysis of the geometry of the spinel structure. The A-B interaction at 125°9′ is by far the strongest and is the only significant magnetic interaction in ferrites.

Therefore, with the A-B interactions at 125°9′ predominating, the spins of the A and B site ions in ferrites will be oppositely magnetised with a resultant magnetic moment equal to the difference between those of A and B site ions. With this theory, Néel was able to explain the ferrimagnetism of ferrites.

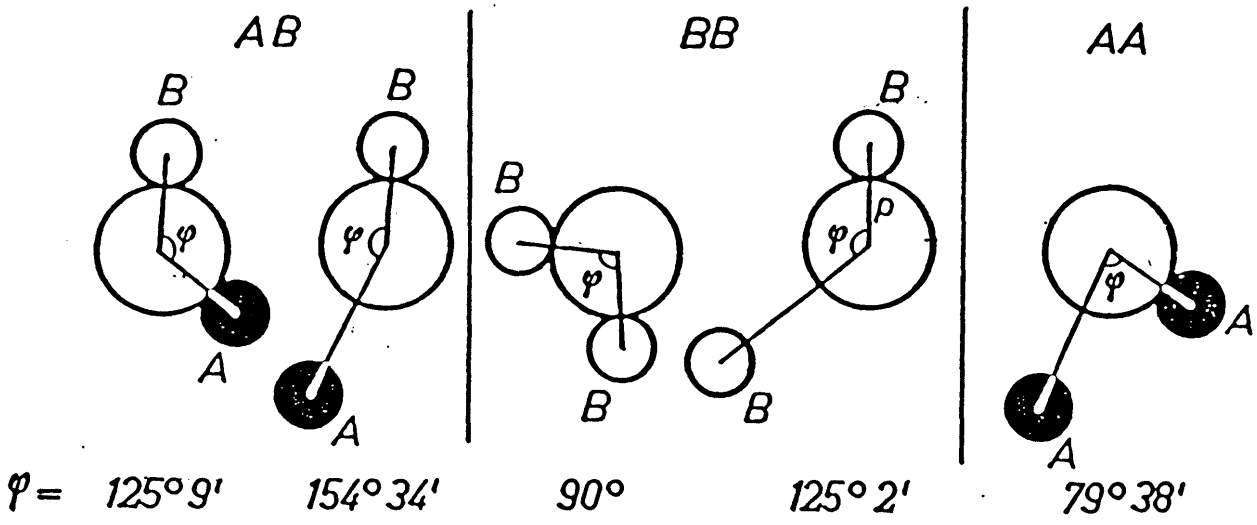


Figure 1.6 Interionic distances and angles in a spinel structure for the different types of lattice sites interactions.[11]

1.4.3 Normal and Inverse Spinels

If spinels display occupancy of A (tetrahedral) and B (octahedral) sites by M^{2+} and Fe^{3+} ions respectively, they are described as having the normal spinel structure. An example of this would be zinc ferrite with the Zn^{2+} ions occupying the eight tetrahedral sites (co-ordination preference) and the Fe^{3+} ions occupying the sixteen octahedral sites, see **Figure 1.7.** Zinc ions, being non-paramagnetic, produce no antiferromagnetic orientation of the ions on the octahedral sites (Fe^{3+} ions). Also Fe^{3+} (B-B) interactions are so weak as to be unimportant and therefore zinc ferrite is not ferrimagnetic.

However, a number of ferrites, including magnetite and Ni-ferrite, crystallise in an "inverse spinel" structure, in which the eight divalent cations occupy the octahedral sites and the sixteen ferric ions are evenly divided to occupy tetrahedral and octahedral sites, Figure 1.7. For example in $NiFe_2O_4$, the ferric ions preferentially fill the tetrahedral sites but there is only room for half of them (eight). The remaining eight fill the octahedral sites, as do the eight Ni^{2+} ions giving an inverse spinel structure. The antiferromagnetic interactions orient the eight Fe^{3+} moments and eight Ni^{2+} moments antiparallel to the eight Fe^{3+} moments in the tetrahedral sites. The Fe^{3+} moments cancel, but the moments on the Ni^{2+} ions give rise to an uncompensated moment or magnetisation. Many of the commercially important ferrites are inverse spinels. The occupancy of the two kinds of sites by different cations is compared between normal and inverse spinel structures in Figure 1.7.

	Normal spinel structure	Inverse spinel structure
1. Formula units/unit cell	$8(M^{II})[Fe_2^{III}]O_4$	$8(Fe^{III})[M^{II}Fe^{III}]O_4$
8 M^{II} ions occupy	(A) sites	[B] sites
16 Fe^{III} ions occupy	[B] sites	8 (A) sites 8 [B] sites
2. Typical example	$8\{ZnFe_2O_4\}$	$8\{NiFe_2O_4\}$
Spin coupling:		
Spins on 8 (A) sites	Zn^{II} - 00000000	Fe^{III} -↓↓↓↓↓↓↓↓
Spins on 8 [B] sites	Fe^{III} -↑↑↑↑↑↑↑↑	Fe^{III} -↑↑↑↑↑↑↑↑
Spins on 8 [B] sites	Fe^{III} -↓↓↓↓↓↓↓↓	Ni^{II} -↑↑↑↑↑↑↑↑
Resultant moment	0	$2\times8 = 16\ \mu_B$/unit cell
3. Other examples	$CdFe_2O_4$	$MnFe_2O_4$, Fe_3O_4, $CoFe_2O_4$, $CuFe_2O_4$, $MgFe_2O_4$, and $Li_{0.5}Fe_{2.5}O_4$

Figure 1.7 Metal ion distribution in ferrites.[17]

It is also possible to obtain mixtures of normal and inverse spinels. This situation is represented by the formula $(M^{2+}_{\delta}Fe^{3+}_{1-\delta})[M^{2+}_{1-\delta}Fe^{3+}_{1+\delta}]O_4$, where cations in the parentheses are at the A sites and those in square brackets are at the B sites. The extreme case $\delta = 1$ corresponds to the normal spinel structure and the other extreme case of $\delta = 0$ corresponds to the inverse spinel structure. The factors that determine the distribution of cations are ionic radius, electronic configuration, electrostatic energies and polarisation effects.[18] Neutron diffraction has confirmed the structure of normal and inverse spinels[19] since this technique can distinguish between Fe^{3+} ions and divalent cations involved in the ferrite (X-ray diffraction techniques cannot be used for this purpose).

1.4.4 Mixed Zinc Ferrites

Only simple ferrites which contain a single species M^{2+} ion have been described so far. Nearly all simple ferrites are capable of dissolving each other to form a series of solid solutions known as "mixed ferrites". Typically mixed ferrites contain both Zn and Ni or Zn and Mn as well as Fe. As previously stated, Zn^{2+} ions prefer tetrahedral sites to octahedral sites. Therefore, Zn^{2+} ions fill the tetrahedral sites before the ferric ions. This preference is used in mixed zinc ferrites where Zn^{2+} ions replace some of the magnetic Ni^{2+} or Mn^{2+} ions. This leads to an enhancement of the net magnetic moment of the Ni-Zn or Mn-Zn ferrite, see **Figure 1.8**. At first glance this enhancement seems rather odd because Zn-ferrite itself has no net magnetic moment per unit formula. However, this effect can be explained in terms of the formula previously given for the mixed ferrites. Based on the formula $(Zn^{2+}_{\delta}Fe^{3+}_{1-\delta})[M^{2+}_{1-\delta}Fe^{3+}_{1+\delta}]O_4$[20] and the known number of unpaired electrons of 0, 5.0 and **m** per ion for Zn^{2+}, Fe^{3+} and M^{2+} respectively, the total magnetic moment on the A and B sites per formula unit would be $2[5(1-\delta) + 1]^{1/2}$ and $2[m(1-\delta) + 5(1+\delta) + 1]^{1/2}$ (see equation [6]) in units of B.M., respectively. Because these moments are antiparallel, the resulting moment is obtained by taking their difference. Hence, the net magnetic moment ($\mu_{.eff}$) of such a mixed ferrite is expected to be:

$$\mu_{.eff} = 2[10\delta + m(1-\delta) + 1]^{1/2} \qquad [7]$$

in units of Bohr-Magnetons. The values of m for Mn^{2+}, Fe^{2+} and Ni^{2+} ions are 5, 4 and 2 respectively. Using these values, the calculated values for μ_{eff} (= μ_B) as a function of the concentration of the zinc-ferrite δ, are represented in **Figure 1.8.** As expected, the increase in moment with zinc concentration is quite linear until at about 50 percent replacement, the curve heads downward. This is due to the dilution of the spin moments, which weakens the A-B interaction by increasing the distance between the spins.

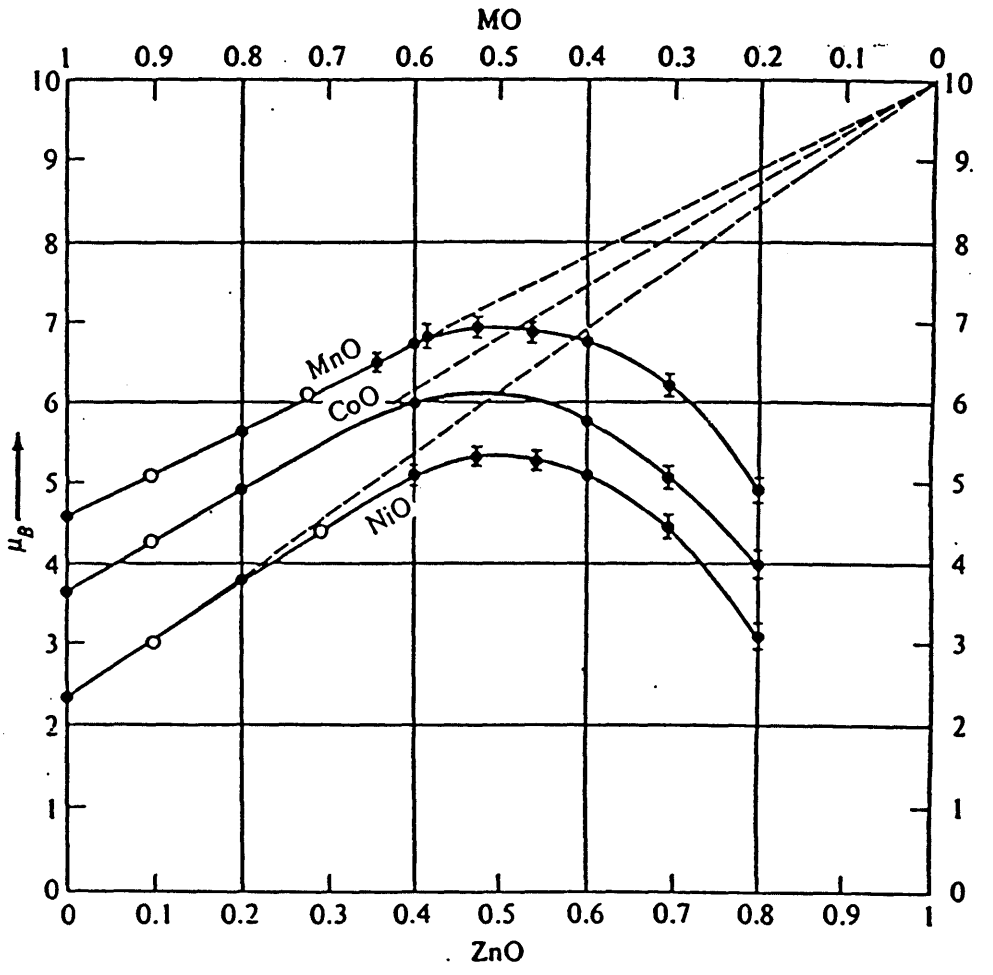


Figure 1.8 Effect of zinc concentration on the magnetic moments of some ferrites.[21]

Any ferromagnetic material that is at a temperature below T_c can be considered to be composed of small volume regions in which there is a mutual alignment in the same direction of all magnetic dipole moments. Such a region is called a "domain" and the term "spontaneous magnetisation" is used to describe the magnetic property. Bloch[23] first proposed the idea of magnetic domains with domain walls separating them. Domains contain about 10^{12} - 10^{15} atoms and their dimensions are of the order of microns (10^{-4} cm). Domain boundaries or walls (Bloch Walls), across which the direction of magnetisation gradually changes, separate adjacent domains as shown in **Figure 1.9**. In a macroscopic piece of material (e.g. polycrystalline specimen) there will be a large number of domains and all may have different magnetisation directions. The magnitude of the magnetisation field (M) for the entire solid is the vector sum of the magnetisations of all the domains, which is be approximately zero in the absence of an external field.

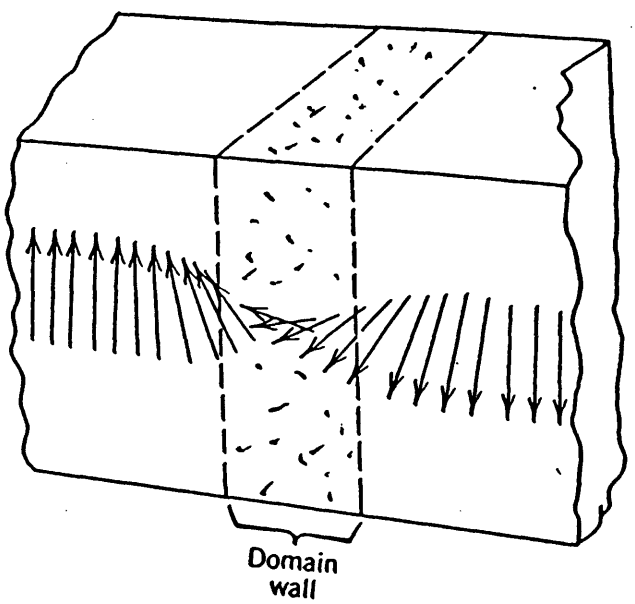


Figure 1.9 The gradual change in a magnetic dipole orientation across a domain wall.[24]

The size and shape of a domain may be determined by the minimisation of several types of energies:

(1) Magnetostatic energy: This is the work needed to put magnetic poles in special geometric configurations and it decreases as the width of the domain decreases.
(2) Magnetocrystalline anisotropy energy: In most magnetic materials, the domain magnetisation tends to align itself along one of the main crystal directions. The magnetocrystalline anisotropy energy is the difference in energy between a state where the magnetisation is aligned along an "easy direction" (i.e. a direction along the crystallographic axes such as along the edge of a cube body or a body diagonal) and a state where the magnetisation is aligned along a "hard direction" (i.e. a direction which is not of the crystallographic axes). The energy of the domain can be lowered by the anisotropy energy by aligning the moments (ferrimagnetics) along an easy direction of magnetisation.
(3) Magnetostrictive energy: When a magnetic material is magnetised, small changes in its dimensions occur. The relative change is called magnetostriction and the energy of magnetostriction depends on the amount of stress introduced on magnetisation. Stresses in ferrites can be introduced by firing, grinding or machining.
(4) Domain Wall energy: This energy decreases with an increase in the width of the wall.

The whole array of domains will be ordered in such a way as to minimise the total energy of the system composed of the above four energies.

1.5.1 Dynamic Behaviour of Domains

The magnetisation in a domain (and therefore a sample) can be changed when placed in a magnetic field in two ways. The first acts by rotating the magnetisation toward the direction of the field. The other way, which is called the domain wall motion, does not change the direction of magnetisation but instead changes the volume occupied by different domains. **Figure 1.10** shows an idealised arrangement of domains.

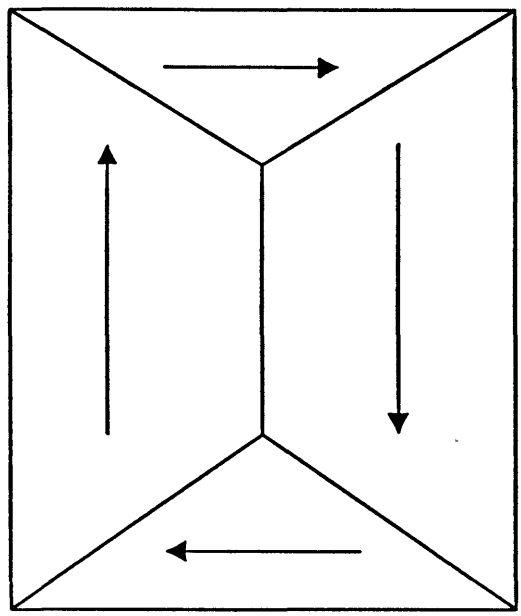


Figure 1.10 A Schematic diagram of an idealised domain pattern.

If an external field, H, is applied, the domain walls experience a pressure which tends to make those domains having a component of magnetisation, M, in the direction of the field grow at the expense of the unfavourably orientated domains as shown in **Figure 1.11(a)-(f)**. The effect of increasing the applied field in the domain is represented by the figures in the left-hand side of **Figure 1.11**. The corresponding effect of increasing the field on the flux density of the sample, B, is shown in the diagrams to the right-hand side in **Figure 1.11** [note: for $M >> H$, $B = \mu_o M$, where $\mu_o = 4\pi \times 10^{-7}$ $VA^{-1}m^{-1}s$]. In the absence of an applied field the walls are straight and might occupy the positions shown in **(a)**. The dots represent imperfections. If a small field is applied in the direction shown in **(b)** the walls remain pinned by the imperfections and are characterised by reversible domain wall movements and rotations. As the field increases the pressure on the walls overcomes the pinning effect and the walls move by a series of jumps **(c, d, e)**. These movements are irreversible. Finally further increases in field strength cause the magnetisation vector to rotate reversibly towards the external field direction until complete alignment is approached **(f)**. No further increase in magnetisation is then possible and the material is referred to as saturated.

If the magnetic field, having reached the maximum value corresponding to **Figure 1.11(f)**, is made to alternate cyclically about zero at the same maximum amplitude, the initial magnetisation curve will not be retraced. Due to the irreversible domain wall movements the magnetisation will always lag behind the field and an open loop will be formed. This phenomenon is known as magnetic hysteresis and the loop is called a hysteresis loop, **Figure 1.12.**

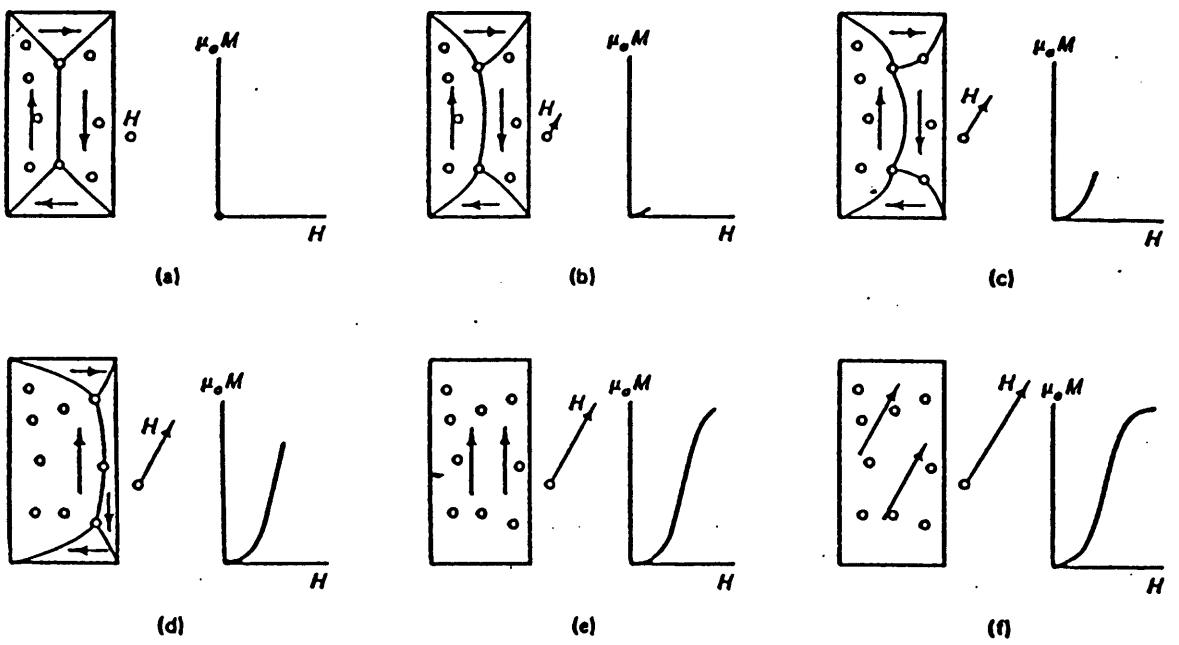


Figure 1.11 A simplified representation of the part played by domain boundaries in the process of magnetisation.

The maximum value of **B** is the saturation flux density B_s, and the corresponding magnetisation is the saturation magnetisation M_s. Since the permeability of the sample is defined as the slope of the **B** vs **H** curve, it is clear that the permeability changes with **H**. At **H** = 0 tesla, the slope of the **B** vs **H** curve is specified as a material property called the initial permeability, μ_i. The chemical composition of the ferrite, the grain size of the ferrite and the porosity of the ferrite can all affect the permeability. Another material property that can be described from the hysteresis loop is called the

coercive force or coercivity (H_c). This is the value of the reverse field needed after saturation to reduce the induction to zero - see **Figure 1.12.**

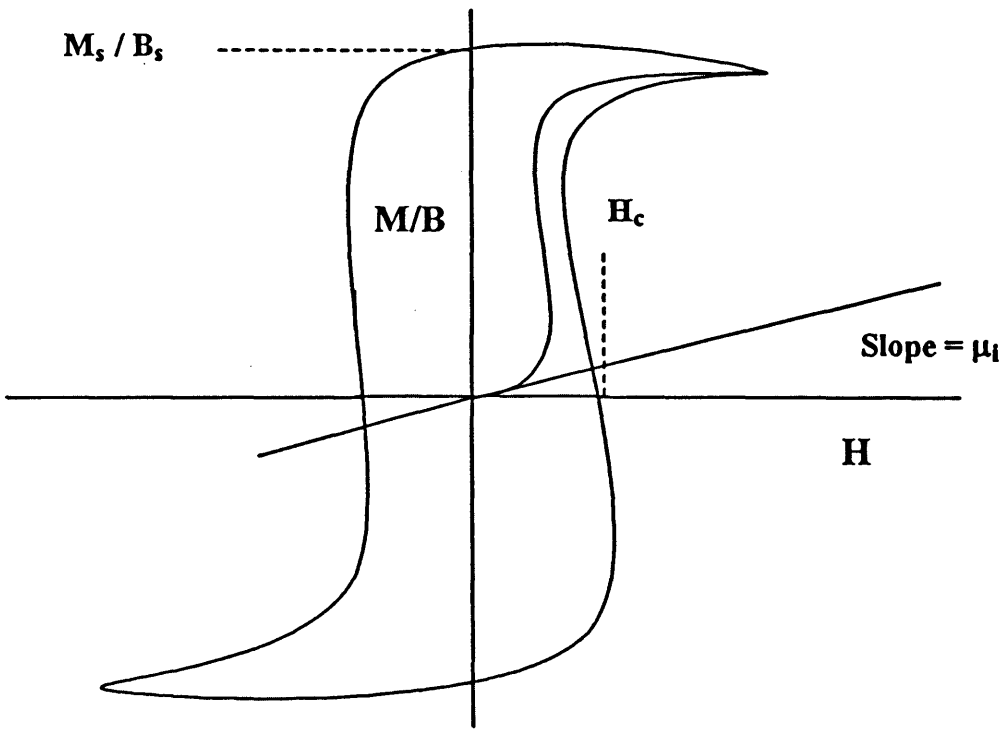


Figure 1.12 A schematic diagram of a hysteresis loop.

1.6 Properties of "Soft" Ferrites (such as Mn-Zn and Ni–Zn Ferrites)

"Soft" ferrites are used in devices that are subjected to alternating magnetic fields and in which energy losses must be low (e.g. transformer cores). The area contained in the hysteresis loop is indicative of the losses in the material during the cyclic magnetisation process. Therefore, the relative area within the hysteresis loop must be small, i.e. it is characteristically thin and narrow as in **Figure 1.13**. Consequently, a "soft" ferrite must have high initial permeability and a low coercivity. "Hard" ferrites are materials that require large magnetic fields for either magnetisation or demagnetisation. Thus, their hysteresis loops are square blocked and they have a large coercivity value. These ferrites are used in permanent magnet applications such as loudspeakers and permanent magnet motors.

There are three major loss factors (as shown below) that contribute to the overall core loss of the ferrite material. These losses must be reduced as much as possible to increase the efficiency of the soft ferrite.

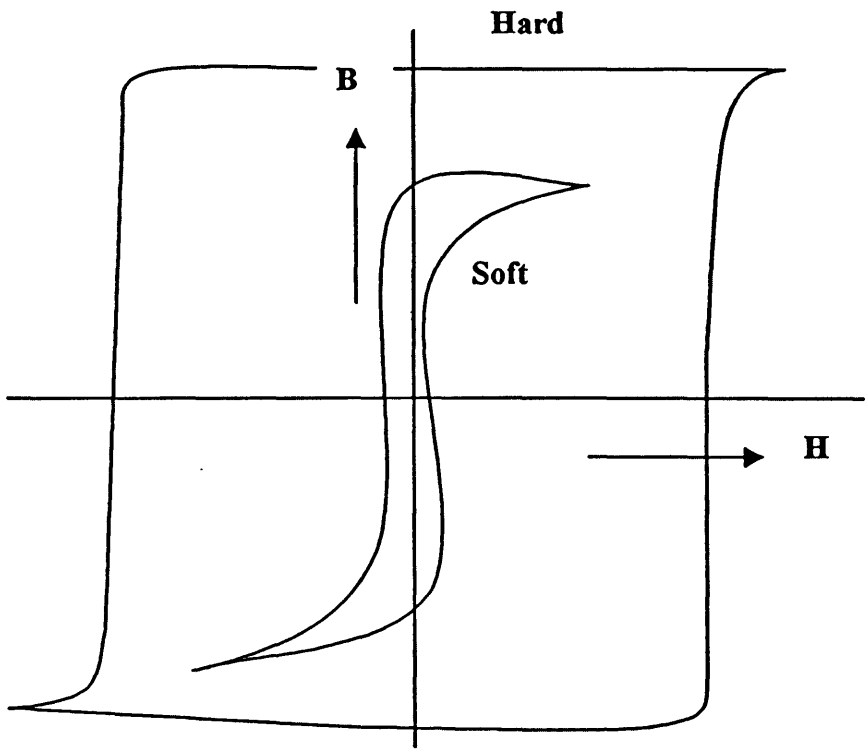


Figure 1.13 Schematic magnetisation curves for soft and hard magnetic materials.[25]

(1) Hysteresis loss: The area inside a hysteresis loop is proportional to the hysteresis energy losses by the ferrite. The loss is produced by irreversible domain changes of the ferrite and is linked to the porosity of the ferrite.

(2) Eddy Current Losses: Energy losses may result from electrical currents that are induced in a magnetic material by a magnetic field that varies in magnitude and direction with time, these are called eddy currents. This energy loss can be minimised by increasing the electric resistivity of the soft ferrite. Additives such as SiO_2, CaO_2, TiO_2, SnO_2, etc. can increase the resistivity of the grain boundary. Lead borosilicate glass is also used to augment the resistivity of ferrites and is of particular interest to this thesis.

(3) Loss tangent: Initial permeability (μ_i) of a ferrite material has two components, namely, the real and imaginary parts. The ratio of the imaginary part representing

the losses in the material to the real part of the permeability is a measure of the inefficiency of the magnetic system and is called the loss tangent.

1.7 Preparation of Ferrites

Ferrites can be prepared by a wide variety of techniques commonly used in solid-state chemistry, leading to samples in a variety of forms, such as polycrystalline aggregates, thin and thick films or single crystals. The oldest technique, the ceramic method (or the "shake and bake" method) involves the same operations as the classical techniques for the fabrication of conventional ceramics. The raw materials are usually iron oxide (α-Fe_2O_3) and the oxide or carbonate of the other cations in the desired ferrite. These are combined according to the overall reactions for spinels, garnets and hexagonal ferrites, respectively, where **M** represents a divalent cation and **RE** a rare earth trivalent cation.

$$Fe_2O_3 + MCO_3 \longrightarrow MFe_2O_4 + CO_2 \quad [8]$$

$$5Fe_2O_3 + 3RE_2O_3 \longrightarrow 2RE_3Fe_5O_{12} \quad [9]$$

$$6Fe_2O_3 + BaCO_3 \longrightarrow BaFe_{12}O_{19} + CO_2 \quad [10]$$

The iron oxide and the carbonates or oxides are generally mixed dry and milled in ball-mills and then calcined at temperatures above 900°C. Calcining involves heating the blended material to a high temperature which is usually about 100 to 300°C below the final firing temperature of > 1,000°C. This begins the process of forming the ferrite lattice by inter-diffusing the substituent oxides into a chemically and crystallographically uniform structure. Calcining has the obvious advantage of homogenising the material. The material is finally baked in ovens at temperatures between 1000 and 1400°C to complete the formation of the ferrite powder.

This method has the advantage of being inexpensive and adaptable to large-scale production. However, it has several drawbacks, including (a) limited stoichiometric control, (b) the necessity of a time- and energy-consuming calcination step (c) the possible introduction of impurities from the grinding process and (d) the relatively

coarse particles of the product. Despite these disadvantages, the large majority of ferrite powders are made currently by this process.

Numerous methods have been developed to overcome the limitations of the ceramic technique. These processes usually involve producing the ferrite powder by a "wet" method. In the most common method, a solution is formed with the cation stoichiometry of the desired ferrite. Then, a controlled precipitation (coprecipitation) is instigated which leads to a mixture of very small particles containing the cations in the right proportions. In a modification of this method, the equivalent to the "precipitation" occurs by the removal of the solvent either by evaporation (spray drying)[26] or by the solidification of the solvent (freeze-drying)[27] or by the addition of a different solvent (sol-gel formation).

Another recent approach to ferrite preparation involves molecular precursors.[28] The technique is based on the preparation of a single molecular species which contains the cations of the ferrite in the stoichiometric proportions. A molecular precursor for nickel ferrite was prepared recently.[29] The precursor, hexaaquannickel(II) [chloro (hydrogen)ethylenediaminetetraacetato]ferrate(III) tetrahydrate, $[Ni(H_2O)_6][FeCl(EDTA)H]_2.4H_2O$, was prepared at room temperature and contained the metal cations in the correct proportion to form $NiFe_2O_4$. In all the above wet methods, the precipitate or organic precursor is heated to form the ferrite. The nickel ferrite molecular precursor was observed to decompose in stages successively losing water, the EDTA ligand and finally HCl to form the ferrite at 900°C.

Recently, two other novel methods for preparing ferrites have appeared. The first method prepared magnetic ferrites in a reversed micelle medium. A reversed micelle medium is a water in oil medium and ferrite particles can be grown to specific nanometre sizes. Iron ferrite and cobalt ferrite particles were prepared by this method.[30] Ferrous and colbaltous dodecylsulphate micellar solutions were added to an aqueous solution containing methylaminehydroxide. The resulting mixture was freeze-dried to form the magnetic ferrite particles.[30] This type of method was also employed in the preparation of polymer-ferrite nanoparticles.[31] Ferrous sulphate and ammonium hydroxide were put into water-in-oil microemulsions (reversed micelles). Polymerisation of *p*-ethylphenol in this environment precipitated ferrite nanocrystals.[31] The authors considered that this technique could be used in medicine for a magnetically guided drug-delivery service.

The second method involves the preparation of Ni ferrites *via* metal carboxylates which are liquids at room temperature.[32] Liquid metal carboxylates of the type $Ni(MEEA)_2$ and $Fe_3O(MEEA)_7$, where MEEA = $CH_3OCH_2CH_2OCH_2CH_2OCH_2CO_2^-$ (a polyether carboxylate anion), were prepared and used in different ways to form Ni ferrites. One way was to disperse Fe_3O_4 powders into $Ni(MEEA)_2$, which on heating to 800°C formed $NiFe_2O_4$ particles.[32] A second way was to dissolve $Ni(NO_3)_2$ into $Fe_3O(MEEA)_7$ and form a precursor to $NiFe_2O_4$. Heating this to 400°C afforded crystalline $NiFe_2O_4$ particles.[32]

Despite the recently developed methods mentioned above, the coprecipitation and the sol-gel techniques are the most widely employed methods used to form ferrites and are described in detail below.

1.7.1 Coprecipitation Technique

This method of ferrite formation is based on the initial preparation of aqueous solutions of chlorides, nitrates or sulphates of Fe^{3+}, Ni^{2+}, Mn^{2+} and Zn^{2+} ions in the required stoichiometries for the ferrite. The ions are simultaneously precipited in the form of hydroxides (by addition of NaOH), or in the form of oxalates (by addition of oxalic acid), or in the form of carbonates (by addition of bicarbonate solution). The precipitate is filtered, washed, dried and fired. Ferrite powders are prepared by the thermal decomposition of the precipitates at temperatures considerably lower than in the ceramic method. Other advantages of coprecipitation over the ceramic method are:

(1) Greater homogeneity;
(2) Greater reactivity;
(3) Higher purity - no grinding;
(4) Fine particle size;
(5) Elimination of calcining step.

Numerous examples of coprecipitation have been reported in the literature. Akashi *et al.*[33] reported the production of ferrites with good magnetic properties from coprecipitated hydroxide powders. Takada and Kiyama[34] obtained similar results from hydroxide precipitates. Goldman and Laing[35] produced ferrites with very low loss

factors from coprecipitated carbonate hydroxide powders. Yu and Goldman[36] reported forming individual spherical ferrite particles by precise control of the carbonate hydroxide coprecipitation and ageing processes. Economos[37] coprecipitated nickel-iron hydroxides with tetramethylammonium hydroxide and decomposed them to form nickel-ferrite. Chaudhuri and Roy[38] prepared some Ni, Co and Mn ferrites with, and without, partial substitution by Zn using coprecipitation by ammonium hydroxide. Goldman[35] reported the use of an amine to coprecipitate nickel-iron and nickel-zinc-iron hydroxides.

As previously mentioned, ferrites can also be synthesised by the decomposition of mixed-metal oxalates. Wickham *et al.*[39] coprecipitated the oxalates of Fe, Co, Ni or Zn by adding ammonium oxalate to the solution of metal sulphates. Firing the resultant oxalate mixture at 800°C formed the ferrites.[39]

Coprecipitates of complex metal citrates have been formed by the alcohol dehydration of mixed metal (Mn, Fe, Zn) citrate solutions.[40] These can be thermally decomposed to ferrites at a relatively low temperature.[40] Iron-manganese hydroxycarbonates were prepared by coprecipitation of the metal chlorides with sodium carbonate in alkaline solution.[41] Thermal decomposition of these precipitates at 400°C produced mixed oxides with a spinel structure.[41]

1.7.2 Sol-Gel Technique

The term sol-gel is used broadly in several areas of chemistry. A "sol" is a suspension of colloidal particles in a liquid. The term "gel" refers to a semi-rigid mass formed when the colloidal particles are linked by surface forces to form a network. The gel is formed usually by the addition of water to the sol, which changes the pH of the system and reduces the repulsion between particles and, therefore, increases the viscosity of the system.

Two different gels may be obtained as a result of the destabilisation of a sol. The aquagel is a colloidal gel which may be formed when water is added quickly to a sol. If water is added slowly and in small amounts, the process of condensation-polymerisation of the sol may form a polymeric gel. Polymeric gels are also known as alcogels. The next stage in sol-gel processing is the drying of the gel, i.e. the removal of the dispersion medium. Fast removal leads to a powder xerogel while very slow

removal may lead to a monolithic xerogel. A basic flow diagram outlining the processing steps for the two methods is shown in **Figure 1.14**.

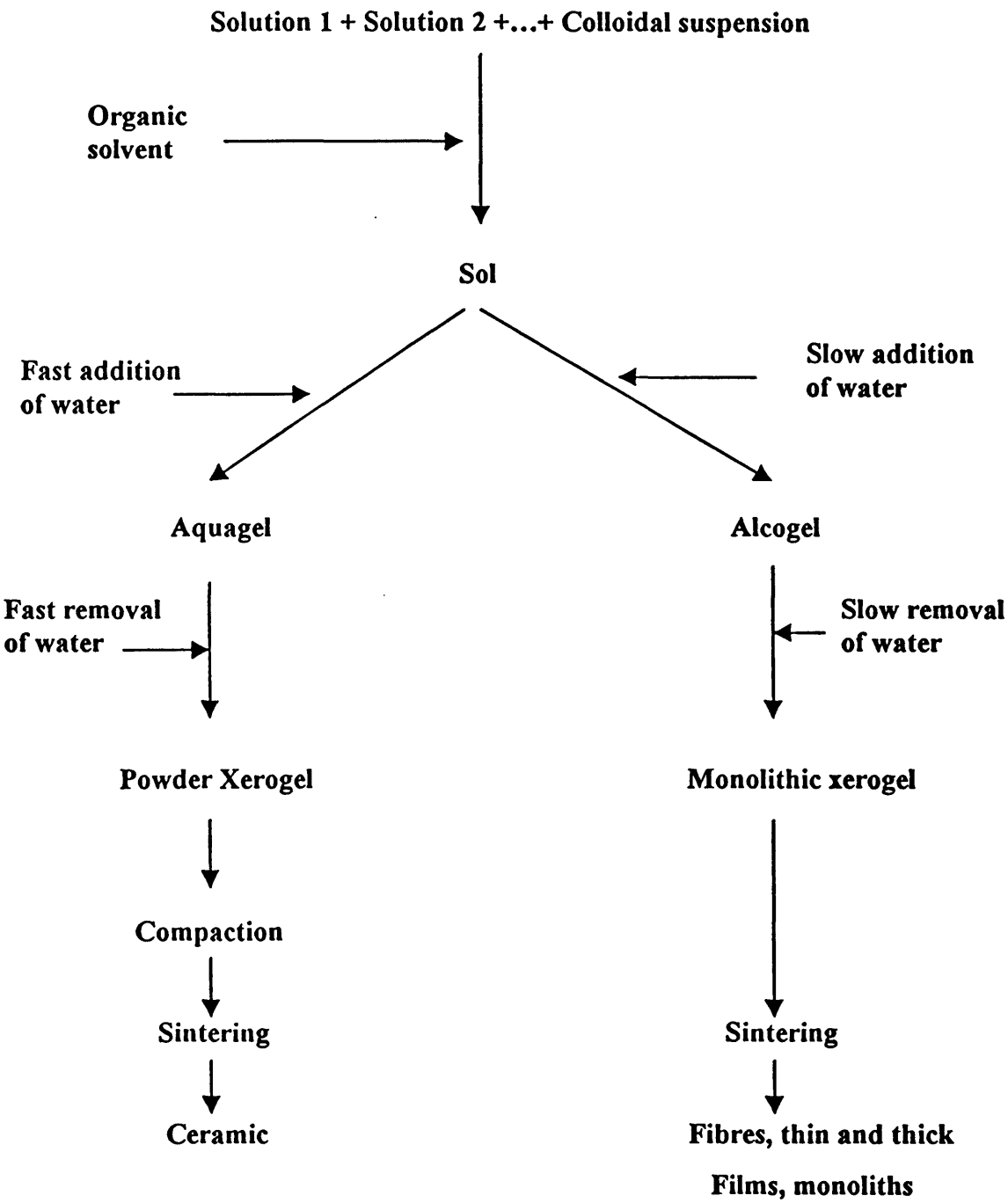


Figure 1.14 Schematic operations in the sol-gel process.

In general, the formation of a gel from a sol medium proceeds through hydrolysis and condensation reaction mechanisms. Taking the example of a tetravalent metal alkoxide, the reactions may be expressed as follows:

(a) Hydrolysis:

$$M(OR)_4 + H_2O \longrightarrow M(OR)_3OH + ROH \quad [11]$$

(b) Condensation:

$$M(OR)_3OH + M(OR)_4 \longrightarrow (RO)_3M - O - M(OR)_3 + ROH \quad [12]$$

$$M(OR)_3OH + M(OR)_3OH \longrightarrow (RO)_3M - O - M(OR)_3 + H_2O \quad [13]$$

These reactions can be accelerated by acid or base catalysis.

A variety of ferrites has been prepared *via* the sol-gel route. Barium hexaferrite has been synthesised from Fe and Ba propoxides and using *iso*-propyl alcohol as the solvent.[42] The sol was gellated by addition of water and the hexaferrite was obtained by calcining to 700°C.[42] Ni-Zn ferrites having dimensions varying from 13 to 35nm (i.e. in the nanocrystalline range) have been formed within a silica glass matrix by a sol-gel route.[43] These ferrites were prepared from their corresponding nitrates and their Mössbauer spectra confirmed the presence of ultrafine particles exhibiting superparamagnetic relaxation.[43]

One of the earliest patents in sol-gel chemistry was issued for the synthesis of a nickel-zinc ferrite.[44] The sol was made from a mixed nitrate solution which yielded colloidal particles on reaction with ammonia. Ageing at temperatures as low as 250°C gave spherical particles which had spinel structures.[44] Nickel, zinc, manganese-zinc and cobalt ferrites have been developed by researchers using the sol-gel method with nitrate solutions which were neutralised with a base.[45] Heating the products at temperatures between 135 and 200°C under a pressure of saturated steam afforded the ferrite particles.[45] The resulting ultrafine powder could be densified to >97% of theoretical value when heated at 1000°C.[45] Powdered Fe_3O_4 was prepared by this method from Fe(III) carboxylate in an alcoholic medium,[46] but the process involved high temperatures and only particles of micrometre sizes were formed.[48] Nanometre sized particles of Fe_3O_4 were prepared hydrothermally from iron(II) 2-methoxyethoxides dissolved in a 2-methoxyethanol / water solvent.[47] The formation of these particles was achieved at low temperatures (140°C) and superparamagnetic properties were observed for the powders.[47] Ultrafine, magnetic nickel ferrite particles were prepared by the hydrolysis of iron(III) and nickel carboxylates in an organic

solution with water at 200°C – 240°C and 0.75 – 1.3MPa in an autoclave.[48] The reaction is given below:

$$Ni(RCOO)_2 + 2Fe(RCOO)_3 + 4H_2O \longrightarrow NiFe_2O_4 + 8RCOOH \quad [12]$$

The size of the particles ranged from 0.5 to 0.05μm and the nickel ferrite was free from organic material.[48]

Thin films of ferrites were also prepared by the sol-gel technique. Thin films consisting of γ-Fe_2O_3 particles were prepared from a solution of ferric nitrate dissolved in ethylene glycol.[49] The iron oxide particles in the films occurred as spheres and the film had no magnetic anisotropy and poor coercive forces. Magnetite (Fe_2O_3) thin films coated on a silica glass substrate have been synthesised.[50] The sol solution for the dip-coating was prepared using $Fe(acac)_3$ as a reagent and acetic acid and nitric acid as solvent and catalyst respectively. The silica glass substrate was dipped into the sol solution and pulled out slowly. Various heat treatments eventually formed Fe_3O_4 particles of approximately 50nm diameter (**Figure 1.15**).[50]

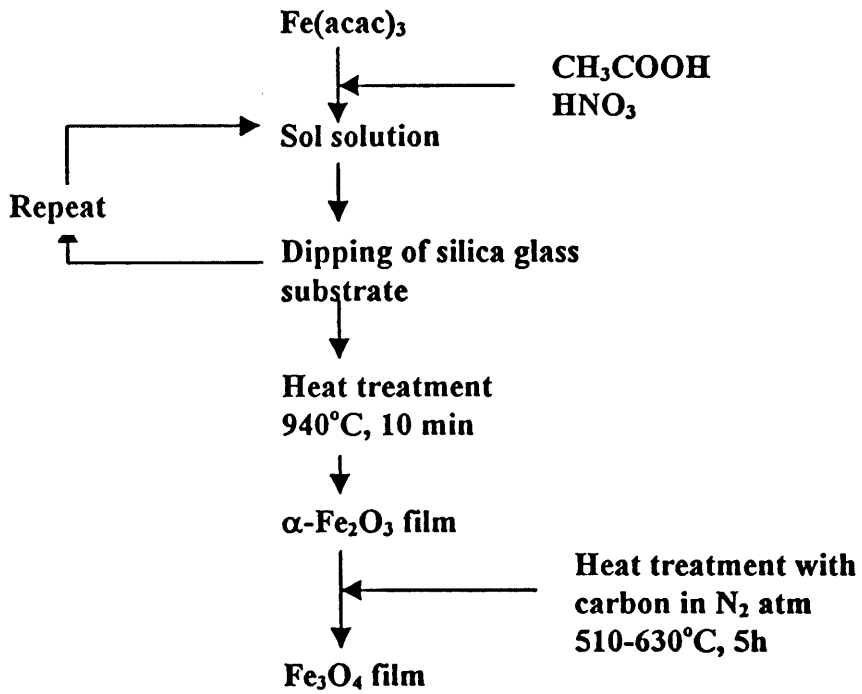


Figure 1.15 Flow chart for the preparation of Fe_3O_4 thin film by the sol-gel method.[50]

Sol-gel methods have been used to produce a coating of additives on ferrite particles prior to sintering in an attempt to achieve good dispersion and to increase the resistivity of the overall material.[51] The coating was a borosilicate material obtained from the corresponding boron and silicon alkoxides which were hydrolysed with hydrofluoric acid as catalyst. The coating thickness was in the range of 5 to 15nm.[51]

1.8 Processing of Ferrite Powders

Properties such as resistivity, permeability and bulk density of ferrites can only be measured with a compact form of the ferrite. To obtain this, the ferrite powder is first dry pressed into the shape of a disc. This process consists of placing the correct quantity of granulated powder into a cylindrical die and then closing the die with a prescribed pressure (~ 4 tonnes cm^{-2}). As the powder is compressed, it builds up friction between its outer surface and the adjacent die walls. Due to this friction and the viscosity of the powder, the pressure and hence the density is not uniform.[52] Inhomogeneous pressing leads to inhomogeneous magnetic properties. Hence, the quality of the die is important and the interior of the die must be highly polished. Binders such as polyvinylalcohol may be added to the ferrite powder to assist in compaction. However, the binder itself may degrade the magnetic properties of the ferrite.

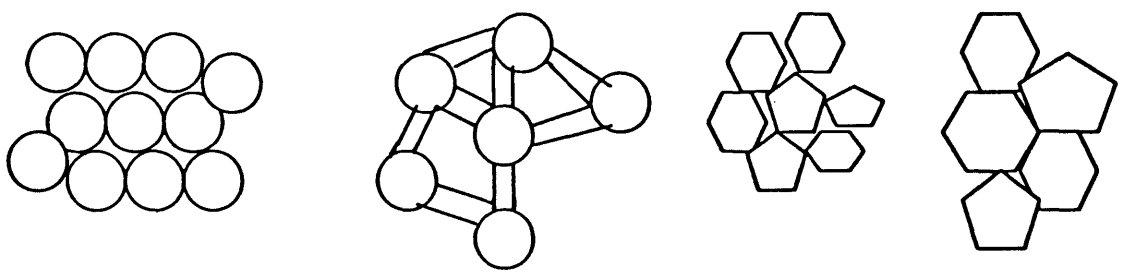
The next stage of processing converts the pressed powder to a compact, dense, form by sintering. Sintering is defined as the process of heating a compacted powder for a certain time at a temperature high enough to promote diffusion of the particles but lower than the melting point of the powder. The ideal sintering process results in a fully dense material by elimination of pores. The driving force for sintering is the reduction in surface free energy of the powder.

Thus, when the compacted powders are heated to temperatures in the region of 1000°C, crystal growth proceeds where the particles are in contact, the free energy decreases and the particles grow together to form crystallite grains with an accompanying increase in density. The rate of grain growth and the resultant micro-structure depends on many factors, such as the sintering temperature, the oxygen partial pressure, stoichiometry of the ferrite, particle shape and size and the presence or otherwise of a liquid phase.[53] A liquid phase occurs when a small fraction of the

material melts at the sintering temperature and thus fills the pores and grain boundaries and increases the density.[54] Although there is a continuous evolution of microstructure during sintering, the process is commonly considered to be divided into three stages.[42] In the first stage, contact area between particles increases due to the formation of interconnections or "necks" between neighbouring particles by the mechanism of surface diffusion, see **Figure 1.16 (a) and (b)**. At this stage, pores appear as voids between at least three contacting particles and shrinkage occurs.

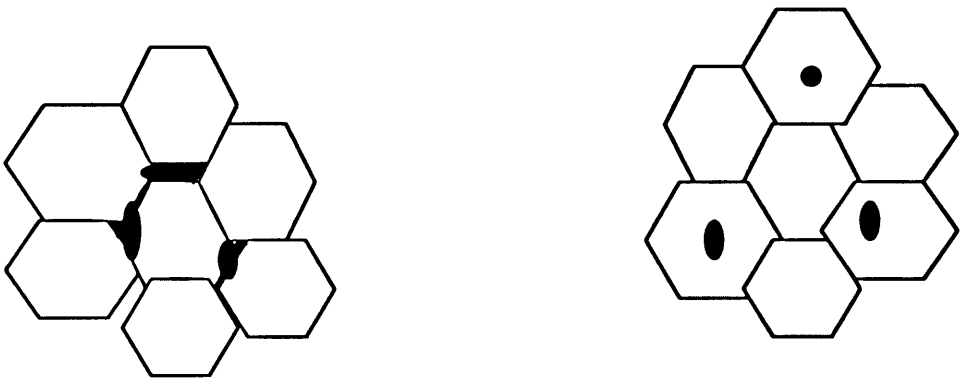
The second stage begins when a three-dimensional network of necks is achieved and the porosity changes from open to closed. To decrease and eventually eliminate pore volume, a net transport of material to the pores by volume diffusion is required.

In the final stage, grain growth is significantly enhanced and the remaining pores become isolated. Even at this stage, two types of porosity still exist, namely; (a) intergranular and (b) intragranular as shown in **Figure 1.17**. Intragranular porosity occurs when grain growth in sintering is so high that the pores may be left behind by rapidly moving grain boundaries resulting in pores that are trapped inside the grain. This porosity is difficult, if not impossible, to remove at a later stage and obviously leads to poor magnetic and mechanical properties of the ferrite concerned.



(a) (b) (c) (d)

Figure 1.16 Schematic representation of sintering stages: (a) "greenbody", i.e. unsintered "as prepared" material, (b) initial stage, (c) intermediate stage with initial stage represented as pentagons or hexagons and (d) final stage.



(a) (b)

Figure 1.17 Porosity character (a) intergranular and (b) intragranular.

The formation of large ferrite grain sizes by sintering usually leads to a higher magnetic permeability in the final material. This occurs because the larger the grains, the fewer the number of grain boundaries present to act as resistance for domain wall movement and thus the higher the permeability. The earliest work on correlating grain size with permeability was reported by Guillard and Paulus on Mn-Zn ferrites.[55] The permeability increased with grain size but levelled out at about 20 microns probably due to intragranular porosity.[55] With careful sintering processes, Roess prepared Mn-Zn ferrites with low porosity factors and hence their permeability values increased by one order with grain size of up to 40 microns.[56]

Guillard et al. studied the detrimental effect on permeability measurements in Ni-Zn ferrites due to intragranular porosity.[57] It was shown that although permeability in Ni-Zn ferrites increased with grain size up to 15 microns, it decreased thereafter due to the intragranular porosity of the ferrites.

Clearly, sintering is an important process to perfect since it affects greatly the magnetic properties of the ferrites. Factors such as sintering temperature, rate of sintering, oxygen partial pressure and particle size must be considered in order to optimise the microstructure of the bulk ferrites.

1.9 Summary

Ferrites of interest to the present work possess the spinel structure. The range of ferrite materials is vast from simple magnetite to complex mixed metal ferrites. They exhibit long-range magnetism *via* the superexchange mechanism in their lattice structure. This type of magnetism is known as ferrimagnetism, and is a form of uncompensated antiferromagnetism. The magnetism of Ni-Zn ferrites is referred to as "soft" because the material can be magnetised and demagnetised easily. The chemical composition and the distribution of the cations in the octahedral and tetrahedral spinel sites control the magnetic and electrical properties of these materials. The microstructure of the ferrite particles also plays an important role in the magnetic properties of the material.

Ferrite materials such as Ni-Zn ferrites have been widely employed as "soft" magnetic materials in industry. Their ability to magnetise and demagnetise quickly, coupled with their high resistivities, makes them applicable as low energy-loss transformers. They can absorb energy at microwave frequencies and this property forms the basis for some of the technologies of space telecommunications and radar.

Industrially, Ni-Zn ferrites are principally manufactured by the ceramic method. Advantages of the ceramic method include the use of cheap starting materials and the ease of preparing ferrite powders on a large scale. However, the method is crude and leads to variation in composition of the ferrite and in shapes and sizes of the ferrite particles. Alternative methods for producing Ni-Zn ferrite powders with regular particle shape are the coprecipitation and sol-gel techniques. Coprecipitation of mixed metal carbonates, hydrocarbonates, hydroxides and oxalates affords mixed metal ferrites, which are usually less than a micron in diameter. The sol-gel technique is a more recent technique for producing ferrites. The method is chemically more subtle than the coprecipitation technique and when successful, it can produce ferrite particles in the 10-100 nanometre range. For all preparations, the processing of the ferrite powders is important if the magnetic properties are to be maximised.

Ni-Zn ferrites of various compositions were synthesised by the coprecipitation and sol-gel techniques in this laboratory and are the subjects of the work reported in **Chapter 2.**

CHAPTER 2

SYNTHESIS AND CHARACTERISATION OF Ni-Zn FERRITE MATERIALS

2.1 INTRODUCTION

2.1.1 Synthesis of Ni-Zn Ferrites

This chapter reports the synthesis and characterisation of Ni-Zn ferrite powders of various compositions by the coprecipitation and sol-gel techniques. The coprecipitation method for preparing ferrites has been discussed in **Section 1.7.1, Chapter 1**. Ni-Zn ferrites with different stoichiometries have previously been formed by several coprecipitation methods. One preparation involved the precipitation of metal hydroxides by ammonium hydroxide from their corresponding metal salts.[38] Firing these hydroxides at temperatures between 700 – 900°C afforded the ferrites.[38] Mixed metal oxalates have also been formed by the coprecipitation technique and used as Ni-Zn ferrite precursors.[39] The sol-gel technique as applied to ferrite preparation was discussed in **Section 1.7.2, Chapter 1**. Nanosized Ni-Zn ferrite particles were synthesised *via* a sol-gel method incorporating a silica matrix.[43] A sol-gel process has also been used to form spherical Ni-Zn ferrite particles at processing temperatures as low as 250°C.[46] Good electrical and magnetic properties were reported in both sol-gel studies.[43,46]

2.1.2 Characterisation of Ni-Zn Ferrites

The materials were characterised structurally by powder X-ray diffractometry (PXRD) and scanning electron microscopy (SEM), magnetically by vibrating sample magnetometry (VSM) and Mössbauer spectroscopy and electronically by resistivity measurements. The reader is referred to **Section 2.4.1** for details on each of the instruments involved in characterisation.

2.1.2.1 PXRD Analysis

Ni-Zn ferrites can be analysed by a number of different methods. Powder X-ray diffractometry (PXRD) is primarily used in the determination of the morphology of a crystalline material, see **Appendix A** for an introduction to PXRD. A PXRD pattern

is a plot of intensity of diffraction peaks versus position of the observed peak. The pattern of a powdered crystalline material contains diffraction peaks and the relative positions of these peaks contain information about the size and structure of the material's unit cell. The intensity of the peaks is associated with the different elements situated in their atomic positions within the unit cell. The particle size of a crystalline powder can also be determined from its PXRD pattern because, for particle sizes less than 2000Å (200nm), broadening of the peaks occurs. Estimations of the particle size can be made from the widths of the peaks at half height using Scherrer's formula[73] (see Section 2.2.2). **Figure 2.1** shows a typical PXRD pattern of a commercial Ni-Zn ferrite. The peak's positions are typical for an inverse spinel phase with a cubic cell. The lattice parameter of this phase is calculated to be 8.39Å from the peaks' positions. The peaks are also very sharp indicating large particle sizes. The particle size is estimated to be greater than 1000Å for this ferrite.

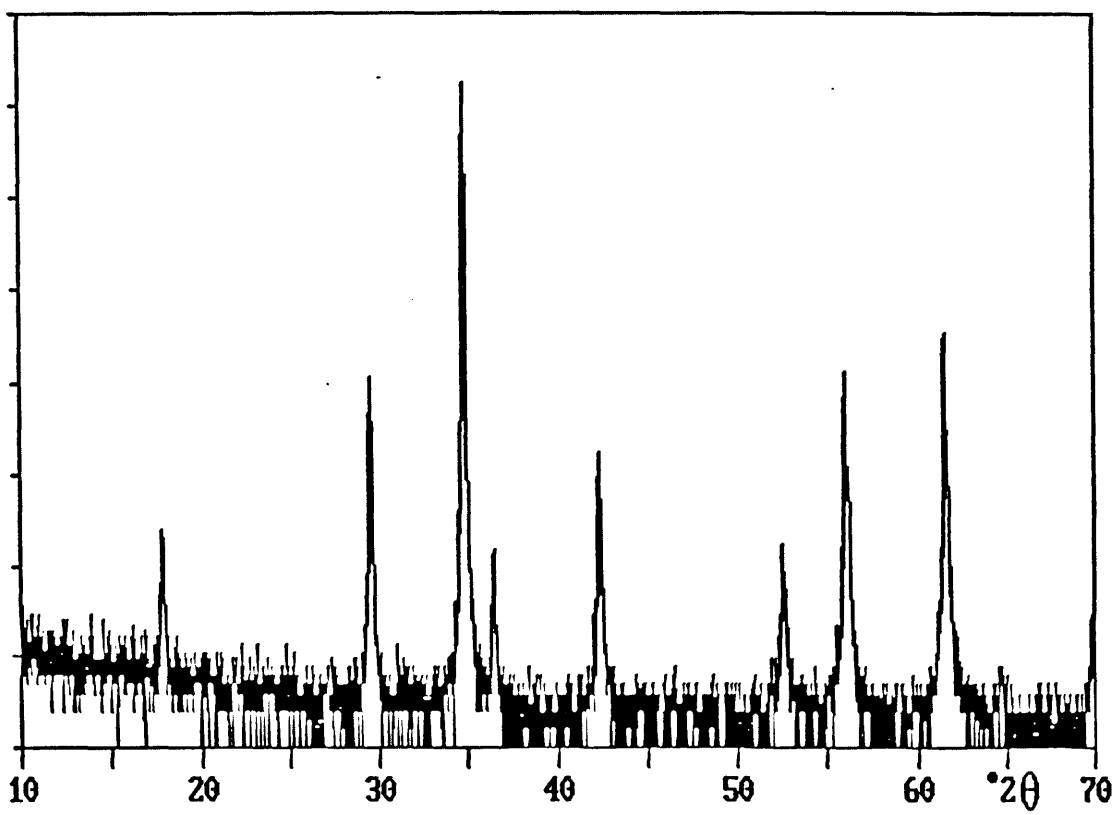


Figure 2.1 PXRD pattern of a commercial Ni-Zn ferrite.

2.1.2.2 SEM Analysis

Scanning electron microscopy (SEM) is used to observe the microstructure of Ni-Zn ferrites, see **Appendix B**. The technique is capable of revealing surface topography down to an in-plane resolution of 1nm. The SEM images of Ni-Zn ferrites prepared by the coprecipitation and sol-gel techniques have been reported to demonstrate regular shapes (often spherical) and sizes.

2.1.2.3 VSM Analysis

Vibrating sample magnetometry (VSM) measures a number of magnetic properties of Ni-Zn ferrites, see **Appendix C**. The technique is often used to measure minute changes in the magnetisation of the ferrite relative to changes in an external magnetic field. Typically, hysteresis loops are obtained for ferrites and since Ni-Zn ferrites are "soft" magnetic materials, the loops quickly magnetise with increasing magnetic field and they tend not to lag when demagnetised. Hence, very small coercivity and remanence values are found which are usually not accurately measurable by this technique. The VSM technique, however, can estimate the saturation magnetisation values (M_s) of the ferrites.

2.1.2.4 Mössbauer Spectroscopy

^{57}Fe Mössbauer spectroscopy is a useful tool in studying Ni-Zn ferrites, see **Appendix D**. The technique investigates the interaction between an iron nucleus and its electronic environment. The interaction differs for iron in different valence and stereochemical states. The different interactions are seen as shifts in absorption spectra and are known as chemical isomer shifts or isomer shifts, IS. In the inverse spinel phase of the ferrites there are three iron types, Fe^{3+} in the tetrahedral sites, Fe^{3+} in the octahedral sites and Fe^{2+} in the octahedral sites. Also, since the ferrites exhibit long range magnetism, a Mössbauer spectrum can be expected to split into a magnetically ordered sextet. With the iron cations in tetrahedral and octahedral sites, a doublet of sextets is observed, with the octahedral sextet twice as big as the tetrahedral sextet.

Figure 2.2 shows a room temperature Mössbauer spectrum of magnetite, $Fe_2O_3.FeO$. The expected doublet of sextets is observed, each sextet representing the Fe cations in the tetrahedral and octahedral sites.

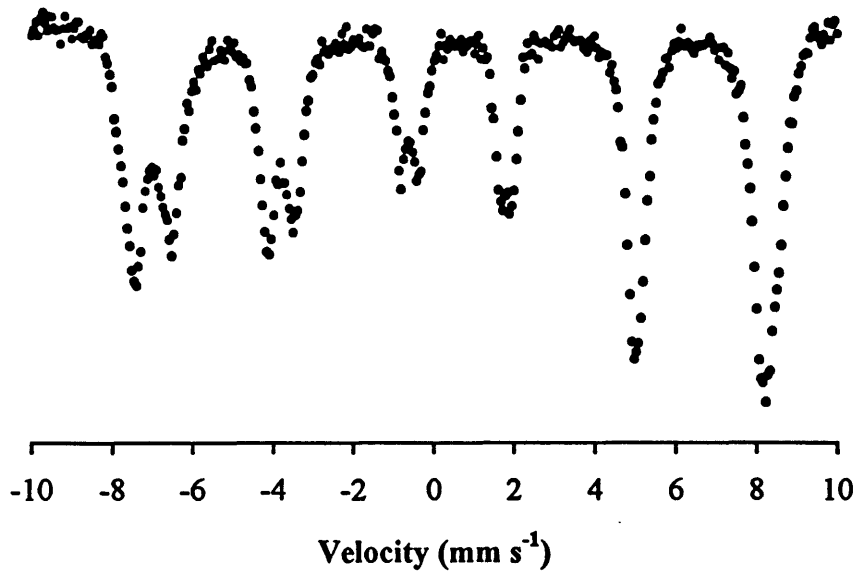


Figure 2.2 Mössbauer spectrum of Fe_3O_4 taken at room temperature.

The Mössbauer effect has been used to study Ni-Zn ferrites[58,59,60] and Sn[61] and Ti[62] substituted Ni-Zn ferrites. It was used to explain the variation in the magnetisation of Ni-Zn ferrites with Zn content in the ferrite. As already discussed in **Chapter 1 (Figure 1.8)**, the magnetic moment of the Ni-Zn ferrites (at near zero Kelvin) increases initially with increasing Zn content, reaches a maximum at around $Ni_{0.5}Zn_{0.5}Fe_2O_4$ and decreases thereafter. The Néel theory[13] is able to account for the initial increase but has problems in explaining the subsequent decrease. Two different models have been proposed to explain the decrease - (1) Yafet-Kittel[63] model and (2) the Gilleo[64] model. In the Yafet-Kittel model, a canted configuration of the atomic spins is assumed to occur as the amount of zinc content increases, while in the Gilleo model, paramagnetic centres or superparamagnetic clusters are assumed to occur during zinc substitution. Neutron diffraction studies have shown evidence for both models. Wilson and Kasper[65a] suggested a non-canted configuration for $Ni_{0.5}Zn_{0.5}Fe_2O_4$ (Gilleo model), while Murthy *et al.* supported the existence of canted spin structures (Yafet-Kittel model).[65b] Ishikawa suggested that superparamagnetic clusters rather than canted spin

structures were present in Ni-Zn ferrites using the evidence gathered on the macroscopic magnetic properties of the Ni-Zn ferrites at high Zn substitution.[66] NMR studies on Ni-Zn ferrites have been inconclusive.[58]

Mössbauer studies on Ni-Zn ferrites have been used more recently to suggest a better explanation of the variation in magnetisation in Ni-Zn ferrites. In Ni-Zn ferrites, Ni cations prefer octahedral [B] sites and Zn cations prefer tetrahedral (A) sites, so that the formula can be written as $(Zn_x^{2+}Fe_{1-x}^{3+})[Ni_{1-x}^{2+}Fe_{1+x}^{3+}][O^{2-}]_4$. As shown schematically in Figure 2.3, each tetrahedral site is surrounded by twelve octahedral B sites and each octahedral site is surrounded by six octahedral and six tetrahedral sites. For the hyperfine interactions influencing the Mössbauer spectrum, only the A-B magnetic interactions are taken into consideration (A-A and B-B magnetic interactions are too weak, see Section 1.4.2). The different surroundings of ferric sites lead to variation in hyperfine fields at each iron nucleus dependent on the number of nearest Fe or Ni neighbours (in the case of (A) sites) or Fe or Zn neighbours (in the case of [B] sites). The number of nearest Zn neighbours for a Fe[B] site varies between n = 0 and 6. This number depends upon x and the probability of occupation of tetrahedral sites by Zn cations and can be determined from the binomial distribution formula:

$$P(n) = 6!x^n(1-x)^{(6-n)} / n!(6-n)! \qquad [1]$$

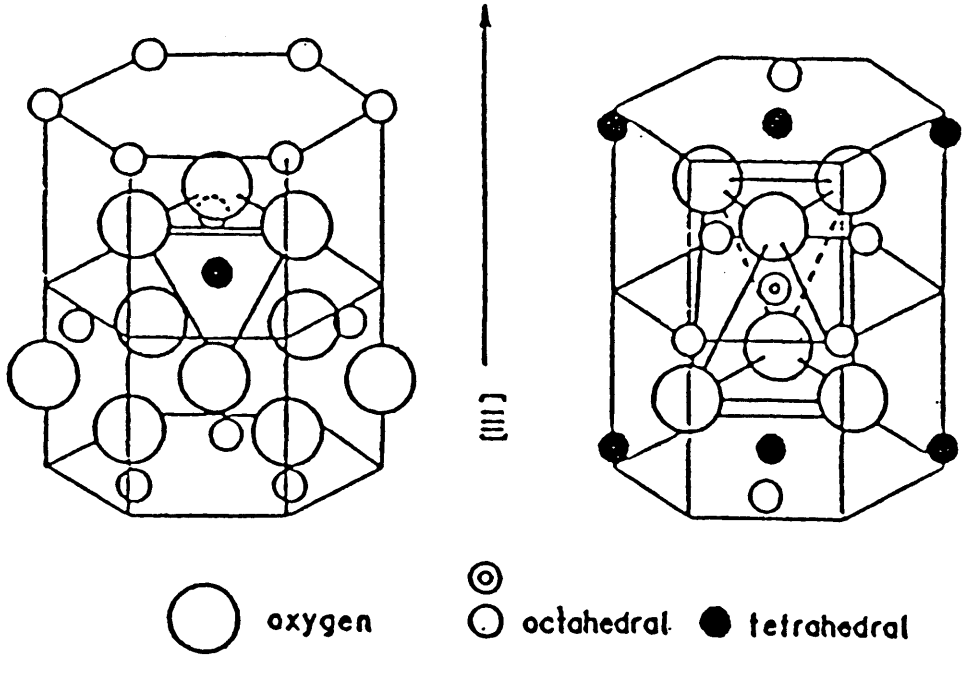


Figure 2.3 Schematic representation of the spinel structure.[66]

Daniels and Rosencwaig used the variation of Mössbauer line width (for tetrahedral and octahedral patterns) with x in $Ni_{1-x}Zn_xFe_2O_4$ materials (prepared by ceramic method) to identify three magnetic regions (see Figure 2.4).[59] Spectra taken at room temperature were considered to correspond to a magnetic region (between 0 = x = 0.4), a relaxation region (between 0.4 = x = 0.7), and a paramagnetic region (between 0.7 = x = 1.0). Spectra taken at liquid nitrogen temperature display the magnetic region between 0 = x = 0.65, the relaxation region between 0.65 = x = 0.80, and the paramagnetic region between 0.80 = x = 1.0. These three regions may explain the variation of the magnetic moment in Ni-Zn ferrites with increasing Zn content. Initial increase in the amount of zinc increases the magnetic moment as the ferrite is in the magnetic region. At about x = 0.5, the value of the magnetic moment levels off as the ferrite is in the relaxation region. Increasing the zinc content above this point decreases the magnetic moment because the ferrite is in its paramagnetic region.

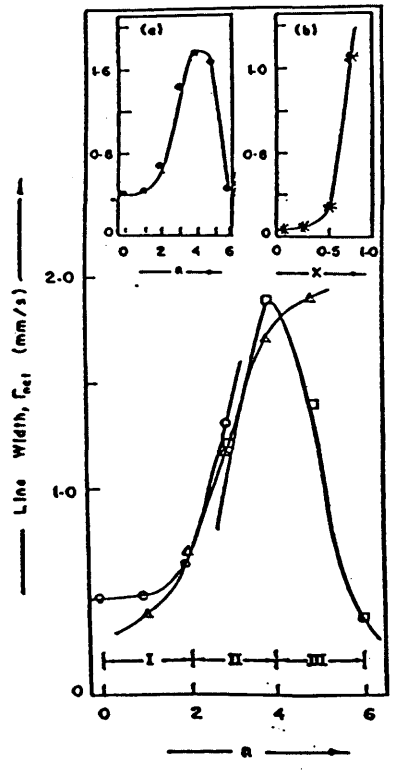


Figure 2.4 Variation in line width associated with octahedral sites, Γ_{oct} with n [x = 0.25(O), 0.50(Δ) and x = 0.75(□)]. I, II and III denotes magnetic, relaxation and paramagnetic regions, respectively. The inset (a) gives the variation in average line width associated with octahedral sites over all x with n (•) and the inset (b) shows the variation in line width of tetrahedral sites with x (*).[59]

Arshed *et al.*[67] also studied $Ni_{1-x}Zn_xFe_2O_4$ (x = 0.0, 0.25, 0.50, 0.75, 1.0) ferrites, that were prepared by the ceramic technique, using the Mössbauer effect and observed the spectra shown in **Figure 2.5** which were recorded at room temperature. For the mixed spinels, with x = 0.25, 0.50 and 0.75, the spectra were fitted with four, five and five sextets, respectively, for octahedral [B] sites, in addition to one sextet for the tetrahedral [A] site. They postulated the existence of the three different magnetic regions for the ferrites to explain the spectra which were magnetic, relaxation and paramagnetic. For $n < 2$ ($0 < x < 0.25$), magnetic behaviour dominates and the familiar doublet of sextets spectrum is obtained; for $2 < n > 5$ ($0.25 < x < 0.75$), relaxation behaviour occurs and a collapsed doublet of sextets spectrum is observed. Finally for $n > 5$ ($x > 0.75$), paramagnetic behaviour occurs and an asymmetric doublet spectrum is produced.

The use of Mössbauer spectroscopy, going from a magnetically ordered sextet to a paramagnetic doublet, has been recorded for other systems, most notably antiferromagnetic materials such as perovskites.[68] One such perovskite, $EuFeO_3$, gives a magnetically ordered sextet at room temperature. The reason for this is that the material has a high Néel temperature (~ 662K) and hence the material contains antiferromagnetic ordering at room temperature. However, if the material is doped with another transition metal cation such as Co^{3+} to give $EuCo_zFe_{1-z}O_3$, the antiferromagnetic interactions are disturbed and the Néel temperature is lowered. At a high enough dopant level (z = 0.6), the Néel temperature is reported to be 85K and a paramagnetic doublet is observed in the spectrum. Since this trend is also observed for Ni-Zn ferrites, it is reasonable to presume that a similar magnetic ordering temperature effect is observed for the ferrites. At zinc levels greater than 0.7 molar, the temperature is lowered to such an extent that it becomes less than room temperature and a paramagnetic species is detected by Mössbauer spectroscopy.

The size of the ferrite particles can also have a marked effect on the Mössbauer spectrum. It is well documented that ultafine magnetic particles (less than 100Å) exhibit superparamagnetism at room temperature.[69,70] This happens because the very small particles have enough energy at room temperature for continuous movement which is so fast that the particles are observed to have no magnetic ordering on the time-scale of Mössbauer spectroscopy.. The Mössbauer spectrum consequently shows

a paramagnetic doublet. However, by placing the sample in liquid nitrogen, the particles no longer have the energy to flip and so cannot exhibit superparamagnetism. The usual doublet of sextets spectrum is then detected for the sample.

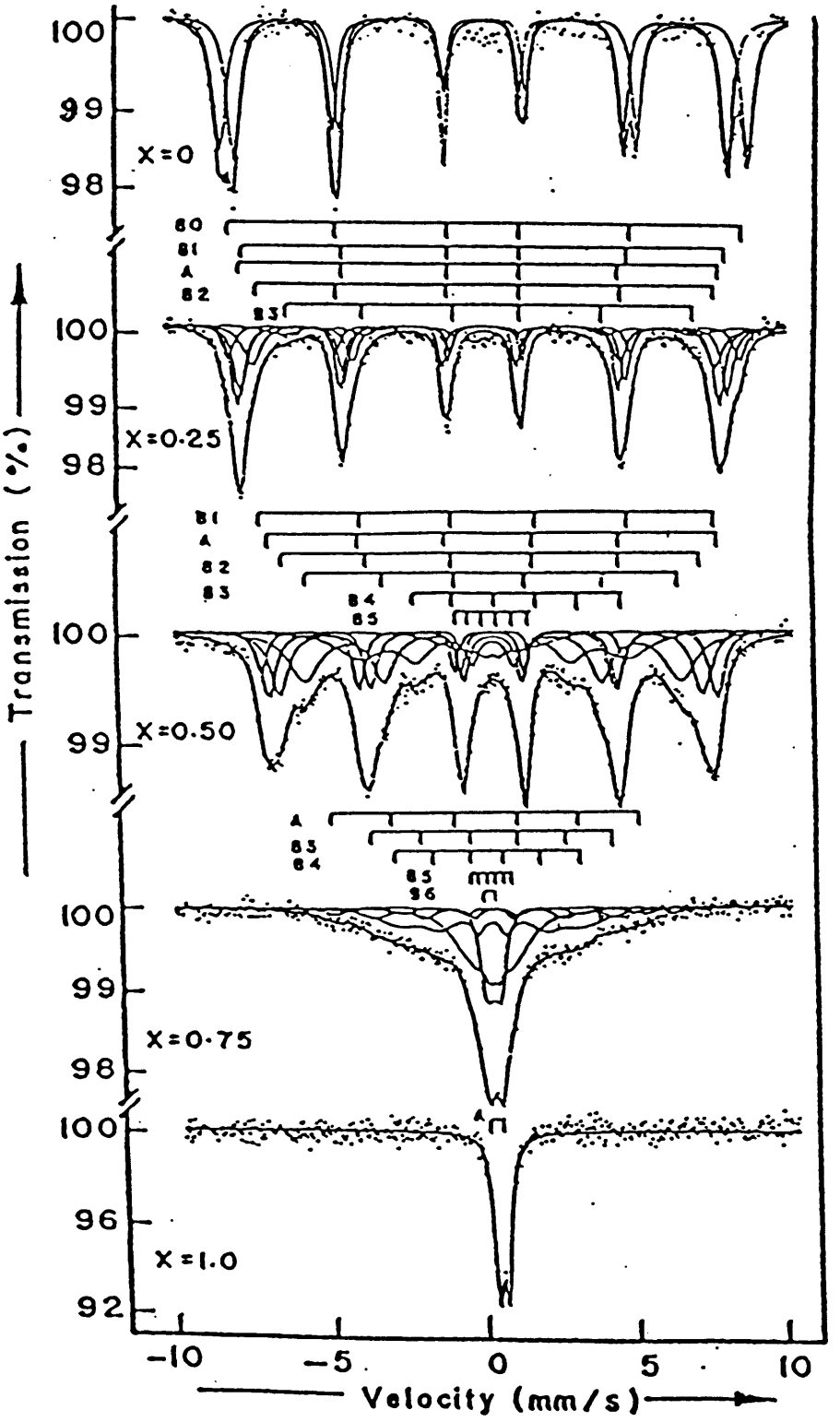


Figure 2.5 Mössbauer spectra of $Ni_{1-x}Zn_xFe_2O_4$ with x = 0.0, 0.25, 0.50, 0.75 and 1.00. A denotes the tetrahedral sites while B0, B1, B2,..., B6 denote the number of Zn^{2+} ions, i.e. zero, one, two,..., six on the tetrahedral sites around an octahedral site.[67]

2.1.2.5 Electrical Resistivity Analysis

The resistivity values of the Ni-Zn ferrites can be estimated from a four-point conductivity method, see **Appendix E.** Commercial Ni-Zn ferrites exhibit high resistivities, typically of the value $10^5\Omega$ m. Soft ferrites are required to be very electrically resistive so as to prevent major core losses via eddy currents. The major form of conductivity in ferrites is electron hopping between metal ions. For Mn-Zn ferrites this occurs between Mn^{2+} and Fe^{3+} ions but in Ni-Zn ferrites it cannot occur with Ni^{2+} or Zn^{2+} ions. Instead electron hopping may occur between Fe^{2+} and Fe^{3+} ions.[77] Commercial Ni-Zn ferrites usually contain some additives to prevent this conductivity. One type of additive forms an insulating glassy layer around each of the particles. The layer is usually calcium silicate or lead borosilicate glass.

2.2 RESULTS AND DISCUSSION

2.2.1 Synthesis of Ni-Zn Ferrites.

Coprecipitation and sol-gel methods were employed to prepare Ni-Zn ferrites of several compositions. One coprecipitation method (CP) was a variation of the method of Wickham *et al.* who used metal sulphates and ammonium oxalate as reagents.[39] In the present work, a mixture of metal sulphates and metal acetates were used, while oxalic acid was used instead of its ammonium salt. A schematic diagram of this method is given in **Figure 2.6.** Ni-Zn ferrites were also produced by a second coprecipitation method, which may be called the **MNCD** technique. The **MNCD** technique is taken from the first initials of Mathoniere, Nutall, Carling and Day[81] who prepared mixed metal oxalates similarly to the method described here (see **Section 2.4.3.3**). The Ni-Zn ferrites were produced from the precipitates by heating 400 to 1100°C.

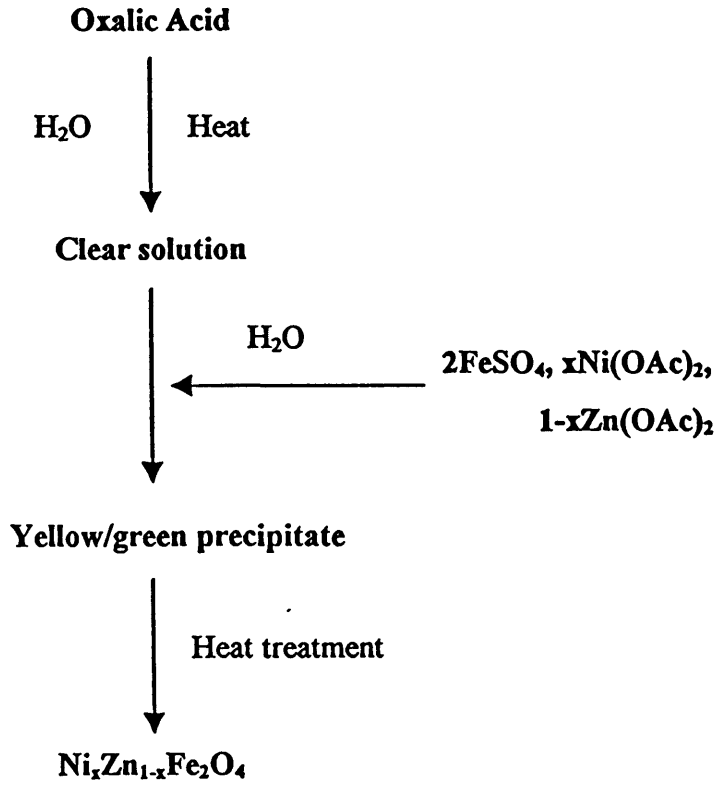


Figure 2.6 Schematic diagram of first coprecipitation (CP) method.

The second coprecipitation technique, the MNCD method, used $K_3Fe(C_2O_4)_3$ mixed with nickel and zinc sulphates and coprecipitated as mixed metal oxalate with tetrabutylammonium cation as the counter-ion. **Figure 2.7** demonstrates the MNCD process schematically.

The sol-gel (SG) technique employed in this research used $Fe(acac)_3$, $Zn(acac)_2$, $Zn(OAc)_2$ and $Ni(OAc)_2$ as reagents with *iso*-propyl alcohol (IPA) as solvent. The reagents were dissolved in IPA at 60°C. The solution was consequently hydrolysed by rapid addition of water and a little nitric acid as catalyst to form an aquagel, **Figure 2.8**. The solvent was evaporated in a 60°C oven to yield a powdered xerogel. The powders were magnetic and were shown to have an inverse spinel structure (see **Section 2.2.2**). The process of hydrolysis and condensation may be visualised as follows, taking $Fe(acac)_3$ and $Ni(OAc)_2$ as examples:

(a) Hydrolysis:

$$Fe(acac)_3 + H_2O \xrightarrow{H^+} Fe(acac)_2OH + Hacac$$

$$Ni(OAc)_2 + H_2O \xrightarrow{H^+} Ni(OAc)OH + HOAc$$

(b) Condensation:

$$Fe(acac)_2OH + Ni(OAc)_2 \longrightarrow (acac)_2Fe - O - Ni(OAc) + HOAc$$

$$Ni(OAc)OH + Fe(acac)_3 \longrightarrow (OAc)Ni - O - Fe(acac)_2 + Hacac$$

$$Fe(acac)_2OH + Ni(OAc)OH \longrightarrow (acac)_2Fe - O - Ni(OAc) + H_2O$$

Traces of carbon (amounts < 1%) and hydrogen (amounts < 1%) were still evident in the magnetic powders produced at this low temperature as determined by chemical analyses. These were removed at high temperatures (~800°C) and the ferrites produced at these temperatures were crystalline.

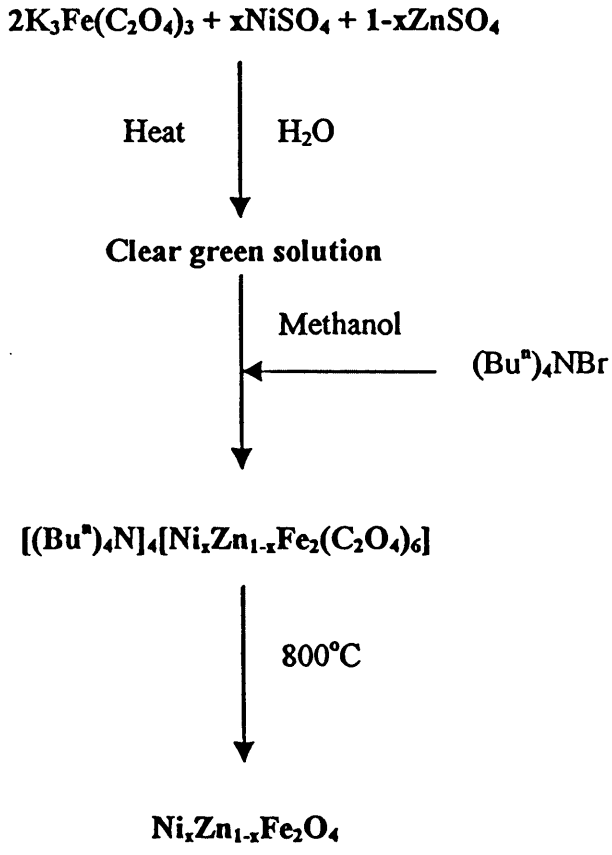


Figure 2.7 Schematic diagram of MNCD technique for preparing Ni-Zn ferrites.

This sol-gel process is interesting since it produced magnetic powders at a very low processing temperature (60°C). The amount of water added was critical. Too much water produced non-magnetic powders, which contained hematite as well as the ferrite when fired at 800°C. The optimum condition for producing pure ferrites was a 1:3 water/alcohol ratio. **Table 2.1** lists the ferrites ($Ni_xZn_{1-x}Fe_2O_4$) prepared with the various amounts of reagents used in the reactions.

Table 2.1 Names of Ni-Zn ferrites prepared by the three methods.

Value of x	**Coprecipitation**	**MNCD**	**Sol-gel**
0.25	NiZnCP1	NiZnD0	NiZnSG1
0.33	NiZnCP2	NiZnD1	NiZnSG2
0.50	NiZnCP3	NiZnD2	NiZnSG3
0.75	NiZnCP4	NiZnD3	NiZnSG4
1.0	———	NiZnD4	———

The coprecipitation and sol-gel methods produced magnetic powders with chemical compositions close to the Ni-Zn ferrite expected from the reagents. For example, NiZnSG1 gave a material with the composition of $Ni_{0.29}Zn_{0.71}Fe_{1.94}O_{4-y}$ instead of $Ni_{0.25}Zn_{0.75}Fe_2O_4$. The MNCD technique, however, gave magnetic powders with unusual chemical composition that deviated from the amounts of starting materials added. These materials exhibited deviations in the nickel content of the ferrite materials. This will be explained in the next section. The Fe, Ni and Zn compositions of all the ferrites were estimated from elemental analyses using atomic absorption spectroscopy.

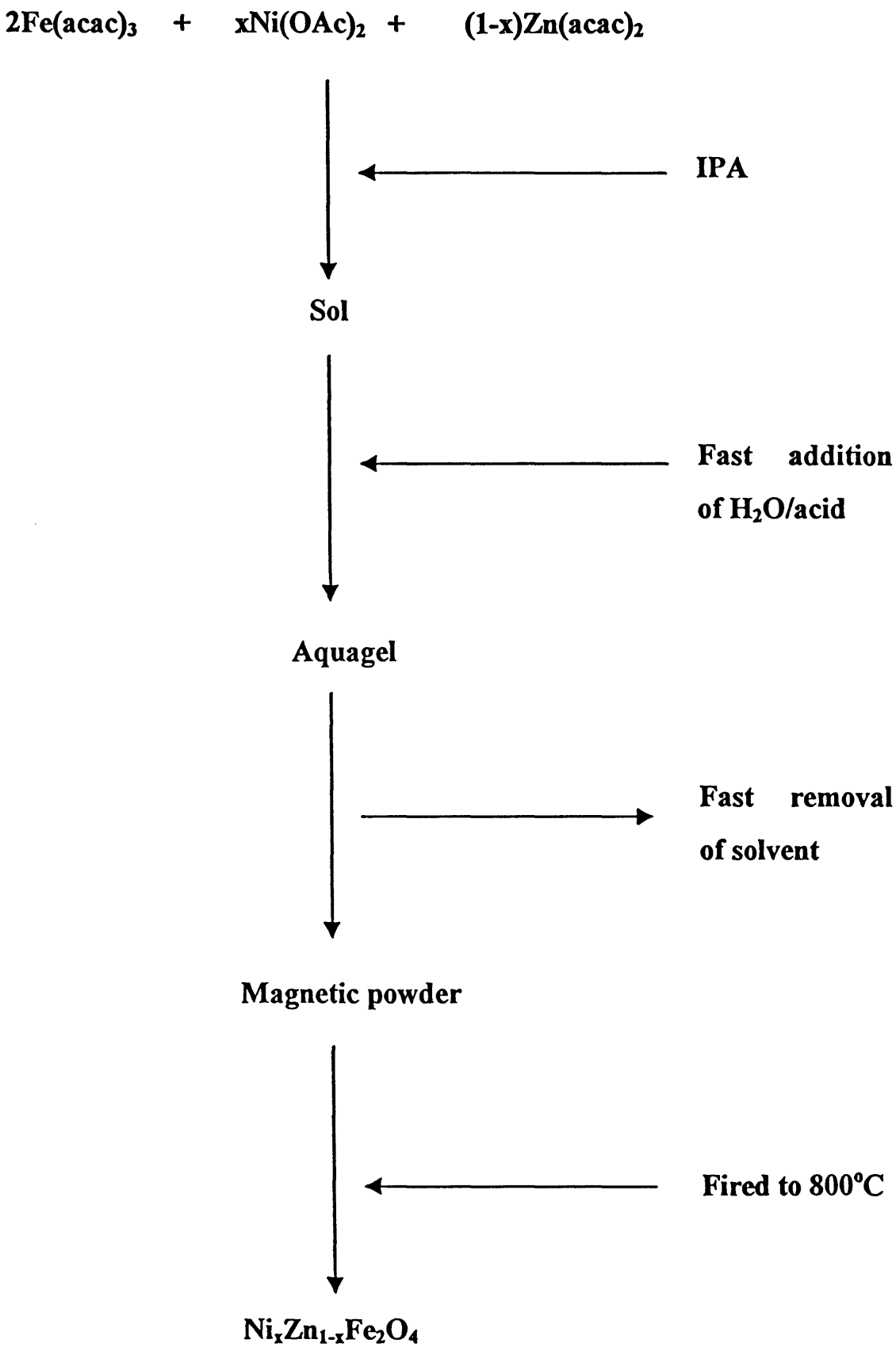


Figure 2.8 Schematic diagram of sol-gel process.

2.2.2 *PXRD Analysis*

(a) Ni-Zn Ferrites Prepared by Coprecipitation Method (CP)

The PXRD profiles of the Ni-Zn ferrites (fired at 800°C) prepared by the coprecipitation method (CP) are displayed in **Figure 2.9**. The diffractograms show excellent examples of the inverse spinel phase of the ferrite as already shown for the commercial Ni-Zn ferrite in **Figure 2.1**. Common impurities in ferrites such as hematite (α-Fe_2O_3) and maghemite (γ-Fe_2O_3) are not present in any of these materials. The profiles display a shift of the diffraction peaks with compositional changes. As the composition of Zn^{2+} ions increases in the ferrite, the diffraction peaks shift to the left, i.e. they appear at lower 2θ values and hence, the unit cell expands. This can be easily rationalised by recalling that Zn^{2+} ions fill the tetrahedral sites before the ferric ions because of their co-ordination preference for those sites. The radius of a Zn^{2+} ion (0.60Å) is larger than the radius of a Fe^{3+} ion (0.40Å)[71] and therefore, as the zinc cations enter the small tetrahedral sites, the sites expand to accommodate them. Consequently, the unit cell lattice expands and the lattice cell parameter, **a**, increases. The expansion of the unit cell infers that the X-rays diffract at lower incident angles. The unit cell parameter (**a**-values) of the ferrites can be calculated from their PXRD profiles from the mathematical description given below. For X-rays making an incident angle θ with a diffraction grating of inter-planar separation **d**, Bragg's law states:

$$n\lambda = 2d\mathrm{Sin}\theta \qquad [2]$$

where λ = X-ray wavelength

For the ferrite cubic spinel system, $a = b = c$, $\alpha = \beta = \gamma = 90°$, d can be expressed as:

$$1/d^2_{hkl} = h^2 + k^2 + l^2/a^2 = 4\mathrm{Sin}^2\theta/\lambda^2, \text{ where h, k, l are Miller indices} \qquad [3]$$

$$\text{Thus, } h^2 + k^2 + l^2 = \mathrm{Sin}^2\theta(a^2.4/\lambda^2) \qquad [4]$$

Then a plot of $h^2 + k^2 + l^2$ versus $\mathrm{Sin}^2\theta$ should give a straight line with slope equal to

$a^2.4/\lambda^2$. From this slope the a-value can be calculated. Figure 2.10 shows one of these plots. Using this method, the a-values of the coprecipitated Ni-Zn ferrites were estimated.

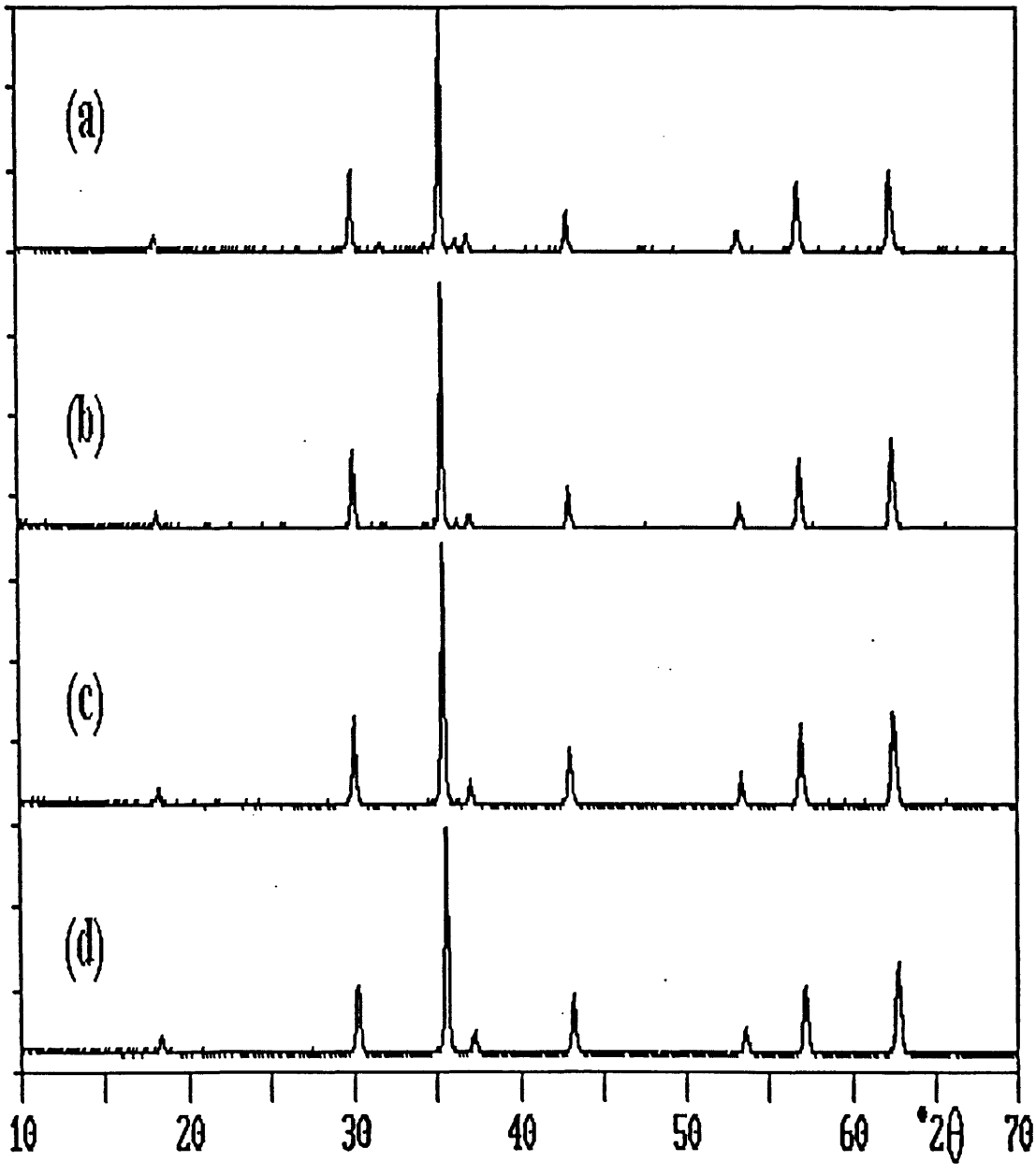


Figure 2.9 The PXRD profiles of (a) NiZnCP1, (b) NiZnCP2, (c) NiZnCP3 and (d) NiZnCP4, all prefired in air at 800°C for 1.5 hours

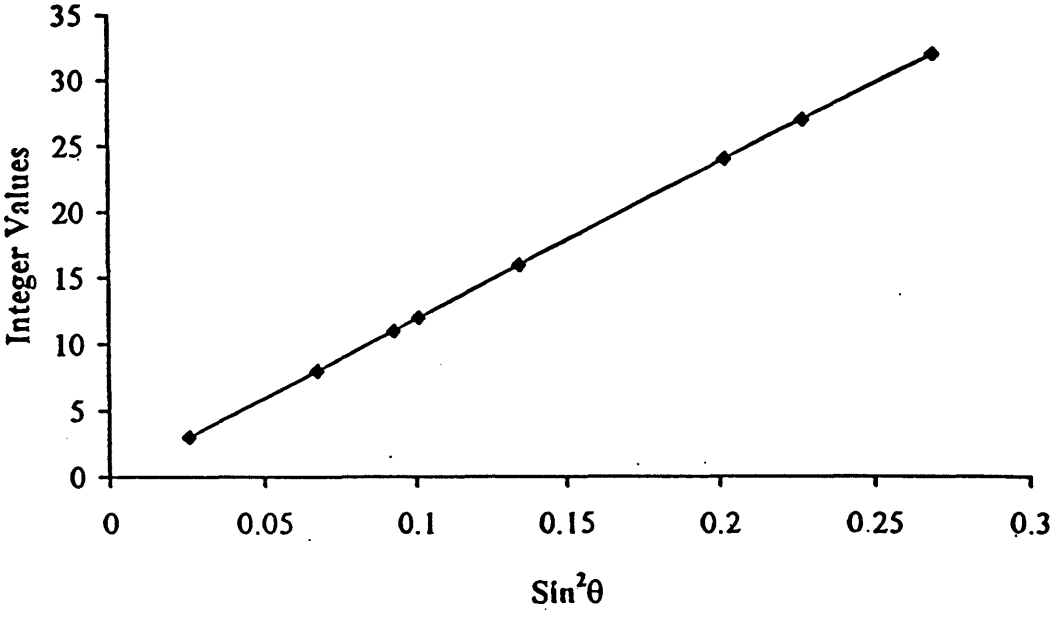


Figure 2.10 Plot of $h^2+k^2+l^2$ versus $Sin^2\theta$ with slope equal to a^2x4/λ^2 for NiZnCP1.

A plot of a-values versus value of x in $Zn_xNi_{1-x}Fe_2O_4$ (as estimated from chemical analyses) in the ferrites is shown in **Figure 2.11** and a reasonably straight line is observed. This plot compares well with that predicted by Globus *et al.*, who reported the expansion of the a-values of Ni-Zn ferrites with increasing zinc substitution.[72]

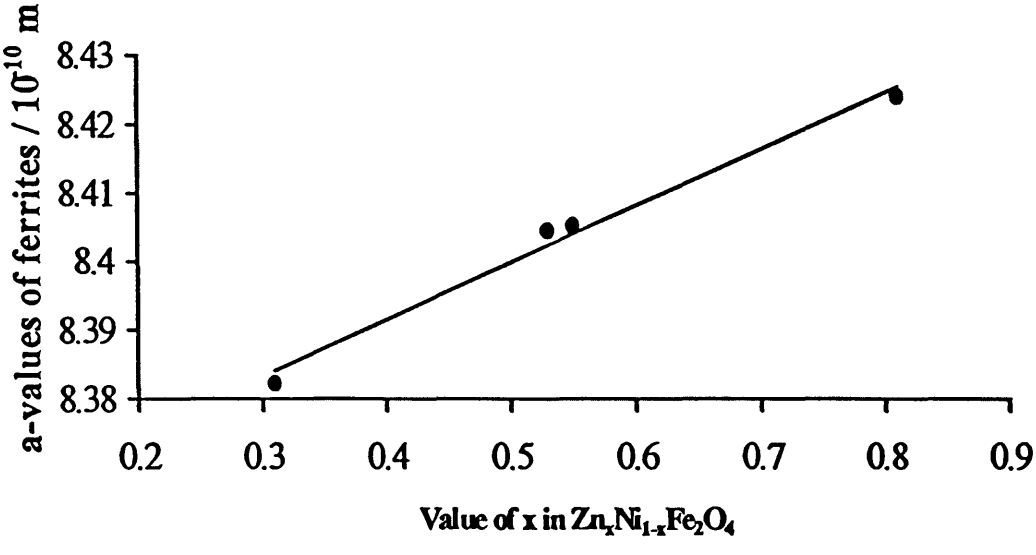


Figure 2.11 Plot of a-values of coprecipitated Ni-Zn ferrites (fired at 800°C) versus value of x in $Zn_xNi_{1-x}Fe_2O_4$.

The theoretical densities (ρ_x) of the ferrites can be calculated using the measured a-values to estimate the volume and ferrite formulae (as estimated from chemical analyses) to calculate the mass. The densities (ρ_s) of the bulk ferrites were also measured from their sintered pressed discs (with the assumptions that the disc is a perfect cylinder and that the density is uniform throughout the disc). The porosity (P), equation [5], of the ferrites can thus be estimated from the two calculated densities. **Table 2.2** compares the densities and porosities of each Ni-Zn ferrite.

$$P = 100(1-\rho_s/\rho_x) \text{ percent} \qquad [5]$$

Table 2.2 Physical properties of coprecipitated Ni-Zn ferrites (fired at 800°C).

Ferrite	a-values / 10^{-10}m	ρ_x / kg m^{-3}	ρ_s / kg m^{-3}	P (%)
NiZnCP1 $Ni_{0.27}Zn_{0.73}Fe_{1.70}O_{4-y}$	8.424053	5335.7	4533.2	15.04
NiZnCP2 $Ni_{0.36}Zn_{0.64}Fe_{2.63}O_{4+y}$	8.404347	5335.2	4425.2	17.06
NiZnCP3 $Ni_{0.51}Zn_{0.49}Fe_{1.67}O_{4+y}$	8.405135	5312.2	4742.3	10.73
NiZnCP4 $Ni_{0.71}Zn_{0.29}Fe_{1.76}O_{4+y}$	8.382282	5339.5	4366.5	18.22

The porosities of the coprecipitated ferrites range approximately from 11 to 18%. These values are high when compared to the ferrite particles (synthesised by a sol-gel method) that could be densified to > 97% theoretical value.[47]

The PXRD patterns of one coprecipitated ferrite (NiZnCP1) processed at different temperatures are given in **Figure 2.12**. The diffraction peaks clearly become sharper as the firing temperature increases indicating that the particle size of the ferrite is also increasing. The mean particle size of the sample is calculated using the Scherrer's formula, equation [6].[73]

$$d = 0.9\lambda/(\beta-\beta_1)\text{Cos}\theta \qquad [6]$$

where **d** is the grain diameter, β is the width at half height of the relevant diffraction peak, β_1 is the width at half height due to instrumental broadening (~0.07°), λ is the X-ray wavelength (~1.5418 x 10^{-10}m) and θ is the angle of diffraction of the relevant peak. Calculated particle sizes are shown in **Table 2.3** for the coprecipitated ferrites at their different firing temperatures.

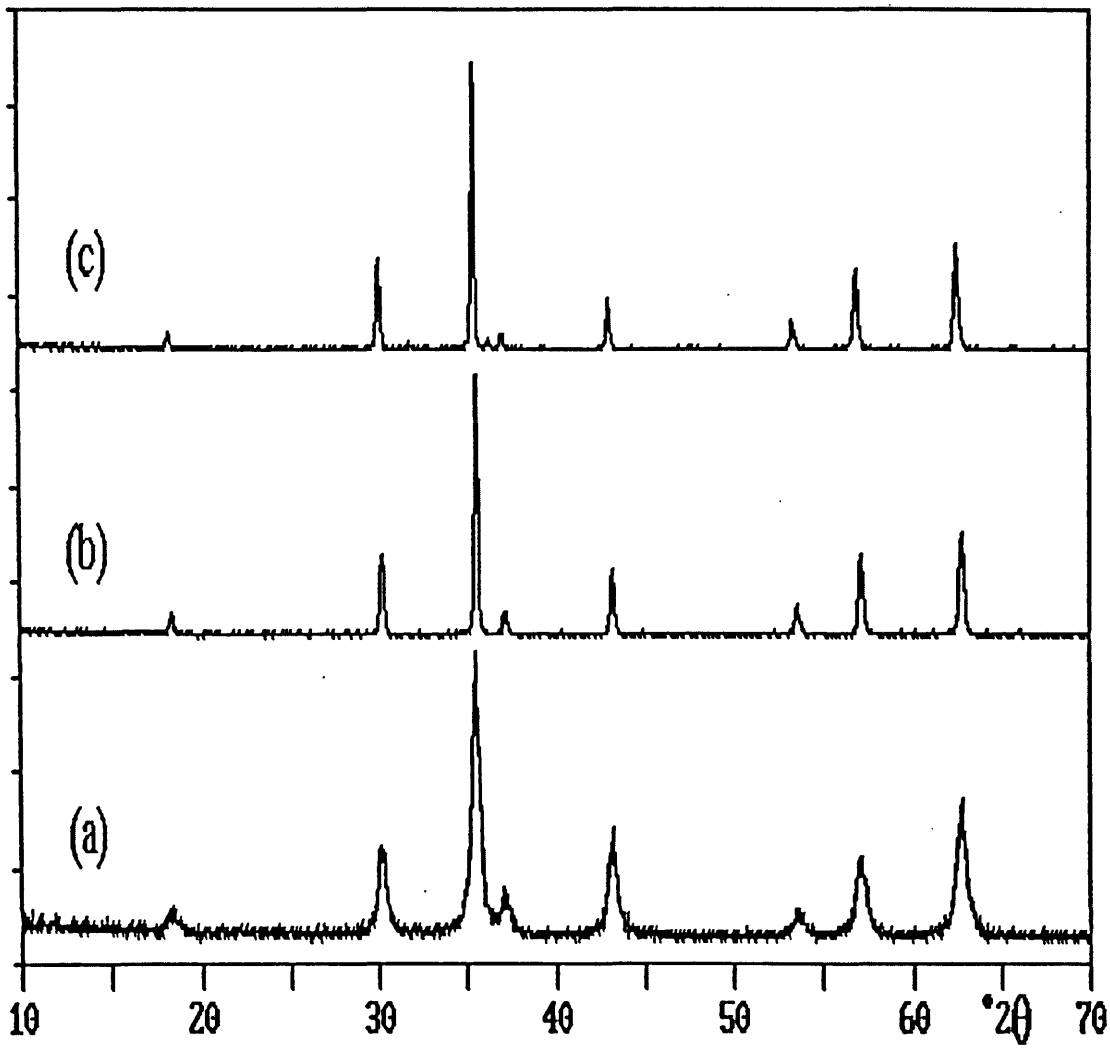


Figure 2.12 The PXRD profiles of NiZnCP1 at different firing temperatures, (a) 400°C, (b) 800°C and (c) 1100°C for 1.5 hours each.

Table 2.3 Particle sizes of coprecipitated ferrites at different firing temperatures.

Ferrite	Heat treatment / °C	Particle size / nm (+/- 2nm)
NiZnCP1	400	14
	800	88
	1100	105
NiZnCP2	400	15
	800	76
	1100	100
NiZnCP3	400	17
	800	72
	1100	105
NiZnCP4	400	18
	800	70
	1100	100

At the processing temperature of 400°C, the particle sizes of the four ferrites are small, ranging from approximately 14nm to 18nm. A sharp increase in size is observed when the ferrites are heated at 800°C. This increase may suggest more than just growth of particles by sintering. There appears to be a structural change in the ferrites between the two temperatures. At 400°C, the ferrite structure has only started to form, see **Figure 2.12**, i.e. an almost amorphous phase is observed by PXRD, which may be compared with the calcination step in the ceramic method as explained in **Section 1.7, Chapter 1**. At 800°C, the ferrite's structure is fully formed, i.e. its crystalline phase is clearly observed by PXRD. The increase in particle size from 800 to 1100°C is probably due only to the sintering process.

(b) Ni-Zn Ferrites Prepared by the Sol-Gel Technique (SG)

The PXRD patterns of the Ni-Zn ferrites prepared by the sol-gel method are shown in **Figure 2.13**. The spinel phase structure is clearly seen in the profiles with no indication of impurities such as hematite.

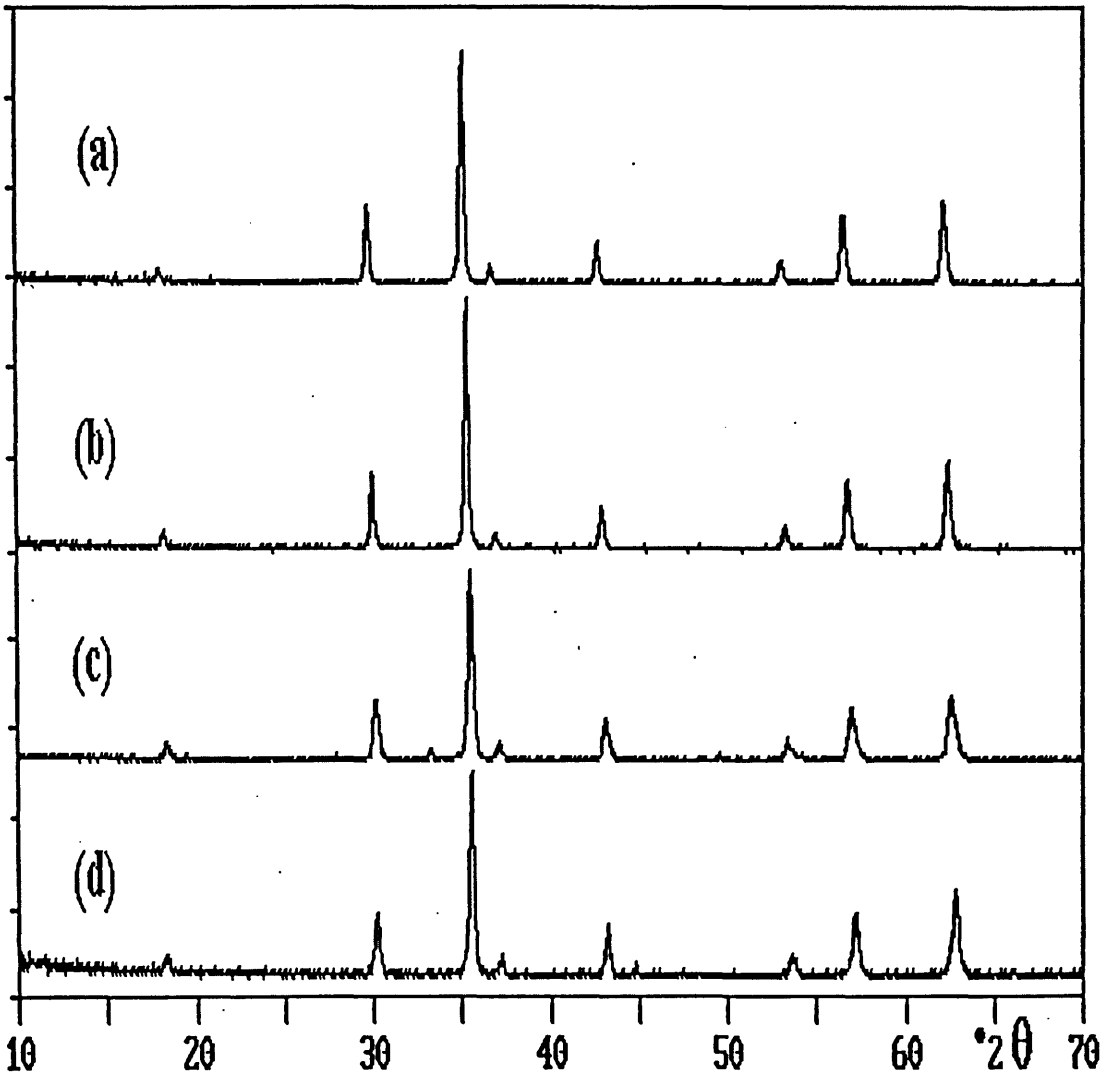


Figure 2.13 The PXRD profiles of (a) NiZnSG1, (b) NiZnSG2, (c) NiZnSG3 and (d) NiZnSG4, fired at 800°C for 1.5 hours.

The diffraction peaks are again observed to shift to a lower 2θ value with increasing concentration of zinc cations in the ferrites. The lattice parameter, **a**, of each ferrite is calculated as before and a plot of these measurements versus value of x in $Zn_xNi_{1-x}Fe_2O_4$ is displayed in **Figure 2.14**. A reasonably linear plot is observed as predicted.[72]

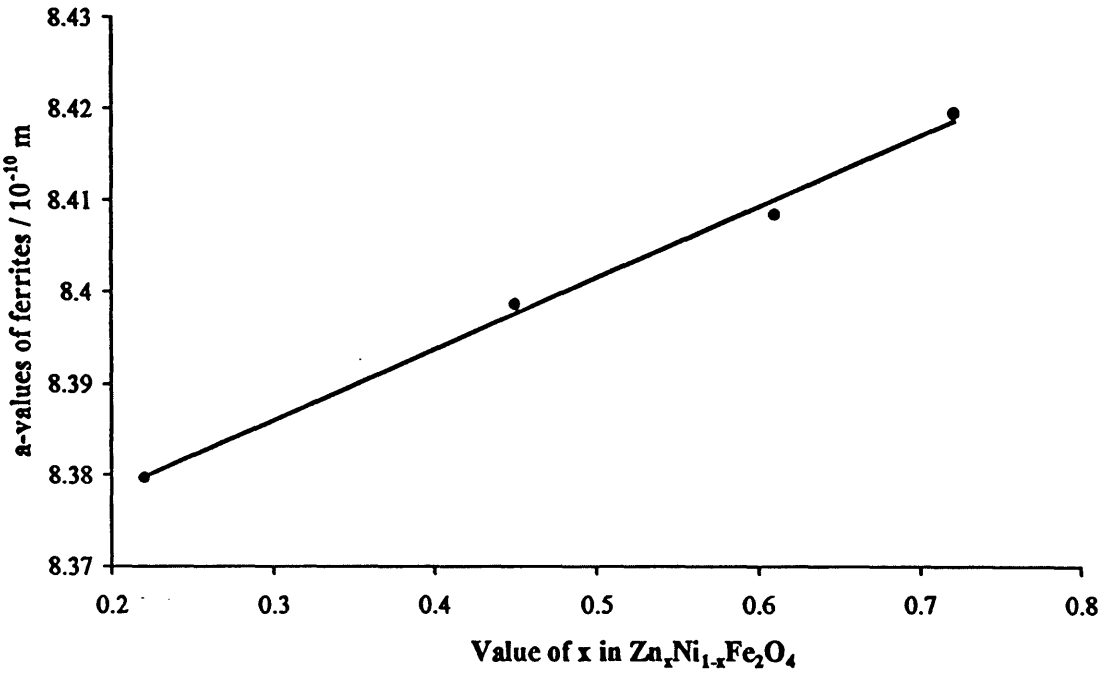


Figure 2.14 Plot of a-values of sol-gel Ni-Zn ferrites (fired at 800°C) versus value of x in $Zn_xNi_{1-x}Fe_2O_4$.

Theoretical densities of the ferrite powders and measured bulk densities of their sintered discs were calculated and are shown in **Table 2.4** along with their respective porosity values.

Table 2.4 Physical properties of Ni-Zn ferrites (fired at 800°C) prepared by the sol-gel technique.

Ferrite	a-values / 10^{-10}m	ρ_x / kgm^{-3}	ρ_s / kgm^{-3}	P (%)
NiZnSG1 $Ni_{0.29}Zn_{0.71}Fe_{1.94}O_{4-y}$	8.419595	5325.1	4219.9	20.75
NiZnSG2 $Ni_{0.36}Zn_{0.64}Fe_{2.18}O_{4+y}$	8.408524	5325.3	4181.1	21.49
NiZnSG3 $Ni_{0.50}Zn_{0.50}Fe_{2.33}O_{4+y}$	8.398731	5316.9	4095.5	22.97
NiZnSG4 $Ni_{0.75}Zn_{0.25}Fe_{2.45}O_{4+y}$	8.379718	5316.6	4165.7	21.65

The porosity values of the sol-gel ferrites are larger than the porosity values estimated for the coprecipitated ferrites by between 5 to 10%. Therefore, the sol-gel ferrites contain more or larger pores. Scanning electron microscopy (SEM) imaging confirm this. **Figure 2.15** and **Figure 2.16** display SEM images of a Ni-Zn ferrite powder (NiZnSG2) produced *via* the sol-gel method and a Ni-Zn ferrite powder (NiZnCP2) prepared through the coprecipitation method, respectively. The image of the sol-gel ferrite displays not only irregular shaped and sized particles but also pores within the grains, i.e. intragranular porosity. However, the image of the coprecipitated ferrite reveals evenly sized, well defined rectangular shaped particles with no apparent intragranular porosity. This explains how the coprecipitated ferrites can form a compact, highly densified bulk ferrite more readily than the sol-gel products.

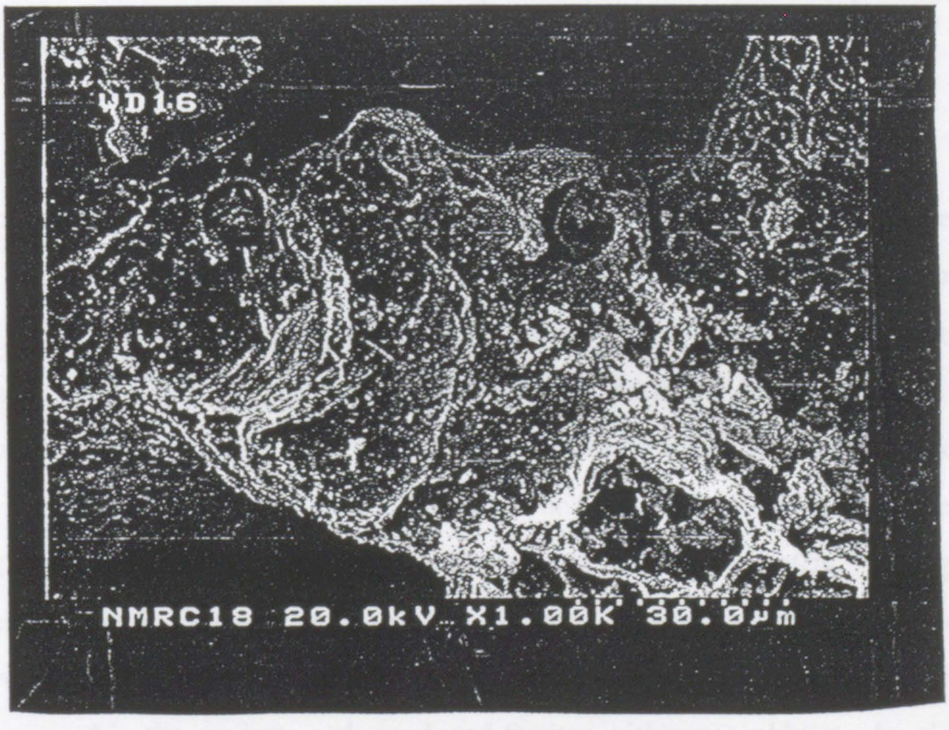


Figure 2.15 A SEM image of a sol-gel Ni-Zn ferrite (NiZnSG2 at 800°C) powder.

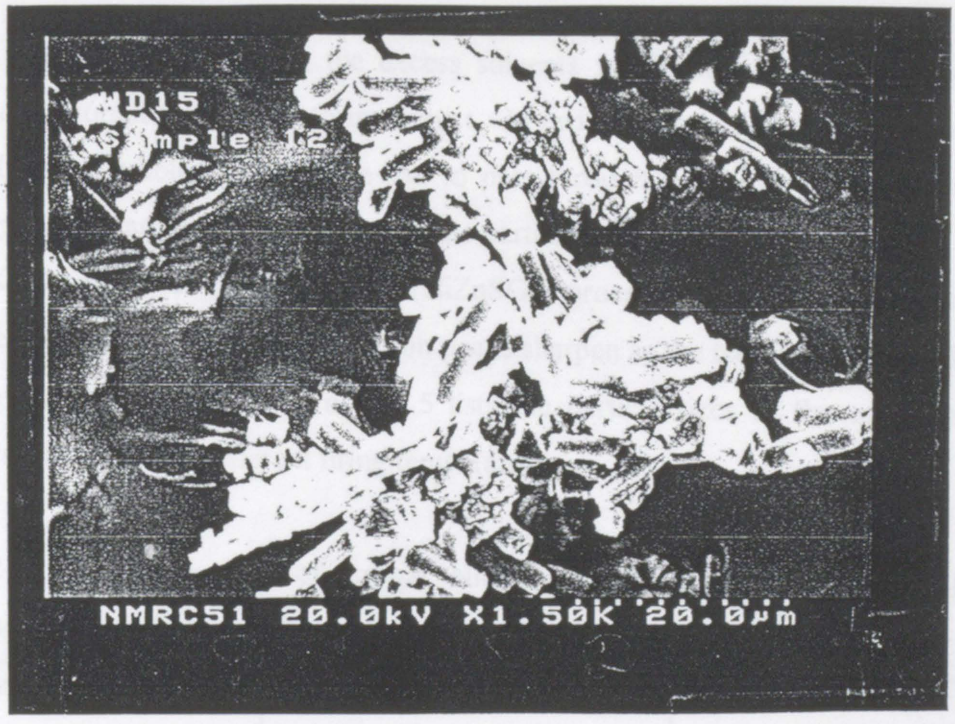


Figure 2.16 A SEM image of a coprecipitated (CP) Ni-Zn ferrite (NiZnCP2 at 800°C) powder.

From previous work, both preparation techniques (coprecipitation and sol-gel) for ferrites may be expected to form small regular shaped and sized particles with precise control of particle size and shape.[35,46] Furthermore, the coprecipitation technique has previously been used to prepare spherical ferrite particles from a mixed metal carbonate hydroxide starting material.[36] Several studies on the production of nanosized ferrites by sol-gel processes have been reported and Ni-Zn ferrites with particle sizes varying between 13 and 35nm have been prepared in a silica matrix.[43] Magnetite particles of 50nm in diameter were also formed using $Fe(acac)_3$ as reagent, acetic acid as solvent and nitric acid as catalyst in a sol-gel method.[45] The coprecipitation technique used in the present work produced ferrites with reasonably regular size and shape. The particles were clearly defined as rectangular. However, the sol-gel technique failed to produce regular shape and size ferrite particles and moreover, the ferrites contained large intragranular pores.

The drying process of the gel may afford an explanation of the formation of the more porous ferrite particles. The ferrite powders were formed in a 60°C oven overnight. Hence, the drying of the gel was rapid. The top half of the gel sample dried first and,

as the lower half was drying, the excess solvents would have found it difficult to evaporate through the already formed crust. In order to escape, the vapour, possibly in the form of bubbles, would have had to pass through the ferrite particles and this may explain the large intragrane pores in the particles.

The PXRD profiles of a sol-gel ferrite (NiZnSG1) processed at different temperatures are given in **Figure 2.17**. The diffraction peaks sharpen as the temperature rises due to the growth of the particles. **Table 2.5** lists the particle sizes of the calculated by Scherrer's formula[73] at different firing temperatures.

Table 2.5 Particle sizes of sol-gel Ni-Zn ferrites formed at different firing temperatures.

Ferrite	**Temperature / °C**	**Particle size / nm (+/- 2nm)**
NiZnSG1	60	31
	800	46
	1100	87
NiZnSG2	60	23
	800	34
	1100	11
NiZnSG3	60	19
	800	53
	1100	88
NiZnSG4	60	14
	800	56
	1100	86

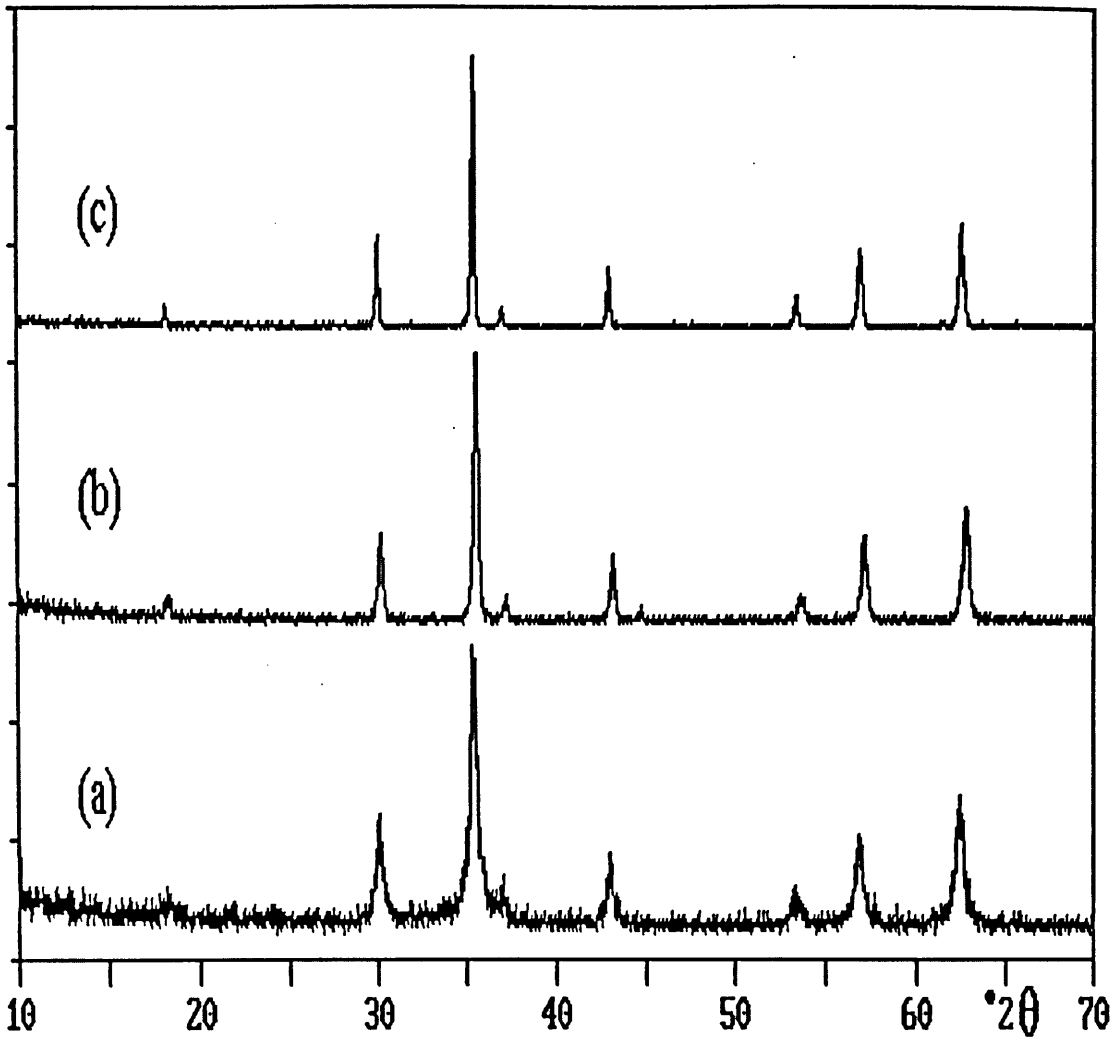


Figure 2.17 PXRD patterns of NiZnSG1 at different heat treatments, (a) 60°C, (b) 800°C and (c) 1100°C for 1.5 hours.

At the first processing temperature (60°C) of the ferrites, the particle sizes are at their lowest, ranging from 14nm to 31nm. This relatively large variation indicates a large distribution in particle sizes and highlights again the unsatisfactory results obtained with this method at 60°C. As the processing temperatures were raised the particle sizes increased, presumably due to the sintering process. Ferrites NiZnSG3 and NiZnSG4 show a gradual increase but NiZnSG1 and NiZnSG2 demonstrate a dramatic increase in particle size on going from 800°C to 1100°C. This is demonstrated graphically in **Figure 2.15**. Such an increase is probably due not only to a sintering process but also due to the formation of a fully structured ferrite.

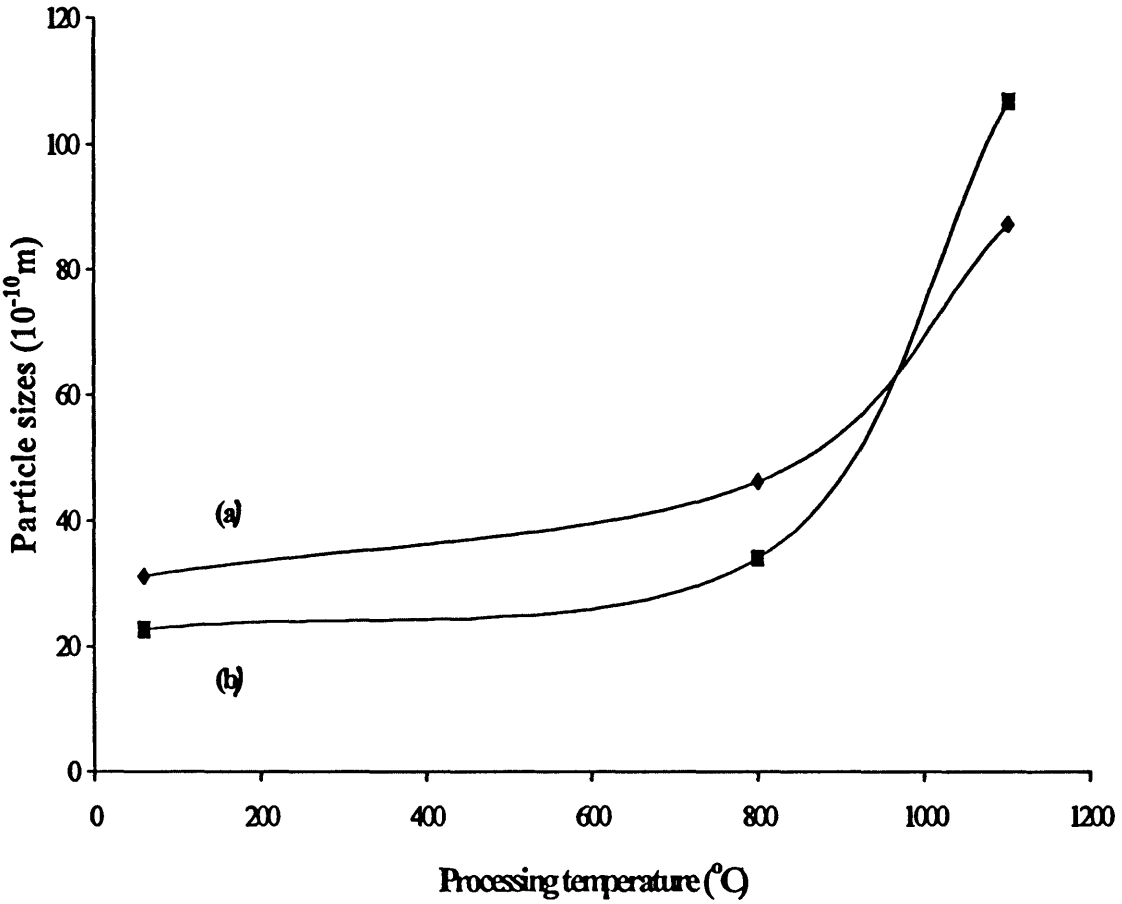


Figure 2.18 Change of particle size of (a) NiZnSG1 and (b) NiZnSG2 with processing temperatures.

(c) Ni-Zn Ferrites Prepared by Coprecipitation Method MNCD

The PXRD profile of the Ni-Zn ferrite prepared by the MNCD method (NiZnD0) is shown in **Figure 2.19** along with profiles of Ni-Zn ferrite and NiO phases. The profile of NiZnD0 displays the spinel phase pattern with no sign of impurities such as α-Fe_2O_3. However, the profile does differ from the profile of the Ni-Zn. Close examination of NiZnD0 PXRD pattern reveals that the relative intensities of the diffraction peaks are different from the Ni-Zn ferrite's pattern. The diffraction peaks at 2θ = 36.4°, 42.5° and 62.0° of the MNCD material are notably more intense than expected. The inclusion of a NiO phase with the ferrite phase in the MNCD material accounts for this observation. A NiO pattern is given in **Figure 2.19** to demonstrate

how its peaks overlap three of the ferrite's peaks. This type of ferrite-NiO system has been reported previously.[278,279] The materials were formed by the addition of either sodium[278] or tetramethylammonium[279] hydroxide to an aqueous solution of the metal nitrates to coprecipitate the metal hydroxides.

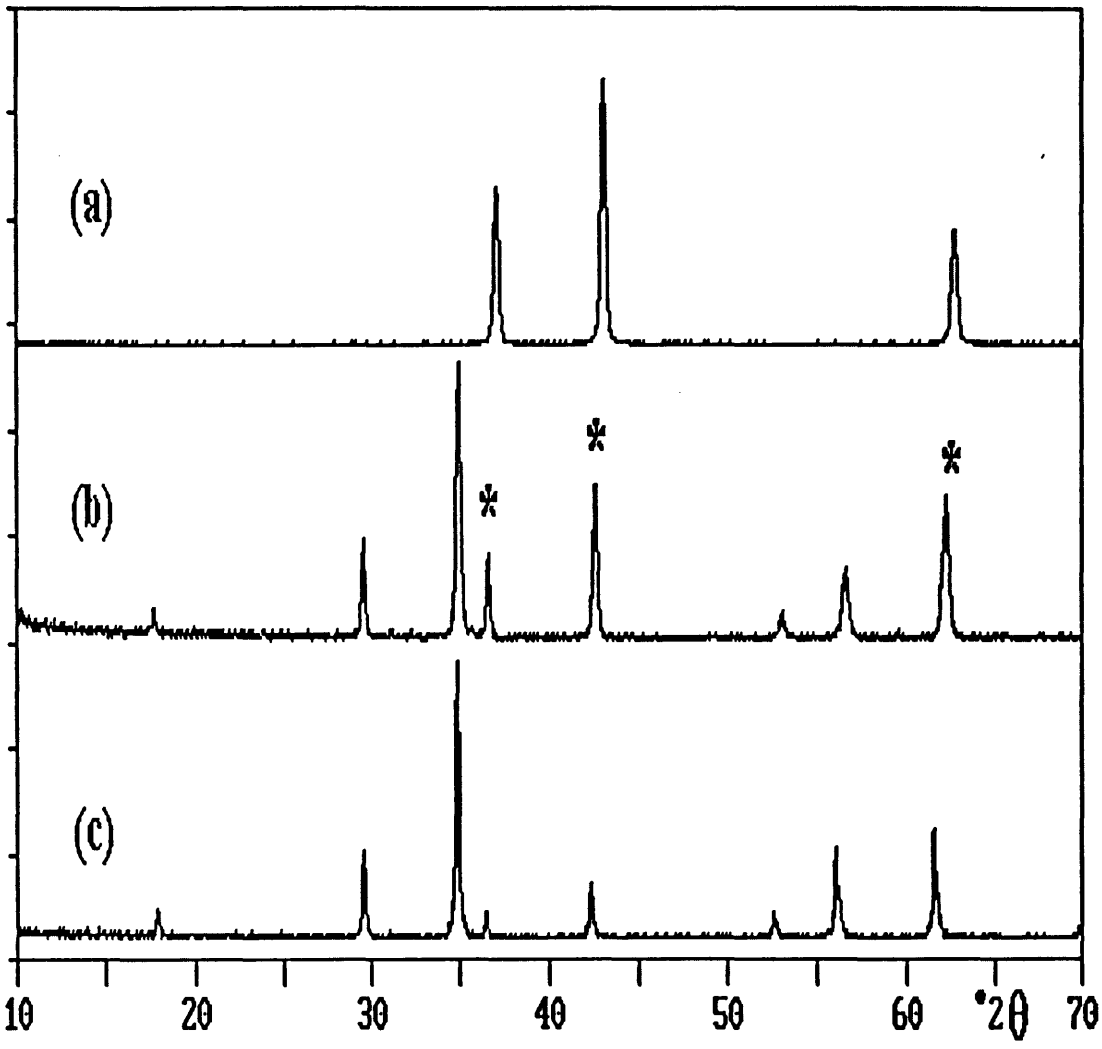


Figure 2.19 The PXRD profiles of (a) NiO, (b) NiZnD0 fired at 800°C for 1.5 hours and (c) Ni-Zn ferrite. *s denote the positions of overlap of NiO and ferrite peaks.

The PXRD patterns of the other MNCD prepared materials are similar to NiZnD0 (see **Figure 2.20**). As the zinc cation concentration in the ferrite is decreased, the patterns show a gradual change in the relative intensity of the diffraction peaks so much so that the last pattern (NiZnD4) is almost unrecognisable as the normal Ni-Zn ferrite pattern.

The materials patterns are showing an increase in the amount of NiO formed relative to the ferrite as the percent of nickel is increased in the system. As will be observed in later sections, the NiO is external to the ferrite and hence, it doesn't appear to affect the ferrite's properties such as expansion of the lattice due to increase in zinc content, as well as its magnetic and Mössbauer results.

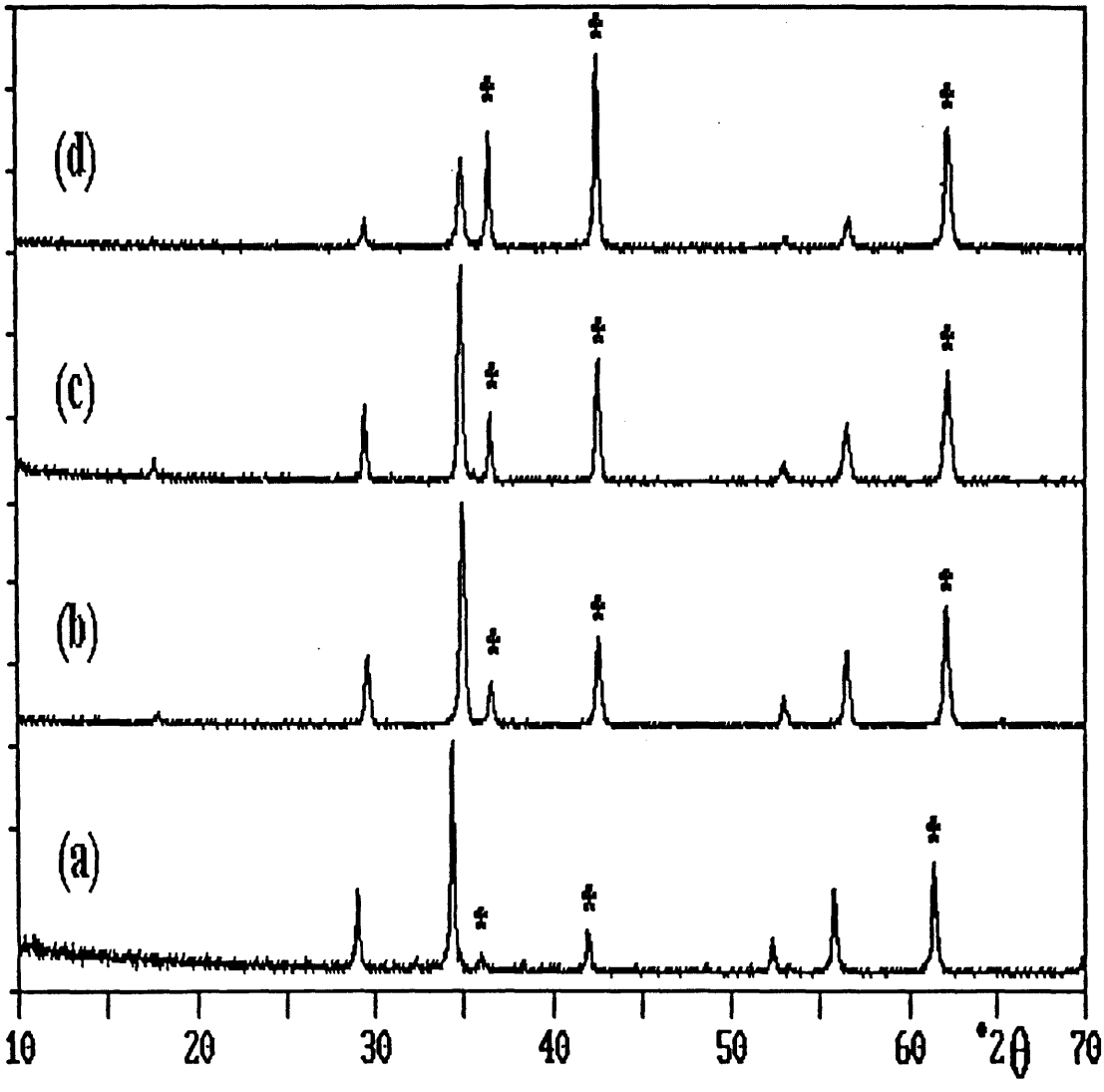


Figure 2.20 The PXRD profiles of (a) NiZnD1, (b) NiZnD2, (c) NiZnD3 and (d) NiZnD4, ired at 800°C for 1.5 hours. The (*)s denote the peaks for NiO overlapping the ferrite's peaks..

The lattice parameter a-values of the unit cell of the MNCD materials were calculated from the ferrite-only peaks in their PXRD patterns are listed in **Table 2.6**. The a-values increase with increasing zinc content in the ferrites as is the case with the other

Ni-Zn ferrites. This may suggest that these materials behave in a similar manner to the ferrites prepared by the other two techniques in respect to the zinc cations filling the tetrahedral sites.

Table 2.6 Calculated of a-values and densities of MNCD materials.

Ferrite component of material (at 800°C)	a / 10^{-10} m
NiZnD0 $Ni_{0.06}Zn_{0.94}Fe_{1.78}O_{4-y}$	8.553517
NiZnD1 $Ni_{0.33}Zn_{0.67}Fe_{1.34}O_{4-y}$	8.546218
NiZnD3 $Ni_{0.41}Zn_{0.59}Fe_{1.71}O_{4-y}$	8.538214
NiZnD4 $Ni_{0.76}Zn_{024}Fe_{1.73}O_{4-y}$	8.523937
NIZnD5 $NiFe_{1.91}O_{4-y}$	8.518358

It is also noticed that the a-values of these materials are slightly larger than those previously discussed. However, the values should not be compared with those of the ferrites prepared by the other methods as the MNCD materials contain NiO impurities. A plot of a-values versus value of x in $Zn_xNi_{1-x}Fe_2O_4$ component of the MNCD materials is shown in Figure 2.21 and a linear plot is observed.

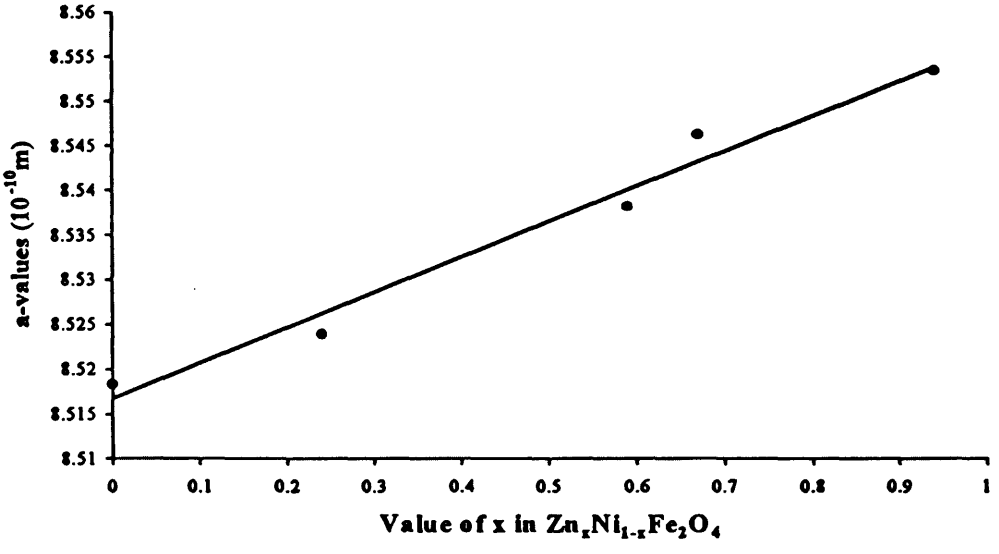


Figure 2.21 Plot of a-values of ferrite component of MNCD materials (fired at 800°C) versus value of x in $Zn_xNi_{1-x}Fe_2O_4$.

The SEM images of the **MNCD** prepared particles, see **Figure 2.22(a)** and **(b)** for a typical example (NiZnD3) suggest that the particles are roughly circular and of the same size. They show no signs of intragranular porosity (unlike the sol-gel ferrites).

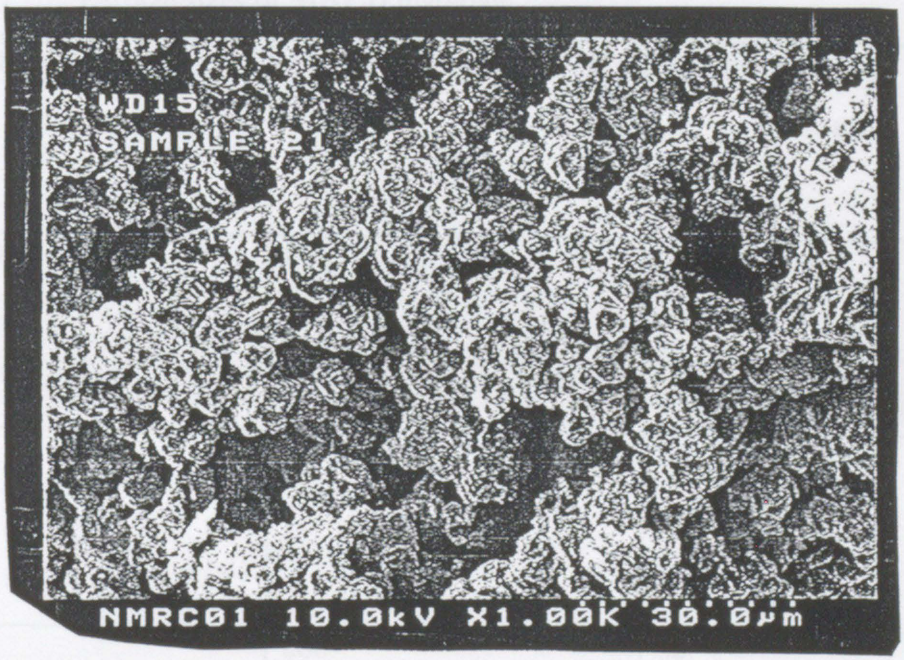


Figure 2.22(a) A SEM image of a **MNCD** material powder (NiZnD3 heated at 800°C) at 1 x 10^3 magnification.

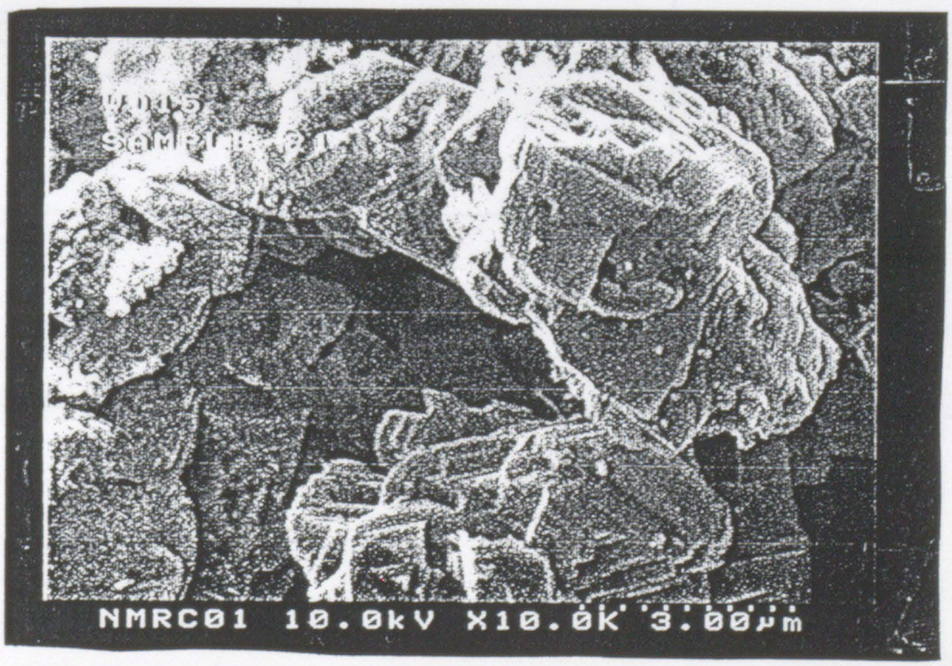


Figure 2.22(b) A SEM image of a **MNCD** material powder (NiZnD3 heated at 800°C) at 1 x 10^4 magnification.

The particle sizes of these powders were calculated using Scherrer's equation[73] and are shown in **Table 2.7**. The particle sizes are approximately the same as those observed from the other methods when sintered at the same temperature.

Table 2.7 Particle sizes of MNCD materials

Material	**Firing temperature / °C**	**Particle size / nm (+/- 2nm)**
NiZnD0	800	74
NiZnD1	800	51
NiZnD2	800	54
NiZnD3	800	61
NiZnD4	800	58

2.2.3 *VSM Measurements*

Magnetic measurements were obtained on powdered samples using a vibrating sample magnetometer which is described in **Appendix C.** A M-H hysteresis loop was obtained for each sample and saturation magnetisation (M_s) values of the samples were estimated from the loops. Since these ferrites are magnetically "soft", their coercivity, H_c, values are very small and not measurable by this technique.

(a) Ni-Zn Ferrites Prepared by Coprecipitation Method (CP)

Figure 2.23 demonstrates a typical hysteresis loop obtained for each coprecipitated Ni-Zn ferrite. The loop is characteristic of a "soft" ferrite. The M_s value corresponds to the point where the loop flattens. This value indicates the magnetic strength of the ferrite; for the example shown in **Figure 2.23**, this value is 40.0 J $T^{-1}kg^{-1}$.

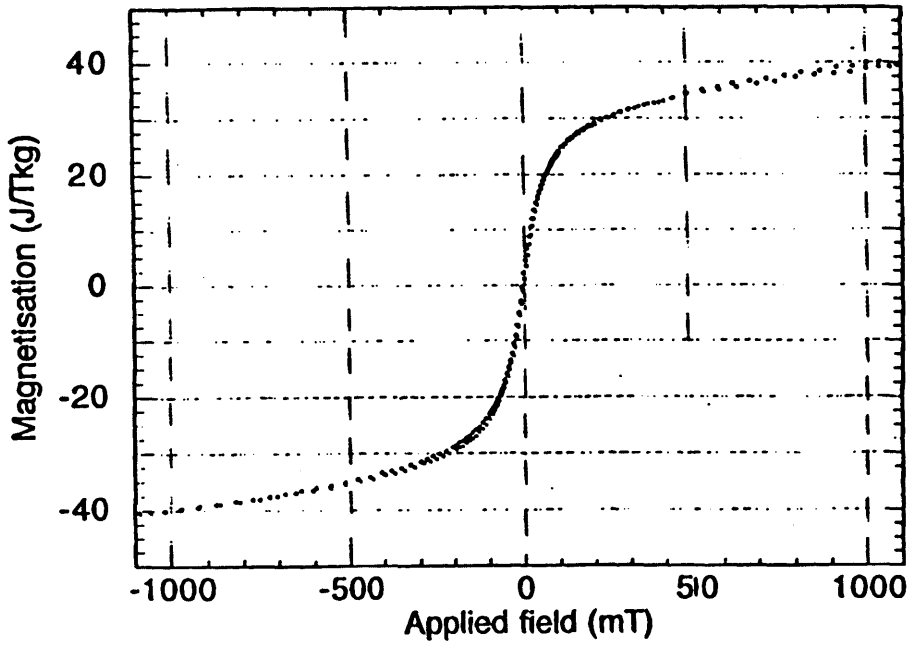


Figure 2.23 Hysteresis loop for NiZnCP1 fired at 1100°C.

Another magnetic property of ferrites that can be calculated from their M_s values is their saturation flux density (B_s). Equation [3] in **Section 1.3.1** explained the relation between the flux density and the magnetisation of a material. For the situation where $M >> H$, the B_s values are calculated from the formula:

$$B_s = \mu_0 M_s . \rho_x \qquad \text{where } \mu_0 = \text{permeability of vacuum} = 4\pi \times 10^{-7}\ Hm^{-1} \qquad [7]$$

where ρ_x = theoretical density of ferrite (kg m^{-3})

Table 2.8 gives a list of the M_s and corresponding B_s values of the coprecipitated ferrites. The M_s (and hence B_s) values of the ferrites increase with increasing zinc content in the ferrites. Smit and Wijn reported that the flux densities (σ is equivalent to B_s/ρ) of Ni-Zn ferrites (prepared by the ceramic method) varies with temperature, see **Figure 2.24**.[74] The flux densities of these materials at room temperature can be estimated from **Figure 2.24** and compared with the results obtained in this work. This is shown graphically in **Figure 2.25**. Both sets of ferrites follow a similar trend, with the highest B_s values occurring between 0.3 and 0.5 molar concentration of zinc ions. At higher zinc concentrations, magnetisation values decrease sharply for both sets of samples.

Table 2.8 Magnetic properties of coprecipitated Ni-Zn ferrites (fired at 1100°C).

Ferrite	M_s / J T^{-1} kg^{-1} (+/- 0.4)	B_s / mT
NiZnCP1 $Ni_{0.27}Zn_{0.73}Fe_{1.70}O_{4-y}$	40.0	268.2
NiZnCP2 $Ni_{0.36}Zn_{0.64}Fe_{3.64}O_{4+y}$	53.9	359.8
NiZnCP3 $Ni_{0.51}Zn_{0.49}Fe_{1.67}O_{4-y}$	70.0	469.3
NiZnCP4 $Ni_{0.71}Zn_{0.29}Fe_{1.76}O_{4-y}$	74.0	496.5

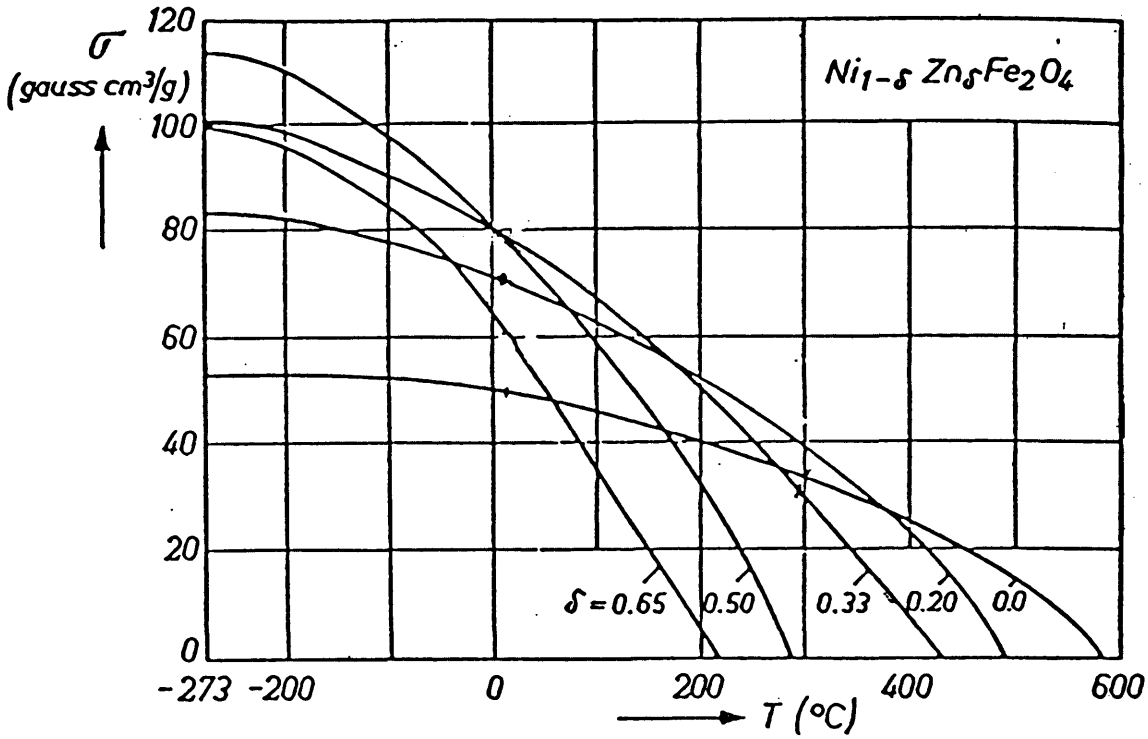


Figure 2.24 The temperature dependencies on magnetisation values of Ni-Zn ferrites.[74]

The different firing conditions of the ferrites also changed their magnetisation. **Table 2.9** gives the M_s values of one coprecipitated Ni-Zn ferrite, NiZnCP2, fired at various temperatures. The magnetisation values increase with increasing processing temperature. As mentioned previously, when considering the growth of ferrite particles in **Section 2.2.2**, the ferrite's structure only fully forms at the high firing temperatures and hence, its magnetic properties are consolidated only at these temperatures. This is confirmed by the results in **Table 2.9**.

Table 2.9 The M_s values of coprecipitated Ni-Zn ferrite fired at different firing temperatures.

Ferrite	Heat treatment / °C	M_s / J T^{-1} kg^{-1} (+/- 0.4)
NiZnCP2	400	36.2
	800	44.9
	1100	53.9

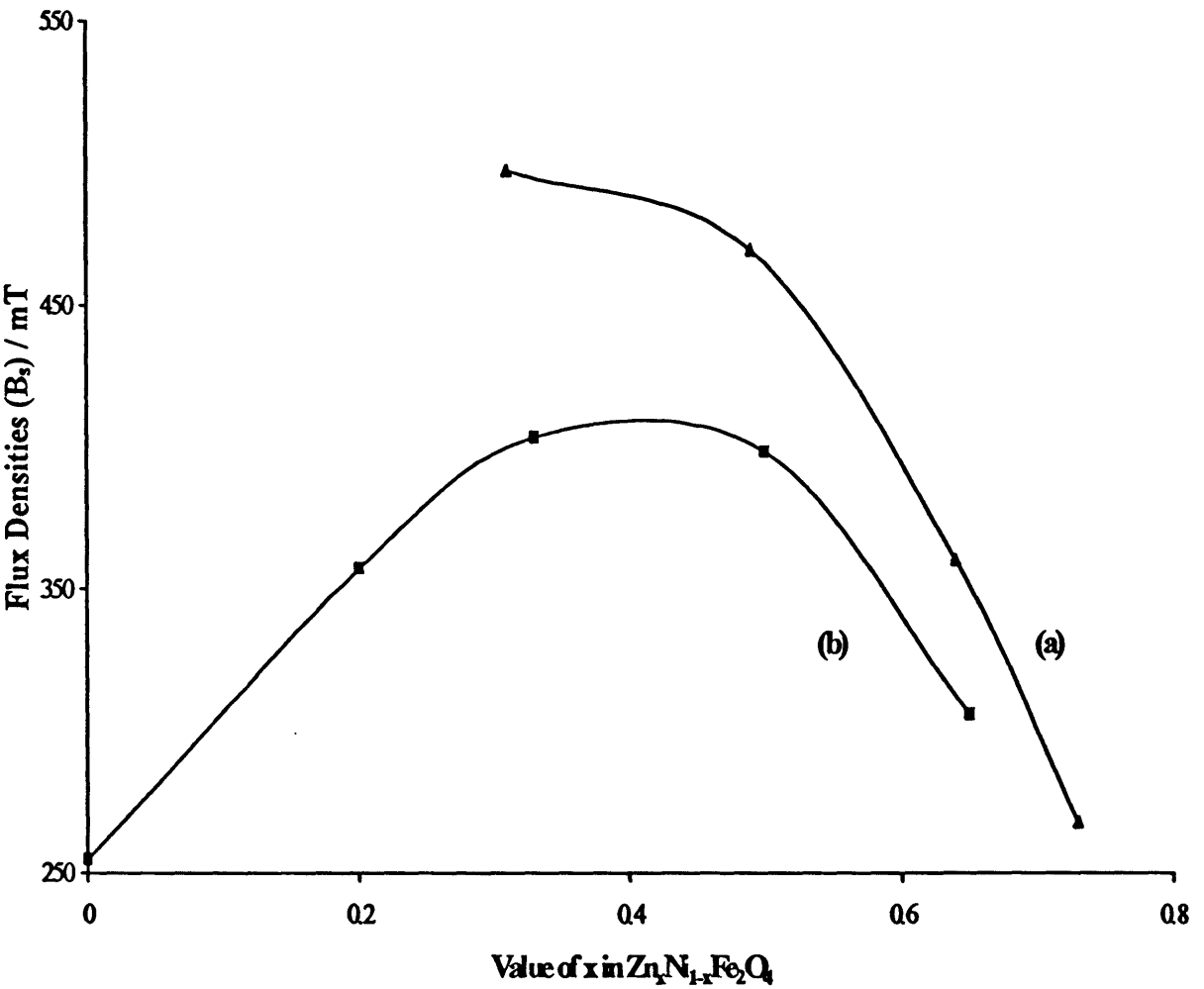


Figure 2.25 Flux densities versus value of x in $Zn_xNi_{1-x}Fe_2O_4$ for (a) coprecipitated Ni-Zn ferrites (fired at 1100°C) prepared by the present work and (b) Ni-Zn ferrites (fired at 1100°C) prepared by ceramic method from ref. 74.

(b) Ni-Zn Ferrites Prepared by Sol-Gel Method

Sol-gel Ni-Zn ferrites gave the expected hysteresis loops for "soft" ferrites. **Figure 2.26** shows the hysteresis loop for NiZnSG2 fired at 800°C. Once again, magnetic properties such as coercivity and remanence are too small to be estimated from these loops.

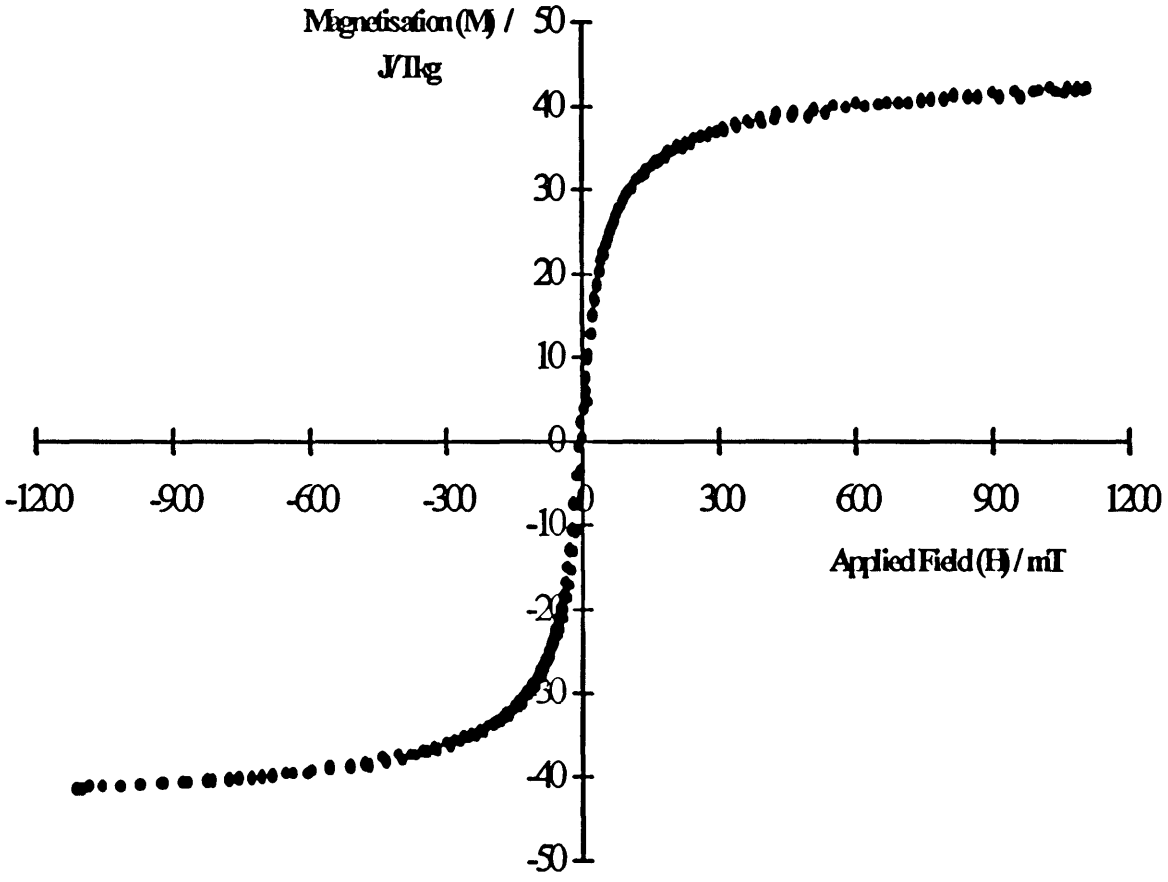


Figure 2.26 Hysteresis loop of NiZnSG2 fired at 800°C.

Table 2.10 gives a list of the saturation magnetisation, M_s, values for the sol-gel ferrites as estimated from their respective hysteresis loops. M_s values are not only given for the compositional changes in the ferrites but also for their different processing temperatures. **Table 2.10** gives the respective B_s values, as well.

Table 2.10 The M_s and B_s values of sol-gel Ni-Zn ferrites.

Ferrite	Heat treatment / °C	M_s / J T^{-1} kg^{-1} (+/- 0.4)	B_s / mT
NiZnSG1	60	14.9	99.7
$Ni_{0.29}Zn_{0.71}Fe_{1.94}O_{4-y}$	800	27.0	180.8
	1100	33.45	223.8
NiZnSG2	60	30.4	203.4
$Ni_{0.36}Zn_{0.64}Fe_{2.18}O_{4+y}$	800	41.5	277.7
	1100	52.4	350.7
NiZnSG3	60	38.2	255.2
$Ni_{0.50}Zn_{0.50}Fe_{2.33}O_{4+y}$	800	42.5	284.0
	1100	55.2	368.8
NiZnSG4	60	39.7	265.2
$Ni_{0.75}Zn_{0.25}Fe_{2.45}O_{4+y}$	800	52.5	350.8
	1100	64.8	432.9

The composition of the sol-gel ferrites clearly has a marked affect on the M_s (and B_s) values of the ferrite as expected. The trend is generally the same as for the coprecipitated ferrites. The B_s results are compared in **Figure 2.27.** The magnetisation values also rise with firing temperature for each ferrite. The formation of improved ferrite structure at higher processing temperatures (as observed in the coprecipitated ferrites) explains this phenomenon.

The M_s values for sol-gel ferrites are noticeably lower than the corresponding coprecipitated ferrites. The difference is a consequence of the difference in porosity of the ferrites. The saturation magnetisation of a ferrite should increase with decreasing porosity because of the increase in density, i.e. the packing of more magnetic material in a specific volume. Studies on Ni-Zn ferrites of changes in B-H loops with porosity confirm this, i.e. an increase in porosity leads to a decrease in B_s (or M_s) of the ferrite as demonstrated in **Figure 2.28.**[75]

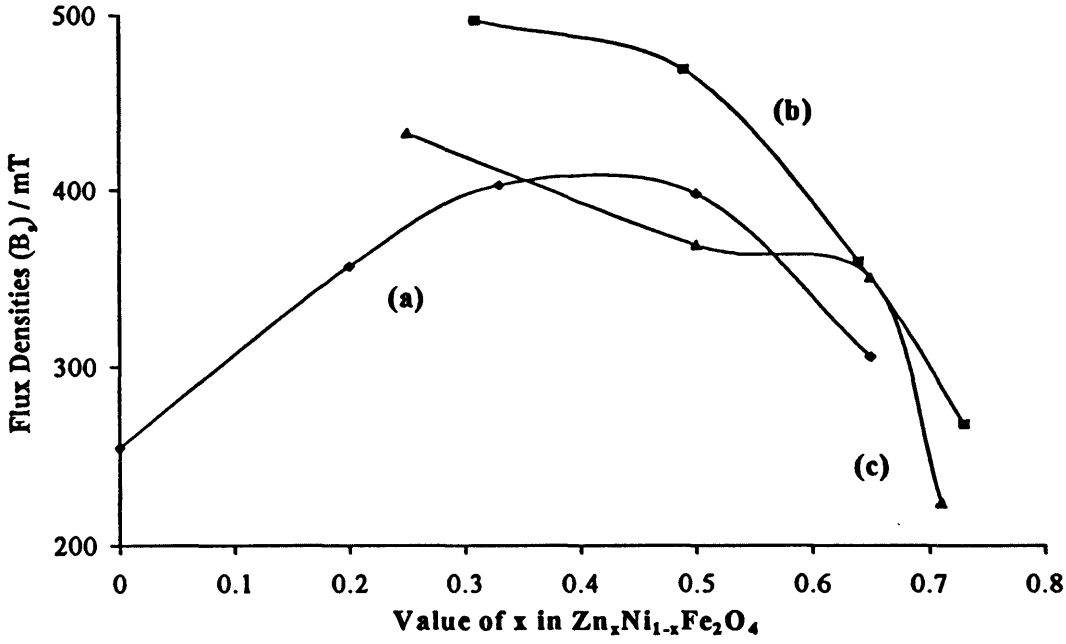


Figure 2.27 Flux densities values versus value of x in $Zn_xNi_{1-x}Fe_2O_4$ for (a) Ni-Zn ferrites of ref. 74, (b) Ni-Zn ferrites produced by the coprecipitation technique and (c) Ni-Zn ferrites prepared by the sol-gel technique. All fired at 1100°C

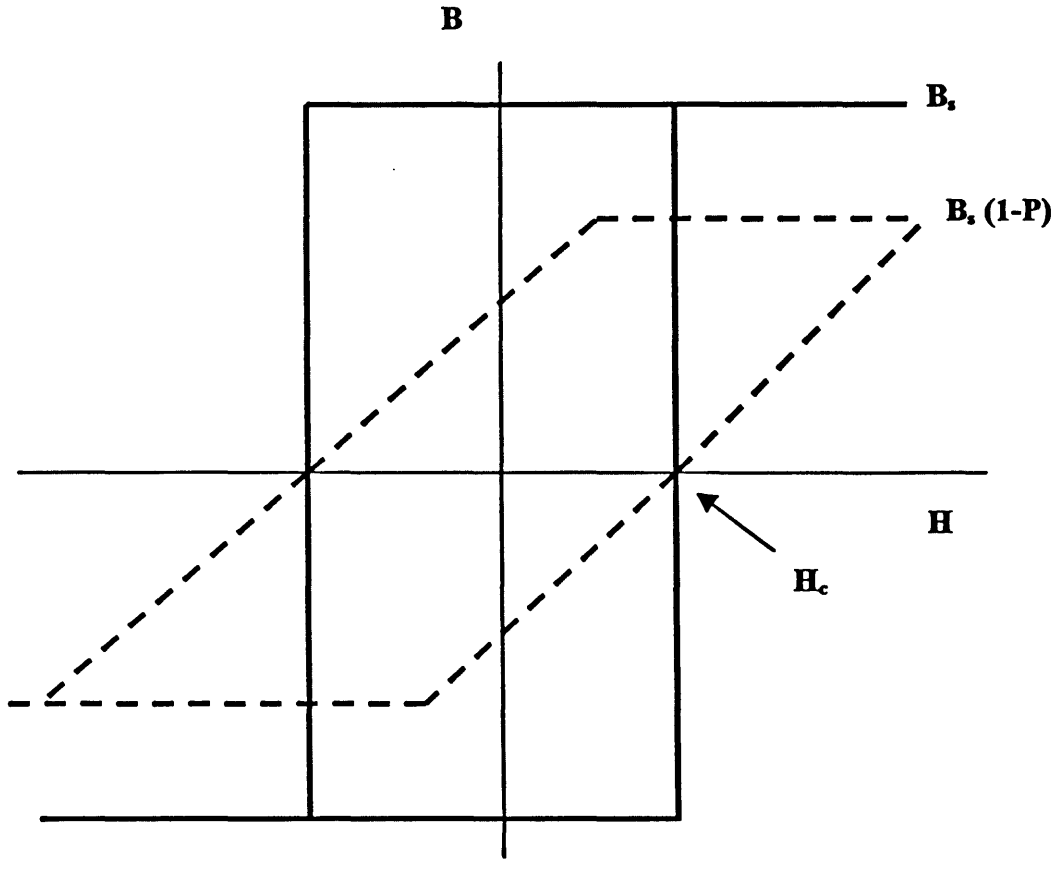


Figure 2.28 Change of hysteresis loop of a Ni-Zn ferrite due to an increase in porosity.[75] B_s = saturated flux density, H_c = coercivity value and P = porosity.

As previously mentioned, sol-gel ferrite particles showed intragranular porosity in their SEM images while this was largely absent in the coprecipitated ferrites. Hence, the higher porosity in the sol-gel ferrites explains their lower magnetisation values when compared with their corresponding coprecipitated ferrites.

(c) Ni-Zn Ferrites Prepared by the Coprecipitation Method MNCD

These prepared materials contain both ferrite and NiO phases. The NiO does not possess long range magnetic properties and hence, the magnetic values given below are due only to the ferrite phase in these materials. The values are not accurate as the NiO mixture affects the masses of the materials. However, the values may be compared relatively to each other. The hysteresis loop obtained for the Ni-Zn ferrite (NiZnD0) produced from the MNCD method is shown in **Figure 2.29**. As is characteristic of a "soft" ferrite, the loop is narrow and reaches its saturated magnetisation, M_s, value very quickly (i.e. in a small applied magnetic field).

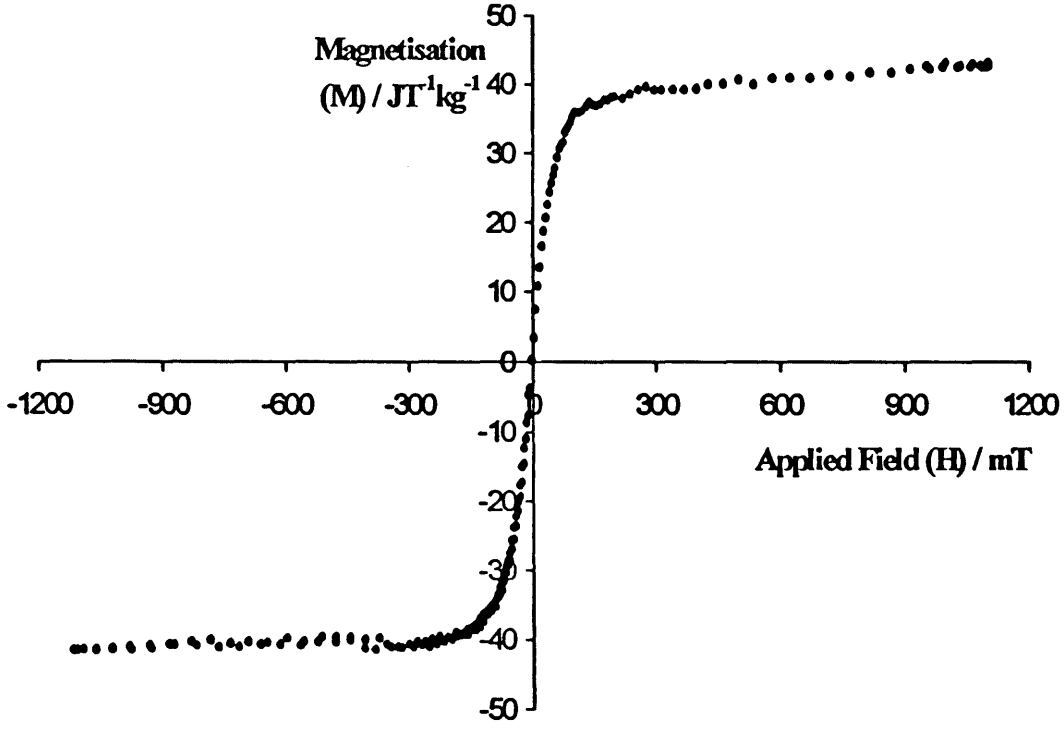


Figure 2.29 Hysteresis loop of NiZnD0 material fired at 1100°C.

The other materials prepared by the MNCD method also gave typical hysteresis loops of Ni-Zn ferrites. **Table 2.11** gives the M_s and their corresponding B_s values (flux densities values were calculated using an average density = 5.2×10^3 kg m^{-3}) of all the MNCD materials.

Table 2.11 Magnetic properties of materials prepared by MNCD method.

Ferrite component of material	M_s / J T^{-1} kg^{-1} (+/- 0.4)	B_s / mT
NiZnD0 $Ni_{0.06}Zn_{0.94}Fe_{1.78}O_{4-y}$	43.07	277.0
NiZnD1 $Ni_{0.33}Zn_{0.67}Fe_{1.34}O_{4-y}$	50.32	323.1
NiZnD2 $Ni_{0.41}Zn_{0.59}Fe_{1.71}O_{4-y}$	59.11	379.1
NiZnD3 $Ni_{0.76}Zn_{0.24}Fe_{1.73}O_{4-y}$	52.00	331.9
NiZnD4 $NiFe_{1.91}O_{4-y}$	17.00	109.1

The magnetisation values increase initially with increasing zinc content in the ferrite until at about 0.6 molar concentration. The M_s (and B_s) values then fall with increasing zinc concentration. This result is not unlike the data in the graph obtained by Smit and Wijn[74] (see **Figure 2.24**) for the variation of magnetic moments of Ni-Zn ferrites with zinc content at room temperature. **Figure 2.30** compares the flux densities values of the Ni-Zn ferrites prepared with the three methods to the values of the Ni-Zn ferrites from Smit and Wijn.[74]

Figure 2.30 shows that the Ni-Zn ferrites produced by the three methods used in the present work have flux densities values that follow similar trends to those observed previously by Smit and Wijn.[74] The highest values for the sol-gel and coprecipitated ferrites are at the Zn^{2+} molar concentration range of 0.2-0.3. The MNCD materials however give the highest value at about 0.6. The coprecipitated ferrites give the

highest magnetisation values (at Zn^{2+} molar concentrations less than 0.50). The sol-gel Ni-Zn ferrites have magnetisation values below the coprecipitation (CP) ferrites but generally higher than the MNCD materials. The sol-gel ferrites may have inferior magnetic properties to the coprecipitation ferrites because of poorer microstructure.

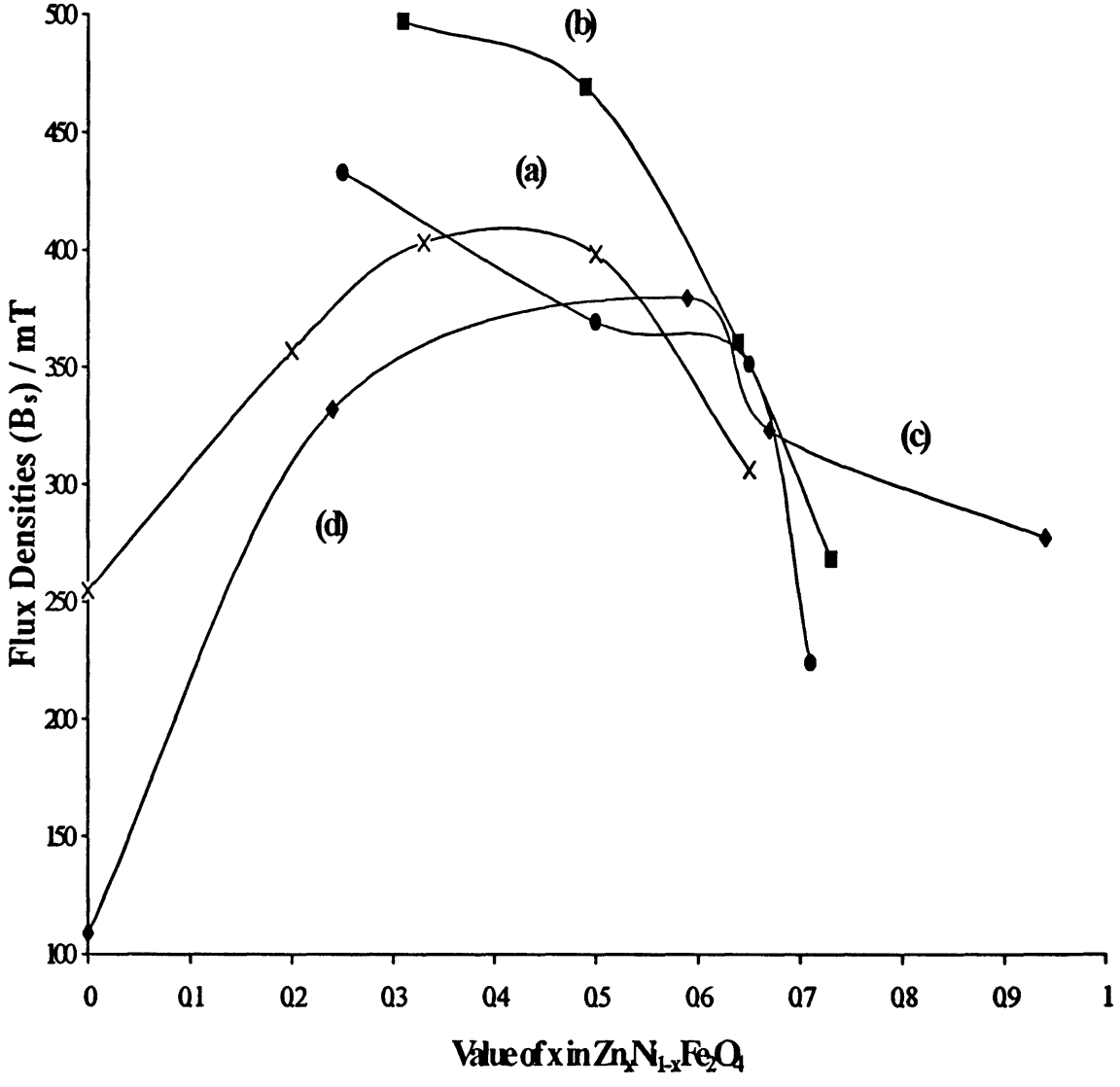


Figure 2.30 Flux densities versus value of x in $Zn_xNi_{1-x}Fe_2O_4$ in (a) Ni-Zn ferrites produced in ref. 74, (b) Ni-Zn ferrites prepared by the coprecipitation technique, (c) Ni-Zn ferrites produced by the sol-gel method and (d) Ni-Zn ferrites produced by the MNCD method. All ferrites fired at 1100°C.

2.2.4 *Mössbauer Spectroscopy*

Mössbauer spectroscopy has been used extensively to study ferrites[58,59,60] since it can provide detailed information about the Fe nucleus, such as its oxidation state, the symmetry of the crystal site it occupies and the magnitude of the local magnetic field. A detailed explanation of the Mössbauer effect and the apparatus used to measure it is given in **Appendix D**.

Mössbauer studies have previously been made on Ni-Zn ferrites with composition $Ni_xZn_{1-x}Fe_2O_4$, $0 < x < 1$.[59,67] The results of these studies are discussed in **Section 2.1.2.4** but are summarised here. The Ni-Zn ferrites can be placed in three magnetic categories. For $x > 0.6$, the ferrites showed a doublet of sextets in the spectra, which is typical for a magnetically ordered species. For $0.6 < x < 0.3$, the ferrites displayed progressively collapsing sextets in the spectra, characteristic of a species becoming magnetically relaxed. For $x < 0.3$, the ferrites displayed spectra of quadrupole doublets, which are indicative of paramagnetic species. Lowering the temperature changes the balance between the three magnetic regions described above. At liquid nitrogen temperatures, the magnetic regions shift to lower x values, i.e. for $x > 0.5$, the ferrites are in a magnetic state, for $0.5 < x > 0.2$, the ferrites are in a magnetically relaxed state and for $x < 0.2$, the ferrites are in the paramagnetic state.

Mössbauer spectroscopy can also be influenced by particle size of the Ni-Zn ferrites. For fine particles at room temperature the magnetic ordering of the species may not be observed on the Mössbauer time-scale. Instead a "paramagnetic" doublet is observed. This phenomenon is termed superparamagnetism.[69,70] The doublet will generally transform back to the doublet of sextets if the spectrum is taken at liquid nitrogen temperature because the rate of movement is reduced and magnetic ordering can now be detected.

(a) Ni-Zn Ferrites Prepared by Coprecipitation Method (CP)

The Mössbauer spectra of the coprecipitated Ni-Zn ferrites (all fired at 800°C) measured at room temperature are shown in **Figure 2.31**. The trend is similar to the one obtained by Daniels and Rosencwaig[59] and Arshed *et al.*[67] **(Figure 2.5)** with an initial doublet of sextets spectrum changing to the paramagnetic doublet as the zinc

content in the ferrite is increased. It should be noted here that the ferrites prepared by Daniels and Rosencwaig[59] and Arshed *et al.*[67] were formed at 1200°C and 1300°C respectively, by the ceramic method. The ferrites by Arshed *et al.* were characterised by PXRD profiles (although the diffractograms were not given) to ensure no impurities existed.[67] In the present work, the ferrites were prepared by a chemical means and fired at 800°C. However, the results are similar and they suggest that the postulated three magnetic regions in Ni-Zn ferrites are also detected here. Ferrites NiZnCP4 and NiZnCP3 display the doublet of sextets spectrum of the magnetic region, NiZnCP2 displays the collapsed doublet of sextets of the relaxation region and NiZnCP1 display the doublet spectrum of the paramagnetic region.

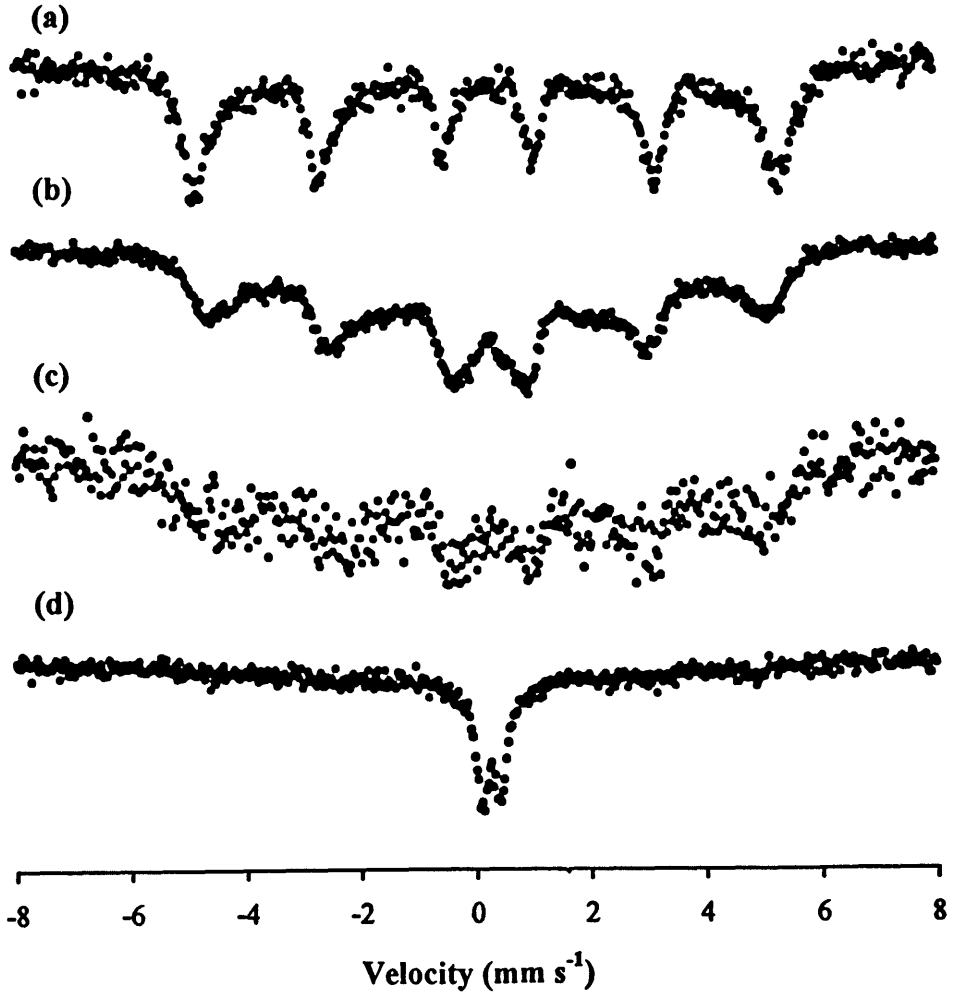


Figure 2.31 Mössbauer spectra of coprecipitated Ni-Zn ferrites (fired at 800°C) at 294 K: (a) NiZnCP4 ($Ni_{0.71}Zn_{0.29}Fe_{1.76}O_{4-y}$), (b) NiZnCP3 ($Ni_{0.51}Zn_{0.49}Fe_{1.67}O_{4-y}$), (c) NiZnCP2 ($Ni_{0.36}Zn_{0.64}Fe_{2.63}O_{4+y}$) and (d) NiZnCP1 ($Ni_{0.27}Zn_{0.73}Fe_{1.70}O_{4-y}$).

A Mössbauer spectrum of NiZnCP1 (fired at 800°C) was also taken at liquid nitrogen temperature and is reported in **Figure 2.32**. The spectrum shows a collapsed doublet of sextets plus an inner asymmetric doublet. Hence, a transition from a paramagnetic species to a magnetically relaxed species has occurred on lowering the temperature. This transition was also reported by Daniels and Rosencwaig at liquid nitrogen temperature for the ferrite with x = 0.70.[59] This transition happens because the experimental temperature is once again lower than the magnetic ordering temperature and hence, Mössbauer spectroscopy observes a magnetically ordered species. Another explanation for the transition may have been the halting of superparamagnetism in small particles in the ferrite at the liquid nitrogen temperature. However, the particle sizes of NiZnCP1 at the processing temperature of 800°C is of the order of 880Å (see **Table 2.3**), which is too big to exhibit superparamagnetism (particles have to be *circa* 100Å or below). The possibility that some particles are less than 880Å (and hence show superparamagnetism) is small as the SEM of this ferrite showed particles with a small particle size distribution (850 +/- 50Å).

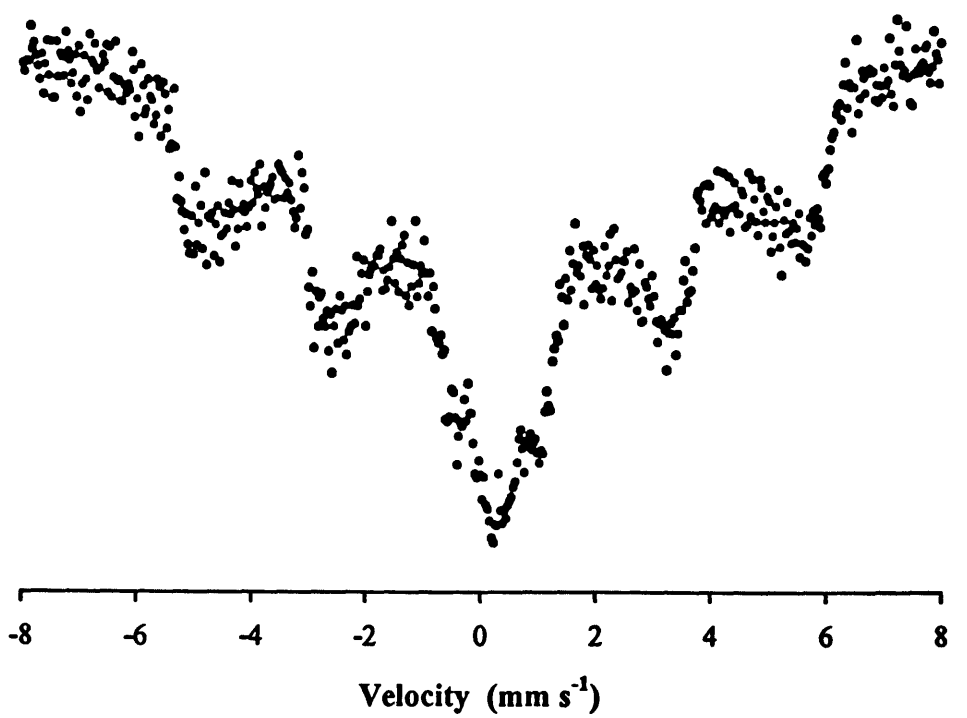


Figure 2.32 Mössbauer spectrum of NiZnCP1 ($Ni_{0.27}Zn_{0.73}Fe_{1.70}O_{4-y}$ fired at 800°C) taken at liquid nitrogen temperature.

(b) Ni-Zn Ferrites Prepared by Sol-Gel Method

The Mössbauer spectra of the sol-gel Ni-Zn ferrites (fired at 800°C) were measured at room temperature and are shown in **Figure 2.33**. Once again, the pattern changes from a doublet of sextets spectrum through a collapsed doublet of sextets to an asymmetric doublet, as the zinc content is increased in the ferrites.

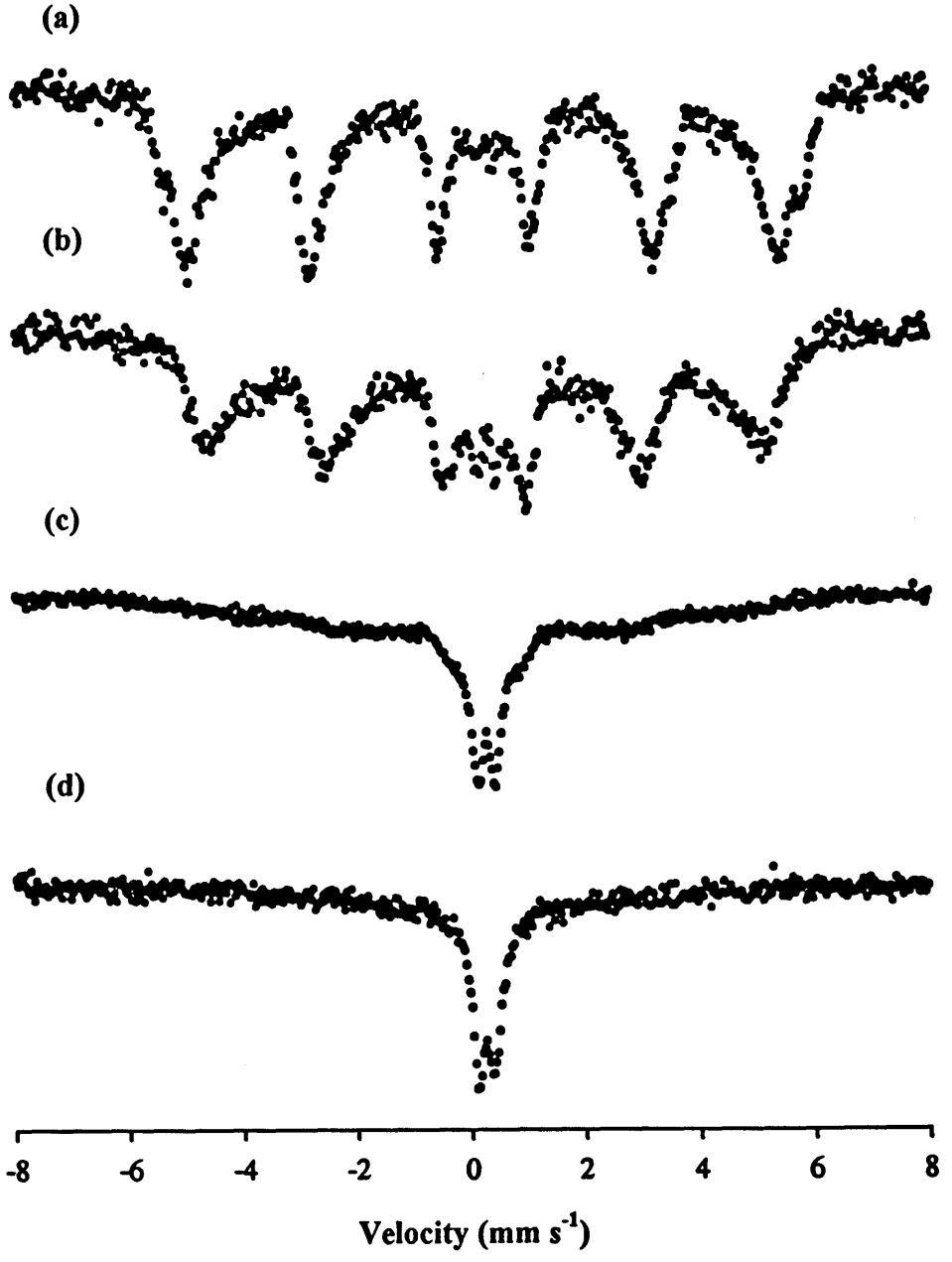


Figure 2.33 Mössbauer spectra of sol-gel Ni-Zn ferrites (fired at 800°C) at 293 K: (a) NiZnSG4 ($Ni_{0.75}Zn_{0.25}Fe_{2.45}O_{4+y}$), (b) NiZnSG3 ($Ni_{0.50}Zn_{0.50}Fe_{2.33}O_{4+y}$), (c) NiZnSG2 ($Ni_{0.36}Zn_{0.64}Fe_{2.18}O_{4+y}$) and (d) NiZnSG1 ($Ni_{0.29}Zn_{0.71}Fe_{1.94}O_{4-y}$).

The only difference between these spectra and those of the coprecipitated ferrites is the appearance of a central doublet in all the spectra. This may suggest the presence of very small particles exhibiting superparamagnetism in the ferrite. The particles of the sol-gel ferrites at the firing temperature of 800°C are smaller than the corresponding coprecipitated ferrites. For example, the particle size of NiZnSG3 is approximately 530Å (see **Table 2.5**) and these particles are too large to show superparamagnetism. However, a SEM image (see **Figure 2.15**) of the sol-gel ferrites showed particles of different shapes and sizes (i.e. with a large size distribution). Hence, it is possible that the sol-gel ferrites may contain some very fine particles that can exhibit superparamagnetism. A Mössbauer spectrum was recorded for NiZnSG3 at liquid nitrogen temperature and is shown in **Figure 2.34**. The spectrum shows a distinct doublet of sextets with no central doublet in evidence. Therefore, it appears that lowering the temperature had removed the superparamagnetic effect due to the fine particles.

From their room temperature Mössbauer spectra, the sol-gel ferrites can be placed into three magnetic regions. Ferrite NiZnSG4 displays the doublet of sextets spectrum of the magnetic region. Ferrites NiZnSG3 and NiZnSG2 display the collapsed doublet of sextets spectra of the relaxation region, and ferrite NiZnSG1 displays the asymmetric doublet of the paramagnetic region.

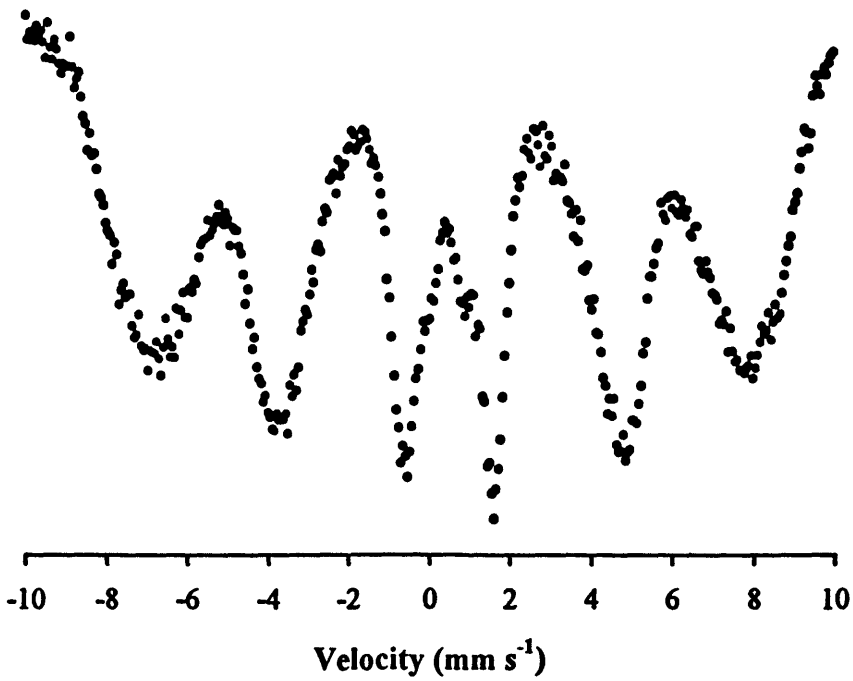


Figure 2.34 Mössbauer spectrum of NiZnSG3 (fired at 800°C) taken at 77K.

(c) Ni-Zn Materials Prepared by MNCD Method

If the suggestion that the MNCD materials have a ferrite component whose magnetic properties are unaffected by NiO, then this should be apparent from their Mössbauer spectra. The spectra of the MNCD materials (fired at 800°C) at room temperature are shown in **Figure 2.35**.

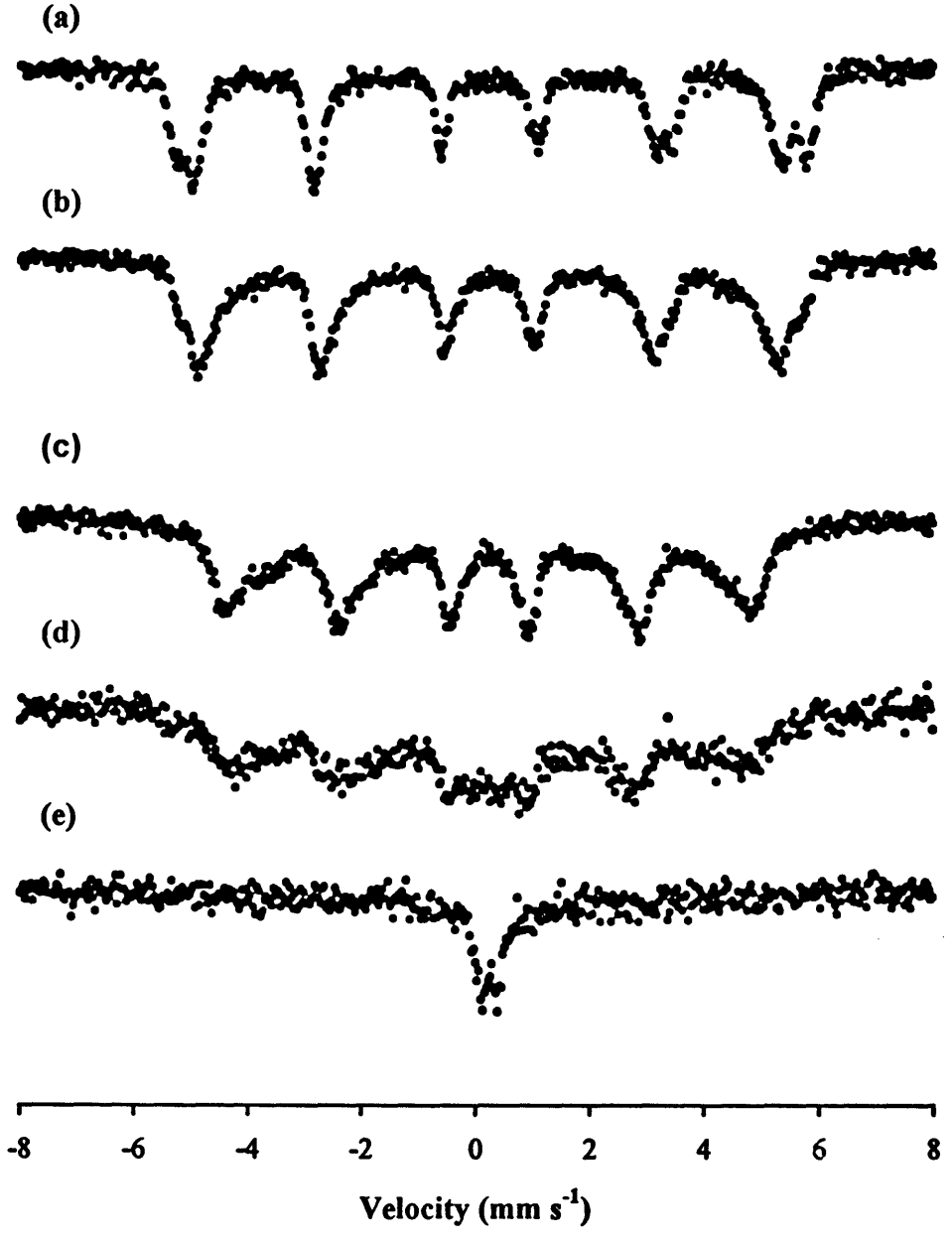


Figure 2.35 Mössbauer spectra of the MNCD ferrites (fired at 800°C) at 294 K: (a) NiZnD4 ($NiFe_{1.91}O_{4-y}$), (b) NiZnD3 ($Ni_{0.76}Zn_{0.24}Fe_{1.73}O_{4-y}$), (c) NiZnD2 ($Ni_{0.41}Zn_{0.59}Fe_{1.71}O_{4-y}$), (d) NiZnD1 ($Ni_{0.33}Zn_{0.67}Fe_{1.34}O_{4-y}$) and (e) NiZnD0 ($Ni_{0.06}Zn_{0.94}Fe_{1.78}O_{4-y}$).

The previous trend for Ni-Zn ferrites, prepared by coprecipitation (CP) and sol-gel (SG) techniques, from a doublet of sextets to an asymmetric doublet as the zinc concentration in the ferrite is increased is clearly observed. The ferrite components in the MNCD materials are referred to in the proceeding sentences. Ferrites NiZnD4 and NiZnD3 display the doublet of sextets spectrum of the magnetic region. Ferrites NiZnD2 and NiZnD1 display a progressively collapsing spectrum of the magnetic relaxation region and ferrite NiZnD0 shows the asymmetric doublet of the paramagnetic region. **Figure 2.36** illustrates the Mössbauer spectrum of NiZnD1 at liquid nitrogen temperature. A slightly relaxed doublet of sextets spectrum is observed. The transition from a completely collapsed spectrum to a slightly collapsed spectrum is due to the lowering of the temperature. The transition is not related to superparamagnetism as the particles are too large (~510Å, see **Table 2.7**) and SEM images of the MNCD materials [see **Figures 2.22(a)** and **2.22(b)**] suggested a small particle size distribution akin to the coprecipitated ferrites. These data are clear evidence that ferrite formation has occurred with the MNCD method.

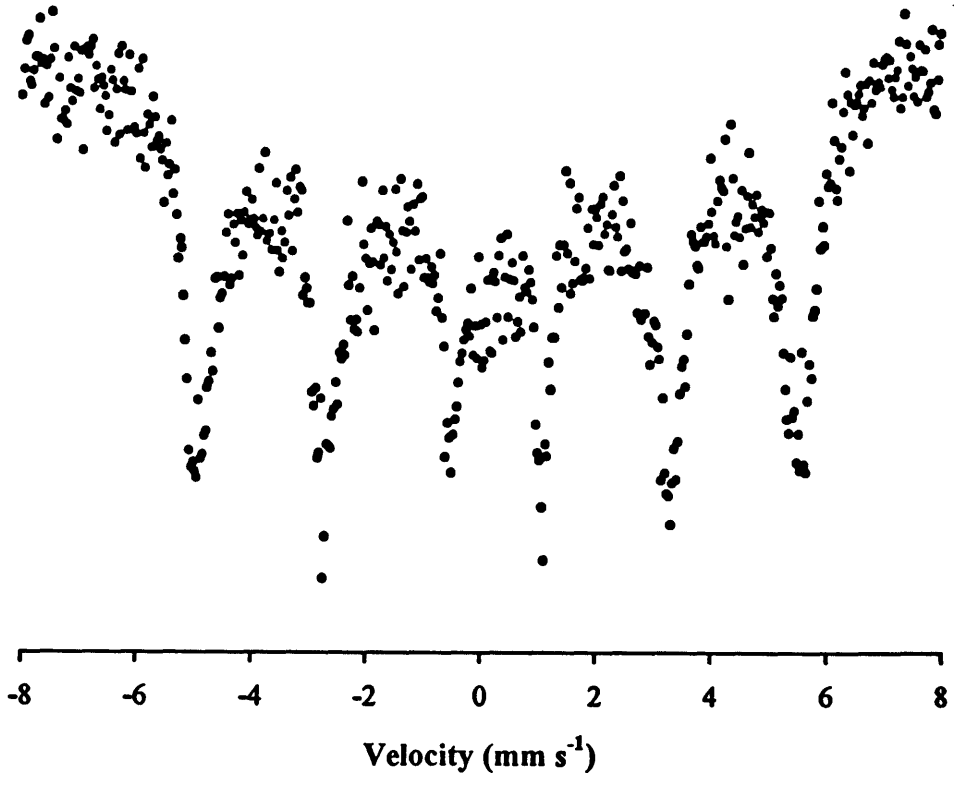


Figure 2.36 Mössbauer spectrum of NiZnD1 (fired at 800°C) taken at liquid nitrogen temperature.

2.2.5 *Resistivity Measurements*

The resistivity measurements were carried out on pressed sintered discs of the ferrites by a standard technique explained in **Appendix E**. Only the ferrites prepared by the coprecipitation and sol-gel techniques were tested. The pressed discs were prepared by applying a pressure of four tonnes per cm^2 to powdered samples in a die and then sintering the discs at 1100°C for 1.5 hours.

Eddy current losses in a ferrite become an important factor as the ferrite is subjected to higher frequencies. Sano *et al.*[76] showed that eddy current loss was proportional to d^2/ρ at high frequencies, where d is the grain size and ρ is the resistivity of the ferrite. Therefore, increasing the resistivity of the ferrite materials decreases the losses caused by eddy currents. Conductivity in ferrites can be viewed simply as electron hopping between Fe^{2+} and Fe^{3+} ions.[77] A decrease in the number of these ions would increase the ferrite's resistivity. Ni-Zn ferrites are more resistive than Mn-Zn ferrites and their resistivity values are usually of the order of $10^3\Omega$ m. For practical purposes these values are still too low, so additives are usually mixed with the Ni-Zn ferrite to increase its resistivity to *circa* $10^5\Omega$ m.

Increasing the specific resistivity of the grain boundary with additives such as SiO_2 and CaO can increase the bulk resistance of a ferrite. These additives form highly resistive glassy phases (calcium silicate) at the grain boundaries when the ferrite and additives are sintered. Another common additive is lead borosilicate glass. This glass has a low glass transition temperature and can therefore densify the bulk ferrite at relatively low processing temperatures, thereby increasing its resistivity significantly.

(a) Ni-Zn Ferrites Prepared by Coprecipitation Method

Table 2.12 shows the measured resistivity values of the coprecipitated Ni-Zn ferrites. The resistivities of these ferrites vary dramatically.

The ferrite with the lowest resistivity (NiZnCP2) has an excess of iron and so contains Fe^{2+} and Fe^{3+} ions. The ferrous ions were detected by standard potassium permanganate redox titration techniques and measurements are reported in **Section 2.2.6(b)**. These ions increase the conductivity of the system and lower the resistivity of the ferrite. The other three ferrites contain a deficiency of iron and therefore no

ferrous ions. The lack of both Fe^{2+} and Fe^{3+} ions in the ferrites increases their resistivity values.

Table 2.12 Resistivity measurements for coprecipitated Ni-Zn ferrites.

Ferrite	Chemical composition	Resistivity (Ω m)
NiZnCP1	$Ni_{0.27}Zn_{0.73}Fe_{1.70}O_{4-y}$	8.16×10^{7}
NiZnCP2	$Ni_{0.36}Zn_{0.64}Fe_{2.62}O_{4+y}$	7.66×10^{3}
NiZnCP3	$Ni_{0.51}Zn_{0.49}Fe_{1.65}O_{4-y}$	3.25×10^{5}
NiZnCP4	$Ni_{0.71}Zn_{0.29}Fe_{1.76}O_{4-y}$	5.24×10^{6}

To illustrate the impact of iron content in ferrites, **Figure 2.37** shows the resistivity of Ni-Zn ferrites dropping dramatically from 10^9 to 10^3 ohm-cm (10^7-$10^1\Omega$ m) at 50 mole percent iron oxide composition as the iron content is increased.[78]

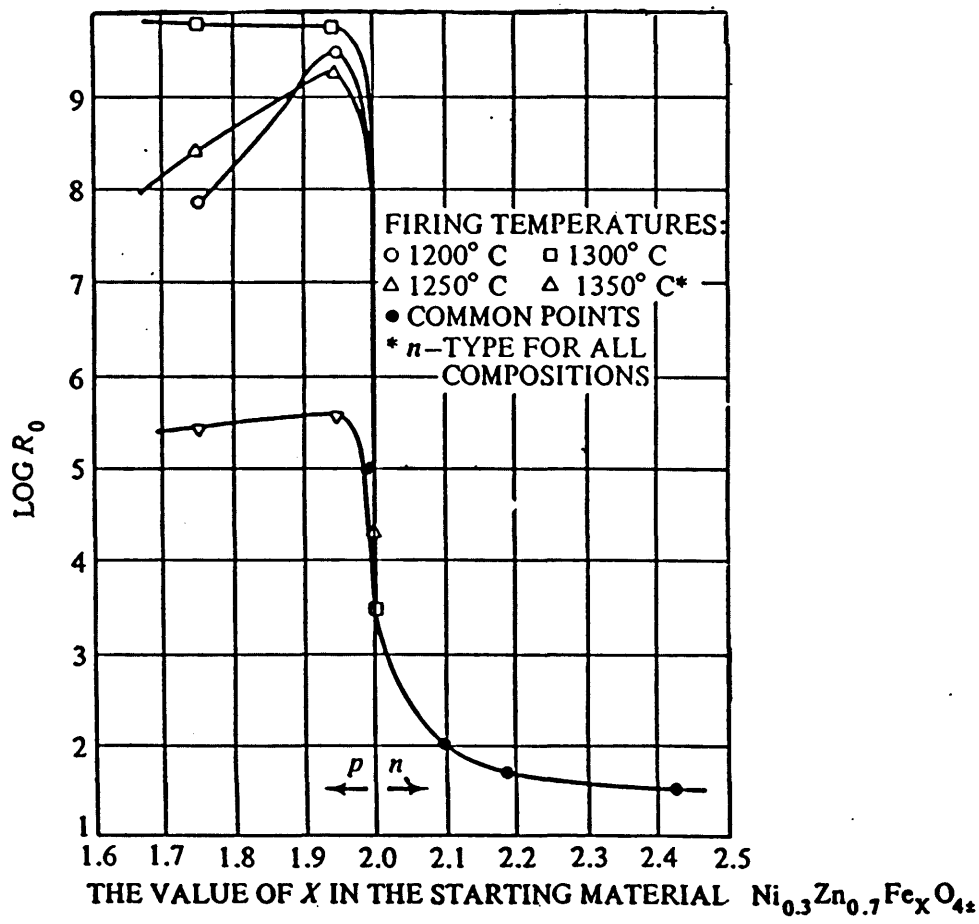


Figure 2.37 Variation of the resistivity of Ni-Zn ferrites as a function of Fe_2O_3 content in the starting material.[78]

The ferrites discussed in **Figure 2.37** have been prepared by the ceramic method and fired at different temperatures. The trend is the same for the differently heated ferrites, at high iron content, the resistivity values are low and at low iron content, the resistivity values are high. The ferrites prepared by the coprecipitation method in this work follow a similar trend.

(b) Ni-Zn Ferrites Prepared by Sol-Gel Method

The resistivity values of the sol-gel ferrites are shown in **Table 2.13**. Estimations of the ferrous content in each ferrite (done by standard redox techniques) are also given in **Table 2.13**. The variation of the resistivity values here is not as dramatic as found for the coprecipitated ferrites.

Table 2.13 Resistivity measurements of sol-gel Ni-Zn ferrites.

Ferrite	Chemical composition	Resistivity (Ω m)	% of Ferrous ions
NiZnSG1	$Ni_{0.29}Zn_{0.71}Fe_{1.94}O_{4-y}$	5.9×10^3	< 1.0
NiZnSG2	$Ni_{0.35}Zn_{0.65}Fe_{2.18}O_{4+y}$	2.3×10^3	3.2
NiZnSG3	$Ni_{0.50}Zn_{0.50}Fe_{2.33}O_{4+y}$	3.6×10^2	4.1
NiZnSG4	$Ni_{0.75}Zn_{0.25}Fe_{2.45}O_{4+y}$	No Reading	5.8

The ferrite with highest resistivity has the lowest iron content (NiZnSG1), i.e. the lowest metal ion concentration for electrical conductivity. This ferrite also contained no appreciable concentration of ferrous ions. The ferrite with the highest iron content (NiZnSG4) had such a low resistivity that it was not possible to measure it by this technique (the ferrite disc was so conducting that it drained the battery supply and became very hot). This ferrite had the highest ferrous ions content which gave the ferrite a mechanism (electron hopping between Fe^{2+}/Fe^{3+} ions) for conductivity.

The resistivity values of the sol-gel ferrites are very much lower than their corresponding coprecipitated ferrites. The generally higher iron content (and hence ferrous ions content) in the sol-gel ferrites may explain this result. **Figure 2.38** shows the change in resistivity values for the Ni-Zn ferrites prepared by the coprecipitation and sol-gel methods as a function of Fe content in the ferrites. Both traces in **Figure 2.38** resemble the trend shown in **Figure 2.37** in that the resistivity values are at their highest when the Fe contents are at their lowest and vice-versa.

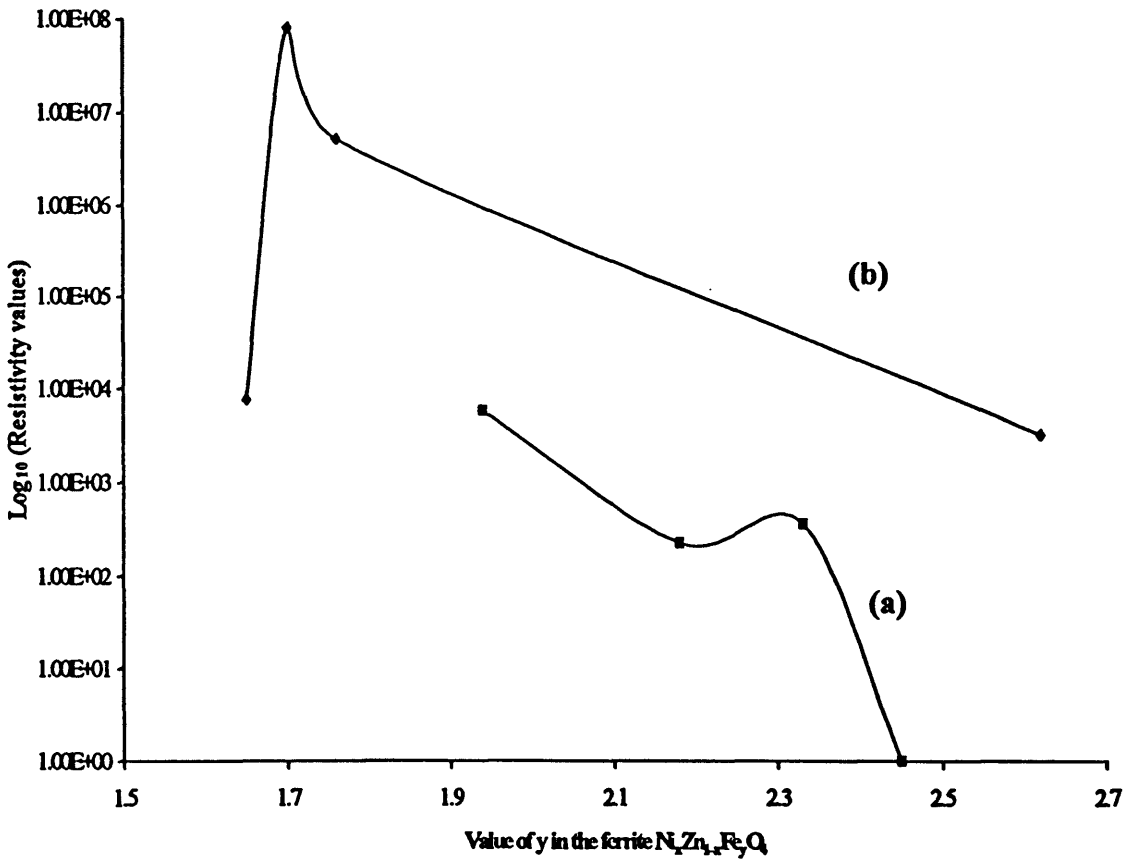


Figure 2.38 Change in resistivity values for (a) sol-gel ferrites and (b) coprecipitated ferrites respect to iron content in the ferrites.

From the point of view of high resistivities, the coprecipitated ferrites clearly have superior electrical properties than their corresponding sol-gel materials.

Attempts to increase the resistivity values of the sol-gel ferrites were made by adding CaO and SiO_2 powders in approximately 1% w/w to the ferrite powder before pressing and sintering the ferrite disc.[79] The ferrite powder and additives were mixed with *iso*-propyl alcohol in a mortar with a pestle for twenty minutes and then pressed and sintered. It was hoped that the resistivity value of the ferrite (NiZnSG2) would increase due to the formation of the highly resistive calcium silicate glass at the grain boundary of each particle. However, no significant increase was observed (value = 2.5 x 10^3 Ω m). A SEM image of the ferrite (NiZnSG2) containing CaO and SiO_2 additives is shown in **Figure 2.39**. The glassy phase (dark shiny parts in the image) has not formed homogeneously throughout the ferrite. Since not all the particles were coated, the ferrite remained as conducting as before.

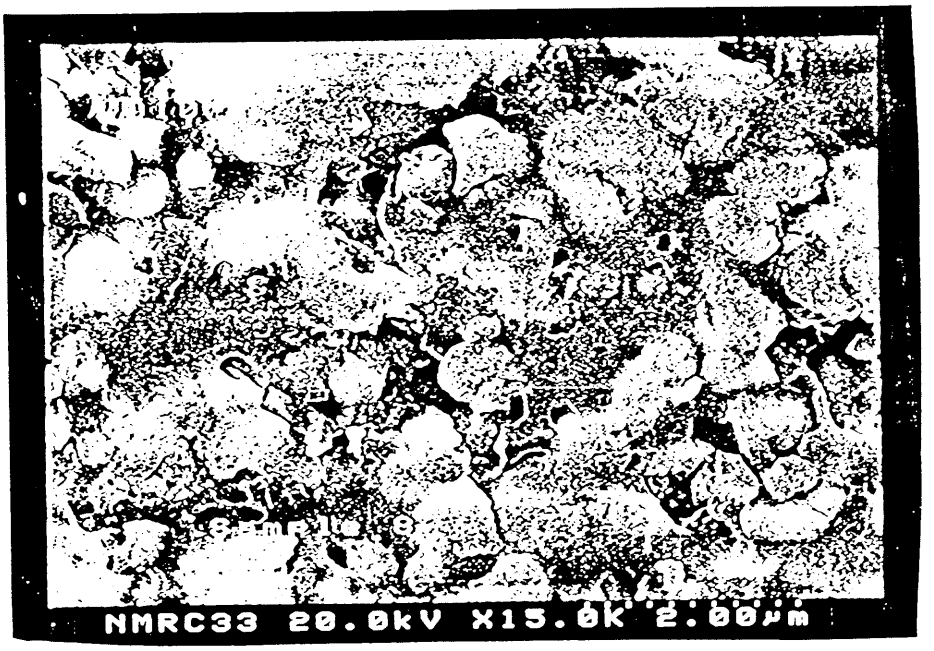


Figure 2.39 A SEM image of sol-gel Ni-Zn ferrite (NiZnSG2) with CaO and SiO_2 additives.

Instead of SiO_2, other tetravalent metal oxides can be used in more than trace amounts to increase the resistivity of ferrites. One such compound is TiO_2.[80] The main function

of the titanium oxide is to interact with Fe^{2+} ions in the ferrite lattice so that one valence electron from the ferrous ion can resonate between the Fe^{2+} and the Ti^{4+} ions. The net result is then the equivalent of a Fe^{3+} ion and a Ti^{3+} ion, equation [8].

$$Fe^{2+} + Ti^{4+} \longrightarrow Fe^{3+} + Ti^{3+} \qquad [8]$$

The localising of the valence electron from the Fe^{2+} ion reduces the conductivity in the ferrite. TiO_2 was added to the sol-gel ferrites (NiZnSG2) and crushed in a mortar and pestle with *iso*-propyl alcohol as the medium. The powder was dried, pressed and sintered at 1100°C for 1.5 hrs. Once again no significant increase in resistivity was observed (value = 3.2×10^3 Ω m). The reason for this may have been that the diffusion process needed higher sintering temperatures (~1300°C) than were employed here.

(c) Summary

The resistivity values for the coprecipitated ferrites are very high and the ferrites are potentially useful as prepared. However, the sol-gel ferrite's resistivity values are too low to be of any practical use as their core losses would be very large due to eddy currents (**Chapter 3** describes the addition of lead borosilicate glass to the sol-gel ferrites and the consequential improvement of the ferrite's resistivity measurements).

2.3 SUMMARY AND CONCLUSIONS

This chapter reported the preparation of Ni-Zn ferrites with varying compositions by three methods, namely: (1) coprecipitation method; (2) sol-gel method and (3) a method referred to as the MNCD method (named after a similar technique devised by Mathoniere, Nutall, Carling and Day,[82] see **Section 2.4.3.3**). The coprecipitation technique was a variation of Wickham *et al.*'s method.[39] It used ferrous sulphate, nickel acetate and zinc acetate as reagents. The sol-gel process used ferric

acetylacetonate, nickel acetate, zinc acetylacetonate and zinc acetate as reagents and had some novel features and was capable of producing ferrites at very low processing temperatures (60°C). The MNCD procedure was based on a coprecipitation technique for forming ferrites and potassium ferric oxalate, nickel sulphate and zinc sulphate were used as reagents.

Atomic absorption spectroscopy was used to analyse the concentration of the metal ions in each ferrite, and hence, determine the formula of each ferrite. The coprecipitated Ni-Zn ferrites generally gave chemical formulae with the correct Ni/Zn content but with a reduced concentration of iron content in the ferrite (i.e. less than 50% molar of Fe_2O_3, see **Section 2.4.3.1**). On the other hand, the sol-gel Ni-Zn ferrites exhibited chemical formulae with the correct Ni/Zn content but with an excess of iron (i.e. greater than 50% molar of Fe_2O_3, see **Section 2.4.3.2**). This suggested that Fe^{2+} ions existed in these ferrites. The MNCD materials had a very high nickel content shown later to be due to NiO.

The ferrites were analysed by powder X-ray diffractometry (PXRD). The PXRD data provided information on the ferrite's structure, the unit cell (**a**-value), and the average particle size. The coprecipitated and sol-gel ferrites showed only the inverse spinel structure in their PXRD profiles. The MNCD materials, however, showed the presence of two compounds, i.e. the inverse spinel ferrite and a NiO, which overlapped some of the spinel peaks in the PXRD patterns (at $2\theta = 36.4°$, 42.5° and 62.0°). The coprecipitated and sol-gel Ni-Zn ferrites had **a**-values for their unit cells that were typical of Ni-Zn ferrites.[72] Slightly larger **a**-values were calculated for the MNCD ferrite components.

The porosities of the Ni-Zn ferrites were estimated from the theoretical and measured densities. The lowest porosity compound for the coprecipitation (CP) and sol-gel methods is given below in **Table 2.14**.

Table 2.14 The lowest porosity values found for the Ni-Zn ferrites prepared by the coprecipitation and sol-gel techniques.

Ferrite	Preparative method	Porosity (P) in percent
NiZnCP3	Coprecipitation	10.73
NiZnSG1	Sol-gel	20.75

The coprecipitated Ni-Zn ferrites had much lower porosity than the sol-gel ferrites. SEM images of the ferrites confirmed that the sol-gel ferrites exhibited intragranular porosity. This is almost impossible to remove even by sintering at very high temperatures. The formation of intragranular pores possibly occurred during removal of the solvent in the sol-gel process. The coprecipitated ferrites had no intragranular porosity and were of regular size and shape. The coprecipitation method thus produced ferrite particles with superior microstructural properties as compared with the sol-gel method.

From the VSM results the conclusion was drawn that the coprecipitated Ni-Zn ferrites have better magnetic properties than either the sol-gel ferrites or MNCD materials. **Table 2.15** lists the highest M_s and B_s values for each preparative method. NiZnCP4 clearly has the highest magnetisation value.

Table 2.15 Highest M_s and corresponding B_s values of Ni-Zn ferrites prepared by the three different techniques.

Ferrite	Preparative method	M_s / $JT^{-1}kg^{-1}$	B_s / mT
NiZnCP4	Coprecipitation	74.0	469.3
NiZnD2	MNCD	59.11	379.1
NiZnSG4	Sol-gel	52.5	350.8

In general, the coprecipitated Ni-Zn ferrites are superior magnetically.

The Mössbauer spectroscopy results on the Ni-Zn ferrites prepared by the three methods support the Yafet-Kittel model.[63] The Gilleo model[64] which suggests the formation of superparamagnetic clusters in Ni-Zn ferrites as the amount of zinc is increased is not supported by the Mössbauer results. There is no evidence that the particles decrease in size as the zinc content increases in the ferrites.

All three preparative methods produced samples which showed the three magnetic regions for the Ni-Zn ferrites. At low zinc content, < 0.5 molar, a doublet of sextets was observed in a magnetically ordered region. At 0.5 < zinc < 0.7 molar, a collapsed doublet of sextets was observed in a relaxed magnetic region. And at high zinc content, > 0.7 molar, an inner doublet was found corresponding to a paramagnetic region. When Mössbauer spectra of ferrites from all three methods were measured at liquid nitrogen temperatures, the spectra indicated magnetically ordered materials. Superparamagnetic effects were apparent in the sol-gel ferrites as these materials were seen to possess clusters of fine particles (see SEM result, **Figure 2.15**). These effects were neutralised on cooling the ferrites to liquid nitrogen temperature.

The resistivity measurements of the coprecipitated and sol-gel Ni-Zn ferrites were consistent with the operation of a conducting mechanism involving electron hopping between Fe^{2+} and Fe^{3+} ions in the ferrite lattice.[77] The ferrous ions' contents in the ferrites were detected and measured by standard redox techniques involving potassium permanganate. If the concentration of Fe^{2+} ions in the ferrite was decreased then the conductivity decreased. The sol-gel ferrites had an excess of iron in their composition and substantial concentration of Fe^{2+} ions were found in these ferrites. This led to a high conductivity and low resistivity values were recorded for these materials. The coprecipitated ferrites were of the opposite type, they contained a deficiency of iron. With no ferrous ions in these ferrites, they were resistive and gave very high resistivity values (~10^4 times higher than the sol-gel ferrites). Commercial ferrites usually contain additives such as glass frit to increase their resistivities but the coprecipitated ferrite's resistivity values were high without any glass addition.

Powdered CaO and SiO_2 additives were mixed with the sol-gel ferrites in order to increase their resistivities. However, SEM images of the pressed sintered ferrites with these additives showed that, although the glass phase had formed, it was not distributed homogeneously amongst the particles but rather appeared in 'clumps'.

Hence, there was no increase in resistivity. TiO_2 powder was also added to the sol-gel ferrites to increase their bulk resistivity but this was not successful.

Overall, the coprecipitation method prepared Ni-Zn ferrites with the required structure, regular particle size and shape, and with good electrical and magnetic properties. The method was repeatable and gave ferrites with Ni and Zn compositions close to theoretical. The sol-gel technique produced Ni-Zn ferrites with the correct structure but the ferrite particles were irregular in size and shape and the material possessed intragranular pores. As a result, the electrical and magnetic properties of these ferrites were less satisfactory. The process was, however, repeatable and it formed ferrite particles at processing temperatures as low as 60°C. Therefore, the sol-gel method has potential and more research should be carried out to optimise the conditions of the technique such as changing the catalyst and solvents, investigating the conversion of the sol into gel and careful firing of the xerogel. The MNCD method provided an interesting means of producing ferrites with unusual compositions. However, the materials contained two compounds, namely: the ferrite and NiO. The reproducibility of the method was poor.

2.4 EXPERIMENTAL DETAILS

2.4.1 Instrumentation

Elemental analyses were performed at the Microanalytical Laboratory, University College, Cork. Infrared spectra were recorded as KBr discs in the range 4000 – 440 cm^{-1} on a Perkin Elmer FTIR Paragon 1000 spectrometer. Relative intensities are designated as vs, very strong; s, strong; m, medium; w, weak; vw, very weak; sh, shoulder; br, broad. Mössbauer spectra were measured at room and liquid nitrogen (77K) temperatures using a commercial constant acceleration drive unit and transducer (Harwell Instruments) in conjunction with a Canberra System 40 multichannel analyser. The source was ^{57}Co in Rh and was of 20mC nominal strength. All data was referred to the spectrum of iron foil as standard. Masses of samples varied between 100 and 150 mg. Data collection times varied from 24 – 48 hours. Powder X-ray diffraction (PXRD) patterns were collected on a Phillips PW3710 MPD apparatus using $CuK_{\alpha 1}$ (1.5418Å) radiation with an anode current of 30 mA and accelerating voltage of 40 kV. Data was collected between 10° and 70° 2θ using the standard θ/2θ geometry. In all diffractograms, a step size of 0.03 degrees (2θ) with a data collection time of 1.5 seconds per step was used. Vibrating sample magnetometer (VSM) measurements were obtained at room temperature on a Magnetic Solutions magnetometer. The magnetic field was generated using permanent magnets and the maximum applied field is +/-1.1 T. Resistivity measurements were made on pressed sintered ferrite discs using criteria taken from the ASTMD 257-78 standard with a four-point probe technique. All discs were formed with a pressure of 4 tonnes on a 1cm-diameter die. Standard volumetric redox techniques using potassium permanganate were used to estimate the concentration of ferrous ions in the ferrites. A Hitachi S4000 instrument at the National Microelectronics Research Centre (NMRC), Cork was used for all scanning electron microscopy (SEM) images. A Carbolite RWF 1215 oven was used to process the materials between 650 and 1100°C.

2.4.2 *Starting Materials*

The following reagents were used as supplied from Aldrich: potassium permanganate, ferrous sulphate hexahydrate, nickel sulphate heptahydrate, zinc sulphate heptahydrate, tetrabutylammonium bromide, nickel acetate tetrahydrate, zinc acetate dihydrate, manganese(II) acetate anhydrous, manganese acetate tetrahydrate, zinc acetylacetonate hydrate, ferric acetylacetonate and 65% nitric acid. $K_3[Fe(C_2O_4)_3].3H_2O$ was prepared according to a literature synthesis.[81] Triply distilled water, 99% *iso*-propylalcohol (Aldrich) and 99% methanol (Aldrich) were used as received.

2.4.3 *Preparation of Ni-Zn Ferrites*

2.4.3.1 *Coprecipitation Method*

Ni-Zn ferrites of composition $Ni_xZn_{1-x}Fe_2O_4$ with x = 0.25, 0.50, 0.75 were synthesised by this method. A Ni-Zn ferrite of composition $Ni_{0.33}Zn_{0.67}Fe_{2.42}O_{4+y}$ was also prepared and is given as a typical sample preparation below.

Ferrous sulphate (4.082g, 14.68mmol), nickel acetate (0.498g, 2.00mmol) and zinc acetate (0.892g, 4.06mmol) were dissolved in distilled water (75mls). Oxalic acid (2.623g, 20.74mmol) was dissolved in distilled water (75mls). Both solutions were heated with continuous stirring to 50°C. The solution of mixed salts was slowly added to the oxalic acid solution with constant stirring to yield immediately a yellow/green precipitate. The solution was aged for five minutes at 95°C and cooled to room temperature. The mixed metal oxalate precipitate was collected on a sintered glass crucible by vacuum filtration. The powder was dried at 60°C for two hours. The oxalate powder was then fired to form the corresponding Ni-Zn ferrite powder at temperatures of 400°C, 800°C and 1100°C.

Similar procedures were carried out for the ferrites with composition x = 0.25, x = 0.50 and x = 0.75. The quantities of reagents used are given in the table below.

	← x = 0.25 →		← x = 0.50 →		← x = 0.75 →	
Starting reagent	**Qty of reagent (g)**	**Qty of reagent (mmol)**	**Qty of reagent (g)**	**Qty of reagent (mmol)**	**Qty of reagent (g)**	**Qty of reagent (mmol)**
$FeSO_4 7H_2O$	2.224	8.00	2.223	8.00	2.223	8.00
$Ni(OAc)_2 4H_2O$	0.249	1.00	0.498	2.00	0.747	3.00
$Zn(OAc)_2 2H_2O$	0.659	3.00	0.439	2.00	0.219	1.00
$(COOH)_2 2H_2O$	1.513	12.00	1.512	12.00	1.514	12.00

The chemical analyses of the ferrites fired at 800°C are given below along with their theoretical values.

Value of x	**Ferrite**	**Theoretical composition**	**Actual composition**
0.25	NiZnCP1	$Ni_{0.25}Zn_{0.75}Fe_2O_4$	$Ni_{0.27}Zn_{0.73}Fe_{1.70}O_{4-y}$
0.33	NiZnCP2	$Ni_{0.33}Zn_{0.67}Fe_2O_4$	$Ni_{0.36}Zn_{0.64}Fe_{2.63}O_{4+y}$
0.50	NiZnCP3	$Ni_{0.50}Zn_{0.50}Fe_2O_4$	$Ni_{0.51}Zn_{0.49}Fe_{1.67}O_{4-y}$
0.75	NiZnCP4	$Ni_{0.75}Zn_{0.25}Fe_2O_4$	$Ni_{0.71}Zn_{0.29}Fe_{1.76}O_{4-y}$

2.4.3.2 *Sol-Gel Method*

Ni-Zn ferrites of composition $Ni_xZn_{1-x}Fe_2O_4$ with x = 0.25, 0.33, 0.50 and 0.75 were prepared using the method described below for x = 0.25.

Ferric acetylacetonate (2.826g, 8.00mmol), zinc acetylacetonate (0.795g, 3.00mmol) and nickel acetate (0.253g, 1.00mmol) were mixed together in *iso*-propyl alcohol (80 mls). This suspension was heated slowly with continuous stirring until the materials had dissolved to give a dark-red solution. Water (25mls) was added along with 65% HNO_3 acid (1.5mls) as catalyst and this solution was heated with constant stirring until its volume was reduced to ~ 30mls. The beaker was placed in a 60°C oven overnight. A brown-black magnetic powder was received the next day. Chemical analyses of this powder suggested trace amounts of carbon and hydrogen remained (at less than one percent). The powder was processed in air with firing temperatures of 800°C and 1100°C.

This procedure was carried out exactly for x = 0.33, 0.50 and 0.75 with the exception of using $Zn(OAc)_2.2H_2O$ instead of $Zn(acac)_2.H_2O$ for x = 0.75.

	← x = 0.33 →		← x = 0.50 →		← x = 0.75 →	
Starting reagent	**Qty of reagent (g)**	**Qty of reagent (mmol)**	**Qty of reagent (g)**	**Qty of Reagent (mmol)**	**Qty of reagent (g)**	**Qty of reagent (mmol)**
$Fe(acac)_3$	2.826	8.00	2.825	8.00	2.826	8.00
$Ni(OAc)_24H_2O$	0.328	1.32	0.498	2.00	0.747	3.00
$Zn(acac)_2H_2O$	0.696	2.64	0.528	2.00	None	None
$Zn(OAc)_22H_2O$	None	None	None	None	0.219	1.00

The chemical analyses (Fe, Ni and Zn) of the ferrites fired it 800°C are given below along with their theoretical values.

Value of x	Ferrite	Theoretical composition	Actual composition
0.25	NiZnSG1	$Ni_{0.25}Zn_{0.75}Fe_2O_4$	$Ni_{0.29}Zn_{0.71}Fe_{1.94}O_{4-y}$
0.33	NiZnSG2	$Ni_{0.33}Zn_{0.67}Fe_2O_4$	$Ni_{0.36}Zn_{0.64}Fe_{2.18}O_{4+y}$
0.50	NiZnSG3	$Ni_{0.50}Zn_{0.50}Fe_2O_4$	$Ni_{0.50}Zn_{0.50}Fe_{2.33}O_{4+y}$
0.75	NiZnSG4	$Ni_{0.75}Zn_{0.25}Fe_2O_4$	$Ni_{0.75}Zn_{0.25}Fe_{2.45}O_{4+y}$

2.4.3.3 MNCD Method

This procedure is based on the preparation used by Mathoniere, Nutall, Carling and Day[82] to form mixed valency metal oxalates of the form $R_4N[M^{2+}Fe^{3+}(C_2O_4)_3]$ where R = Pr^i, Bu^n and Bu^t and M = Fe and Mn. In this case, however, a trimetal oxalate of the composition $[(Bu^n)_4N][Ni_{0.5}Zn_{0.5}Fe(C_2O_4)_3]$ was prepared and used.

Potassium ferric oxalate (0.982g, 2.00mmol) in water (8mls) was added to an aqueous solution (10mls) of nickel sulphate (0.263g, 1.00mmol) and zinc sulphate (0.288g, 1.00mmol) with stirring at room temperature. After one hour, the solution was filtered to remove the small amount of $Fe(C_2O_4).2H_2O$ (confirmed by infrared and chemical analyses) which formed. A methanol solution (8mls) of $(Bu^n)_4NBr$ (0.645g, 2mmol) was added to the filtrate whereupon a green precipitate began to form. The solution was left to stand for two days at room temperature before filtering the green-yellow product. Found: Fe, 8.56; Ni, 5.06; Zn, 4.62; C, 43.77; H, 6.21; N, 2.53%. $C_{22}H_{36}FeNNi_{0.5}Zn_{0.5}O_{12}$ requires: Fe, 8.14; Ni, 4.70; Zn, 5.24; C, 42.32; H, 5.81; N, 2.24%. FTIR (KBr) ν_{max} / cm^{-1}: 2971(s), 2880(m), 1630(vs), 1452(vs), 1429(vs),

1386(m), 1349(s), 1304(s), 1158(w), 1066(w), 1038(w), 905(m), 813(s), 536(s), 485(vs). Blue-green crystals were also obtained in low yield as a side-product to the reaction. X-ray crystallography data suggested the compound $K_2[Ni_{0.93}Fe_{0.07}(OH_2)_6](SO_4)_2$.[83] The compound is isomorphous with the pure nickel complex, $K_2[Ni(OH_2)_6](SO_4)_2$, with 7(2)% of the Ni atoms replaced by iron atoms.
The green-yellow precipitate was fired to 800°C for 1.5 hours to give a brown magnetic material of composition shown below.

Ferrite	Theoretical composition	Actual composition
NiZnD0	$Ni^{2+}Zn^{2+}Fe_2^{3+}O_4$	$Ni_{0.06}Zn_{0.94}Fe_{1.78}O_{4-y}$ + zNiO

A series of Ni-Zn ferrites of composition $Ni_xZn_{1-x}Fe_2O_4$ with x = 0.25, 0.50, 0.75 and 1.0 were synthesised using the procedure above.

$$xNiSO_4 + (1-x)ZnSO_4 + 2K_3Fe(C_2O_4)_3 \xrightarrow{4(Bu^n)_4NBr} [(Bu^n)_4N]_4[Ni_xZn_{1-x}Fe_2(C_2O_4)_6]$$

The amounts of reagents used in the reactions are given below:

	← x = 0.25 →		← x = 0.50 →	
Starting reagent	**Qty of reagent (g)**	**Qty of reagent (mmol)**	**Qty of reagent (g)**	**Qty of reagent (mmol)**
$K_3Fe(C_2O_4)_3.3H_2O$	1.964	4.00	1.963	4.00
$NiSO_4.7H_2O$	0.132	0.50	0.263	1.00
$ZnSO_4.7H_2O$	0.433	1.50	0.288	1.00
$(Bu^n)_4NBr$	2.583	8.00	2.582	8.00

	← x = 0.75 →		← x = 1.0 →	
Starting reagent	**Qty of reagent (g)**	**Qty of reagent (mmol)**	**Qty of reagent (g)**	**Qty of reagent (mmol)**
$K_3Fe(C_2O_4)_3.3H_2O$	1.964	4.00	1.963	4.00
$NiSO_4.7H_2O$	0.395	1.50	0.527	2.00
$ZnSO_4.7H_2O$	0.144	0.50	None	None
$^nBu_4NBr$	2.586	8.00	2.585	8.00

The precipitates that were afforded from the above reactions were fired to 800°C for 1.5 hours to yield magnetic dark brown powders. The chemical compositions of these ferrites are given below:

Value of x	Ferrite	Theoretical composition	Actual composition
0.25	NiZnD1	$Ni_{0.25}Zn_{0.75}Fe_2O_4$	$Ni_{0.33}Zn_{0.67}Fe_{1.34}O_{4-y}$ + zNiO
0.50	NiZnD2	$Ni_{0.5}Zn_{0.5}Fe_2O_4$	$Ni_{0.41}Zn_{0.59}Fe_{1.71}O_{4-y}$ + zNiO
0.75	NiZnD3	$Ni_{0.75}Zn_{0.25}Fe_2O_4$	$Ni_{0.76}Zn_{0.24}Fe_{1.73}O_{4-y}$ + zNiO
1.00	NiZnD4	$NiFe_2O_4$	$NiFe_{1.91}O_{4-y}$ + zNiO

CHAPTER 3

SYNTHESIS AND PROPERTIES OF Ni-Zn FERRITE MATERIALS WITH LEAD BOROSILICATE GLASS ADDITIVES

3.1 INTRODUCTION

The coprecipitated Ni-Zn ferrites prepared in **Chapter 2** exhibited high resistivity values but the sol-gel Ni-Zn ferrites had poor resistivity values. Poor resistivity values lead to high core losses *via* eddy currents. Therefore, augmentation of the ferrites's resistivity values was attempted by additions of CaO, SiO_2 and TiO_2. However, due to a combination of poor homogeneous mixing and low sintering temperatures, these additives had little effect on the resistivity values. The resistivities of ferrites are commonly improved in industry by adding glass frit (~1%) into the ferrite powder. The mixture is ball-milled, compacted and sintered to give a highly resistive bulk ferrite of the order of $10^5\Omega$ m. Lead borosilicate glass is invariably used as the glass frit because it melts at reasonably low temperatures (500-900°C) and therefore can achieve densification of the bulk ferrite at low sintering temperatures. This chapter thus concentrates on:

(1) Preparation of a suitable lead borosilicate glass by chemical means.
(2) Mixing the lead borosilicate glass with Ni-Zn ferrite which was synthesised in **Chapter 2**.
(3) Characterising the products by chemical analyses (Fe, Ni, Zn and Pb), infrared spectroscopy, powder X-ray diffractometry (PXRD), scanning electron microscopy (SEM), vibrating sample magnetometer (VSM) measurements, Mössbauer spectroscopy and electrical resistivity analysis.

A brief account will first be given on glass and its special properties.

3.1.1 Definition of Glass

Glass can be defined in a number of ways including: an extremely viscous, metastable supercooled liquid; a melt that has solidified without being subject to crystallisation.[84] The diagram relating specific volume and temperature for glass and a crystalline material explains to some extent the process of glassing, **Figure 3.1**.

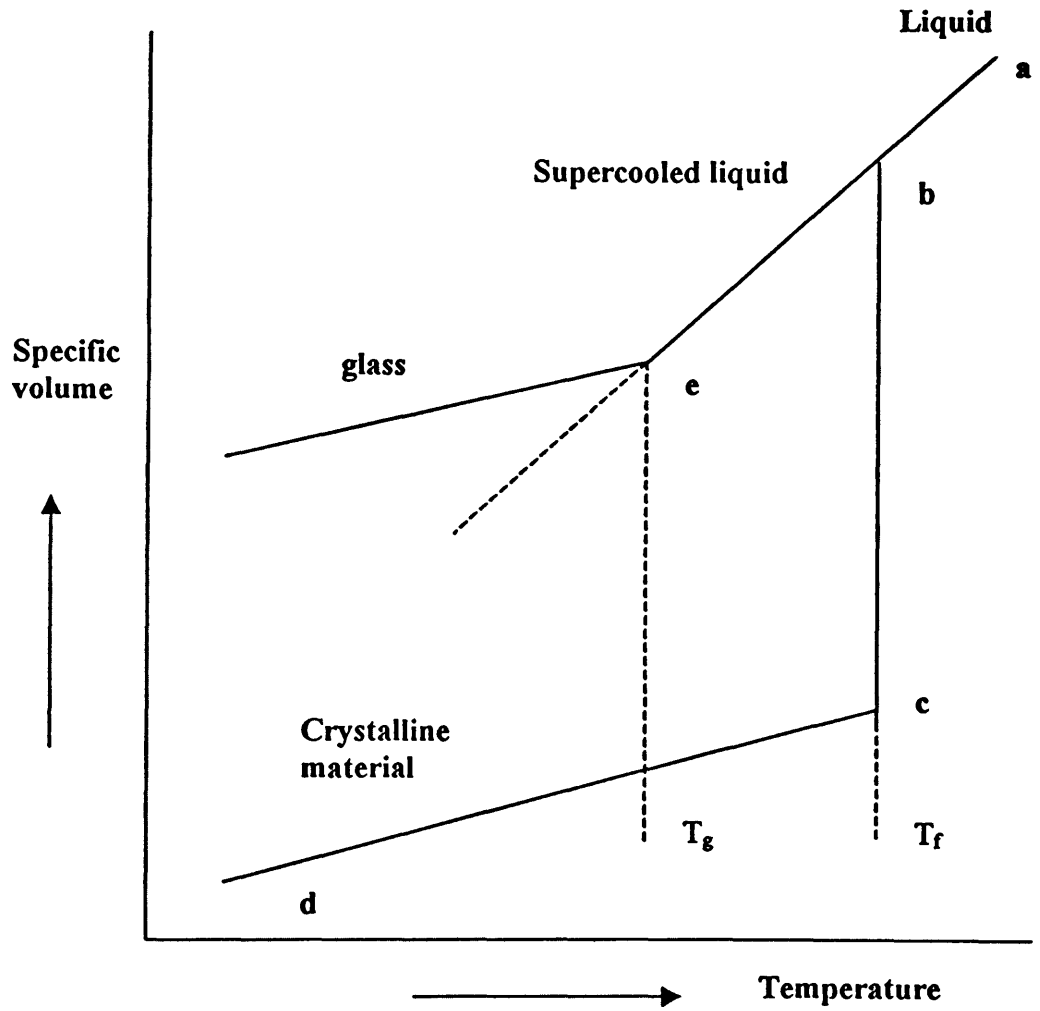


Figure 3.1 Specific volume versus temperature for glass and crystalline materials.

On cooling a liquid from an initial state represented by point **a**, the volume of a given mass decreases steadily along the line **ab**. At point **b**, the liquid can be transformed to a crystallised material with an abrupt decrease in volume to **c** at the temperature T_f. This temperature is the melting point of the crystalline product. This occurs if the rate of cooling is sufficiently slow and crystallising nuclei are present in the melt. On further cooling, the crystalline material contracts along **cd**. However, if the rate of cooling is sufficiently rapid, crystallisation may not take place at T_f and the volume of the supercooled liquid decreases along the line **be** which is a smooth continuation of **ab**. At a temperature T_g, the volume temperature curve of the supercooled liquid undergoes a marked change in direction and continues parallel to the contraction

curve of the crystalline material. The temperature T_g is called the glass transition temperature. Only below T_g is it correct to describe the material as a glass.

3.1.2 Structure of Glass

A structure for glass was first postulated by Zachariasen in the 1930s.[85] He described glass as a network and developed a set of empirical rules (Zachariasens' rules) that attempted to explain bonding in glass. According to these rules, elements that form oxides which are "glass formers" generally have element-to-oxygen bond strengths greater than 335 kJ mol^{-1}. In multicomponent oxide systems, elements with low element-to-oxygen bond strengths, ~ 200 kJ mol^{-1}, do not become part of the glass network and are called "modifiers". **Table 3.1** lists some common formers and modifiers in glass components.[86]

Zachariasen accepted that practically nothing was known about the atomic arrangement in glass but today the structure of glass has been elucidated with the aid of X-ray and spectroscopic techniques in combination with kinetic and thermodynamic considerations. Bonding distances, atom distances and co-ordination polyhedra in glass can now be estimated. The glass structure can be described as being a continuous random network possessing medium range order. This is essentially the same view that Zachariasen had for glass over sixty years ago.

Table 3.1 Data of some common glass formers and modifiers.

Type of Glass	M in MO_n	Valence	Coordination Number	Single bond Strength (kJ mol^{-1})
Glass formers	B	3	4	373
	Si	4	4	443
	Al	3	4	331 – 470
Glass modifiers	Pb	2	4	151
	Ba	2	8	108
	Ca	2	8	134

3.1.3 *Lead Borosilicate Glass: Preparation and Properties*

Lead borosilicate glass of varying composition is commonly formed by the ceramic method. The raw materials include sand, borax, boric acid, lead carbonate and lead oxide. These are first ball-milled, then heated to above 1000°C and quickly cooled to form the glass. The glass may be dry ball-milled to form glass frit. The ceramic technique presents several difficulties in controlling the stoichiometry and homogeneity of the glass, even though it has the advantages of using cheap starting materials and being applicable to large-scale production.

Other preparative techniques for lead borosilicate glass exist that can control the stoichiometry and homogeneity of the final product more finely. These include the sol-gel technique,[87,88] metal-organic decomposition,[89,90] vapour deposition and shock wave vitrification. These methods generally produce glass with low glass transition temperatures and with high densities.

The sol-gel method is of particular interest as this is one of the preparative methods employed for the production of Ni-Zn ferrites in **Chapter 2**, see **Section 1.7.2**, and it produces glass at much lower firing temperatures than those used for glass formed from mixtures of the powdered oxides. Three approaches are generally used in the preparation of multicomponent silicate glass by the sol-gel process. One is to form a gel by employing an alkoxide sol as a starting material for the precursor gel.[91,92] This route is widely used but can be difficult if the available alkoxides are only slightly soluble in common organic solvents. Another way is to use an alkoxide for the main oxide component such as SiO_2 and introduce the raw materials for modifier cations in the form of aqueous solutions.[93,94] The third way is to use colloidal sols.[95,96] The gel (whichever way it is formed) is dried, powdered and subjected to densification by heat treatment (500 – 700°C) to give the final glass. The sol-gel process is important in the fabrication of lead-containing gradient-index (GRIN) glass rod with variations in refractive index.[97] The sol-gel method is the one employed in the preparation of lead borosilicate glass in this chapter. The starting materials are of the alkoxide and metal-organic type and the process is base catalysed hydrolysis-polycondensation.

Lead borosilicate glasses have several unique properties that make them desirable as glass additives in the ferrites industry. These glasses possess low glass transition temperatures (especially those prepared by the sol-gel process) and hence promote densification of the bulk ferrite at low sintering temperatures. The thermal expansion

of lead borosilicate glass for the range 20 – 200°C is of the order 10^{-6} °C. This is the same order for the thermal expansion of the alumina (Al_2O_3) ceramic [$7x10^{-6}$ °C, (25-500 °C)]. Therefore, lead borosilicate glass has been used in the ferrite thin-film industry as a very good adhesive to an alumina substrate.

3.1.4 Glass Additives for Ferrites

As mentioned previously, the addition of glass frit to ferrite powder to produce high resistivity ferrite is a common practice in industry. When glass is added to a ferrite powder and the powder subjected to heat treatment above the melting temperature of the glass, a glassy phase is formed around each particle as schematically represented in **Figure 3.2**. This produces an insulating effect on the grain boundary of the particle and hence increases the overall resistivity of the ferrite. Questions remain as to whether these coatings affect the microstructure of the particles.

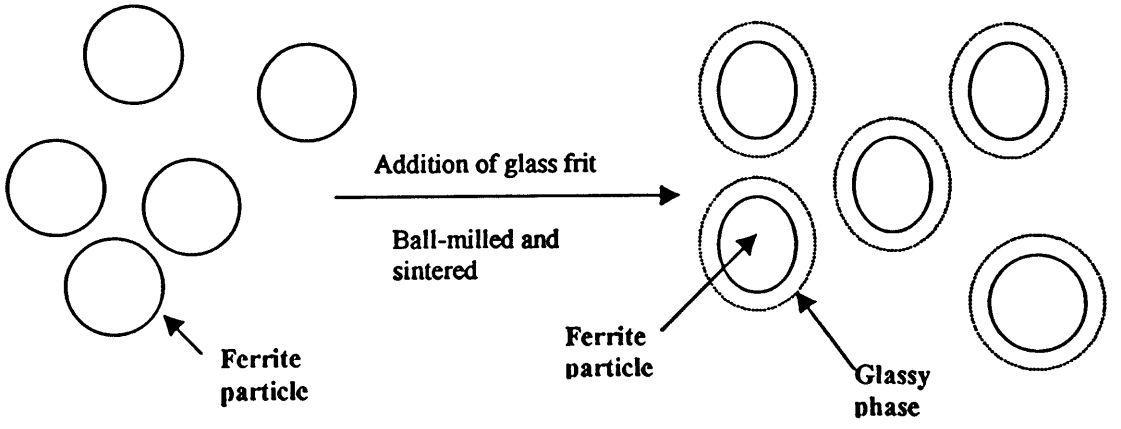


Figure 3.2 Schematic diagram of the coating of ferrite particles with glass.

Brooks *et al.* reported the successful sol-gel coating of lithium zinc ferrite powders with a borosilicate material.[51] Tetraethoxysilane (TEOS) and triethoxyborane (TEB) were used as reagents to form the gel. Transmission electron microscopy (TEM) and diffuse reflectance Fourier transform infrared spectroscopy (FTIR) were the primary analytical techniques used to characterise the gel coatings. TEM results suggested that the sol-gel coatings formed with thickness of the order of 5 to 15 nm while diffuse reflectance FTIR gave evidence of B-O, Si-O and Si-O-B bonds in the coatings.[51] However, Brooks did not investigate the effects of heating the samples,

which would conceivably produce a borosilicate glass coating around the ferrite particles.

Numerous studies have reported calcium silicate glassy phases on Mn-Zn ferrites.[98,99] When calcium silicate is melted onto the ferrite particles the calcium ions diffuse into the ferrite lattice with consequential lattice expansion. The silicate ions, however, remain in the glassy phase of the grain boundary. The movement of Ca ions into the ferrite structure alters its magnetic properties as some of the iron atoms are displaced. Several reports have suggested improved magnetic characteristics of Mn-Zn ferrites due to calcium silicate additives.[100-103]

The interface reactions between Mn-Zn ferrites and SiO_2-PbO binary glass melts have been reported.[104] It was shown by electron probe microanalysis and X-ray diffraction techniques that the deposition of $Pb_2(Mn,Fe)_2Si_2O_9$ and $Pb_8(Mn,Fe)Si_6O_{21}$ crystals occurred at the interface of the glass and ferrite in several steps.[104] The first step observed the dissolution of Zn^{2+} and Mn^{2+} ions from the ferrite's lattice into the glass melt. This occurred when the heat treatment of the samples was just above the glass melting point. In the next step, the iron ions in the octahedral sites of the weakened ferrite lattice dissolved into the glass melt. In the final step, an intermediate layer formed on further heating and was composed of solid solutions of $Pb_2(Mn,Fe)_2Si_2O_9$ and $Pb_8(Mn,Fe)Si_6O_{21}$.[104] This layer was formed in close vicinity to the interface of the Mn-Zn ferrite and the SiO_2-PbO glass. **Figure 3.3** shows the movement of ions in the three stages.

The dissolution of ferrite by the glass melt obviously has some bearing on the overall magnetism of the ferrite. Nitta *et al.* have recently observed changes in the saturation magnetic moment of Mn-Zn ferrites due to the addition of SiO_2-PbO glass.[105] The Mn-Zn ferrite powders were mixed with SiO_2-PbO glass frit (which had been prepared by the ceramic technique) and heat-treated at different temperatures ranging from 500 – 1000°C under Ar gas.[105] The saturation magnetic moment of these different heat-treated powders was measured using a vibrating sample magnetometer (VSM). The results showed that, as the temperature of the mixtures increased to values greater than 500°C (the melting temperature of the glass), the saturation magnetic moment of the mixture decreased. The decrease occurred due to the dissolution of the ferrite into the glass melt. The saturation magnetic moment reaches a minimum at 800°C and then increases slightly as the temperature is raised further.

The increase is due to the extra magnetic moments generated by the intermediate layer (i.e. $Pb_2(Mn,Fe)Si_2O_9$ and $Pb_8(Mn,Fe)Si_6O_{21}$).

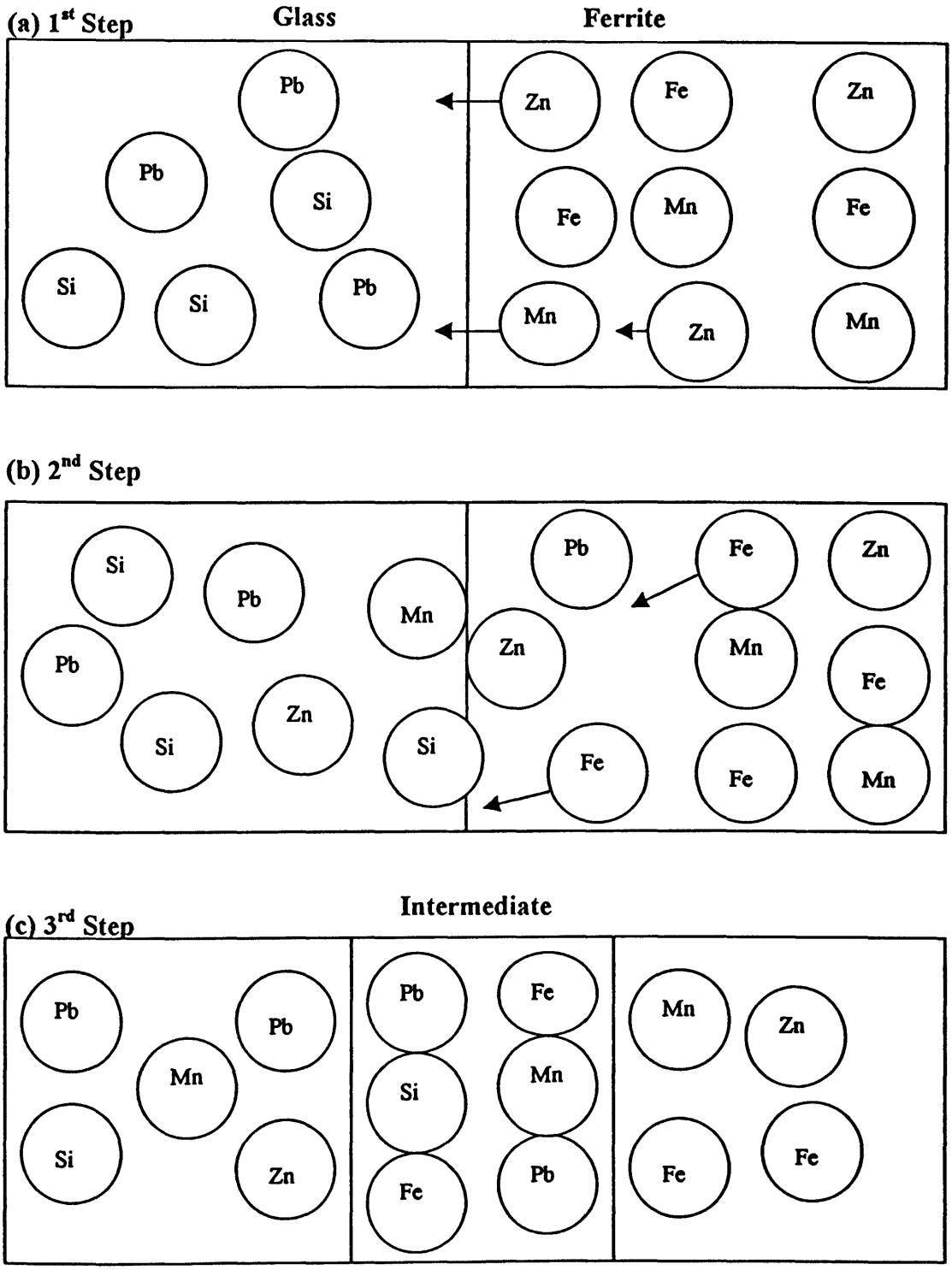


Figure 3.3 Mechanism of interface reaction between SiO_2-PbO glass and Mn-Zn ferrite. (a) 1st step: Mn and Zn ions in the ferrite dissolve into the melt. (b) 2nd step: Fe ions in the ferrite dissolves in the melt. (c) 3rd step: Intermediate layer forms.[104]

The interface reactions between Ni-Zn ferrite and SiO_2-PbO glass melts were also studied by Nitta *et al.*.[106] They reported no intermediate layer formation at the ferrite-glass interface and hence concluded that Ni ions from the Ni-Zn ferrite had not dissolved into the glass melt. However, results from saturation magnetic moment measurements of the Ni-Zn ferrite and glass mixture suggested that some dissolution of Ni ions into the melt had occurred.[106] The results showed a decrease in the saturation magnetic moment as the temperature of the mix is raised to 800°C. The dip in saturation magnetic moment was not as dramatic as that recorded for the Mn-Zn ferrite and therefore it can be concluded that the Ni ions dissolve very slowly into the glass melt.

Finally, Muller *et al.* have coated magnetite with a $PbO-B_2O_3-SiO_2$ glass (prepared by the ceramic method) at 590°C in air.[107] The magnetite and glass were attrition milled in *iso*-propanol. Data from scanning electron microscopy (SEM) and powder X-ray diffractometry (PXRD) prompted the conclusions that the glass coating was free of cracks and there was a thin intermediate layer (<20μm) of hematite between the glass and magnetite.[107]

3.1.5 Summary

The addition of glass to a ferrite is an important procedure as it dramatically improves the electrical properties of the ferrite. Lead borosilicate glass appears to be a good choice for adding to a ferrite because not only does it improve the electrical resistivity of the material but it also lowers the densification temperature of the ferrite. However, magnetic and microstructure properties of the ferrite may also be affected by glass addition. For example, the magnetic properties may decrease due to partial dissolution of the ferrite into the glass melt.

This chapter records attempts to produce a lead borosilicate glass by a novel method and to mix it with Ni-Zn ferrites prepared in **Chapter 2**. Electrical, magnetic and microstructure properties of the resulting Ni-Zn ferrites are recorded and interpreted.

UNIVERSITY COLLEGE Library CORK

3.2 RESULTS AND DISCUSSION

3.2.1 Preparation and Analysis of Lead Borosilicate Glass

Lead borosilicate glass was successfully prepared by a sol-gel technique. The sol was prepared from element-organic reagents, namely: lead bis(dodecanoate); tetraethoxysilane (TEOS); tributoxyborane (TBB), mixed together in a toluene/*iso*-propanol (IPA) solvent. The hydrolysis and polycondensation reactions involving the silicate and borate groups were initiated by the addition of the base, tetrabutylammonium hydroxide. The solution became opaque and slightly more viscous. This gel-type system was then destabilised by rapid removal of solvent to yield a viscous white gel, which was the lead borosilicate glass precursor. **Figure 3.4** demonstrates the preparation method schematically.

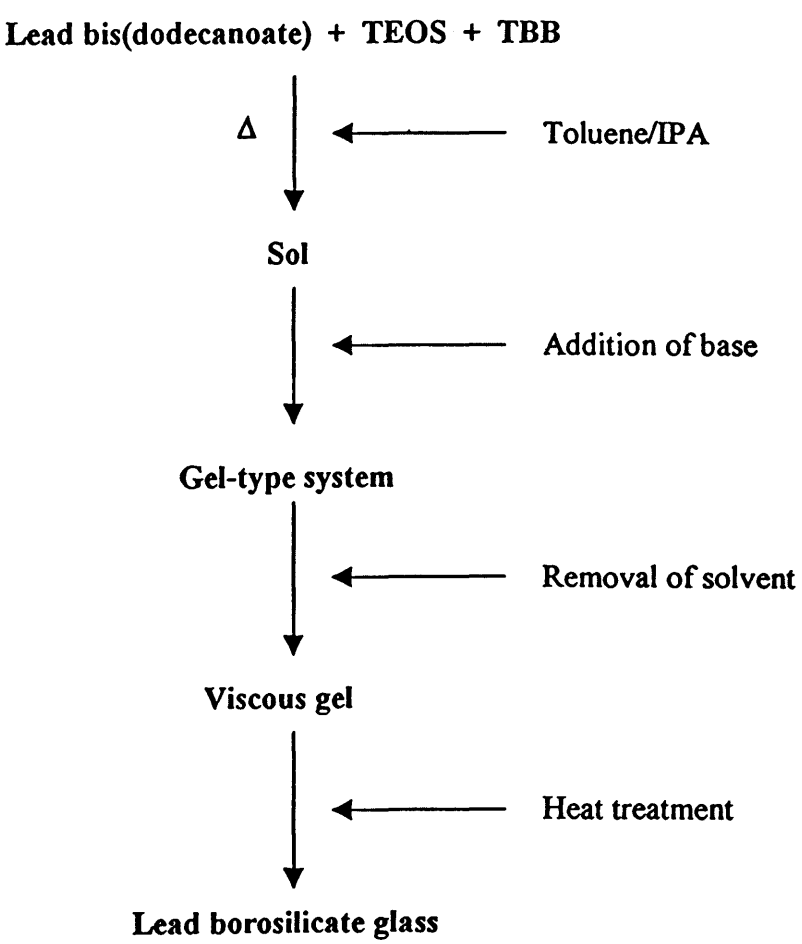


Figure 3.4 Schematic diagram of the preparation of lead borosilicate glass

The last step in the diagram is the conversion of the gel to a clear glass. The lead borosilicate glass precursor had a glass transition temperature of *circa* 600°C. The glass transition temperature was determined from PXRD studies. **Figure 3.5** shows the conversion of the gel into a glass as followed through PXRD patterns. The first pattern is that of a completely dried gel (glass precursor). It displays a PXRD pattern identical with pure lead bis(dodecanoate). This suggests that the hydrolysis and condensation of the lead bis(dodecanoate) didn't occur fully during gel formation. According to the PXRD patterns, heat treating the dried gel causes the disappearance of lead bis(dodecanoate) with formation of a new crystalline phase belonging to lead oxide (PXRD pattern (c) in **Figure 3.5**). The PbO phase eventually disappears to leave just an amorphous phase (between $2\theta = 25 - 30°$), indicating formation of the glass, at the heat treatment temperature of 600°C.

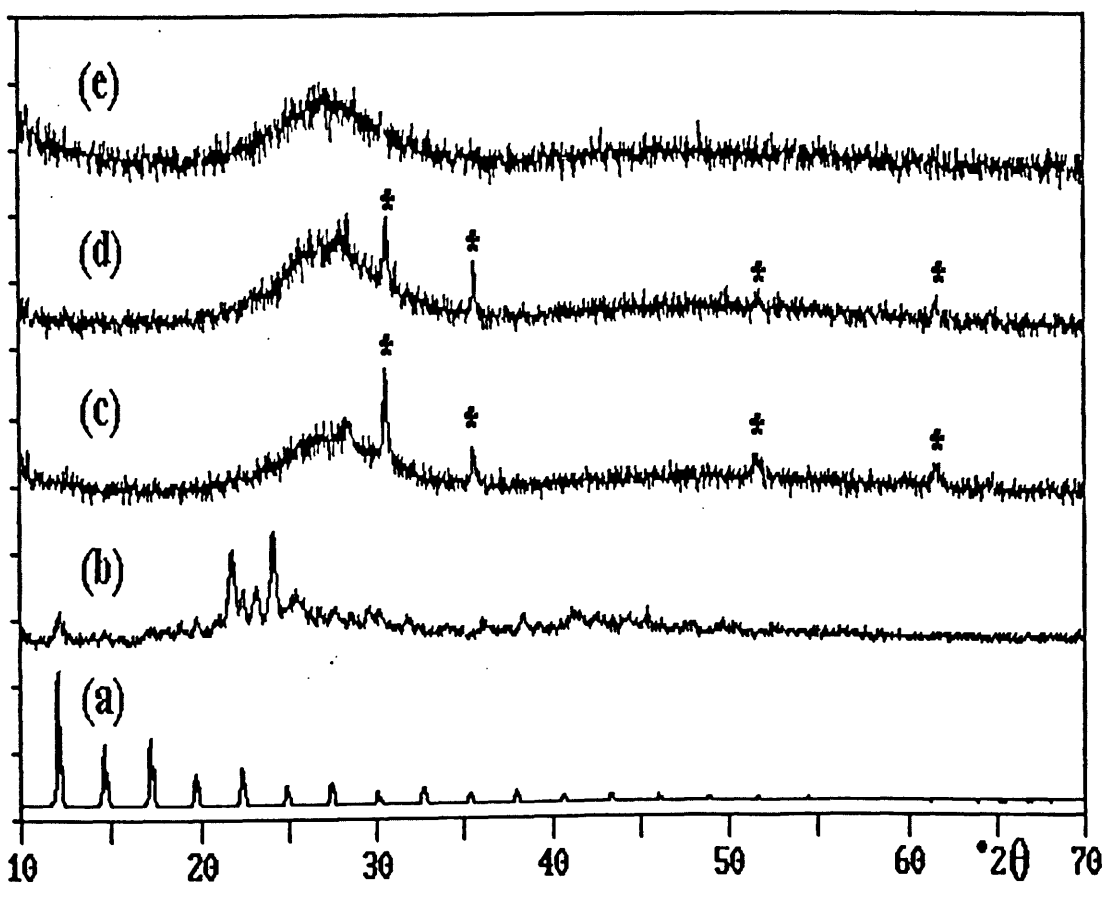


Figure 3.5 PXRD patterns of lead borosilicate precursor treated at (a) room temperature, (b) 200°C, (c) 350°C, (d) 500°C and (e) 600°C, * indicates peaks belonging to the lead oxide phase.

FTIR spectroscopy was also used to observe the glass transition of the lead borosilicate precursor. The FTIR spectrum of the dried lead borosilicate gel displayed the peaks belonging to the organic groups of lead bis(dodecanoate). This result confirmed the observation in the PXRD data, shown in **Figure 3.5(a)**. FTIR spectra of the different heat-treated gels showed the disappearance of the organic groups and the appearance and increasing in intensity of peaks due to B-O (1250-1350 cm^{-1}), Si-O (900-1150 cm^{-1}) and Si-O-B (1300-1400 cm^{-1}) bonds. Hence, FTIR spectroscopic data confirm the formation of glass from the dried gel during the heating process.

3.2.2 Preparation of Ni-Zn Ferrite with Lead Borosilicate Glass Additives

The synthesis of Ni-Zn ferrites with added glass (glass-ferrites) was achieved by two very different methods. The first way (Method A) prepared a gel incorporating the Ni-Zn ferrite precursor and the lead borosilicate glass precursor. **Figure 3.6** summarises the procedure involved in this method. The precursor gels were mixed in *iso*-propylalcohol (IPA). Evaporation of the solvent yielded a viscous gel. This gel was dried in a 60°C oven to afford a dry powdered solid. In **Chapter 2**, the sol-gel Ni-Zn ferrites exhibited spontaneous magnetism at this stage of their preparation. In the case of the glass-ferrite precursors formed, as shown in **Figure 3.6**, their magnetic properties depended on the percent of glass added (by weight) to the ferrite. Addition of 2.5% and 5% glass by weight to the ferrite (i.e. CG4 and CG3, respectively) formed magnetic powders (i.e. the powders were attracted to a hand held bar magnet) while addition of 10% and 36% glass by weight to the ferrite (i.e. CG2 and CG1, respectively) gave non-magnetic powders. This suggests that a large amount of glass precursor mixed with the ferrite precursor may have prevented the inverse spinel structure of the ferrite from forming.

The second way (Method B) prepared glass-ferrites by a more traditional means. First the Ni-Zn ferrite powder was synthesised by ageing its dried powder precursor at 1100°C. This ageing temperature was used to form a ferrite of the highest magnetic quality (as explained in **Section 2.2.3, Chapter 2**). The lead borosilicate gel precursor was added to this ferrite powder and mixed in IPA with a sonic bath to ensure that each ferrite particle was coated with the glass precursor. Evaporation of the IPA afforded a magnetic material. This material was aged at different

temperatures to form the glass-ferrites. Method B is schematically explained in Figure 3.7.

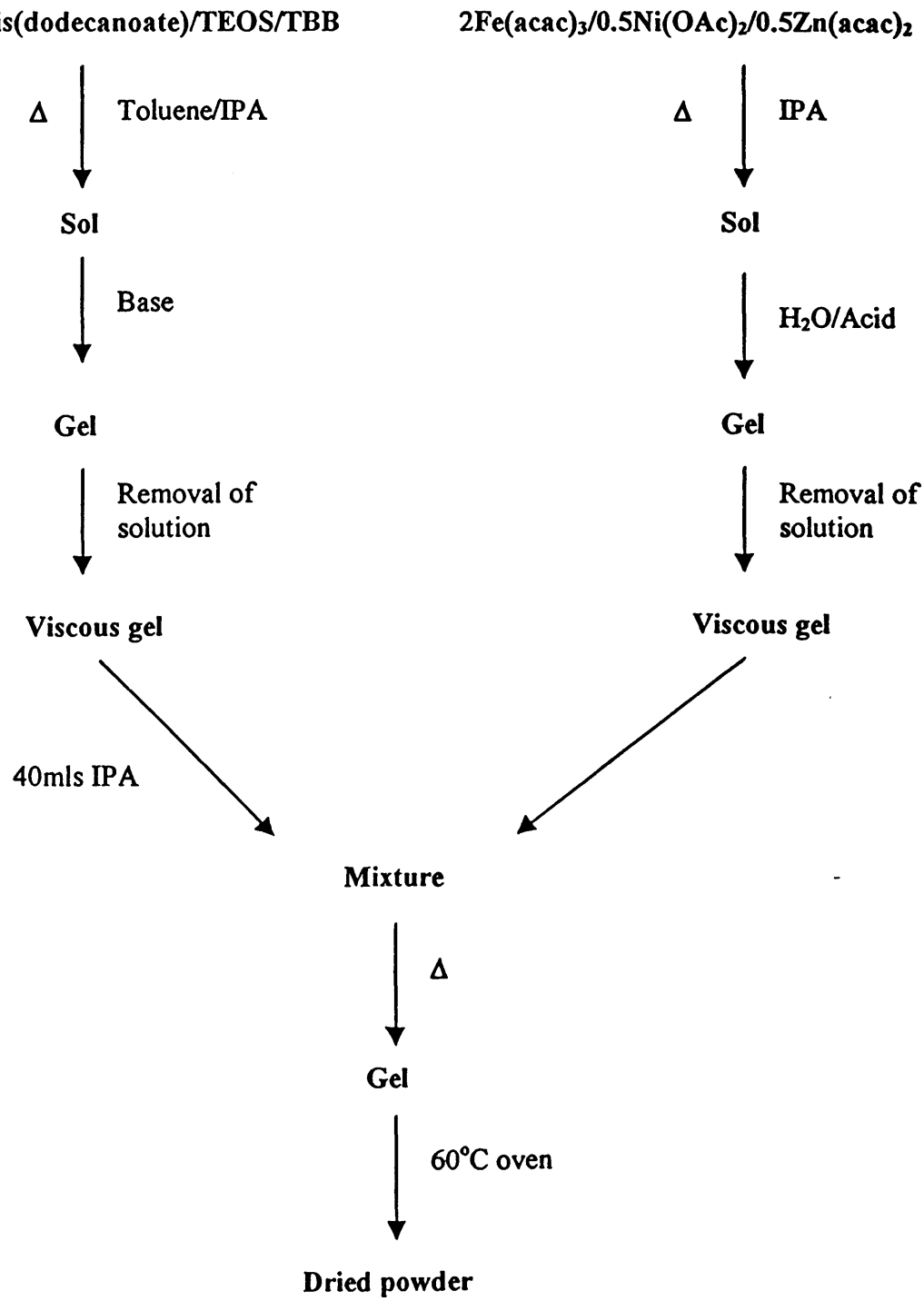


Figure 3.6 Schematic diagram for Method A, (TEOS = tetraethoxysilane and TBB = tributoxyborane).

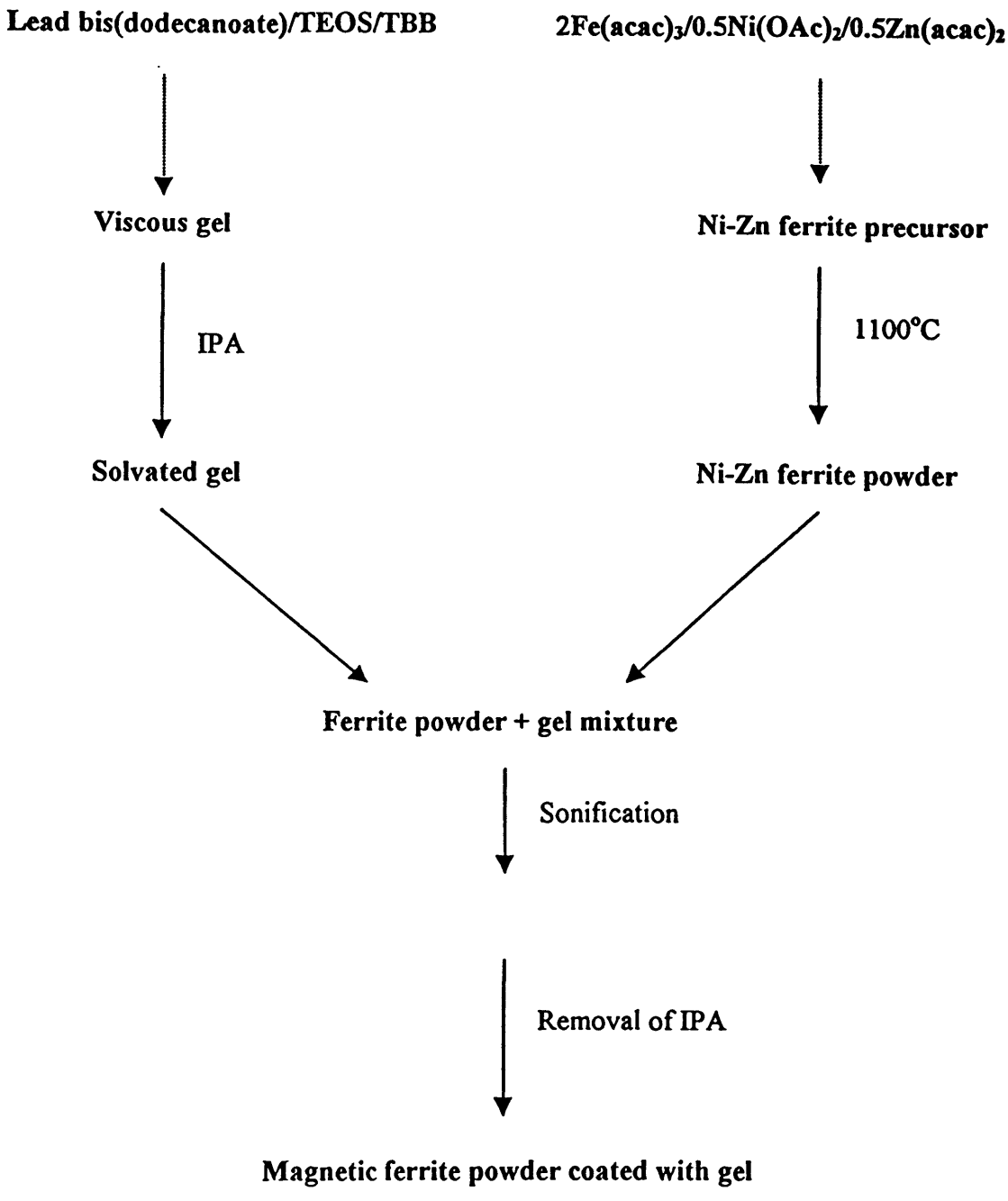


Figure 3.7 Schematic diagram for Method B.

Methods A and B are novel preparations of glass-ferrite materials. Method A involves a complicated system of metallic silicate and borate ions, cogelling together. That CG3 (5.0% glass added) and CG4 (2.5% glass added) gave magnetic glass-ferrite precursors on drying suggests that the spinel structure of the ferrite has formed at a low temperature even with the glass precursor present. Method B is a simpler process with, first, the formation of a calcined Ni-Zn ferrite and then the coating of its

particles with the glass precursor. This is a similar approach to that adopted by Brooks *et al.* in the sol-gel coating of lithium-zinc ferrite powder with a borosilicate material.[51]

The glass-ferrite precursors prepared by each method were heated to 650, 800, 950 and 1100°C to form the glass-ferrites. Elemental analyses (Fe, Ni, Zn and Pb) of these materials showed that the correct percent of lead borosilicate glass by weight to the ferrite was achieved, see **Sections 3.4.5** and **3.4.6**. **Table 3.2** lists the identification codes of the compounds formed by each method. These will be used for the rest of the chapter.

Table 3.2 Names of glass-ferrites formed from the two methods.

Name of glass-ferrite	Synthetic method	Percent of glass added by weight (%)
CG1	Method A	36.0
CG2	Method A	10.0
CG3	Method A	5.0
CG4	Method A	2.5
HM1	Method B	36.0
HM2	Method B	10.0
HM3	Method B	5.0
HM4	Method B	2.5

Note: CG stands for cogelled system, while HM stands for heterogeneously mixed system.

3.2.3 *Characterisation of Glass-Ferrite Compounds*

The main tools used to analyse these compounds structurally were Fourier transform infrared spectroscopy (FTIR), powder X-ray diffractometry (PXRD) and scanning electron micrometry (SEM). From these, the size and shape of particles, compound's lattice structures and type of bonds in the glass-ferrites can be elucidated. The magnetic properties of the glass-ferrites were analysed by vibrating sample magnetometry (VSM) and Mössbauer spectroscopy while the electrical resistivity measurements of the compounds were done by the four point probe method as described in **Appendix E.**

3.2.4 *Infrared Spectroscopy*

Evidence of B-O, Si-O, Si-O-B and Fe-O bonding was found for each sample with characteristic frequencies apparent in the infrared spectra. **Table 3.3** lists ranges of wavenumbers for each type of bonding found. Spectral analysis of uncoated ferrite powder did not indicate overlapping peaks in this region of the spectrum (900-1400 cm^{-1}). The only major difference between the samples was the increase in intensity of the B-O, Si-O and Si-O-B peaks relative to Fe-O peak at ~570 cm^{-1} as the percent of the glass to ferrite increased.

Table 3.3 Wavenumbers of bonding observed in glass-ferrites.

Type of Bonding	**Wavenumbers of spectral peaks (cm^{-1})**
B – O	1250-1350
Si – O	900-1140
Si – O – B	1330-1380
Fe - O	550-590

3.2.5 *PXRD Analysis*

Several physical properties of Ni-Zn ferrites were assessed in **Chapter 2** from PXRD studies including the purity of the ferrite's spinel phase, the lattice parameter **a**, and particle size. **Figures 3.8(a)** and **(b)** show PXRD patterns of two glass-ferrites (CG2 and HM2 both fired at 950°C), prepared by Method A and Method B, respectively. The patterns are similar to those recorded for the Ni-Zn ferrites prepared in **Chapter 2** (see **Section 2.2.2**) with the inverse spinel phase of the Ni-Zn ferrite clearly detectable. No other crystalline phases of any iron oxide e.g. hematite, a common impurity in ferrites, were detected. However an anomalous peak was observed at $2\theta = 22°$. The peak signals the formation of cristobalite, a crystalline phase of SiO_2, in the glass. This has been reported to occur for lead borosilicate glass when processed at temperatures greater than 700°C.[108] An amorphous phase is also perceived in the two diffractograms between $2\theta = 25 - 30°$ as a very broad peak. This phase is assigned to the lead borosilicate glass. PXRD studies thus showed glass and ferrite phases intermingled and confirmed the formation of glass-ferrites by the two methods.

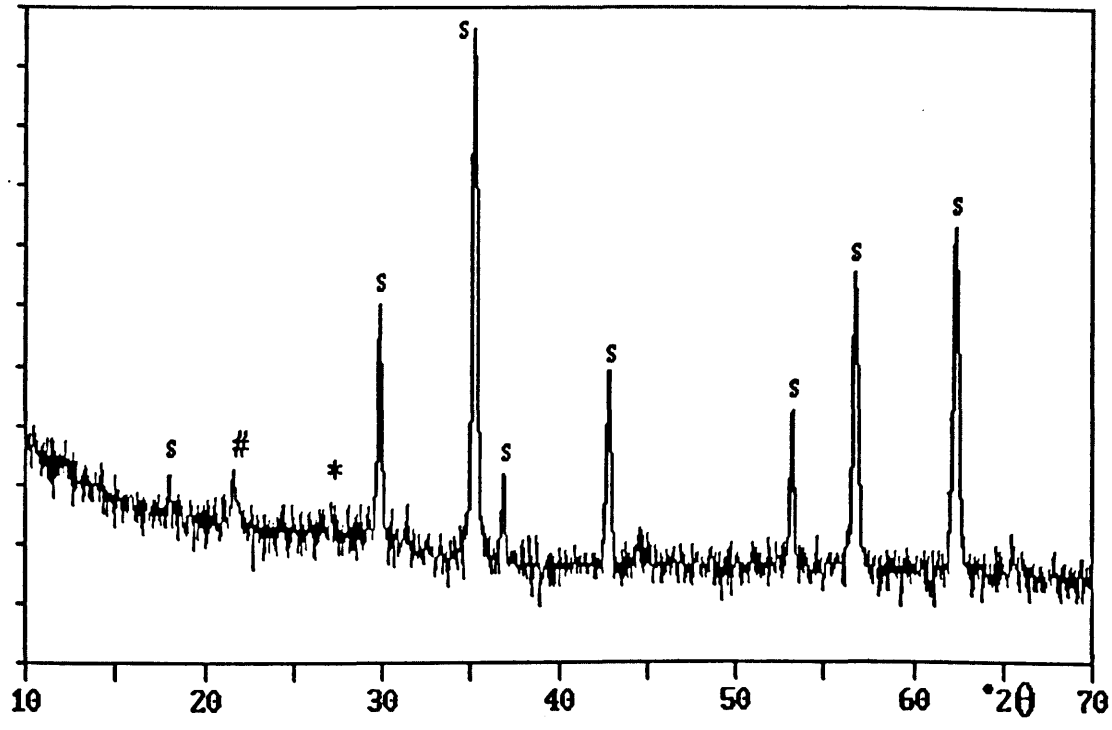


Figure 3.8(a) A PXRD pattern for CG2 (addition of 10% glass to ferrite) prepared by Method A and calcined at 950°C, s = spinel peaks, * = amorphous region and # = cristobalite peak.

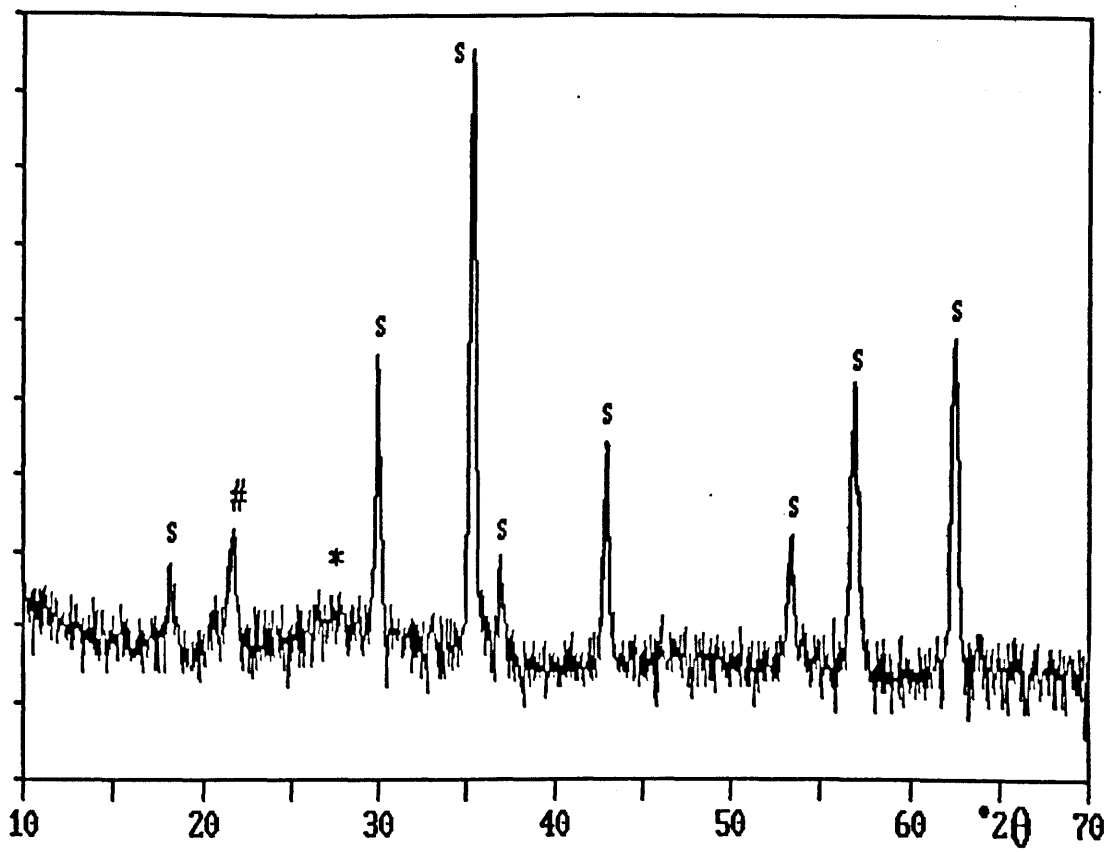


Figure 3.8(b) A PXRD pattern for HM2 (addition of 10% glass to ferrite) prepared by Method B and calcined at 950°C, s = spinel peaks, * = amorphous region and # = cristobalite peak.

Figure 3.9 displays the PXRD patterns for a glass-ferrite, CG2 (10% glass added), aged at several different temperatures. An extra peak ($2\theta = 22°$) develops in the glass amorphous phase as the temperatures become greater than 800°C. This is assigned to the cristobalite (SiO_2) phase forming. Since the formation of this phase may reduce the performance of the glass as an insulator,[109,110] several researchers have tried to suppress it by addition of gallium oxide or alumina. All the glass-ferrites expressed this phase when fired at temperatures greater than 800°C and the phase was more noticeable for ferrites that contained a higher percent of glass.

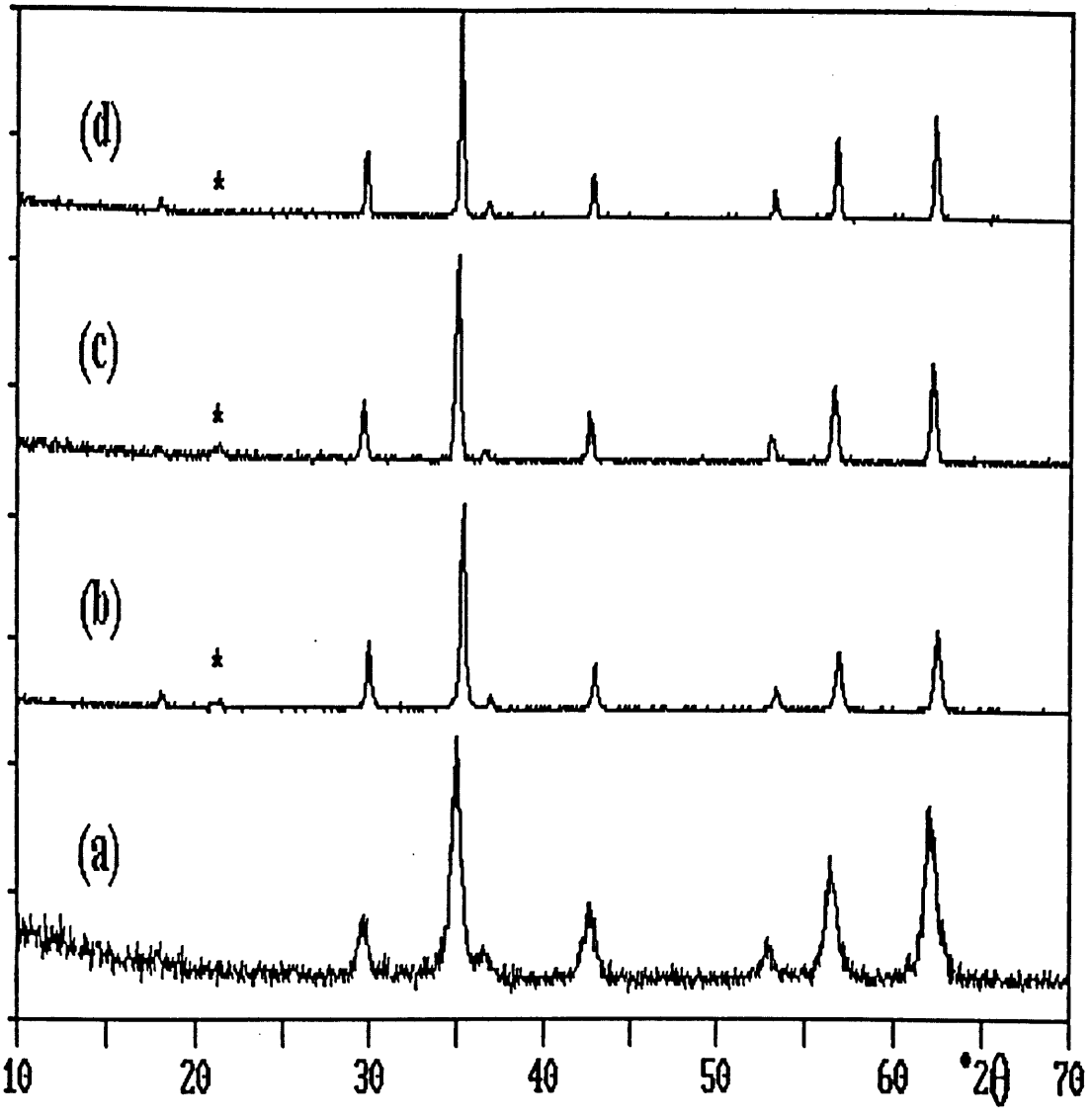


Figure 3.9 PXRD patterns of the glass-ferrite prepared by Method A (CG2) and aged at (a) 650°C, (b) 800°C, (c) 950°C and (d) 1100°C, * = cristobalite peak.

The lattice parameters (a-values) for each of the glass-ferrites were calculated as demonstrated in Section 2.2.2, Chapter 2. Table 3.4 lists the results. It is worth recalling here that the a-value of glass-free ferrite, NiZnSG3 fired at 800°C, is *circa* 8.399Å, Table 2.4, Section 2.2.2. The a-values for all the glass-ferrites are above this value. Hence the glass-ferrites exhibit lattice expansion. The movement of Pb^{2+} ions from the glass into the ferrite structure as the ferrite dissolves into the glass melt may account for this expansion. It has been reported that for Mn-Zn ferrites and $PbO\text{-}SiO_2$

glass melts, the ferrite dissolves into the glass melt by migration of Zn^{2+} ions from the tetrahedral sites to eventually form an intermediate phase of lead iron silicate at the interface.[103] Therefore it is reasonable to postulate the movement of some Pb^{2+} ions into the tetrahedral sites vacated by the Zn^{2+} ions. Pb^{2+} ions have a structural chemistry similar to Zn^{2+} ions since they also prefer tetrahedral coordination. This would lead to expansion of the lattice as the Pb^{2+} ions (~1.17Å) have larger ionic radii than Zn^{2+} ions (~0.60Å).

Table 3.4 Lattice parameters of glass-ferrites.

Method A				
Temp. (°C)	2.5% glass(Å) CG4	5% glass (Å) CG3	10% glass (Å) CG2	36% glass (Å) CG1
650	8.564	8.592	8.534	8.637
800	8.432	8.416	8.438	8.409
950	8.606	8.563	8.663	8.579
1100	8.425	8.567	8.568	8.541
Method B				
Temp. (°C)	2.5% glass (Å) HM4	5% glass (Å) HM3	10% glass (Å) HM2	36% glass (Å) HM1
650	8.498	8.618	8.615	8.604
800	8.461	8.424	8.438	8.444
950	8.500	8.587	8.513	8.575
1100	8.490	8.487	8.506	8.572

Another interesting result gathered from **Table 3.4** is that the lowest lattice expansion for all the glass-ferrites occurs at the same calcining temperature, namely 800°C. In some cases the lattice parameters of these glass-ferrites are almost the same as that of the glass-free Ni-Zn ferrite. The reason for this isn't clear but it may be linked to the formation of cristobalite in the glass at this temperature.

Figure 3.9 demonstrated the formation of an extra crystalline phase in the glass. It also highlights particle growth of the glass-ferrites as the ageing temperatures are raised. As explained in **Chapter 2**, particle growth leads to a sharpening of peaks in the PXRD patterns. Scherrer's formula[73] was used to estimate particle sizes and these are listed for the glass-ferrites prepared by Method A in **Table 3.5**. The particle sizes are observed to steadily increase as the temperature increases due to the process of sintering. This happens irrespective of the percent of added glass. The particle sizes from compounds processed at 800°C are relatively small, between 250 – 480Å. The particle sizes of glass-free ferrite processed in an 800°C oven are approximately 530Å (see **Table 2.5, Chapter 2**). Hence, it appears that the addition of glass has kept ferrite particles apart at 800°C. Moreover, the particles of glass-ferrite do not appear to grow as large as the particles of glass-free ferrite even when heated at higher temperatures. For example, the largest estimated particle size recorded for the glass-ferrites is ~840Å (CG4 processed at 1100°C), yet this is smaller than the average particle size of the glass-free ferrite (~880Å) processed at the same temperature.

Table 3.5 also shows the effect of increased percent glass on average particle size for the glass-ferrites processed at the same ageing temperatures. **Figure 3.10** graphs particle size versus percent of glass added for ferrites processed at 1100°C. Between 5 and 10% added glass, the particle size increases dramatically. After this, the increase is small. The glass appears to act as a flux to bring ferrite particles together. This is most effective between 5-10 % of added glass.

Table 3.5 Particle sizes of glass-ferrites prepared by Method A.

Name of glass-ferrite	Percent of Glass Precursor (%)	Firing Temperature / °C	Particle size / Å (+/- 20Å)
CG4	2.5	650	151
		800	255
		950	463
		1100	591
CG3	5	650	144
		800	350
		950	436
		1100	607
CG2	10	650	131
		800	432
		950	504
		1100	797
CG1	36	650	138
		800	484
		950	511
		1100	842

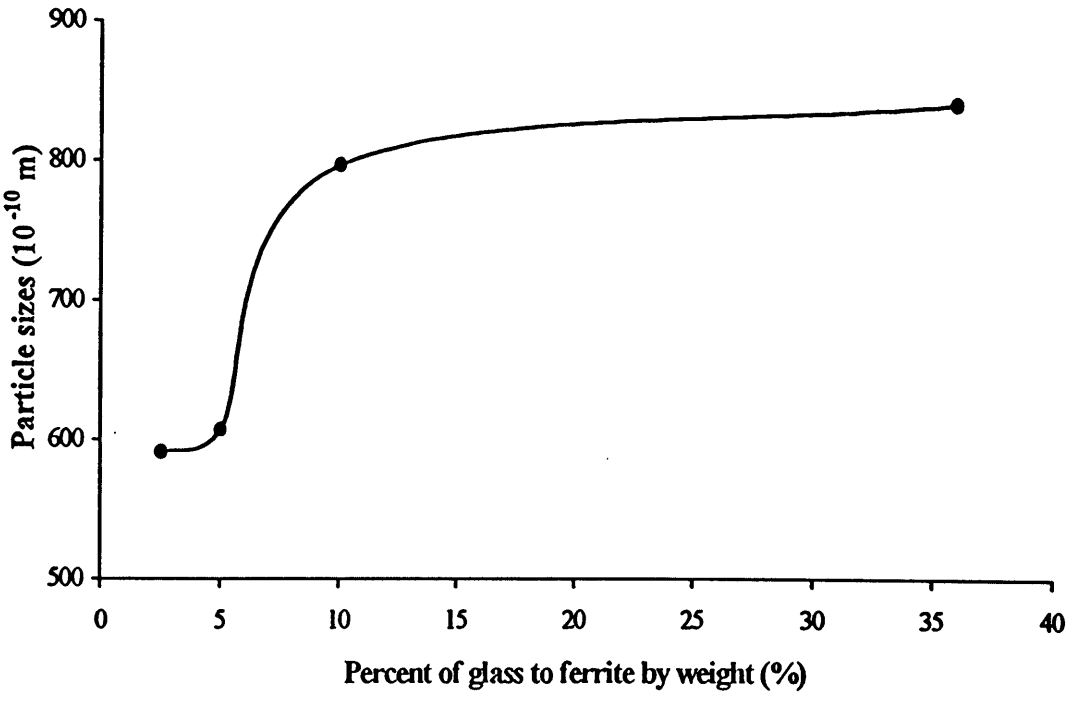


Figure 3.10 Particle size of glass-ferrites prepared by Method A and processed at 1100°C versus percent of glass in ferrites.

Table 3.6 lists the particle sizes of the glass-ferrites prepared by Method B, i.e. the heterogeneous mixing of glass gel with preformed ferrite powder. As mentioned previously, the estimated particle size of a sol-gel Ni-Zn ferrite aged at 1100°C is approximately 880Å and this is somewhat larger than the ferrite particles produced by Method B (between ~ 15-25% larger) when 5% or more glass is added. The particle size of the glass-ferrites with 2.5% glass added (HM4) is even more notably smaller, at ~300Å than the glass-free ferrite. Recall that Method B involved the sonication of the ferrites with the glass precursor. This agitation of the ferrite particles ensured complete mixture with the glass precursor but it may also have broken up the particles. A PXRD pattern of this material was recorded (HM4) and the particle size was estimated to be ~460Å. Therefore, the particles had been disassociated by sonication and the results in **Table 3.6** shows the reassembling of the particles with the aid of the glass as a "flux". As already observed in **Table 3.5** (and shown in **Figure 3.10**), the particles grew larger with increased glass added.

The process of particle break-up by sonication may also be assisted by the presence of the intragranular pores (see **Figure 2.15, Chapter 2**). **Figure 3.11** demonstrates the disassociation of large ferrite particles by sonication. The particles are riddled with intragranular pores and it is at those points that cleavage occurs to form the smaller particles.

Table 3.6 Particle sizes of glass-ferrites formed by Method B.

Name of glass-ferrite	Percent of Glass Precursor (%)	Firing Temperature / °C	Particle size / Å (+/- 20Å)
HM4	2.5	650	542
		800	474
		950	456
		1100	535
HM3	5	650	779
		800	723
		950	1017
		1100	870
HM2	10	650	557
		800	674
		950	682
		1100	650
HM1	36	650	750
		800	745
		950	752
		1100	703

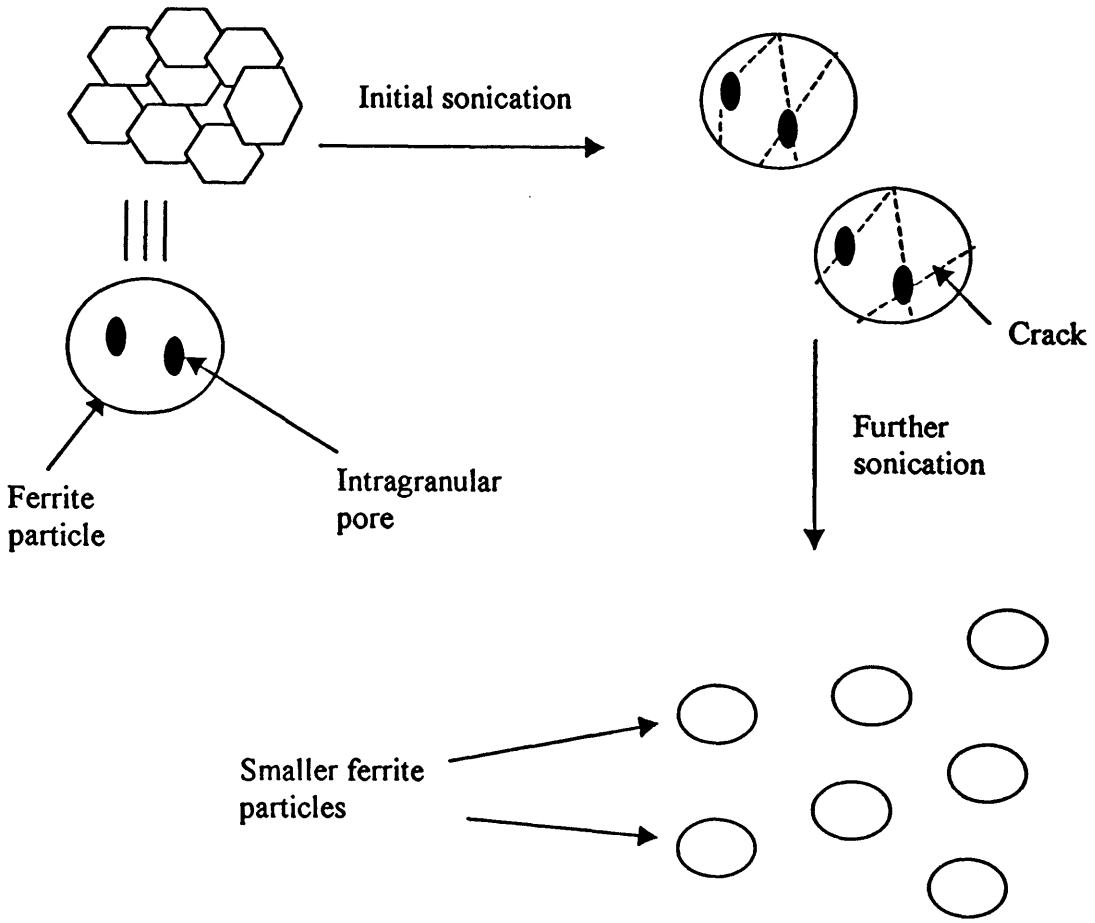


Figure 3.11 Schematic diagram demonstrating the change in microstructure of ferrite particle due to sonication.

The difference in particle sizes between **Table 3.5** and **Table 3.6** demonstrates significant differences according to preparatory methods. Method A produced the glass-ferrite by heating a cogelled system of glass and ferrite precursors. Hence, the glass-ferrite particles are small at low processing temperatures and increase by the sintering process as the temperature is raised. Method B prepared the glass-ferrite by heating the mixture of glass precursor with a preformed ferrite with "fixed" particle size. Therefore particle growth is already established in this system and explains why the glass-ferrites of Method B have greater particle sizes than their corresponding glass-ferrites formed by Method A at the low processing temperatures.

3.2.6 SEM Analysis

SEM images were taken for the glass-ferrites, CG2 and HM2, processed at 650, 800 and 1100°C. **Figures 3.12(a)-(c)** show the SEM images of CG2 while **Figures 3.13(a)-(c)** show the images of HM2. The images are remarkably different from those of the glass-free ferrite (see **Figure 2.15, Chapter 2**). The glass-free ferrite had particles of irregular shape and size, which also exhibited intragranular porosity. The particles of CG2 processed at 650°C were almost flake-like and possessed no significant intragranular porosity. At higher ageing temperatures, the particles densified and became linked together by the glass melt. The SEM image for CG2 heated at 1100°C showed regular shaped and sized particles. They appeared to have glaze-like features, presumably due to the lead borosilicate glass covering. The glass necking of the particles (i.e. the linking of the particles) can be clearly seen in the SEM image. The SEM images of HM2 showed the particles covered with glass with a shiny appearance. At the ageing temperature of 1100°C, the particles are linked together to produce an appearance like molten-lava. Intragranular porosity is noticeably missing in these images.



Figure 3.12(a) A SEM image of CG2 (10% glass added) processed at 650°C

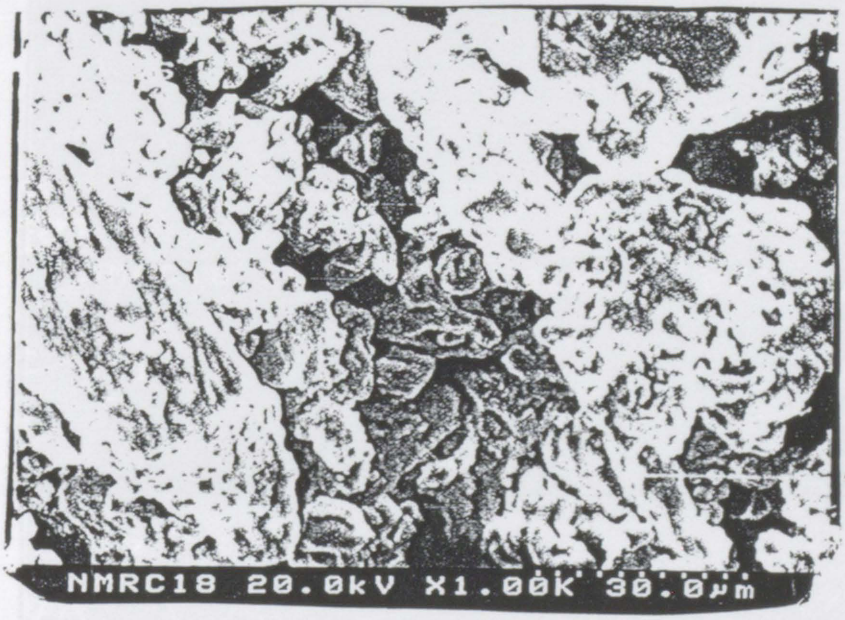


Figure 3.12(b) A SEM image of CG2 (10% glass added) processed at 800°C.



Figure 3.12(c) A SEM image of CG2 (10% glass added) processed at 1100°C.

(a)

(b)

(c)

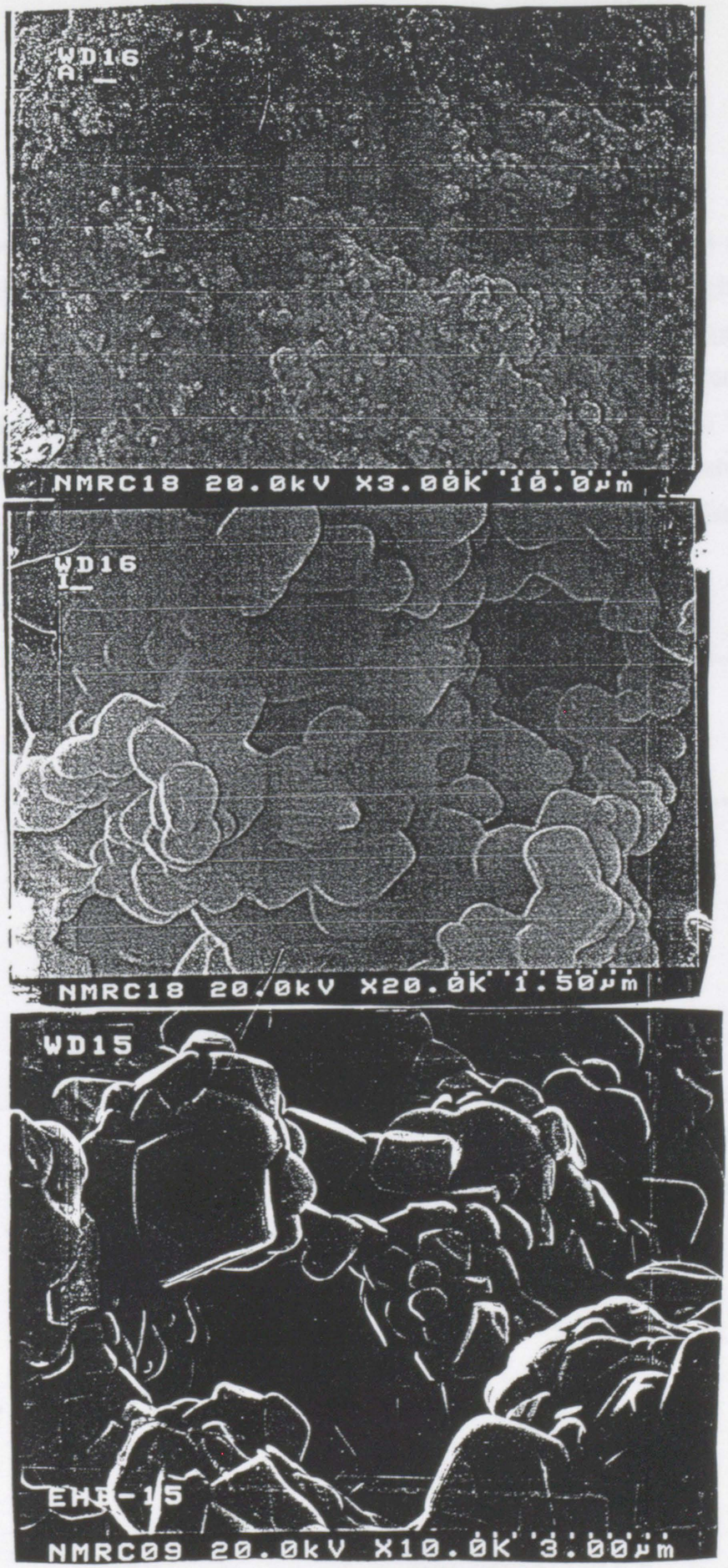


Figure 3.13 The SEM images of HM2 (10% glass added) processed at (a) 650°C, (b) 800°C and (c) 1100°C.

3.2.7 *VSM Analysis*

The VSM measurements were not taken for all the glass-ferrites prepared but rather for a selected few. The objective was to investigate the effect of addition of glass to the ferrite's magnetic properties. The PXRD and SEM measurements had suggested pronounced alterations in the microstructure of the Ni-Zn ferrite on glass addition.
All the VSM results for the glass-ferrites gave the expected hysteresis loop of "soft" magnetic materials, i.e. the materials saturated quickly and had very low coercivities. **Figure 3.14** gives one example of such a loop (CG3) and **Table 3.7** lists the saturation magnetisation values (M_s) of the glass-ferrites

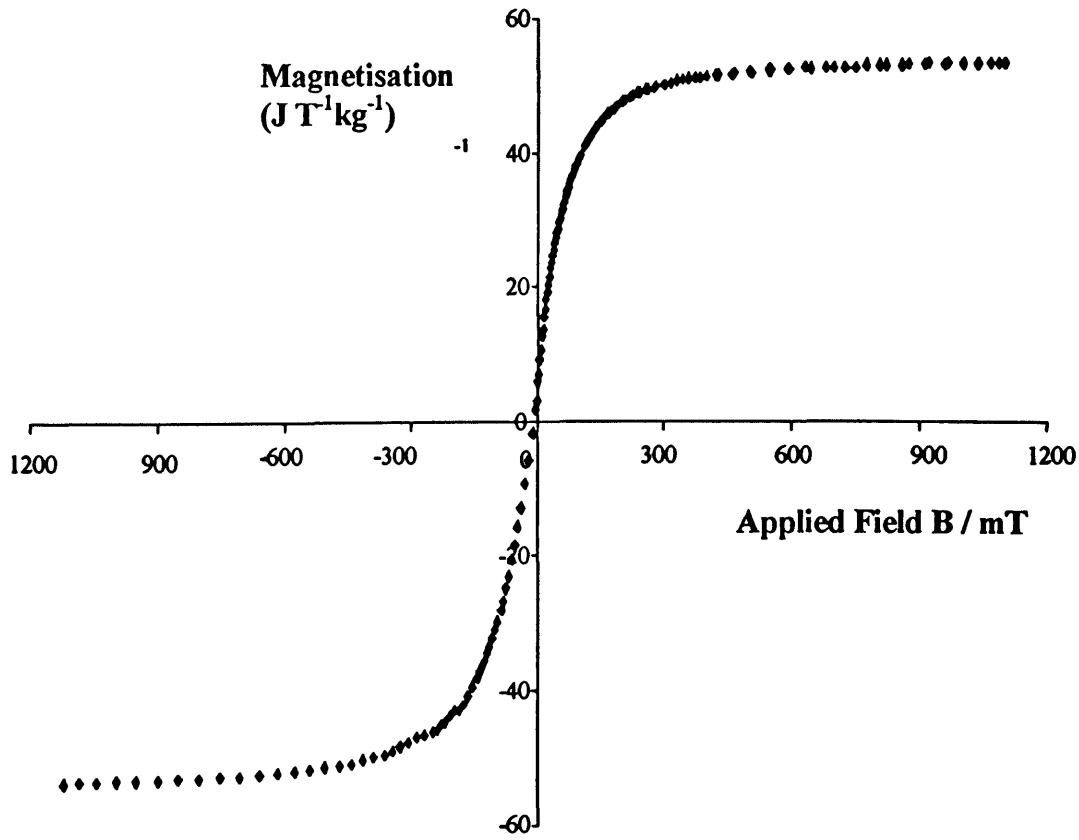


Figure 3.14 Hysteresis loop of the glass-ferrite CG3 (5% glass added) processed at 1100°C

Table 3.7 Saturation Magnetisation values of glass-ferrites prepared by the two methods and of the glass-free ferrite.

METHOD A		
Name	**Processing temperature (°C)**	**M_s ($J\,T^{-1}kg^{-1}$) (+/- 0.4)**
CG4 (2.5% glass added)	800	53.4
CG3 (5% glass added)	650	46.4
	800	49.4
	950	51.8
	1100	53.5
CG2 (10% glass added)	800	46.2
CG1 (36% glass added)	800	40.1
METHOD B		
HM4 (2.5% glass added)	800	72.3
HM3 (5% glass added)	650	63.5
	800	69.9
	950	60.2
	1100	54.5
HM2 (10% glass added)	800	56.8
HM1 (36% glass added)	800	51.0
NiZnSG3 (glass-free ferrite)	60	38.2
	800	42.5
	1100	55.2

Table 3.7 establishes two significant results which relate to (1) change of M_s values of a glass-ferrite due to different processing temperatures and (2) change of M_s values due to different percentages of glass addition at the same processing temperature. The M_s values for CG3 increase as the ageing temperature increases. Since the ferrite is only fully structurally formed when aged at high temperatures, this result is to be expected. The same trend was found for the glass-free ferrite as reported in Chapter 2 and is recalled again in Table 3.6 for comparison. However, the M_s values between CG3 and its corresponding glass-free ferrite are slightly different, suggesting that glass addition had some influence on the ferrite's magnetic properties. However, a thorough explanation such as that given by Nitta *et al.*[105] for Ni-Zn glass-ferrites (see Section 3.1.4) cannot be postulated here as the system is quite different and complicated by the mixture of metallic ions in the cogelling stage. It is possible that glass dissolution of ferrite does occur for CG3 as the temperature is increased but this feature was not detectable by the methods used in the present study.

The M_s values of the glass-ferrites formed by Method A (CG1 – CG4) and processed at the same temperature (800°C) show a continuous lowering of the magnetisation values in the ferrite as the glass content is raised. This may be as a result of the dissolution of the ferrite in the glass melt. Simply put, a higher content of glass in the ferrite leads to more dissolution of ferrite into the glass melt and therefore, the magnetism of the ferrite decreases.

The M_s values for the glass-ferrites prepared by Method B (e.g. HM3) show an initial increase when processed from 650 to 800°C and a decrease when processed from 800 to 1100°C. This is the complete opposite to the observations of Nitta *et al.* for Ni-Zn ferrites coated with $PbO\text{-}SiO_2$ glass.[105] This observation may be related to the precipitation of cristobalite in the glass at 800°C and upwards.

Table 3.7 clearly demonstrates the decrease in M_s values as the glass content of the compounds produced by Method B increases. The increase in ferrite dissolution due to increase in percent of glass can account for this observation. The last point to note is that the glass-ferrites with 2.5 and 5% glass have higher M_s values than the glass-free ferrite at the same processing temperatures (in the case of HM4, an increase of 32% in M_s). The dissolution of Zn^{2+} ions from the ferrite structure into the glass melt to leave a Ni-richer ferrite of higher saturation magnetisation may account for this observation. This type of increase in M_s values does not occur for the glass-ferrites with 10 and 36% glass. The dissolution of too much Zn^{2+} ions into the glass melt to

leave behind almost a ferrite of $NiFe_2O_4$ formula, which has very low magnetism, may explain this.

The addition of glass to ferrite by either Method A or B has an effect on the ferrite's magnetic properties. Overall, this is a complex effect mainly associated with ferrite dissolution in the glass (possibly involving specific ions being extracted from the ferrite) or the formation of cristobalite phase of SiO_2. In some cases glass addition has a detrimental effect and can be associated with an overloading of glass in the ferrite. However, if this overloading is avoided, the glass additives can enhance the magnetism of the ferrite.

3.2.8 Mössbauer Spectroscopy

Mössbauer spectra were recorded at room temperature for the glass-ferrites, CG2, CG3, HM2 and HM3, processed at 1100°C. All spectra showed a collapsed doublet of sextets, as shown in **Figure 3.15**.

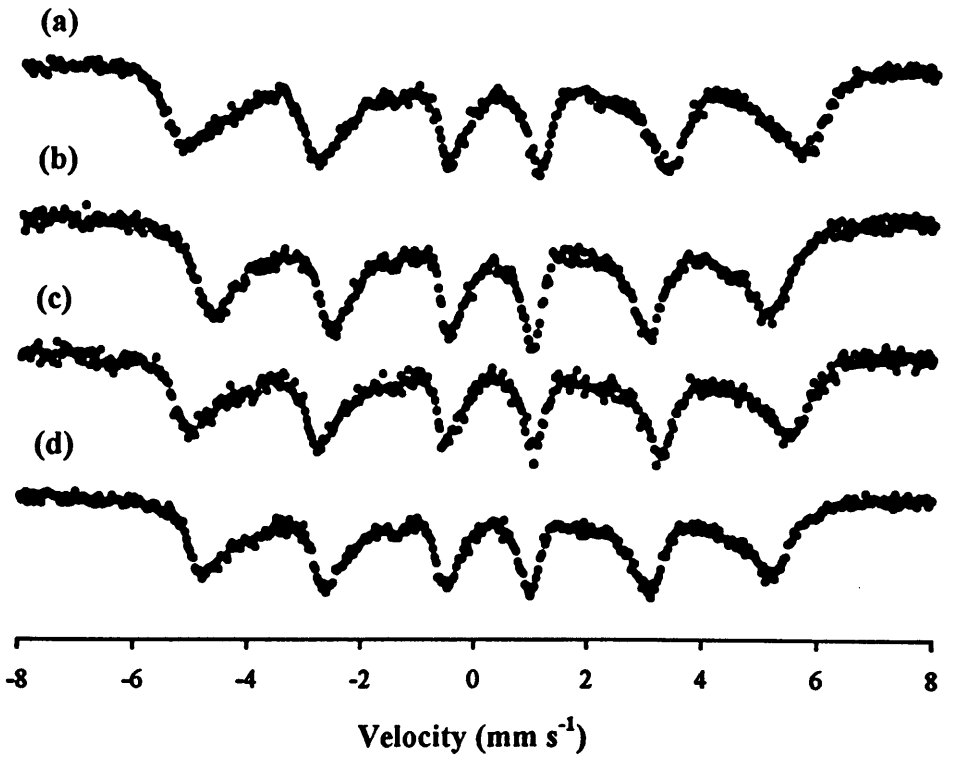


Figure 3.15 Room temperature Mössbauer spectra of (a) CG2, (b) CG3, (c) HM2 and (d) HM3, all processed at 1100°C.

These spectra are the same as the spectrum found for glass-free ferrite (shown in **Figure 2.35(b), Chapter 2**) and are consistent with the Mössbauer results reported by Arshed *et al.* and Daniels and Rosencwaig for the ferrites with a value of $x = 0.50$ and 0.62 in the formula $Ni_{1-x}Zn_xFe_2O_4$, respectively.[67,59] A collapsed spectrum is observed because the ferrite is in a relaxed magnetic phase, see **Section 2.2.5, Chapter 2.** Also, it is worth noting that these spectra do not contain any inner doublet due to small particles exhibiting superparamagnetism.

Room temperature Mössbauer spectra were also taken for CG3 and HM3, both aged at 800°C, see **Figure 3.16.** A central quadrupole doublet is observed as well as the collapsed doublet of sextets. The central doublet may indicate superparamagnetism in the glass-ferrites. The average particle sizes in the samples of CG3 and HM3 are estimated as ~350 and 720Å, respectively. Since these particle sizes are too large to exhibit superparamagnetism, it may be that the glass-ferrites contain some clusters of very small particles, which are superparamagnetic. The central doublet is more pronounced in CG3 than in HM3, which suggests that CG3 contains a larger number of superparamagnetic particles. Mössbauer spectra were taken at liquid nitrogen temperature for these glass-ferrites. The central doublet disappears from both compounds and becomes part of the magnetically ordered doublet of sextets. This confirms that superparamagnetism was the cause of the central doublet. The liquid nitrogen temperature Mössbauer spectra of CG3 and HM3 are given in **Figure 3.17.**

The Mössbauer spectra of the glass-ferrites didn't exhibit any anomalies that could be attributed to the glass additives. This suggests that the magnetic properties of the glass-ferrites are solely from the ferrite structure and there is no contribution from the lead borosilicate glass. Therefore, Mössbauer spectra of the glass-ferrites give no evidence for the formation of a magnetic lead iron oxide intermediate at the glass-ferrite interface. This is in agreement with the PXRD data of the glass-ferrites, which indicated no sign of a lead iron oxide phase.

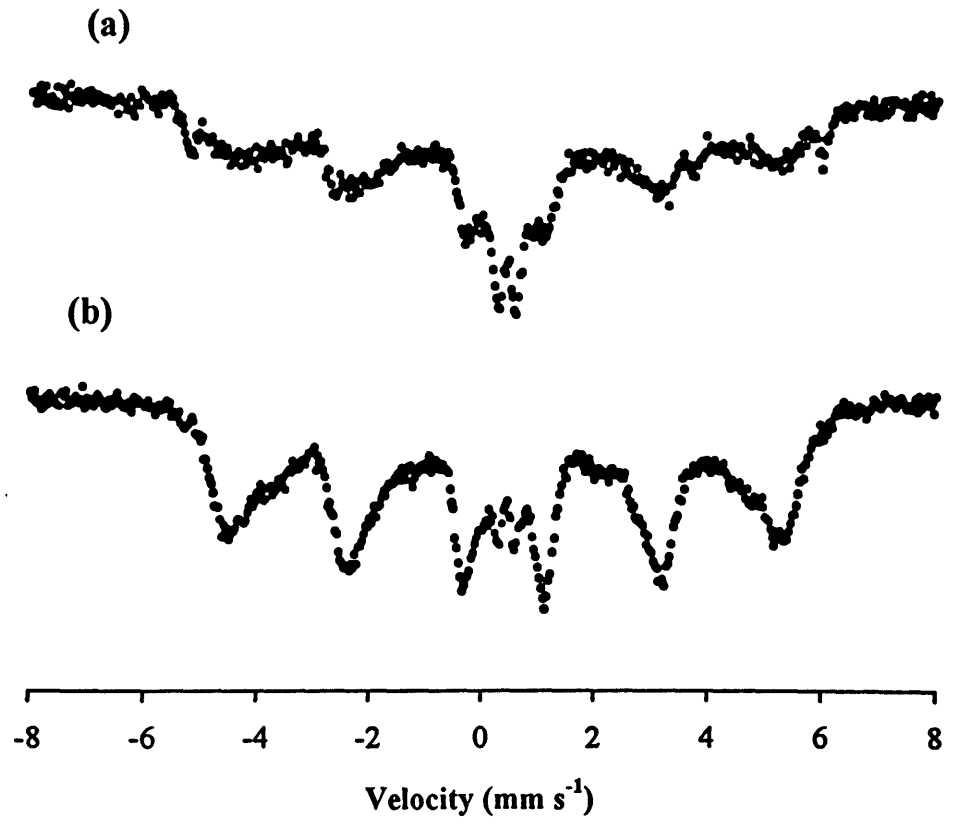


Figure 3.16 Room temperature Mössbauer spectra of (a) CG3 and (b) HM3, processed at 800°C.

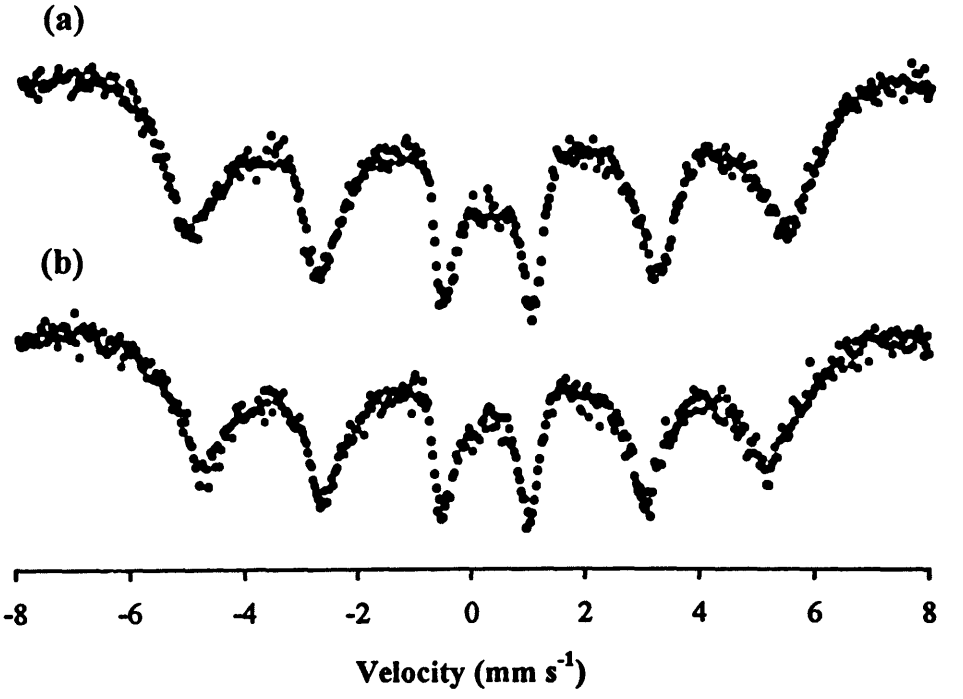


Figure 3.17 Liquid nitrogen temperature Mössbauer spectra of (a) CG3 and (b) HM3, processed at 800°C.

3.2.9 *Electrical Resistivity Analysis*

As mentioned earlier, a larger bulk electrical resistance of a ferrite leads to smaller core losses for that ferrite. This was the objective of adding glass to the ferrites.

Table 3.8 lists the resistivity results found for the glass-ferrites prepared by Method A at the four different processing temperatures as calculated from the four-point probe resistance method. It is worth recalling here that the resistivity of the glass-free ferrite was $3.6 \times 10^2\ \Omega$ m (see **Table 2.14, Chapter 2**). The resistivity values for the glass-ferrites calcined at 650 and 800°C are three to five orders greater than the above value. This is a large increase in resistance for the ferrite and clearly demonstrates the effectiveness of the lead borosilicate glass as an insulating coat around the ferrite particles. While FTIR, PXRD and SEM results suggested that the lead borosilicate had coated the ferrite, the resistivity results give conclusive proof of the coating. However, when these same compounds are aged at higher temperatures (950°C), the resistivity values decrease and eventually return to the value of the glass-free ferrite at 1100°C. The decrease in resistivity of these glass-ferrites at high temperatures may be explained by a combination of two different effects, which occur at high temperatures. The first has been mentioned previously and it involves the precipitation of the crystalline cristobalite from the glass at high temperatures. This precipitation undoubtedly changes several properties of the glass (such as its thermal expansion coefficient) and hence affects the resistivity of the ferrite in a detrimental way. The second change hasn't been mentioned before but nevertheless has important implications for the glass-ferrite's properties. The high vapour pressure of lead (1-10 mm in 950-1150°C range) can induce lead loss during melting.[108] This loss of Pb leads to a glass with a different stoichiometry and hence has different properties (such as glass transition temperature). These changes may cause a decrease in the resistivity of the ferrite. However, the simplest explanation for the decrease in resistivity values may be because of the particle agglomeration observed for these materials at high temperatures [recall SEM images, **Figures 3.12 (c) and 3.13 (c)**].

Table 3.9 reports the resistivity results for the glass-ferrites formed by Method B. Once again, remarkable resistivity values are observed for the glass-ferrites calcined at 650 and 800°C. The values have increased by up to six orders above the value for the glass-free ferrite. Therefore, this method has also been very successful in

producing highly resistant ferrites by the sol-gel coating of lead borosilicate glass around the ferrite's particles.

Table 3.8 Resistivity values of glass-ferrites prepared by Method A.

Name of glass-ferrite	Glass percent (%)	Processing Temperature (°C)	Resistivity value (Ω m)
CG4	2.5	650	2.23E+05
		800	1.54E+07
		950	1.82E+04
		1100	7.89E+02
CG3	5.0	650	2.50E+05
		800	1.04E+06
		950	5.25E+04
		1100	4.18E+03
CG2	10.0	650	2.83E+05
		800	3.17E+06
		950	8.24E+04
		1100	1.50E+04
CG1	36.0	650	8.50E+06
		800	7.25E+06
		950	6.42E+03
		1100	1.50E+02

The resistivity values of the glass-ferrite prepared by Method B and processed at 950 and 1100°C decrease dramatically in the same fashion as observed for the glass-

ferrites formed by Method A. This startling drop may be attributed to the precipitation of cristobalite, the evaporation of Pb from the glass at high temperatures and particle agglomeration.

Both Methods A and B have produced glass-ferrites that have approximately equal resistivity values which show similar variation of resistance with ageing temperatures, see **Figure 3.18**. It is somewhat surprising that glass-ferrites of similar electrical properties have formed from two very distinctly different synthetic methods.

Table 3.9 Resistivity results for glass-ferrites prepared by Method B.

Name of glass-ferrite	Glass percent (%)	Processing Temperature (°C)	Resistivity values (Ω m)
HM4	2.5	650	3.14E+07
		800	4.15E+07
		950	3.25E+05
		1100	1.25E+04
HM3	5.0	650	3.32E+06
		800	7.50E+05
		950	8.52E+03
		1100	6.50E+03
HM2	10.0	650	5.89E+06
		800	2.00E+06
		950	1.40E+04
		1100	5.40E+03
HM1	36.0	650	1.10E+08
		800	3.80E+06
		950	1.00E+05
		1100	4.50E+04

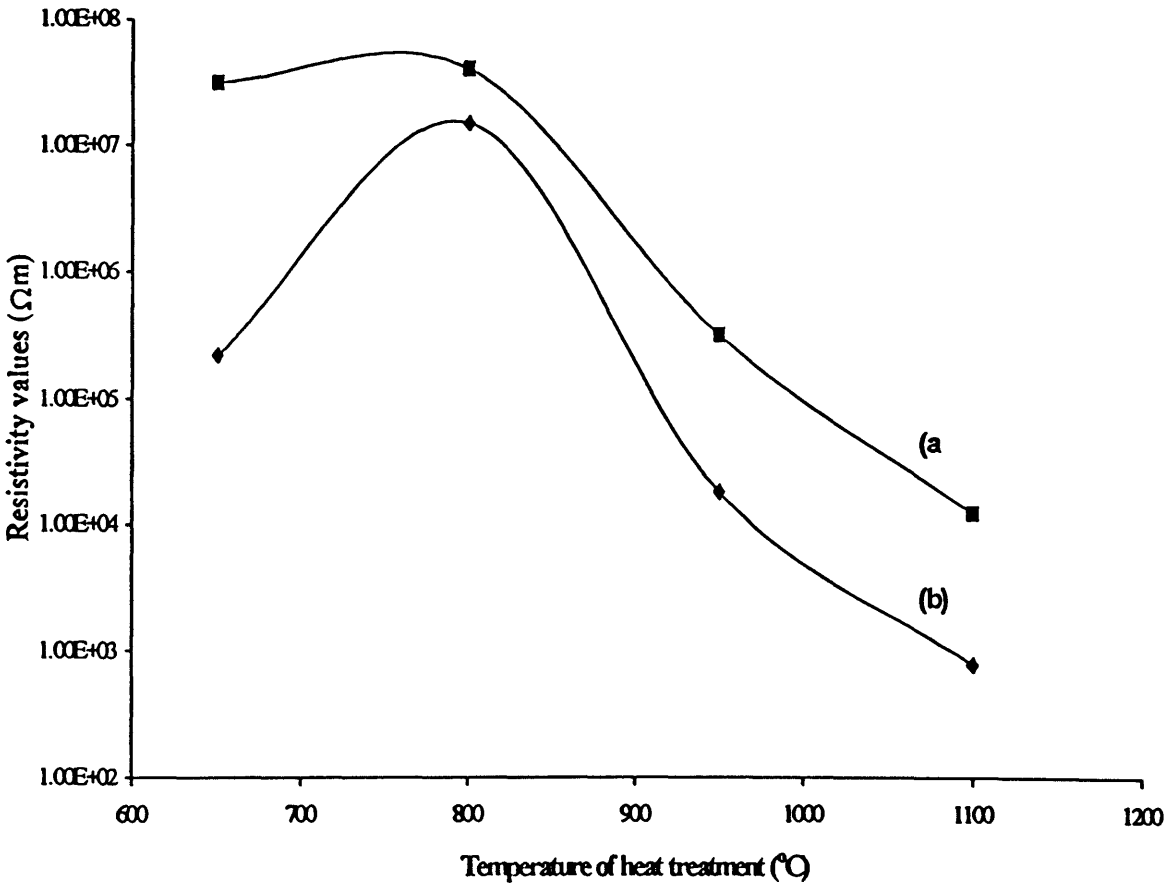


Figure 3.18 Resistivity values versus processing temperatures of glass-ferrites with 2.5% glass added prepared by (a) Method A and (b) Method B.

3.3 SUMMARY AND CONCLUSIONS

Sol-gel Ni-Zn ferrites with varying amounts of lead borosilicate glass additive were successfully prepared by two methods. Method A was a novel preparation involving both the ferrite and glass precursor gels. Method B formed the ferrite powder first and then mixed it with the glass precursor gel. The glass-ferrite precursors were processed at temperatures of 650, 800, 950 and 1100°C to yield the glass-ferrites.

FTIR spectroscopy confirmed glass B–O, Si–O and Si–O–B and ferrite bonds. PXRD patterns of the glass-ferrites indicated the presence of two phases: (1) crystalline inverse spinel phase due to the magnetic ferrite and (2) amorphous phase due to the lead borosilicate glass. At higher ageing temperatures, the amorphous phase disappeared and an additional crystalline phase of SiO_2 (cristabolite) appeared. This is a common feature in lead borosilicate glass heated at *circa* 800°C.

Lattice constants (**a**-values) and particle sizes were estimated from the glass-ferrite's PXRD patterns. The lattice constants were larger than that of glass-free ferrite (by up to 3%) indicating lattice expansions caused, possibly, by dissolution of the ferrite into the glass melt and movement of Pb^{2+} ions into the ferrite structure. The particle sizes of the glass-ferrites also differed significantly from the size of glass-free ferrite particles.

The SEM images of the glass-ferrites demonstrated the remarkable development in the particle structure of the ferrite. Glass-free ferrite possessed irregular shape and sized particles with abundant intragranular porosity. The glass-ferrite's particles showed no intragranular porosity and they were regular shaped and sized. The particles possessed a glossy appearance due to the insulating covering of the glass. At the high processing temperatures, the glass appeared to connect the particles together.

VSM measurements of the glass-ferrites were obtained to determine whether the magnetic properties of the ferrites had altered with glass addition. The results showed increased saturation magnetisation values of the ferrites with glass addition when the glass-ferrites were calcined at relatively low temperatures. It is possible that an initial dissolution of Zn^{2+} ions into the glass melt gave a Ni-richer ferrite (and hence, a higher M_s value, see **Figure 2.24, Chapter 2**). At higher calcining temperatures, the saturation magnetisation values of the glass-ferrites decreased. This may be

associated with a large dissolution of Zn^{2+} ions (to leave just $NiFe_2O_4$ which has a low M_s value).

The Mössbauer spectra of the glass-ferrites did not show any significant differences from the Mössbauer spectra of the corresponding glass-free ferrites. All the spectra exhibited a collapsed doublet of sextets, which is expected for a Ni-Zn ferrite. The Mössbauer spectra of the glass-ferrites processed at 800°C gave an extra inner doublet, which was attributed to superparamagnetism by clusters of small particles. At liquid nitrogen temperature this inner doublet disappeared.

Resistivity measurements recorded spectacular increases in resistivity of the ferrite on glass addition when the glass-ferrite was formed at low processing temperatures (650 and 800°C). The resistivity values fell at higher temperatures, which may be associated with the precipitation of cristobalite, the loss of lead in the glass by evaporation and agglomeration of the particles.

In summary, the electrical and magnetic properties of sol-gel Ni-Zn "soft" ferrites prepared in Chapter 2 have been improved by glass addition. The microstructure of the ferrite has also been improved with the notable loss of intragranular porosity.

3.4 EXPERIMENTAL DETAILS

3.4.1 Instrumentation

Elemental analyses, infrared spectra, Mössbauer spectra, PXRD patterns, VSM measurements, resistivity measurements and SEM images were recorded as outlined in **Section 2.4.1 of Chapter 2.**

3.4.2 Starting Materials

The following reagents were used as received from Aldrich: dodecanoic acid, ferric acetylacetonate, lead nitrate, nickel acetate tetrahydrate, 65% nitric acid, potassium hydroxide, tetraethoxysilane, tetrabutylammonium hydroxide (40% aqueous), tributoxyborane and zinc acetylacetonate. Triply distilled water, 99% *iso*-propylalcohol (Aldrich), 95% ethanol, 99% acetone (Aldrich) and Na/benzophenone dried toluene were used as solvents.

The lead borosilicate glass was prepared by a sol-gel technique involving lead bis(dodecanoate) ($Pb(O_2CC_{11}H_{23})_2$), tetraethoxysilane (TEOS) and tributoxyborane (TTB) as the alkoxide starting materials.
Lead bis(dodecanoate) was prepared by a standard literature method with a slight modification as described below.[111]

3.4.3 Preparation of Lead bis(dodecanoate), $Pb(O_2CC_{11}H_{23})_2$

Dodecanoic acid (12.107g, 60.04 mmol) was dissolved in hot 95% ethanol (100mls). Potassium hydroxide (3.366g, 60.03 mmol) was added. Lead nitrate (9.943g, 30.02 mmol) dissolved in the minimum of water (10mls) was slowly added to the alcohol solution with constant stirring. The white precipitate which formed was washed thoroughly with water, ethanol and acetone. Recrystallisation from hot toluene gave lead bis(dodecanoate) (yield 88%). Found: C, 47.4; H, 7.6%. $C_{24}H_{46}O_4Pb$ requires: C, 47.6; H, 7.65%. FTIR (KBr) ν_{max}/cm^{-1}: 2954(s), 2920(vs), 2847(vs), 1561(m),

1537(m), 1510(vs), 1471(s), 1460(s), 1415(s), 1401(m), 1350(s), 1328(m), 1306(m), 1280(m), 1250(m), 1219(m), 1190(m), 1115(s), 1081(s), 976(s), 930(s), 870(s), 820(s), 775(s), 729(m), 715(m), 705(m), 691(m), 653(s), 650(s).

3.4.4 Preparation of Standard Lead Borosilicate Glass

Lead bis(dodecanoate) (0.606g, 1.00 mmol), TEOS (0.42 mls, 1.87 mmol) and TTB (0.29 mls, 1.06 mmol) were added to 75% (v/v) toluene/ 2-propanol (50mls). The suspension was heated at reflux until it became clear. Tetrabutylammonium hydroxide (40% aqueous) (0.70 mls) was added to the solution, which immediately became cloudy. The solution was stirred at room temperature for 16 hours. Removal of solvents *via* a rotary evaporator yielded a colourless viscous gel. Firing this gel spread on an alumina plate at 600°C in air gave a clear glass. The ratio of the glass is 60:10:30 by weight of the oxide in the form $PbO:B_2O_3:SiO_2$.

The lead borosilicate glass gel precursor was added to the ferrite by two ways. The first way (Method A) involved the cogelling of both the glass and Ni-Zn ferrite precursors. The second way (Method B) heterogeneously mixes the glass precursor and a prefired ferrite powder. The ferrite used for both methods is the sol-gelled Ni-Zn ferrite with the rough stoichiometry $Ni_{0.5}Zn_{0.5}Fe_2O_4$, i.e. NiZnSG3. This ferrite's preparation is described in **Section 2.4.3.2, Chapter 2.**

3.4.5 Method A: Preparation of Cogelled Glass-Ferrite

Different percentages of weight of glass to ferrites were used, namely 2.5%, 5.0%, 10% and 36%. The procedure described below is for the preparation of 36% glass to ferrite.

Lead bis(dodecanoate) (0.606g, 1.00mmol), TEOS (0.42mls, 1.87mmol) and TTB (0.29mls, 1.06mmol) were used to prepare the glass precursor as described already. Ferric acetylacetonate (2.826g, 8.00mmol), nickel acetate tetrahydrate (0.498g, 2.00mmol) and zinc acetylacetonate monohydrate (0.528g, 2.00mmol) were the starting materials for forming the ferrite precursor as described in **Chapter 2.** The glass gel was added to the wet ferrite precursor with 2-propanol used as the medium. This solution was heated with constant stirring until it evaporated to 20mls. A brown

non-magnetic powder was formed after drying overnight in a 60°C oven. Heat treatments of 650, 800, 950 and 1100°C produced magnetic powders. Each of these magnetic powders was free from residual carbon and hydrogen (found: C, 0.2; H, 0.1%).

The 2.5%, 5.0% and 10.0% glass-ferrites were synthesised by the same general method. **Table 3.10** lists the amounts of reagents used.

Table 3.10 Amounts of starting materials

Reagent	2.5% glass	5% glass	10% glass
$Pb(O_2CC_{11}H_{23})_2$	0.042g, 0.07mmol	0.085g, 0.14mmol	0.168g, 0.28mmol
TEOS	0.029mls, 0.13mmol	0.059mls, 0.26mmol	0.117mls, 0.52mmol
TTB	0.020mls, 0.07mmol	0.040mls, 0.15mmol	0.081mls, 0.29mmol

Elemental analyses for the glass-ferrites are given in **Table 3.11**. These are for the glass-ferrites processed at 650°C. However, the other glass-ferrites processed at the higher temperatures gave roughly the same elemental analyses and hence the results in **Table 3.11** are applicable to all the glass-ferrites aged at different temperatures.

Table 3.11 Elemental analyses of the glass-ferrites.

Name of Glass-Ferrite	% of Glass	Expected				Found			
		% Fe	% Ni	% Zn	% Pb	% Fe	% Ni	% Zn	% Pb
CG1	36	34.5	9.1	10.1	14.6	34.1	8.9	9.9	14.1
CG2	10	42.7	11.2	12.5	5.0	42.0	11.0	12.15	5.0
CG3	5	44.7	11.8	13.1	2.6	44.2	11.6	12.9	2.75
CG4	2.5	45.8	12.05	13.4	1.3	45.6	11.7	13.1	1.3

3.4.6 *Method B: Preparation of Heterogeneous Mixed Glass-Ferrite*

This method prepared glass-ferrites with 2.5%, 5%, 10% and 36% glass additives by weight. The amounts of lead borosilicate and ferrite starting materials for each glass additive were the same as in Method A. This method prepared the standard lead borosilicate glass precursor as described previously. The ferrite was prepared by the sol-gel technique in Chapter 2 to produce a magnetic NiZnSG3 at room temperature. This ferrite was calcined at 1100°C.

The ferrite powder and glass gel was mixed in 2-propanol (30mls). The mixture was sonicated for 3h. The propanol was removed on a rotary evaporator affording a magnetic powder. This was processed at 650, 800, 950 or 1100°C. **Table 3.12** gives the elemental results of these glass-ferrite powders.

Table 3.12 Elemental results of glass-ferrites produced by Method B

Name of glass-ferrite	% of glass	Expected				Found			
		% Fe	% Ni	% Zn	% Pb	% Fe	% Ni	% Zn	% Pb
HM1	36	34.5	9.1	10.1	14.6	34.3	8.9	10.0	14.2
HM2	10	42.7	11.2	12.50	5.0	42.4	11.0	12.25	4.6
HM3	5	44.7	11.8	13.1	2.6	44.4	11.5	12.7	2.7
HM4	2.5	45.8	12.05	13.4	1.3	45.3	11.8	13.1	1.7

CHAPTER 4

A STUDY OF COMPOUNDS CONTAINING Fe-O-B, Fe-O-Si AND B-O-Si LINKAGES

4.1 INTRODUCTION

Chapter 3 discussed the homogenous and heterogeneous mixing of lead borosilicate glass precursors with Ni-Zn ferrite powders to form magnetic materials with high electrical resistivities. SEM images of the materials explicitly revealed the glass coating on each ferrite particle. Results from magnetic measurements suggested that some interaction of the glass into the ferrite's lattice had occurred during heat treatment. Therefore, linkages such as Fe–O–B, Fe–O–Si, B-O-Si and Fe–O–Pb may exist in these materials. This introduction discusses the synthesis and structural study of compounds containing Fe-O-B, Fe-O-Si and B-O-Si linkages. The present work reports attempts to synthesis novel Fe-O-B and Fe-O-Si containing compounds and compounds with B-O-Si linkages which also contain iron.

4.1.1 General Considerations of Systems Containing Fe-O-B Linkages.

4.1.1.1 Synthesis of Compounds with Fe-O-B Bonds.

Several minerals are known to exist that involve Fe-O-B bonding. These include iron(III) borate ($FeBO_3$),[112] iron borate oxide $Fe_3(BO_3)O_2$[112] and iron(III) borate oxide $Fe_3(BO_3)O_3$[112]. While these materials are interesting in their own right, they will not be considered further in the present discussion.

Only six molecular compounds containing Fe-O-B units have been structurally characterised by X-ray crystallography. The compounds are shown in **Figure 4.1**.

The metalloxaborane compound $[\eta^6\text{-}C_6(CH_3)_3H_3]FeOB_8H_{10}$ **(1)** was prepared as a side product from the reaction of iron vapour with mesitylene and decaborane, $B_{10}H_{14}$, in a metal atom reactor, reaction **[1]**.[113]

$$B_{10}H_{14} + \eta^6\text{-}C_6(CH_3)_3H_3 + Fe \xrightarrow{\Delta} [\eta^6\text{-}C_6(CH_3)_3H_3]FeOB_8H_{10} \quad \textbf{(1)} \qquad \textbf{[1]}$$

The yield was very low (< 1%).[113]

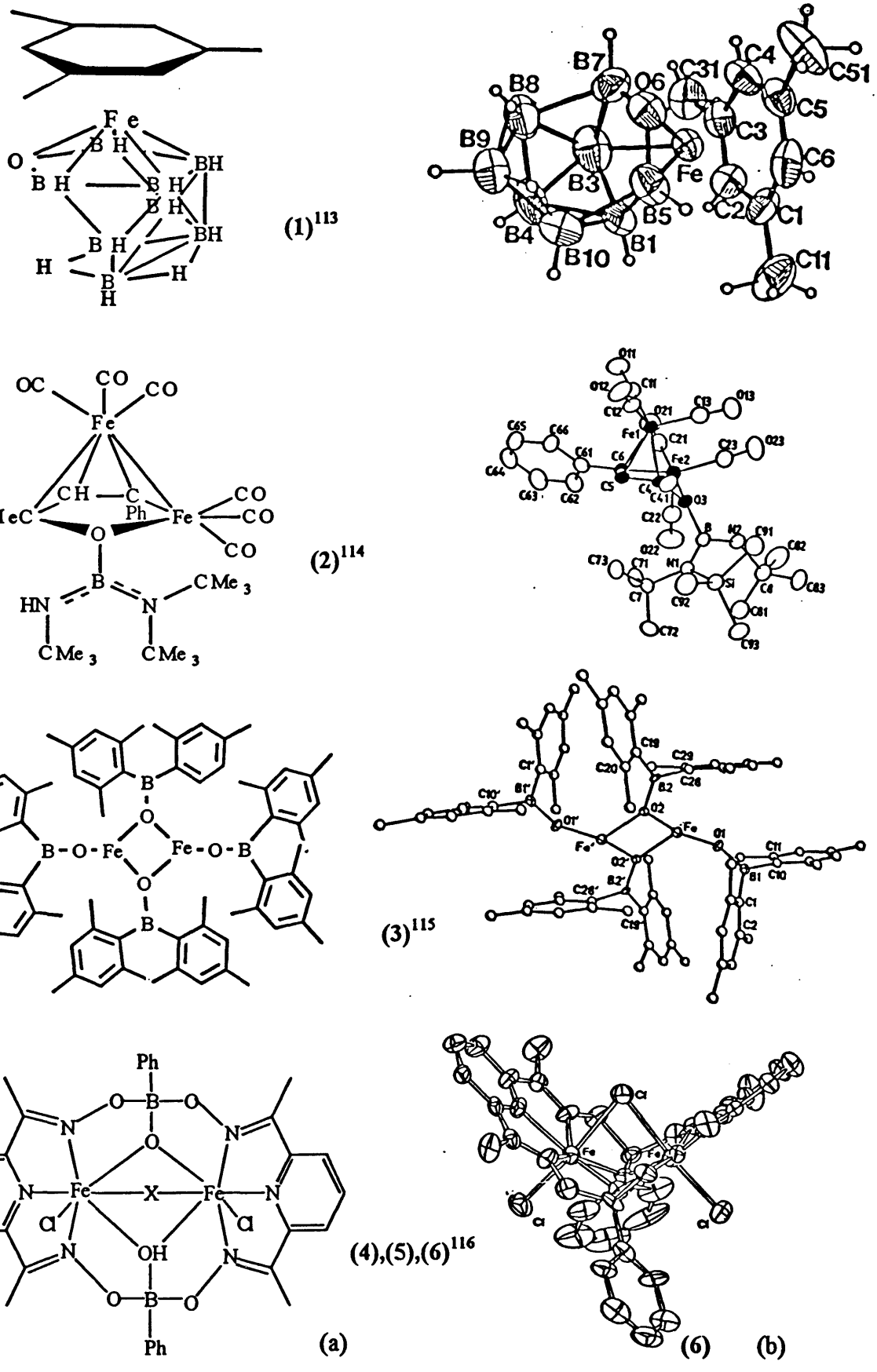
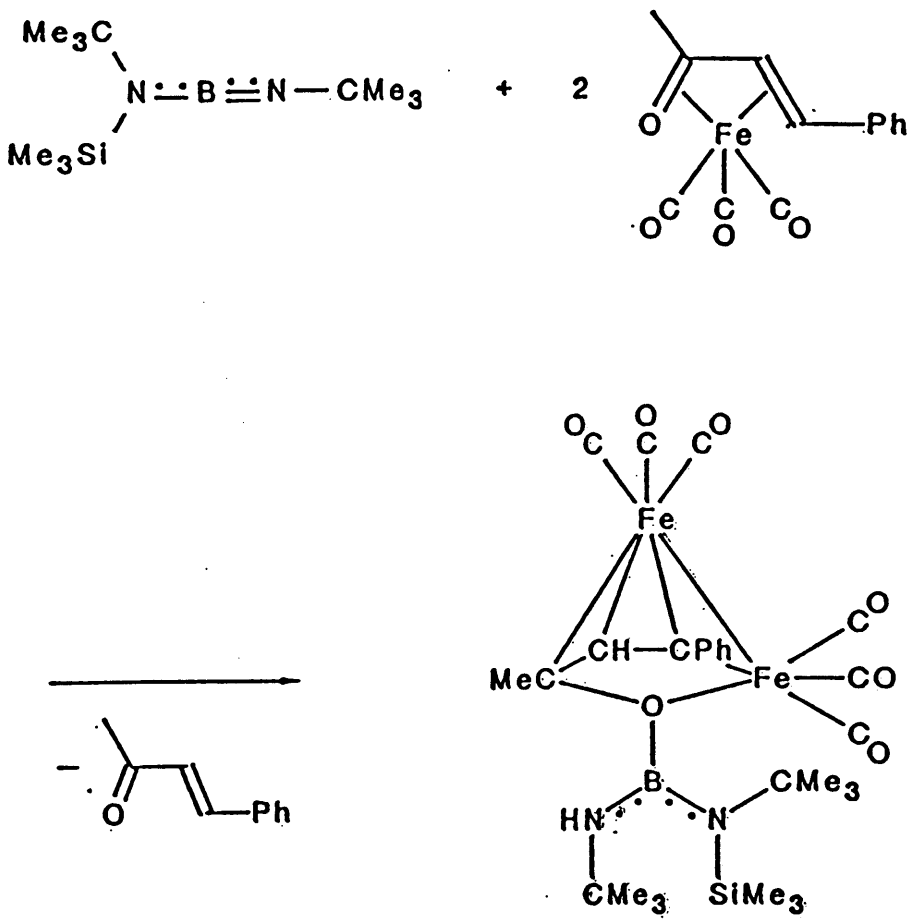


Figure 4.1 (a) Schematic drawings and (b) molecular structures of compounds containing Fe-O-B units. Note, X = OCH_3, for (4); OH for (5) and Cl for (6).

Compound (1) was the first example of a metalloxaborane cluster.[113]

Compound (2) was synthesised according to equation [2].[114] The amino(imino)borane, $Me_3Si(Bu^t)N\text{-}B{=}NBu^t$, was reacted with (benzylideneacetone) tricarbonyliron in a 1:2 molar ratio to form the product in 50% yield with the loss of a benzylideneacetone.[114] The complex structure is based on a pentagonal pyramid with the tricarbonyliron as the apex and a non-planar pentagonal base. It is noteworthy that there is no bond between the apex iron and the oxygen atom.[114]



[2]

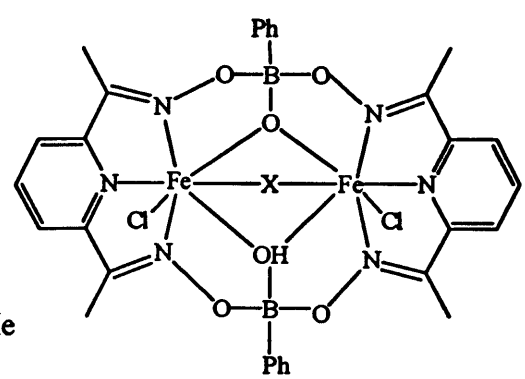
The reaction of dimesityleneboronous acid (Mes_2BOH) with the iron(II) bis(trimethylsilyl)amide, $Fe[N(SiMe_3)_2]_2$ in a 2:1 molar ratio afforded **(3)** with loss of hexamethyldisilazane as shown in reaction **[3]**.[115]

$$2Mes_2BOH + Fe[N(SiMe_3)_2] \xrightarrow{-4HN(SiMe_3)_2} \tfrac{1}{2}[Fe(OBMes_2)(\mu\text{-}OBMes_2)]_2 \quad \textbf{(3)} \qquad \textbf{[3]}$$

The sterically hindering group on the boronous acid is used specifically to halt polymerisation of the final product (*via* $-OBR_2$ bridging).[115] The degree of association was limited to two. Compound **(3)** is the first example of a homoleptic transition-metal boryloxides.[115] Another example is $[Mn(OBTrip_2)(\mu\text{-}OBTrip_2)]_2$ (where Trip = 2,4,6-$Pr^i_3C_6H_2$) which was prepared in a similar reaction to reaction **[3]**.[115] The iron atom centres in **(3)** are tricoordinated with bonding occurring between one terminal boryloxide ligand and two bridging boryloxide ligands. The Fe-O bonding was described as mainly ionic with little evidence of a π-contribution.[115]

Compound **(4)** was prepared from "a self-assembly reaction"[114] between phenylboronic acid, 2,6-diacetylpyridinedioxime, sodium methoxide and ferric chloride hydrate in a methanol solution.[116] A possible reaction pathway probably was *via* dehydration and elimination of HCl, as shown in equation **[4]**.

$$2FeCl_3 + 2PhB(OH)_2 + 2 \text{ (diacetylpyridinedioxime)} \xrightarrow[-2H_2O/-3HCl]{NaOMe/Methanol}$$



X = OMe

(4)

[4]

Compound (4) to (6) all use the 2,6-diacetylpyridinedioxime ($DAPDH_2$) ligand. Several reports of this ligand bonding to transition elements have been published.[117-120] The oxime segment of the ligand may coordinate in four ways as shown below in Figure 4.2. Coordination by modes (a) and (c) are observed most frequently.[121]

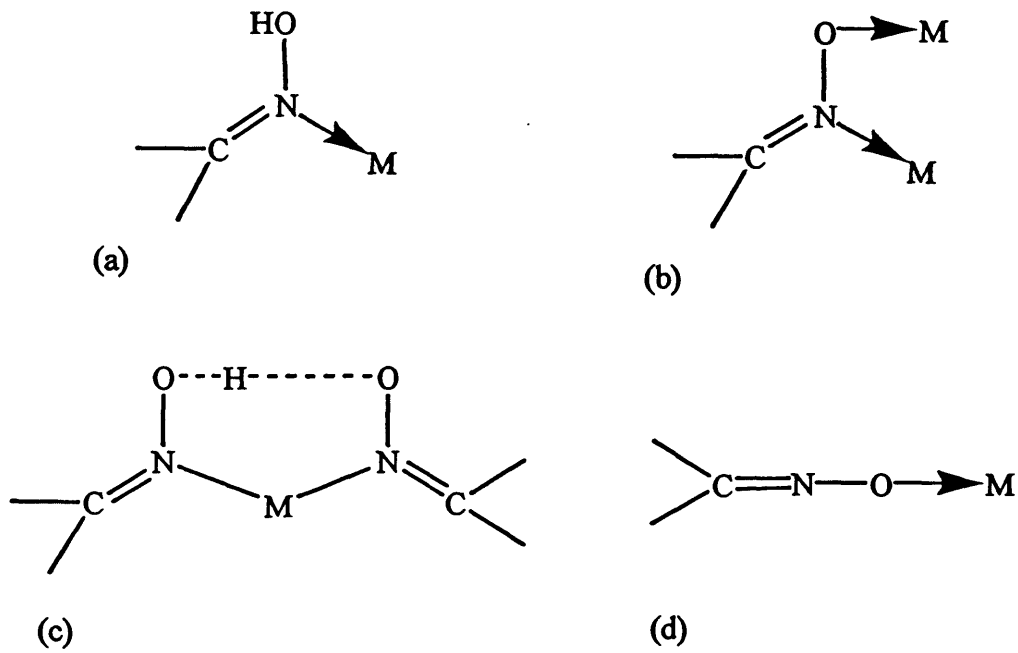


Figure 4.2 Various coordination modes of the oxime ligand to metal (M).[120]

Compound (4) has several interesting structural features. The metal atoms are in their ferric state and are seven-coordinated (pentagonal bipyramidal coordination). They also share three bridging groups. The boron atom is four-coordinated (tetrahedral coordination). One of the bridging oxygen atoms which is bonded to a boron is protonated. Compounds (5) and (6) have similar structures to (4) with the exception of the bridging group. Compound (5) has X = OH and was prepared by the recrystallisation of water-acetonitrile solution of (4) which had been reacted with pyridine.[116] Presumably, the hydrolysis of the methoxide group occurred *via* a pyridine adduct. Compound (6) has X = Cl and was formed in a similar fashion to compound (4) with the use of sodium hydroxide instead of sodium methoxide.[116]

The crystal structure of $Ni(DAPD)_2$ has been reported.[117] The ligand stabilises the Ni(IV) oxidation state.[117] The complex is planar with coordination through nitrogen.

Several copper complexes with this ligand have also been prepared and structurally characterised by X-ray crystallography, namely: $Cu(DAPDH_2)Cl_2$;[118] $[Cu(DAPDH)]_2[BF_4]_2$[119] and $[Cu(DAPDH)]_2Cl_2$.[120] The copper atom in the monomeric species is five coordinated with the Cu atom in the centre of a square pyramid consisting of a Cl and three N atoms in the base and an apical Cl. The dimeric species are four coordinated with a distorted square pyramidal shape at the copper.

4.1.1.2 Structural Studies of Compounds Containing Fe-O-B Linkages.

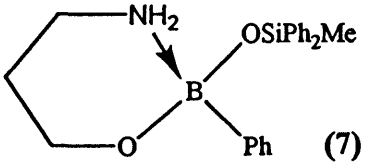
The structurally characterised compounds are listed in **Figure 4.1**. **Table 4.1** reports the relevant Fe-O-B distance and angle data of these compounds.

Table 4.1 Selection of Bond Length (Å) and Bond Angle (°) data for Compounds Containing Fe-O-B linkages.

Compound	d(B-O)	d[Fe-O(-B)]	α(B-O-Fe)	Reference
(1)	1.423(7)	1.942(3)	73.3(3)	113
	1.428(8)		73.4(3)	
(2)	1.467(4)	2.069(2)	-	114
(3)	1.361(10)[a]	2.027(5)[a]	143.2(5)[a]	115
		1.986(5)[a]	107.3(5)[a]	
	1.354(11)[b]	1.821(5)[b]	143.9(5)[b]	
(4)	-	2.00(1)	125(1)	116
	-	2.067(9)	120(1)	
(5)	-	1.976(2)	121.3(2)	116
	-	2.022(2)	122.2(2)	
(6)	-	1.981(4)	123.4(5)	116
	-	1.990(5)	120.2(6)	

[a] = bridging B-O-Fe bonding, [b] = terminal B-O-Fe bonding.

In compound (1), the B-O distances are essentially equal [1.423(7) and 1.428(8)Å][113] and are similar to boron-oxygen bond lengths recorded in cluster complexes e.g. 3-(η^5-C_5H_5)Co-8-$OCOCH_3$-1,2-$C_2B_9H_{10}$ [1.453(7)Å][122] and 8-C_2H_5O-9,9-$(PPh_3)_2$-6-9-$SPtB_8H_9$ [1.476(24)Å][123] which contain an exopolyhedral boron-oxygen single bond. The B-O bond lengths in (1) are longer than typical single boron-oxygen distances involving three-coordinated boron, for example in (3) [1.361(10) and 1.354(11)Å]. This is expected as the oxygen atom in [η^6-$C_6(CH_3)_3H_3$][$FeOB_8H_{10}$] (1) is involved in multicentre bonding in the polyhedral cage. A typical B-O distance with four-coordinated boron systems, such as borosilicate compounds with amine additions, as shown in **Figure 4.3** is 1.439(4)Å.[124]



(7)

$d(B\text{-}O_{Si}) \sim 1.439(4)$Å

Figure 4.3 Structure of amine coordinated borosilicate.[124]

The Fe-O-B angles for (1) are very small and they are indicative of the strain at the oxygen atom in the cluster system.

The B-O bond length observed in (2) is [1.467(4)Å] which is long for a three-coordinate boron site.[114] It was suggested that the boron atom here has a 3.5 bond order because of the resonating double bond in the amino(imino)borane. Hence, an extra electron enters an anti-bonding orbital of the boron-oxygen system and the bond length increases.

Compound (3) contains two different boroxide ligands, namely bridging and terminal.[115] The boron-oxygen distances are typical of tricoordinated boron with values of 1.361(10)Å for the bridging boron and 1.354(11)Å for the terminal boron. The bridging B-O bond length is slightly longer due to the higher coordination number of the bridging oxygen.[115] The terminal Fe-O-B angle is large [143.9(5)°] and may be suggestive of Fe-O π-bonding that involves overlap of the metal d-orbitals and the oxygen lone pairs.[125] However, other evidence suggests that pronounced ionic bonding in the Fe-O system is responsible for the observed angle (as more polar

Fe-O bonds imply a relaxation of the angular restrictions imposed by orbital overlap).[115] The iron-oxygen bond lengths [2.027(5) and 1.986(5)Å for bridging B-O-Fe bonding, 1.821(5)Å for terminal B-O-Fe bonding] are typical.

Compounds (4) to (6) have similar structures with slight differences in one of the bridging groups.[116] As mentioned previously, the iron atoms are seven coordinated with the three N atoms from the dioxime with the two bridging O atoms making up the pentagonal equatorial plane and the X atoms with the other bridging groups [methoxide in (4), hydroxide in (5) and chloride in (6)] being in axial positions. The Fe-O(-B) bonds (mean = 2.034Å, 1.999Å and 1.986Å, respectively) are similar with a small increase observed in (4).[116] The bridging oxygen atoms are almost completely trigonal planar with all the Fe-O-B angles around 120° for the three compounds. There were no data given for the B-O bond distances.

4.1.2 General Considerations of Systems Containing Fe-O-Si Linkages.

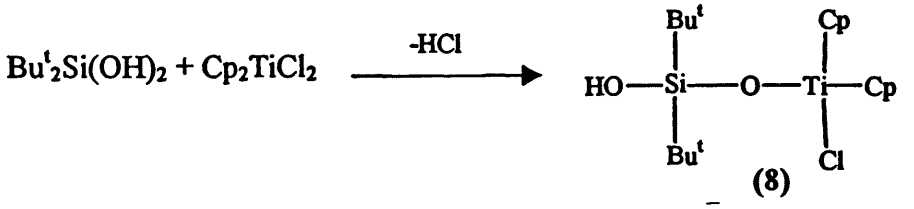
A number of minerals containing Fe-O-Si bonds exist, **Table 4.2**. Molecular compounds, which are more directly relevant to the present work, are virtually unknown.

Table 4.2 A list of naturally occurring iron silicates.

Name	Formula	Name	Formula
Iron(II) silicate[126]	$FeSiO_3$	Ringwoodite[131]	$FeMgO_4Si$
Iron oxide silicate[127]	$Fe_7O_6(SiO_4)$	Feriaksite[132]	$Fe_2K_2Na_2O_{20}Si_8$
Pyroxferroite[128]	$Fe_7O_{21}Si_7$	Emeleusite[133]	$Fe_2Li_2Na_4O_{30}Si_{12}$
Iron lithium silicate[129]	$FeLiO_6Si_2$	Deerite[134]	$Fe_9H_5O_{25}Si_8$
Acmite[130]	$FeNaO_6Si_2$	Grunerite[135]	$Fe_7H_2O_{24}Si_8$

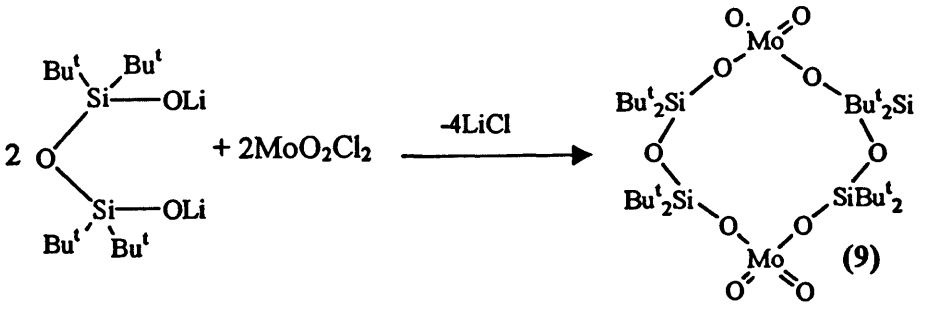
A recent review of metallosiloxanes (containing M-O-Si units) derived from silanediols, disilanols, silanetriols and trisilanols was published by Roesky *et al.*.[136] Details of numerous metallosiloxanes of first row transition metals were given for every element except iron. The metallosiloxanes were prepared using several synthetic routes. These are listed below with a specific example:

(1) reactions involving elimination of HX (X = Cl or Br);[137]



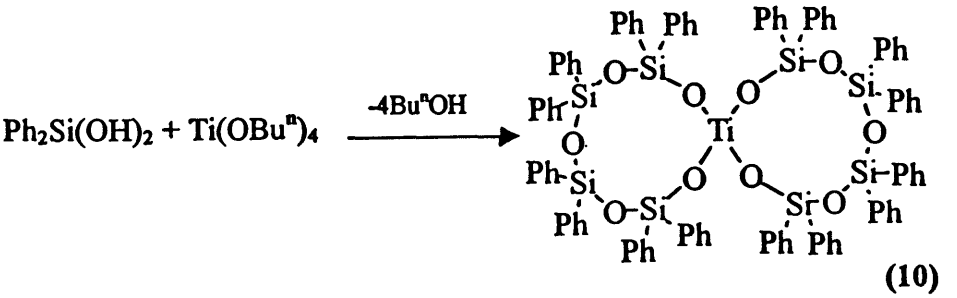
(8) [5]

(2) reactions involving loss of MCl (M = Group 1 metal);[138]



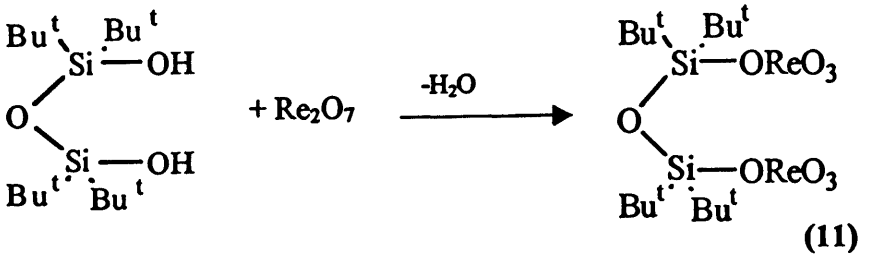
(9) [6]

(3) reactions involving elimination of ROH (R = organic group);[139]



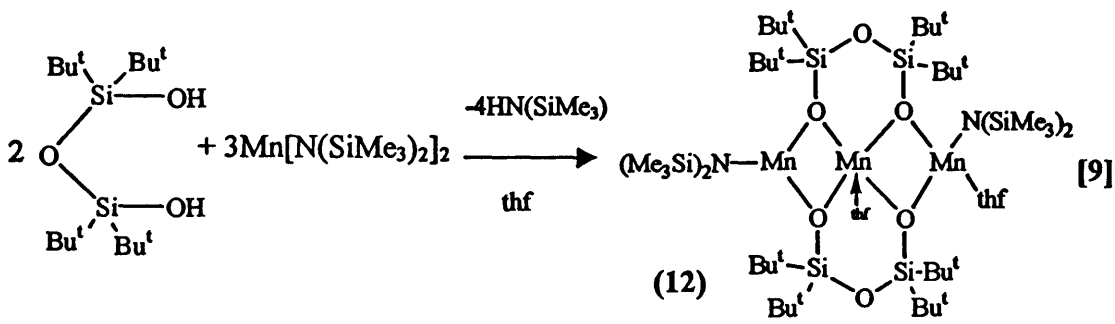
(10) [7]

(4) dehydration reactions;[140]



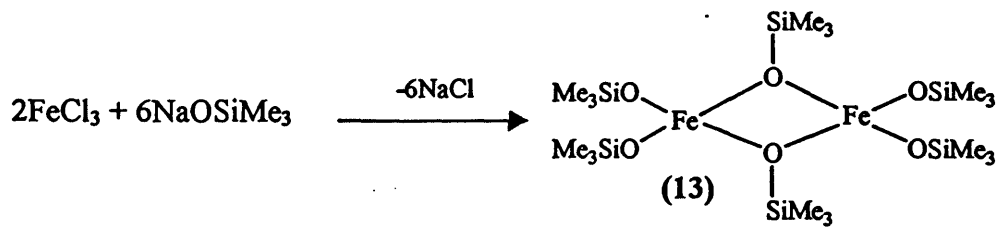
(11) [8]

(5) reactions involving loss of $HN(SiMe_3)_2$ {as in the synthesis of $[Fe(OBMes_2)(\mu\text{-}OBMes_2)]_2$};[141]



[9]

It is therefore surprising that despite the range of synthetic methods, there was no report of a metallosiloxane with Fe-O-Si linkages in Roesky's review. However, in the early sixties, siloxanes of iron were reported from the reaction between ferric chloride with group I metal silanolates in a 1:3 molar ratio as shown in equation [10].[142]



[10]

Schmidbauer and Schmidt reported dimeric tris(trimethylsiloxy)iron **(13)** was produced as yellow-green, wax-like crystals with a melting point of 179-181°C.[142] The material was, however, susceptible to hydrolysis with resultant decomposition to ferric hydroxide and trimethylsilanol.[142] Dimeric tris(triethylsiloxy)iron was also reported to form in a similar reaction.[143]

Addition of another two moles of sodium trimethylsilanolate yielded sodium tetrakis(trimethylsiloxy)ferrate **(14)** as an air-stable yellow crystalline solid.[142,144] The compound decomposed at 200°C to give Fe_2O_3.[145] Similar compounds were prepared from $Li[OSiMe_3]$, $K[OSiMe_3]$ and $Me_4Sb[OSiMe_3]$.[145]

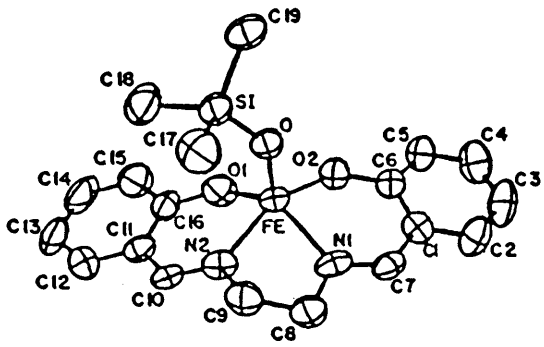


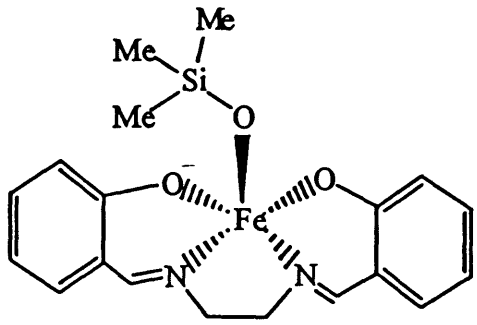
[11]

Most of the physical evidence for these compounds came from infrared spectra and there were no crystallographic data. Strong peaks between 900 and 1000 cm^{-1} were

assigned to vibrational modes of Fe-O-Si bonds.[142] (Attempts to repeat the reaction between ferric chloride and group I metal silanolates were unsuccessful in this present work, see **Appendix F**).

A search in the Cambridge Crystallographic Database revealed only one structurally characterised molecular compound with a Fe-O-Si linkage. The compound, $[Fe(SALEN)]OSi(CH_3)_3$ (15), is shown in **Figure 4.4**.[146]





(15)

Figure 4.4 Structure of $[Fe(SALEN)]OSi(CH_3)_3$ (15).[146]

Compound (15) was prepared from the reaction between $[Fe(SALEN)]_2O$ (where SALEN is the condensation product of salicylaldehyde and ethylenediamine) and excess hexamethyldisilazane in toluene solution under anaerobic conditions.[146] The product precipitated as bright red-orange air-stable crystals after addition of petroleum ether to the toluene solution. The authors made no attempts to rationalise the reaction mechanism but did mention that a trimethylsilyl group may replace an Fe(SALEN) moiety.[146] This type of reaction has been investigated before with vanadyl complexes and hexamethyldisilazane to form μ-oxo silyl compounds.[147] The driving force for these systems appears to be the formation of a silicon-oxygen bond. Compound (15) was extremely inert to aerial oxidation and hydrolysis and did not show any decomposition in solution for up to two weeks.[146] The structure of (15) contains an iron atom which is five-coordinate with a square-pyramidal base. This feature is common in planar iron macrocyclic systems such as iron phthalocyanines. The authors described the SALEN moiety as adopting "the inverted umbrella structure",[146]

which is also found for iron(III)SALEN chloride monomer. Relevant bond angles and distances in (15) and other related compounds which contain oxygen bridged Fe(SALEN) species are given in **Table 4.3**. Note that the crystallography data for $[Fe(SALEN)]_2O.2py$ (16) and $[Fe(SALEN)]_2O$ (18) are very poor.

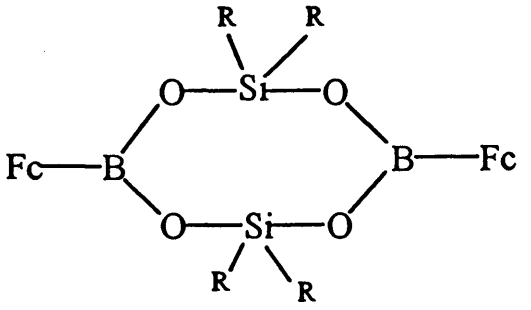
Table 4.3 Selection of Bond Length (Å) and Bond Angle (°) Data for Fe-O systems.

Compound	d[Fe-O(-M')]	d(Si-O)	α[Fe-O(-M')]	Ref.
$[Fe(SALEN)]OSiMe_3$ (15)	1.834(6)	1.633(6)	142.7(4)	146
$[Fe(SALEN)]_2O.2py$ (16)	1.80(1)	-	139.1(9)	148
$[Fe(SALEN)]_2O.CH_2Cl_2$ (17)	1.794(9)	-	142.4(5)	149
$[Fe(SALEN)]_2O$ (18)	1.78(1)	-	144.6(6)	148

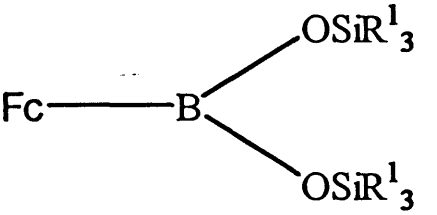
According to **Table 4.3**, the replacement of a Fe(SALEN) group with a trimethylsilyl group has little effect on the iron atom in the structure of complex (15). For example, the Fe-O bonds in (15) and (17) are, within 3 x e.s.d.s, the same and the Fe-O-Si angle in (15), 142.7°, falls within the range of values observed for the other μ-oxo$[Fe(SALEN)]_2$ species. Moreover, data from magnetic susceptibilities and UV-visible spectra reported no discernible change in the electronic structure of the iron due to the silyl group.[146]

4.1.3 *General Considerations of Borosilicate Compounds.*

The synthesis and characterisation of three novel borosilicate compounds are discussed in this chapter. These compounds contain Fe, B and Si atoms but do not have Fe-O-Si or Fe-O-B bonds. The compounds were derived from ferrocenylboronic acid and have the general formulae $[(FcBO)_2(R_2SiO)_2]$ and $[FcB(OSiR^1{}_3)_2]$, where Fc = $CpFe(C_5H_4)$, as shown below.



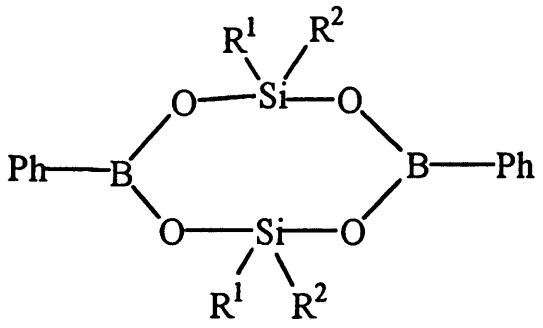
R = Bu^t (19) or Ph (20)
Fc = $CpFe(C_5H_4)$



R^1 = Ph (21)
Fc = $CpFe(C_5H_4)$

Therefore, this section of the introduction to this chapter will be concerned with compounds of the types: (a) $[R^1B(OSiR_3)_2]$, R, R^1 = alkyl or aryl group and (b) cyclic borosilicates containing two boron atoms and four B-O-Si linkages in eight-membered rings. Known compounds, types (a) and (b) are listed below and in **Figure 4.5**.

$R^1B(OSiR_3)_2$ $\{R^1 = Me, R = Et\}$[150], $\{R^1 = Pr^n, R = Me\}$[151], $\{R^1 = Ph, R = Me\}$[151,152], $\{R^1 = Ph, R = Ph\}$[152,153,154], $\{R^1 = Br, R = Et\}$[150], $\{R^1 = CF_3C_2H_4, R = Me\}$[151], $\{R^1 = m\text{-}CF_3C_6H_4, R = Me\}$[151], $\{R^1 = Ph, R = PhMe_2\}$[155], $\{R^1 = Ph, R = Ph_2Me\}$[152], $\{R^1 = Bu^n, R = Ph\}$[155], $\{R^1 = Bu^n, R = PhMe_2\}$[155], $\{R^1 = Bu^n, R = Ph_2Me\}$[155]



$\{R^1 = Ph, R^2 = Me\}$[156,157]
$\{R^1 = R^2 = Et\}$[156,157]
$\{R^1 = R^2 = Ph\}$[158]
$\{R^1 = R^2 = Bu\}$[159]

Figure 4.5 Cyclic borosilicate compounds with eight-membered rings.

Synthetic routes to these compounds may be divided into three categories.

(1) Dehydration reactions.

This is an efficient and popular route to compounds containing B-O-Si bonds. A Dean-Stark apparatus is generally employed to remove the water liberated during the reaction. Toluene and benzene are used as the reaction solvents since they form azeotropic mixtures with water. In a typical reaction $PhB(OSiPh_3)_2$ **(22)** is formed in 76% yield.[153,154]

$$PhB(OH)_2 + 2Ph_3SiOH \xrightarrow[-H_2O]{\text{Toluene, 24h}} PhB(OSiPh_3)_2 \quad \textbf{(22)} \qquad [12]$$

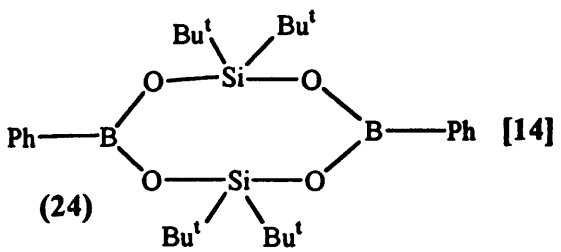
(2) Reactions involving elimination of HX (X = Cl or Br).

The route generally involves the reaction of a boric acid derivative with one or more Si-X bonds (X = Cl or Br).[160]

$$PhB(OH)_2 + 2Et_3SiBr \longrightarrow PhB(OSiEt_3)_2 + 2HBr\uparrow \quad \textbf{(23)} \qquad [13]$$

Borosilicates may also be prepared by the elimination of HX from a mixture of a haloborane and a silanol species as shown below.[159]

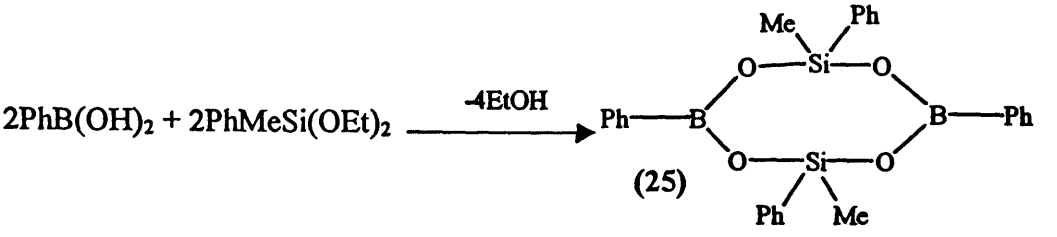
$$2PhBCl_2 + 2Bu_2^tSi(OH)_2 \xrightarrow[-4HCl]{CH_2Cl_2}$$



(24) [14]

(3) Reactions involving elimination of ROH (R = organic group)

The cyclic borosilicate $(PhBO)_2(Ph_2MeSiO)_2$ was prepared by this method in the reaction of phenylboronic acid with diethoxyphenylmethylsilane.[156,157]



(25) [15]

The synthetic route used in the present work was the dehydration reaction.

4.1.3.1 Structural Studies of Compounds Containing B-O-Si Linkages.

The list of borosilicate compounds in **Section 4.1.3** contains 16 compounds but only three have been structurally characterised by X-ray crystallography. The relevant B-O-Si distance and angle data of these compounds are given in **Table 4.4**. In all compounds, the boron atom occupies a trigonal planar sp^2 coordination. The silicon atom is four coordinate and tetrahedral (sp^3).

Table 4.4 Selection of Bond Length (Å) and Bond Angle (°) Data for Borosilicate Compounds.

Compound	d(B-O)	d[Si-O(-B)]	α(B-O-Si)	Ref.
$PhB(OSiPh_3)_2$ (22)	1.351(7)	1.644(4)	139.8(4)	154
	1.369(7)	1.626(3)	157.9(3)	
$(PhBO)_2(Ph_2SiO)_2$ (26)	1.348(5)	1.627(3)	145.3(3)	158
	1.345(5)	1.615(3)	160.9(3)	
$(PhBO)_2(Bu^t_2SiO)_2$ (24)	1.350(4)	1.630(3)	149.1(3)	159
	1.350(5)	1.631(2)	149.9(2)	

The range of B-O distances is 1.345(5)Å in (26)[158] to 1.369(7)Å in (22)[154]. The corresponding Si-O distances vary from 1.615(3)Å in (26)[158] to 1.644(4)Å in (22)[154]. The B-O-Si angles are all within the range 139.8(4)° [(22)][158] to 160.9(3)° [(26)][154]. The structures of compounds (22) and (26) are noteworthy as they contain two distinctly different values for chemically equivalent B-O-Si angles, *viz.* 139.8(4) and 157.9(3)° in (22)[154] and 145.3(3) and 160.9(3)° in (26)[158]. The different angles in compound (26), $(PhBO)_2(Ph_2SiO)_2$ contrasts with the situation in the related compound (24), $(PhBO)_2(Bu^t_2SiO)_2$, where the B-O-Si angles are essentially identical, 149.1(3) and 149.9(2)°.[159] The variation in B-O-Si angles has been rationalised in terms of the very shallow angle deformation energy curve for B-O-Si angles.[154]

4.1.4 Summary

Because of the iron-borosilicate interactions discussed in **Chapter 3**, further studies on these interactions are warranted. This present introduction discussed three different types of interactions between iron, boron and silicon namely those compounds involving Fe-O-B units; compounds involving Fe-O-Si linkages and compounds involving B-O-Si bonding. There are only six structurally characterised compounds with Fe-O-B linkages and only one compound with an Fe-O-Si linkage has been structurally characterised, i.e. [Fe(SALEN)]$OSiMe_3$ **(15)**.[146] Only one acyclic $[R^1B(OSiR^2_3)_2]$ and two cyclic $[(R^1BO)_2(R^2_2SiO)_2]$ borosilicates have been characterised by single X-ray crystallographic analysis.

4.2 Results and Discussion

This section is divided into three segments:

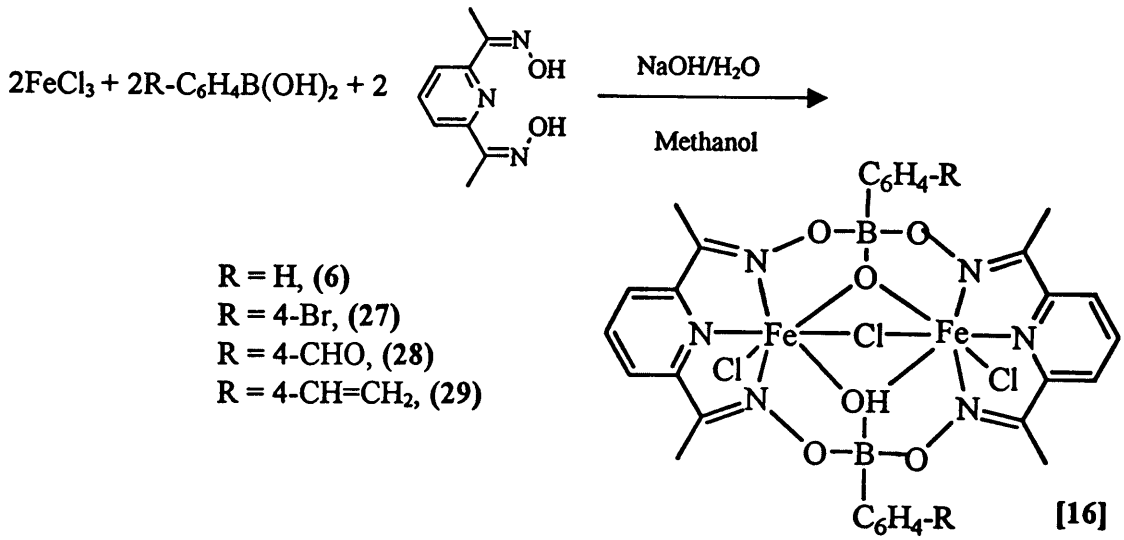
(1) synthesis and characterisation of compounds containing Fe-O-B linkages,
(2) synthesis and structural characterisation of $[Fe(SALEN)]_2O.CH_2Cl_2$ (17), a reagent in the attempted syntheses of Fe-O-Si compounds.
(3) synthesis and characterisation of novel borosilicate compounds which also contain iron sites.

4.2.1 Synthesis and Characterisation of Compounds Containing Fe-O-B Linkages, (6), (27), (28) and (29).

As previously mentioned, only six compounds with Fe-O-B units have been structurally characterised by X-ray crystallographic analysis. Three of these compounds [(4), (5) and (6), see **Figure 4.1**] were prepared by the reaction of ferric chloride with 2,6-diacetylpyridinedioxime and phenylboronic acid.[116] This section reports the synthesis of new compounds related to (4) to (6). The compounds were characterised by elemental (C, H and N) analyses, infrared spectroscopy and Mössbauer spectroscopy. Unfortunately, crystals of these compounds suitable for X-ray crystallographic analysis could not be obtained.

4.2.1.1 Synthesis of (6), (27), (28) and (29).

These compounds were prepared from ferric chloride, 2,6-diacetylpyridinedioxime and several boronic acids, equation [16] in methanol-water solution. The reactions were stirred for 16h at room temperature. Each compound formed a dark-red crystalline product from chloroform solution. All crystalline samples were air-stable.



[16]

Compounds (6), (27), (28), and (29) were isolated in yields of 30%, 15%, 20%, and 22%, respectively. These yields are low. Longer reaction times (> 16 hours) and higher reaction temperatures (> 60°C) did not significantly increase the yields and in some cases, the yields were reduced. The compounds were characterised by elemental analyses (C, H and N), infrared spectroscopy and Mössbauer spectroscopy. Compounds (6), (27), (28) and (29) gave satisfactory elemental analyses (C, H and N).

4.2.1.2 Infrared Spectra

Oxime C=N stretches are reported to occur in the region 1689 – 1471 cm^{-1}.[161] In the spectra of (6), (27), (28) and (29), characteristic oxime C=N peaks were observed between 1610 – 1476 cm^{-1}. This region also included aromatic and aliphatic C-C stretching.[161] B-O stretching absorptions have been assigned in the region 1380 – 1310 cm^{-1};[162] those of (6), (27), (28) and (29) occurred at 1371, 1374, 1376 and 1375 cm^{-1}, respectively. Significant bands near 3000 cm^{-1} in the spectra of the five compounds are indicative of aliphatic and aromatic C-H stretching, while the broad peak at 3400 cm^{-1} seen in all five compound's spectra suggests O-H stretches. Since the only difference between the compounds (6), (27) – (29) is the group attached to the phenyl group on the boronic acid, the spectra of the compounds should also differ by the characteristic frequencies of these groups. The formyl

group, C=O, stretch of (28) is observed at 1686 cm^{-1}, which is the approximate frequency for a C=O group conjugating with a phenyl ring.[161] The peak at 3076 cm^{-1} in the spectrum of (29) is assigned to the C-H stretching on its vinyl group.[161]

4.2.1.3 Mössbauer Spectroscopic Analysis

Mössbauer spectra were recorded for (6), (27), (28) and (29) at room temperature. Each spectrum showed an isomer shift (IS) and a quadrupole splitting (QS) typical of iron in a ferric state with a coordination number of seven.[271(a),271(b)] One such reported seven coordinated iron species, $NH_4HFeDTPA.H_2O$ [H_5DTPA = diethylenetriaminepentaacetic acid), have IS and QS values of 0.36 mm s^{-1} and 1.10 mm s^{-1}, respectively.[271(c)] These values are not unlike the present work's results which are listed in **Table 4.5**. The Mössbauer spectrum for (29) is shown in **Figure 4.6**.

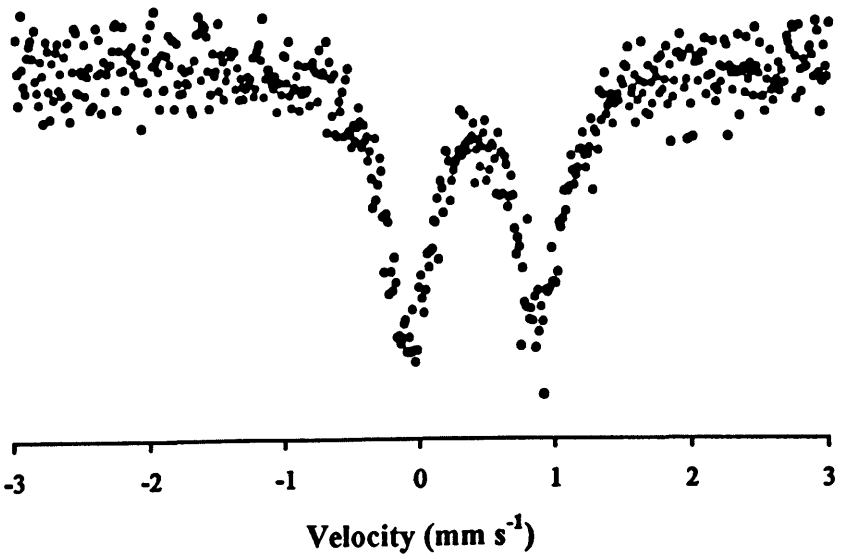


Figure 4.6 Mössbauer spectrum of (29) taken at room temperature.

Table 4.5 lists the quadrupole splitting (QS) and isomer shift (IS) values of compounds (6), (27), (28), and (29). These results are relative to iron foil. The IS values have a very small range of 0.40 to 0.42 mm s^{-1}. As mentioned in **Appendix**

D, the isomer shift depends on the s-electron density at the iron nucleus, which in turn depends on the donation of electron density by the ligands surrounding the iron. Since compounds (6), (27) to (29) have very little difference in ligand orientation about the iron atoms, it isn't surprising that their values are essentially equal. Similarly, the QS values of the compounds are almost identical to each other (range, 0.94 – 0.97 mm s^{-1}). Their values are less than 1 mm s^{-1}, which is characteristic of ferric atoms (ferrous atoms QS values are commonly above 2.0 mm s^{-1}).

Table 4.5 IS and QS room temperature values for (6), (27), (28) and (29).

Compound	IS (mm s^{-1})	QS (mm s^{-1})
(6)	0.42	0.95
(27)	0.41	0.94
(28)	0.42	0.96
(29)	0.40	0.97

None of the above compounds could be crystallised to give a satisfactory crystal for X-ray analysis. The lack of structural data for any of the compounds was disappointing.

4.2.2 Synthesis and Characterisation of [Fe(SALEN)]$_2$O.CH_2Cl_2 (17)

This section reports the characterisation of [Fe(SALEN)]$_2$O.CH_2Cl_2 (17) by infrared spectroscopy, Mössbauer spectroscopy and X-ray crystallography. Although (17) had been structurally characterised with X-ray crystallography before,[149] the refinement was not of high quality with a high R-factor of 10.9%.[149] Therefore, the structure of (17) was redetermined at low temperature (150K). Mössbauer analysis of (17) was used to establish the electronic nature of the iron atoms in the molecule.

As mentioned in Section 4.1.3, only one structurally characterised compound with an Fe-O-Si linkage, namely [Fe(SALEN)]OSiMe$_3$ (15) has been reported.[146] The compound was prepared from the reaction between [Fe(SALEN)]$_2$O and excess hexamethyldisilazane in refluxing toluene, equation [17].[146]

$$[Fe(SALEN)]_2O + HN(SiMe_3)_2 \xrightarrow[\text{reflux}]{\text{Tol./Pet. ether}} 2[Fe(SALEN)]OSiMe_3 \qquad [17]$$

The potential use of [Fe(SALEN)]$_2$O as a reagent to more compounds with Fe-O-Si linkages led us to the synthesis of (17). Unfortunately, this did not prove to be possible despite many attempts to prepare Fe-O-Si containing compounds. These attempts are detailed in **Appendix F2**.

4.2.2.1 Synthesis of [Fe(SALEN)]$_2$O.CH$_2$Cl$_2$ (17)

[Fe(SALEN)]$_2$O was synthesised according to literature reports[163] by the reaction of ferrous acetate with *N,N'*-ethylenebis(salicylideneimine), SALEN-H$_2$, in a 1:2 molar ratio in the presence of oxygen as shown in equation [18].

$$Fe(OAc)_2 + 2SALEN\text{-}H_2 \xrightarrow{O_2} [Fe(SALEN)]_2O + 2HOAc \qquad [18]$$

The product was isolated in 84% yield (lit.,[163] 81%) and characterised initially with elemental analyses (C, H and N) and infrared spectroscopy. Apart from the organic group frequencies of the SALEN moiety, the infrared spectrum exhibited a strong peak at 825 cm^{-1}, which has been assigned as the Fe-O-Fe vibrational frequency.[163] Recrystallisation of [Fe(SALEN)]$_2$O in dichloromethane-hexane solutions afforded (17).

4.2.2.2 Mössbauer Analysis of [Fe(SALEN)]$_2$O.CH$_2$Cl$_2$ (17)

A Mössbauer spectrum of (17) was recorded at liquid nitrogen temperature and is shown in **Figure 4.7**. Pertinent details of the spectrum are given in **Table 4.6** (all values are relative to iron foil). Mössbauer studies of [Fe(SALEN)]$_2$O (18) and

[Fe(SALEN)]$_2$O.2py (16) have been reported and their values are also given in Table 4.6.[271(d)] The IS and QS values reported in the present work are similar to the values for (16) and (18). This confirms that the iron site is ferric with a square pyramidal geometry.[271(b),271(d)]

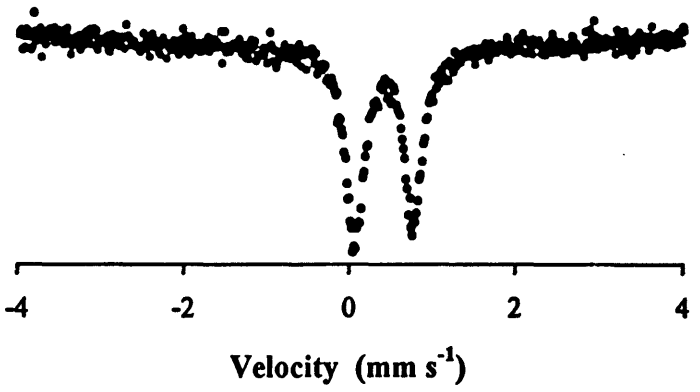


Figure 4.7 Mössbauer spectrum of [Fe(SALEN)]$_2$O.CH_2Cl_2 (17) taken at 77K.

Table 4.6 IS and QS values for [Fe(SALEN)]$_2$O.CH_2Cl_2 (17) from its liquid nitrogen Mössbauer spectrum.

Compound	IS value (mm s^{-1})	QS value (mm s^{-1})
[Fe(SALEN)]$_2$O.CH_2Cl_2 (17)	0.41	0.71
[Fe(SALEN)]$_2$O (18)	0.46	0.78
[Fe(SALEN)]$_2$O.2py (16)	0.44	0.88

4.2.2.3 Structural Study of [Fe(SALEN)]$_2$O.CH_2Cl_2 (17)

Dark-red block crystals of (17) were grown from the slow evaporation of a dichloromethane-hexane solution of [Fe(SALEN)]$_2$O. A crystal of size 0.30 x 0.25 x 0.15 mm was selected for X-ray crystallographic analysis. The structure determination was performed by Dr. Simon Lawrence at University College, Cork, Ireland on an Enraf Nonius Mach 3 diffractometer, see **Section 4.4.4** for details.

The structure of [Fe(SALEN)]$_2$O.CH_2Cl_2 (17) consists of two chemically equivalent Fe(SALEN) groups connected by a bridging oxygen atom, **Figure 4.8**. The iron atoms are five coordinate with approximate square pyramidal geometry and are displaced from the plane containing the O_2N_2 atoms in the SALEN group towards

the bridging oxygen atom. A view along the Fe-O-Fe axis shows the oxygen and nitrogen atoms of the SALEN groups to be in an eclipsed configuration with N and O atoms *trans* to their respective atoms in opposite SALEN groups, see **Figure 4.9.**

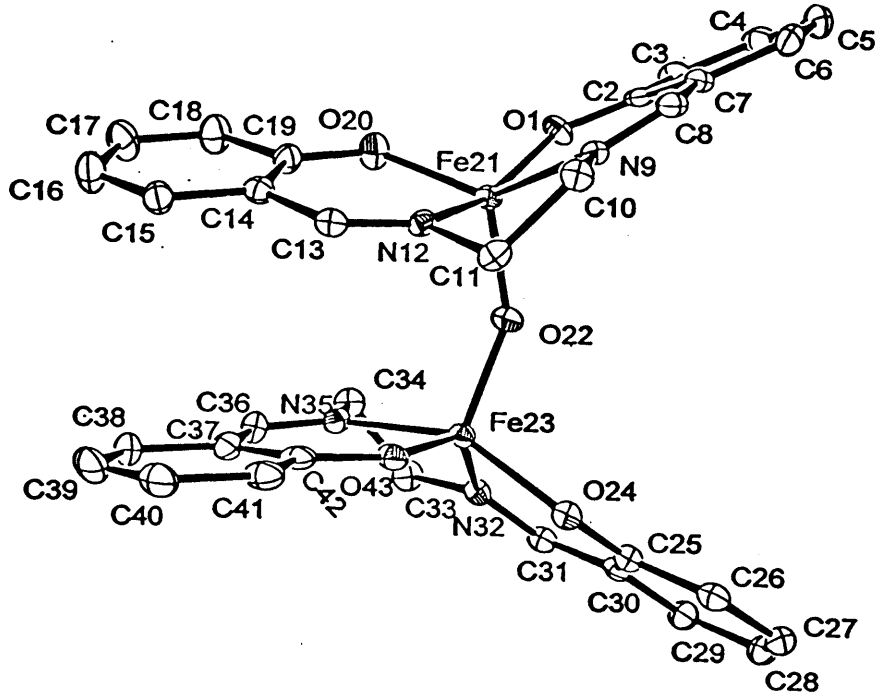


Figure 4.8 An "ORTEP" plot showing a general view of $[Fe(SALEN)]_2O.CH_2Cl_2$ **(17)** and the atom numbering scheme (note: hydrogen atoms and solvent molecule not shown for clarification), R = 7.3%.

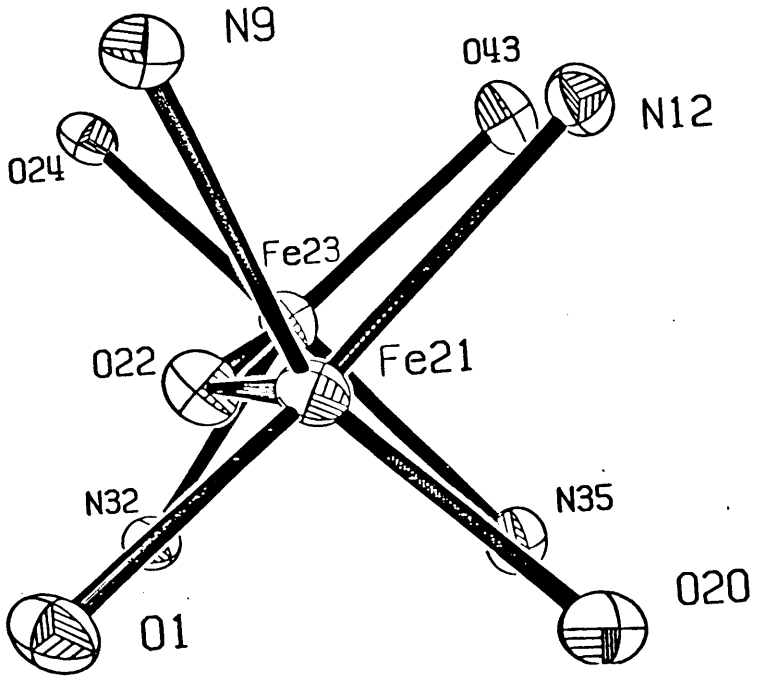


Figure 4.9 An "ORTEP" plot showing a view along the Fe---Fe axis and the nitrogen and oxygen atoms of the SALEN groups.

The important bond distance data around the two iron atoms are given in **Table 4.7**, while the rest of the bond distance data belonging to the SALEN groups and the solvent dichloromethane molecule are listed in **Table 4.8**. Similarly, bond angle data for **(17)** are given in **Tables 4.9** and **4.10**. Comparison of the present data with those for $[Fe(SALEN)_2O].2py$ **(16)** and $[Fe(SALEN)_2O]$ **(18)** will not generally be made because of the relatively inaccurate data for **(16)** and **(18)**.

(i) Fe-O distances

There are four Fe-O(-SALEN) distances in **(17)** measuring from 1.910(9) to 1.945(9)Å with a mean value of 1.932Å. This is in close agreement to the mean value reported by the previous structural analysis of **(17)**, 1.922Å.[149] The average Fe-O(-SALEN) distance in $[Fe(SALEN)]_2O.2py$ **(16)** was reported to be 1.93Å.[148] The Fe-O(-Fe) distances in **(17)** are calculated in the present work to be 1.807(8) and 1.794(7)Å, which are comparable to literature values of 1.797(9) and 1.791(9)Å.[149] The average distance for Fe-O(-Fe) in **(16)** is 1.79Å.[148] Hence, Fe-O(-Fe) distance is considerably shorter than the above Fe-O(-SALEN) distances. This may indicate some degree of π-bonding in the Fe-O bridge systems.

Table 4.7 Bond distance data for **(17)** with respect to iron sites.

Bond	Bond Length (Å)	Bond	Bond Length (Å)
Fe21O1	1.942(7)	Fe23O24	1.945(9)
Fe21N9	2.105(9)	Fe23N32	2.117(8)
Fe21N12	2.101(8)	Fe23O43	1.931(7)
Fe21O20	1.910(9)	Fe23N35	2.106(10)
Fe21O22	1.807(8)	Fe23O22	1.794(7)

(ii) Fe-N distances

The four Fe-N distances in (17) here are the same within 3 x e.s.d. to each other and range from 2.101(8) to 2.117(8)Å. Their mean value is 2.107Å, which is slightly higher than the previous average value (2.105Å).[149] The Fe-N mean distance in (16) was reported to be 2.09Å.[148]

(iii) Other distance data

The average aromatic and aliphatic C-C distances for (17) [1.399 and 1.522Å, respectively] are normal[167] and are comparable to the literature values of (17) [$(C_{Ar}$-$C_{Ar})_{mean}$ = 1.41Å and $(C_{Alp}$-$C_{Alp})_{mean}$, i.e. C10-C11 and C33-C34, = 1.53Å][149]. The other average bond distances in the SALEN motif of (17) are: (C_{Ar}-C_{sp2}), 1.448Å [lit.,[149] 1.44Å]; C_{sp3}-N single bond, 1.475Å [lit.,[149] 1.47Å]; C_{sp2}-N double bond, 1.285Å [lit.,[149] 1.29Å] and aromatic C-O, 1.317Å [lit.,[149] 1.33Å]. These values are similar with other transition metal SALEN complexes such as Fe(SALEN)Cl,[164] Co(SALEN)[165] and [Co(SALEN)]$_2$.[166] The mean C-Cl distance for the dichloromethane solvent molecule is 1.761Å, which is normal for aliphatic C-Cl bonding.[167]

Table 4.8 Bond distance data for (17) with respect to its SALEN groups.

Bond	Number of Bonds	Min. Bond Length (Å)	Max. Bond Length (Å)	Mean Bond Length (Å)
(C_{Ar}-C_{Ar})	24	1.362(12)	1.435(10)	1.399
C10-C11, C33-C34	2	1.508(10)	1.536(11)	1.522
C7-C8, C13-C14 C31-C30, C36-C37	4	1.422(11)	1.477(11)	1.448
C_{sp3}-N	4	1.455(10)	1.490(9)	1.475
C_{sp2}-N	4	1.267(9)	1.296(9)	1.285
(C_{Ar}-O)	4	1.307(9)	1.327(9)	1.317
C-Cl[a]	4	1.740(13)	1.773(12)	1.761

[a] = CH_2Cl_2 solvent molecule is disordered.

Table 4.9 Bond angle data of (17) centred on the iron sites.

Bond Angle	Degrees	Bond Angle	Degrees
N9Fe21O1	86.8(3)	N35Fe23O43	85.7(3)
N9Fe21O20	136.5(3)	N35Fe23O24	150.0(3)
N9Fe21O22	108.2(4)	N35Fe23O22	101.5(3)
N9Fe21N12	76.6(3)	N35Fe23N32	75.5(3)
N12Fe21O1	157.0(2)	N32Fe23O24	86.4(3)
N12Fe21O20	87.0(3)	N32Fe23O22	103.8(3)
N12Fe21O22	96.2(3)	O24Fe23O43	93.6(3)
O1Fe21O20	94.7(3)	O24Fe23O22	106.0(3)
O1Fe21O22	104.1(3)	O43Fe23O22	114.3(3)
O20Fe21O22	113.5(3)	Fe21O22Fe23	141.0(3)

(iv) Square pyramidal geometry of iron atoms in (17)

In a perfect square pyramidal structure, all angles at the central atom will be either 90 or 180°. In (17), this geometry is distorted with the iron atoms displaced from the plane containing the SALEN groups. This is clearly demonstrated in **Figure 4.10**. The displacements of the iron atoms from the mean planes of the SALEN ligands which contained the O_2N_2 ligating atoms measure 0.579(4)Å for Fe23 and 0.542(4)Å for Fe21 (mean value = 0.561Å). The latter is almost exactly the same as the value reported previously, 0.56Å.[149]

The range of O22-Fe-(other donor atoms of SALEN group) is 96.2(3)° (N12Fe21O22) to 114.3(3)° (O43Fe23O22). These values confirm the distorted square pyramidal geometry of (17). The mean values for N-Fe-N, O-Fe-O and N-Fe-O angles in (17) where N and O are each in the same SALEN ligand are 76.1°,

94.2° and 86.5°, respectively and are similar with the previous values of 75.6°, 94.0° and 86.8°.[149]

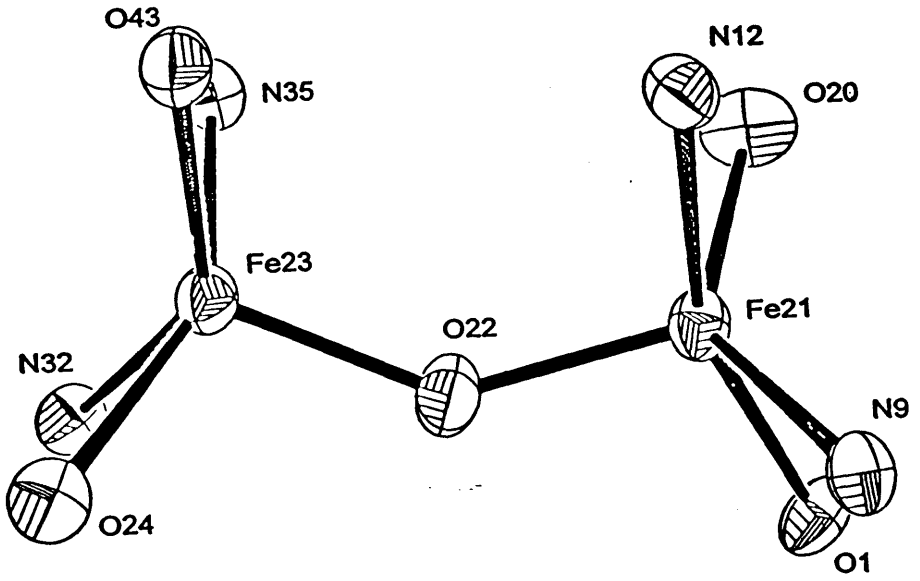


Figure 4.10 An "ORTEP" plot of (17) demonstrating the displacement of the iron atoms from the SALEN plane.

(v) Fe-O-Fe angle

The Fe-O-Fe angle in (17) is 141.0(3)°, which is slightly lower than the value in the literature, 142.4(5)°.[149] This value is within the range of Fe-O-Fe angles reported for other Fe(SALEN) complexes, **Table 4.3** [139.1(9)[148] to 144.6(6)[148]].

(vi) Summary

The crystal structure of $[Fe(SALEN)]_2O$ (17) has been redetermined with higher precision than before.[149] The iron atoms in the molecule are five coordinate with a distorted square pyramidal geometry and are connected to each other through a bridging oxygen atom. New bond distance and angle data for (17) have been calculated, e.g. the Fe-O-Fe angle is 141.0(3)°.

Table 4.10 Bond angle data for (17) with regards to SALEN groups.[a]

Bond Angle	Number of Bonds	Minimum Degree	Maximum Degree	Mean Degree
C_{Ar}-C_{Ar}-C_{Ar}	24	116.2(7)	122.7(7)	120.0
C_{Ar}-C_{Ar}-C_{sp2}	8	116.8(6)	123.5(6)	120.0
C_{Ar}-C_{sp2}-N	4	123.4(6)	125.7(7)	124.8
C_{sp2}-N-C_{sp3}	4	116.1(6)	120.8(7)	118.5
C_{sp2}-N-Fe	4	126.7(5)	128.9(5)	127.9
C_{sp3}-N-Fe	4	110.3(4)	117.2(5)	113.5
N-C_{sp3}-C_{sp3}	4	106.7(6)	107.9(6)	107.1
C_{Ar}-C_{Ar}-O	8	118.8(8)	124.0(7)	121.6
C_{Ar}-O-Fe	4	132.2(5)	134.2(5)	133.0
Cl-C-Cl	2	108.5(9)	113.2(8)	110.9

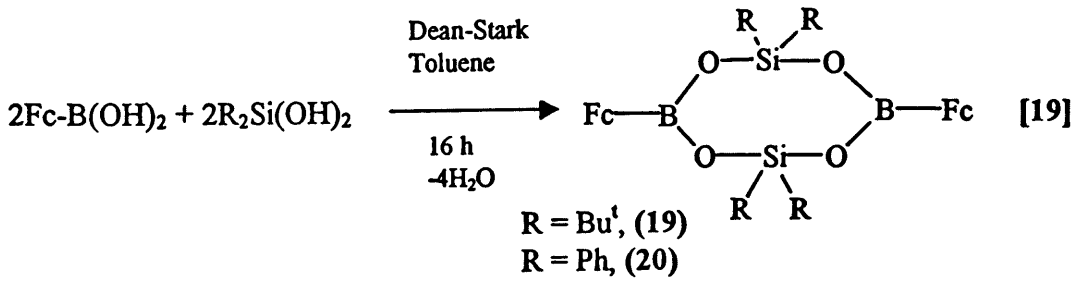
[a] = Other angle data: No unusual angles were observed.[167]

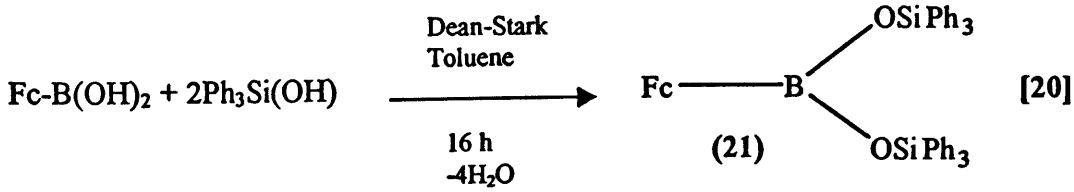
4.2.3 *Synthesis and Characterisation of Three Novel Borosilicate Compounds which also Contain Iron.*

Known borosilicate compounds of the type $R^1B(OSiR^2_3)_2$ and $[(R^1BO)_2(OSiR^3_2)_2]$ (R^1, R^2 and R^3 = any organic group) have been discussed previously (Section 4.1.3). Only three of these compounds have been structurally characterised by X-ray crystallography This section discusses the novel borosilicate compounds [{$(FcBO)_2(OSiBu^t_2)_2$} (19), {$(FcBO)_2(OSiPh_2)_2$} (20) and {$FcBOSiPh_3$} (21)], where Fc = $CpFe(C_5H_4)$. The structural analysis of (19) will also be discussed.

4.2.3.1 *Synthesis of (19), (20) and (21)*

The compounds were prepared from a dehydration reaction involving ferrocenylboronic acid $FcB(OH)_2$ and either di-*tert*-butylsilanediol (30), diphenylsilanediol or triphenylsilanol as shown in reactions [19] and [20] below.





$Bu^t_2Si(OH)_2$ (30) was prepared according to a literature method[168,169] by the hydrolysis of di-*tert*-butyldichlorosilane in an acetone-water mixture. Recrystallisation from ether-cyclohexane (1:3) afforded colourless crystals in 88% yield. Compounds (19), (20) and (21) were isolated as yellow solids from toluene solutions, equations [19] and [20]. Recrystallisation of (19), (20) and (21) from dichloromethane-hexane (1:1) solutions afforded air-stable orange crystals in yields of 14%, 44% and 73%, respectively. The low isolated yield of (19) was partly a

consequence of purifying the product by thin-layer chromatography (dichloromethane-hexane solution).

Compounds (19)-(21) had sharp-melting points [(19): 196-198°C; (20): 186-188°C; (21): 189-190°C]. Elemental analyses (C and H) of (19), (20) and (21) were in excellent agreement with theoretical values, while ^{1}H [(19)-(21)] and ^{13}C [(20) and (21)] NMR solution spectra exhibited no unusual features (see Section 4.4.5 for full assignment of NMR spectroscopic data). The compounds were also characterised by infrared spectroscopy, mass spectrometry and Mössbauer spectroscopy. Although all three compounds yielded crystals, only those of (19) were suitable for X-ray crystallographic analysis.

4.2.3.2 Infrared Spectra

The characteristic B-O-Si stretches[170,171,172] occurred at 1338, 1349 and 1320 cm^{-1} in the spectra of (19), (20) and (21), respectively. An absorption at *ca.* 670 cm^{-1} has been reported to be indicative of the B-O-Si linkage.[173,174] Peaks were observed at 659, 670 and 678 cm^{-1} in the spectra of (19), (20) and (21), respectively. The Si-O stretches[161,162] in (19), (20) and (21) were seen at 1106, 1128 and 1118 cm^{-1}, respectively. The Si-C(aliphatic) stretch has been reported to occur at ~1250 cm^{-1},[175] this stretch is observed in (19) at 1261 cm^{-1}. Strong bands near 3000 cm^{-1} in the spectra of (19), (20) and (21) indicate aliphatic and aromatic C-H stretches.[161] Peaks located between 1600-1400 cm^{-1} in the spectra of (19)-(21) are characteristic of aliphatic and aromatic C-C stretches.[161]

4.2.3.3 Mass Spectra

The parent mass ion was observed in the spectra of (19) [m/z = 740], (20) [m/z = 820] and (21) [m/z = 747]. All the mass spectra of (19)-(21) had peaks corresponding to $(CpFe)^{+}$ [m/z = 121]. The spectrum of (19) showed the loss of half its mass [m/z = 370], suggesting a symmetric molecule. The ferrocenium cation $(Cp_2Fe)^{+}$ [m/z = 185] was detected in the spectrum of (20). Further assignment peaks in the spectra of (19), (20) and (21) are given in Section 4.4.5.

4.2.3.4 Mössbauer Spectra

The ^{57}Fe Mössbauer spectra were recorded for **(19)**, **(20)** and **(21)** at liquid nitrogen temperature and are given in **Figure 4.11**, along with Mössbauer spectrum of ferrocenylboronic acid. Each spectrum exhibited a single quadrupole nuclear splitting with similar parameters for each compound. The quadrupole splitting (QS) and isomer shift (IS) values for the four compounds are listed in **Table 4.11**. Literature values for ferrocene are also listed in **Table 4.11**.[271(e)]

Table 4.11 IS and QS values for **(19)**, **(20)**, **(21)** and ferrocenylboronic acid as calculated from their respective 77K Mössbauer spectra.

Compound	IS (mm s^{-1})	QS (mm s^{-1})
$[(FcBO)_2(Bu^t_2SiO)_2]$ **(19)**	0.55	2.31
$[(FcBO)_2(Ph_2SiO)_2]$ **(20)**	0.54	2.32
$[FcB(OSiPh_3)_2]$ **(21)**	0.53	2.29
$FcB(OH)_2$	0.51	2.16
Ferrocene	0.68	2.37

The IS and QS values for **(19)** to **(21)** and ferrocenylboronic acid are in the same range as those found for ferrocene. This suggests that the iron environment is insensitive to substitution in the cyclopentadienyl rings.[271(b),271(e)]

The three borosilicate compounds have almost identical IS and QS values which are only slightly larger than the IS and QS results for ferrocenylboronic acid. The QS values of **(19)**-**(21)** and ferrocenylboronic acid are greater then 2.00 mm s^{-1}, which is characteristic of high spin iron in its (+2) state.[271(a),271(b)] The IS data suggest that the electronic environment of the iron nucleus is very similar in each compound and is dominated by the two cyclopentadienyl rings. However, there is a slight increase in the IS values of **(19)**-**(21)** compared to ferrocenylboronic acid. This suggests that

there is less s-electron density on the iron atoms in compounds (19), (20) and (21) than the iron atom in ferrocenylboronic acid, which may be a consequence of the electrophilic borosilicate groups in (19), (20) and (21).

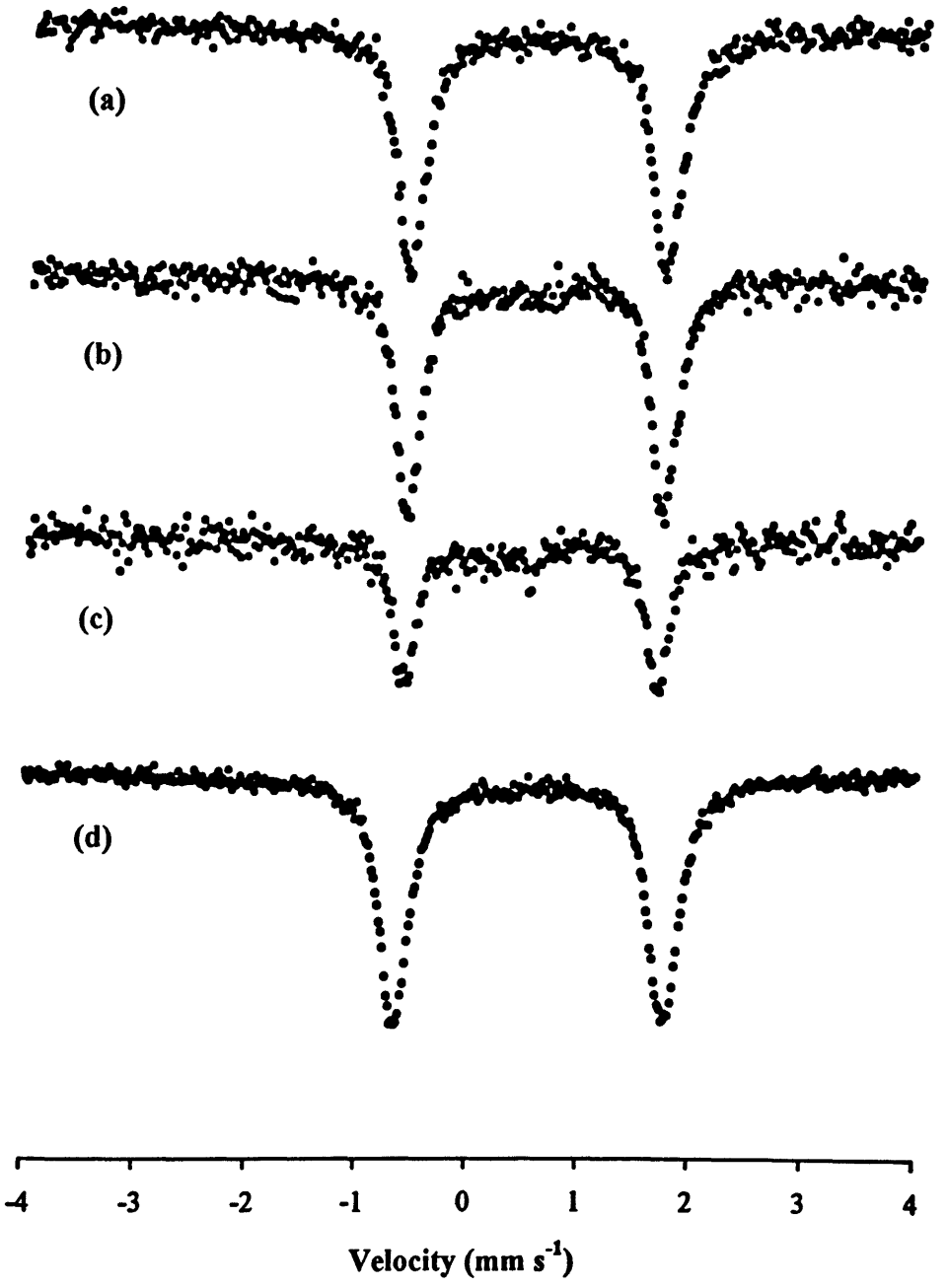


Figure 4.11 Mössbauer 77K spectra of (a) (19), (b) (20), (c) (21) and (d) ferrocenyl boronic acid.

4.2.4 *Structural Study of [(FcBO)$_2$(Bu$^t_2$SiO)$_2$] (19)*

Structural studies of eight-membered cyclic borosilicate systems containing two boron atoms and four B-O-Si linkages are restricted to two compounds, [(PhBO)$_2$(Bu$^t_2$SiO)$_2$] (24)[159] and [(PhBO)$_2$(Ph$_2$SiO)$_2$] (26)[158]. Details of the structures of these compounds are given in Section 4.1.3.1.

Orange plate crystals of (19) suitable for X-ray crystallography were grown from dichloromethane-hexane (1:1) at room temperature. A crystal with size 0.44 x 0.36 x 0.30 mm was selected for structural analysis. The structure determination was carried out by Dr. Simon Lawrence at Univeristy College, Cork, Ireland.

Molecules of (19) contain two tetrahedral Bu$^t_2$SiO$_2$- units and two trigonal planar (Fc)BO$_2$- units held together by an eight atom B$_2$Si$_2$O$_4$ ring as shown in Figure 4.12. The molecules contain an inversion centre in the middle of the borosilicate ring so there is only one unique B-O-Si and O-Si-O angle each. The B$_2$Si$_2$O$_4$ ring is almost planar as shown in Figure 4.13. Figure 4.13 also shows that the *tert*-butyl groups are in an almost eclipsed arrangement to each other.

Relevant bond distance and bond angle data for (19) are given in Tables 4.12 and 4.13, respectively.

Table 4.12 Bond distance data for [(FcBO)$_2$(Bu$^t_2$SiO)$_2$] (19).

Bond	Bond Length (Å)	Bond	Bond Length (Å)
Si14-O13	1.629(4)	B12-O23	1.344(7)
Si14-O23	1.620(4)	B12-C11	1.537(8)
Si14-C19	1.877(7)	(C-C)$_{tBu}$[a]	1.534
Si14-C15	1.858(7)	(C-C)$_{Cp}$[b]	1.419
B12-O13	1.353(8)	(Fe-C)[c]	2.039

[a] = mean C-C bond distances for one *tert*-butyl group, range: 1.525(10) – 1.540(10)

[b] = mean C-C bond distances for one cyclopentadienyl ring, range: 1.402(9) – 1.441(8).

[c] = mean Fe-C bond distances for iron atom connected to one cyclopentadienyl ring, range = 2.033(7) – 2.052(8).

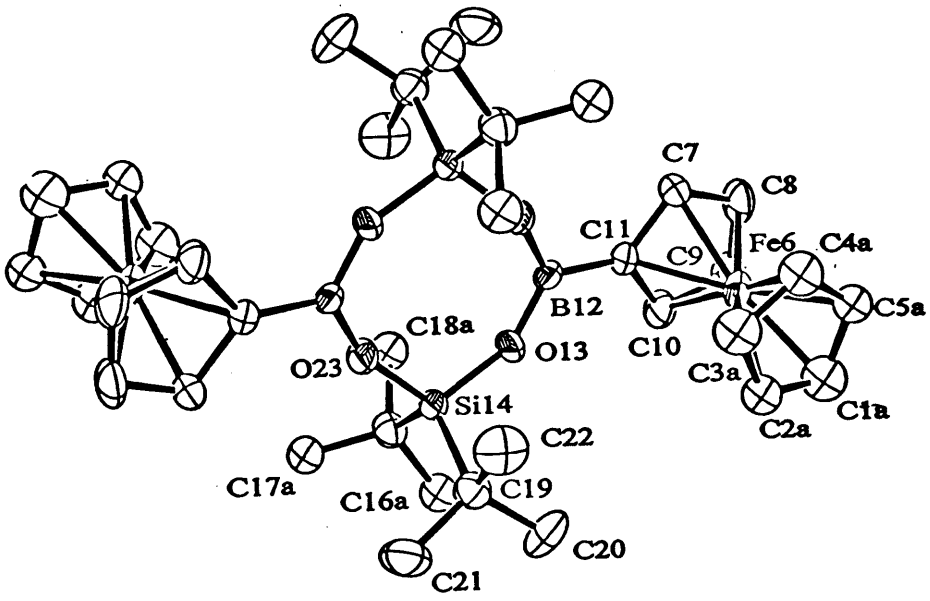


Figure 4.12 An "ORTEP" plot showing a general view of **(19)** and atom numbering scheme.

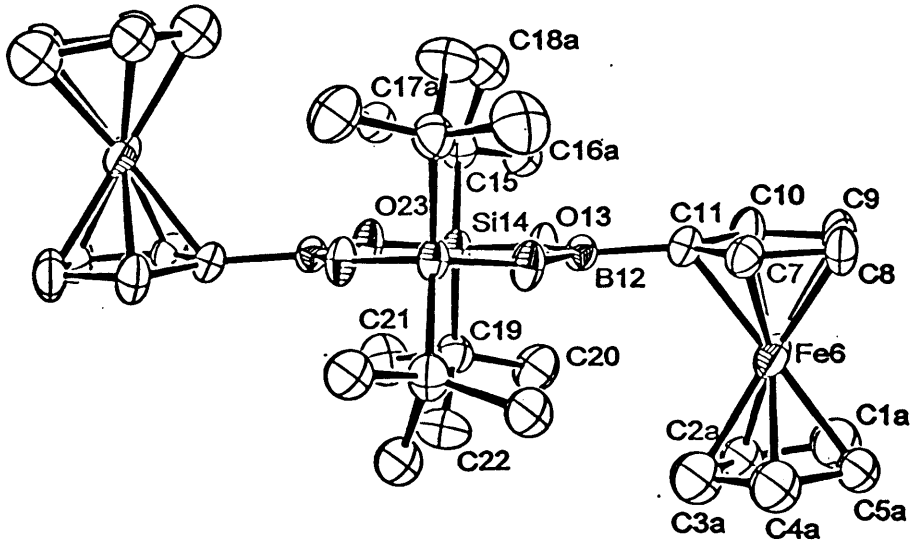


Figure 4.13 An "ORTEP" plot showing the view along the Si---Si axis of **(19)**.

(i) B-O distances

The two B-O distances in **(19)** are 1.353(8) and 1.344(7)Å, which are the same within 1 x e.s.d.. These distances are essentially the same as the B-O distances reported for the cyclic compounds $[(PhBO)_2(Ph_2SiO)_2]$ **(26)**, 1.348(5) and 1.345(5)[158] and $[(PhBO)_2(Bu^t{}_2SiO)_2]$ **(24)**, 1.350(4) and 1.350(5)Å.[159]

(ii) Si-O distances

The two Si-O distances in **(19)** are almost within 1 x e.s.d. of each other; 1.629(4) and 1.620(4)Å. These values are within the range of Si-O distances recorded for **(26)** [1.627(3) and 1.615(3)Å][158] and for **(24)** [1.630(3) and 1.631 (2)Å][159].

(iii) B-C distances

The B-C distance in **(19)** is 1.537(8)Å is slightly less than the mean value of 1.556Å reported for $B\text{-}C_{ar}$ distances, where the boron atom is tricoordinate and the carbon atom C_{ar} is part of an aromatic ring.[167] The B-C distance in **(19)** is also slightly lower than the equivalent distance recorded in **(26)** [1.555(6)Å][158].

(iv) Si-C distances

The two Si-C distances, 1.877(7) and 1.858(7)Å, are similar to the Si-C distances in the centrosymmetric cyclic compound **(24)** [1.869(4) and 1.872(4)Å][159]. Moreover, an overall mean value of 1.863Å has been reported for Si-C bonds, where C is sp^3-hybridised and bonded to carbon or hydrogen atoms only and the silicon atom is four-coordinate.[167] This value lies between the two Si-C distances in **(19)**.

(v) Other distance data

The $(C\text{-}C)_{t\text{-}Bu}$ distances in **(19)** have a mean value of 1.534Å with a range between 1.525(10) and 1.540(10)Å. These distances refer to the *tert*-butyl group (C19-C22) as the other *tert*-butyl group (C15A-C18A) is disordered and was not resolved. The distances are normal for sp^3-hybridised carbon.[167] The $(C\text{-}C)_{Cp}$ distances in **(19)** are only reported from the cyclopentadienyl ring connected to the boron atom (C7-C11) as the other cyclopentadienyl ring experiences some disorder. The mean value for $(C\text{-}C)_{Cp}$ in **(19)** is 1.418Å, while its range is between 1.402(9) and 1.441(8)Å. These distances are normal for aromatic C-C bonds.[167]

The values for Fe-C distances (taken for the bonding between Fe and the cyclopentadienyl ring connected to boron) are between 2.033(7) and 2.052(8)Å, mean = 2.039Å. The mean value for (19) is exactly the same average distance found for Fe-C bond lengths (2.039Å) in the compound $FeNx_3(BFc)_2.2CCl_4$, where H_2Nx = nioxime.[176]

Table 4.13 Bond angle data for $[(FcBO)_2(Bu^t_2SiO)_2]$ (19).

Bond Angle	Degrees	Bond Angle	Degrees
O13Si14O23	112.2(2)	Si14O13B12	146.3(4)
O13Si14C19	106.2(3)	O13B12O23	121.8(5)
O13Si14C15	106.5(3)	O13B12C11	119.2(5)
O23Si14C19	107.3(3)	O23B12C11	119.1(6)
O23Si14C15	106.5(3)	B12C11C7	127.8(8)
Si14C19C21	112.1(5)	B12C11C10	127.6(6)
Si14C19C20	111.9(5)	B12C11Fe6	124.4(5)
Si14C19C22	106.9(5)	$(C\text{-}C\text{-}C)_{Cp}$[a]	108.0
C15Si14C19	119.5(3)	$(C\text{-}C\text{-}C)_{t\text{-}Bu}$[b]	108.6
Si14O23B12	157.O(4)		

[a] = mean C-C-C angle for *cyclo*pentadienyl ring connected to boron, range: 104.6(5) – 109.8(6).

[b] = mean C-C-C angle for *tert*-butyl group (without distortion), range: 108.1(7) – 109.3(6).

(v) B-O-Si angles

The B-O-Si angles in (19) are 146.3(4) and 157.0(4)°. These angles are significantly different to one another although they are chemically equivalent. This situation has been noted before for borosilicates e.g. $[(PhBO)_2(Ph_2SiO)_2]$ (26), with B-O-Si angles of 145.3(3) and 160.9(3)°.[158] $[PhB(OSiPh_3)_2]$ (22) also has two very different values for chemically equivalent B-O-Si angles, *viz.* 139.8(4) and 157.9(3)°.[154] The B-O-Si angles in (19) lie between the respective angles found for (26) and (22). In contrast, the two B-O-Si angles reported for $[(PhBO)_2(Bu^t_2SiO)_2]$ (24) measure 149.1(3) and 149.9(2)°.[159]

(vii) *Angles at boron*

The unique O-B-O angle in (19) measures 121.8(5)°, which is typical for boron of trigonal planar geometry. The angle compares to the unique O-B-O angle in centrosymmetric $[(PhBO)_2(Bu^t_2SiO)_2]$ (24), which measured 122.8(3)°.[159] The O-B-C angles in (19) are found to be 119.1(6) and 119.2(5)°, which are essentially the same and are only slightly less than the O-B-O angle. Once again the angles are typical of trigonal planar boron and comparable angles of 118.5(3) and 118.7(3) were observed in (24).[159]

(viii) Angles at silicon

The unique O-Si-O angle in (19) is 112.2(2)°, which is within 3 x e.s.d. the same as the angle in $[(PhBO)_2(Bu^t_2SiO)_2]$ (24), 111.5(1)°.[159] The O-Si-C angles in (19) range from 106.2(3) to 107.3(3)° with a mean value of 106.6°. These values are significantly smaller than the O-Si-O angles reported above for (19). However, they are comparable to the O-Si-C angles in (24), which were in the range 106.0(2) to 107.0(2)° (mean = 106.5°).[159] The C-Si-C angle in (19) is 119.5(3)°, which is relatively large for tetrahedral silicon. The increase in angle is probably a result of steric repulsion between the two *tert*-butyl groups.

(ix) Other angle data

The two B-C-C angles in (19) are 127.8(8) and 127.6(6)°. The $(C\text{-}C\text{-}C)_{t\text{-}Bu}$ angles in (19) have a mean value of 108.6° and a range of 108.1(7) to 109.3(6)°. Once again, only the angles from the undistorted *tert*-butyl group are reported. These angles indicate tetrahedral geometry at the central carbon of the *tert*-butyl group. The

average $(C\text{-}C\text{-}C)_{Cp}$ angle in (19) [for the cyclopentadienyl ring connected to boron] measures 108.0°, range of 104.6(5) to 109.8(6)°. The B-C-Fe angle in (19) measures 124.4(5)°.

(x) Intramolecular distances

The intramolecular distances across the borosilicate ring in (19) (refer to **Figure 4.12**) are: B12---B'12, 3.999(13)Å; Si14---Si'14, 4.145(3)Å, where B'12 and Si'14 are the atoms symmetry related to B12 and Si14, respectively.

(xi) $B_2Si_2O_4$ ring

The borosilicate ring in (19) is nearly planar as shown in **Figure 4.13** with no atom further than 0.08Å from the mean plane containing the eight atoms. The exact details of the displacement (Å) of each atom from the mean plane are: B12, 0.028(4); O13, 0.038(4); Si14, -0.062(2); O23, 0.079(4); B'12, -0.028(4); O'13, -0.034(4); Si'14, 0.062(2); O'23, 0.079(4), where B'12, Si'14, O'13 and O'23 are symmetry related to B12, Si14, O13 and O23, respectively.

(xii) Summary

The crystal structure of $[(FcBO)_2(Bu^t_2SiO)_2]$ (19) is only the third example of a structurally characterised cyclic borosilicate compound with a central $B_2Si_2O_4$ ring. The other two examples are $[(PhBO)_2(Bu^t_2SiO)_2]$ (24)[159] and$[(PhBO)_2(Ph_2SiO)_2]$ (26)[158]. The structure of (19) is consistent with (24) and (26) as it too is a centrosymmetric compound with a nearly planar central borosilicate ring. Even though (19) has chemically equivalent B-O-Si bonds, two different angles measurements were observed, 146.3(4) and 157.0(4)°. This effect has also been observed for (26), 145.3(3) and 160.9(3)°,[158] but not for (24) which has B-O-Si angles almost equivalent, 149.1(3) and 149.9(2)°.[159]

4.3 Summary and Conclusions

The reactions between ferric chloride, 2,6-diacetylpyridinedioxime, and aryl boronic acids, $RB(OH)_2$ {R = C_6H_5, *p*-C_6H_4Br, *p*-$C_6H_4(CHO)$ or *p*-$C_6H_4(CH{=}CH_2)$}, led to the synthesis of compounds with Fe-O-B linkages. These compounds had the general formula $[Fe_2(C_{18}H_{19}(RB)_2N_6O_6)Cl_3]$ and were characterised by elemental analyses (C, H and N), infrared spectroscopy and Mössbauer spectroscopy. Unfortunately, crystals of these compounds were unsuitable for X-ray crystallographic analysis.

As a prelude to the formation of compounds with Fe-O-Si linkages, $[Fe(SALEN)]_2O$ was prepared and analysed. Recrystallisation from dichloromethane-hexane led to the formation of crystals of $[Fe(SALEN)]_2O.CH_2Cl_2$ **(17)**, which were structurally characterised by X-ray crystallography. The X-ray crystallographic analysis was an improvement on a previous structural analysis.[149] In **(17)**, the two iron atoms are in distorted square pyramidal geometries and are linked to each other through a bridging oxygen. The iron atoms are displaced from the mean SALEN plane by over half an Angström. Attempts to prepare novel Fe-O-Si compounds from **(17)** were unsuccessful, (details are reported in **Appendix F**).

Compounds $[(FcBO)_2(Bu^t_2SiO)_2]$ **(19)**, $[(FcBO)_2(Ph_2SiO)_2]$ **(20)** and $[FcB(OSiPh_3)_2]$ **(21)** were prepared from dehydration reactions between ferrocenylboronic acid and either di-*tert*-butylsilanediol, diphenylsilanediol or triphenysilanol, respectively. The compounds were characterised by elemental analyses (C and H), infrared spectroscopy, ^1H and ^{13}C solution NMR spectroscopy, mass spectrometry and Mössbauer spectroscopy. The results from Mössbauer spectroscopy suggested that the electronic nature of the iron atoms in **(19)**-**(21)** are relatively unaffected by the borosilicate part of the compounds.

Compound **(19)** was also structurally characterised using X-ray techniques. The compound had two very different B-O-Si angles for chemically equivalent B-O-Si angles; similar results have been documented before.[154,158] The rest of the molecular data were generally consistent with those for previously studied compounds.

4.4 Experimental Details

4.4.1 Instrumentation

Elemental analyses were performed at the Microanalytical Laboratory, University College, Cork on a Perkin Elmer 240C Elemental Analyser. Infrared spectra were recorded as KBr discs in the range 4000 – 440 cm^{-1} on a Perkin Elmer FTIR Paragon 1000 spectrometer. Relative intensities are designated as vs, very strong; s, strong; m, medium; w, weak; vw, very weak; sh, shoulder; br, broad. All ^{1}H and ^{13}C NMR spectra were recorded on a JEOL FT NMR Spectrometer, GSX-270 Series. Tetramethylsilane, $(CH_3)_4Si$, was used as standard and deuterated chloroform, $CDCl_3$, as the solvent for all ^{1}H and ^{13}C spectra. All NMR spectra were recorded at ambient temperature. Mass spectra were recorded on a Kratos GC-MS High Resolution Mass Spectrometer at the Mass Spectrometry Laboratory, University College, Cork. Melting points were recorded on an Electrothermal IA 9000 Series Digital Melting Point Apparatus. Mössbauer spectra were measured at room and liquid nitrogen (77K) temperature using a commercial constant acceleration drive unit and transducer (Harwell Instruments) in conjunction with a Canberra System 40 multichannel analyser. The source was ^{57}Co in Rh and was of 20mC nominal strength. All data was referred to the spectrum of iron foil as standard. Masses of samples varied between 25 and 35 mg. Data collection times varied from 24 – 48 hours.

4.4.2 Starting Reagents

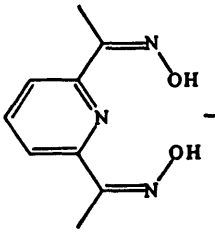
Solvents (supplied by Aldrich) were dried according to literature methods[177] and distilled prior to use. Water was doubly distilled and deionised. The following reagents were used directly as supplied by Aldrich: phenylboronic acid, 4-bromophenylboronic acid, 4-formylphenylboronic acid, 3-nitrophenylboronic acid, ferrocenylboronic acid, potassium trimethylsilanolate, lithium trimethylsilanolate, triphenylsilanol, diphenylsilanediol, di-*tert*-butyldichlorosilane, ferric chloride anhydrous, ferric chloride hexahydrate, iron(II) acetate, sodium hydroxide, 2,6-diacetylpyridine, hydroxylamine hydrochloride, salicylaldehyde, ethylenediamine,

hexamethyldisilazane, 1,3-diphenyl-1,1,3,3-tetramethyldisilazane (see also **Appendix F**).

4.4.3 Synthesis of Boron Oxygen-Bridged Iron Compounds.

Several of these compounds were prepared previously, but the experimental details were minimal.[116] The experimental details used in the current work are given below.

4.4.3.1 Synthesis of $[Fe_2(C_{30}H_{29}B_2N_6O_6)Cl_3]$, (6)

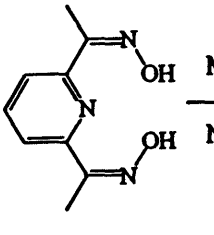


$$2FeCl_3 + 2(C_6H_5)B(OH)_2 + 2 \xrightarrow[\text{NaOH}]{\text{MeOH}} [Fe_2(C_{30}H_{29}B_2N_6O_6)Cl_3] \quad \textbf{(6)}$$

[21]

Phenylboronic acid (0.244g, 2.00mmol), 2,6-diacetylpyridinedioxime [prepared according to the literature report[178]] (0.386g, 2.00mmol) and sodium hydroxide (0.040g, 1.00mmol) were added directly to a stirred methanol (30ml) solution containing ferric chloride hexahydrate (0.541g, 2.00mmol) at room temperature. The solution immediately turned deep red. It was stirred for 16 hours. Removal of methanol on a rotary evaporator gave a dark solid, which was recrystallised from chloroform solution as small dark-red crystals (0.245g, 30.3%). Found: C, 44.1; H, 3.25; N, 10.1%. $C_{30}H_{29}B_2Cl_3Fe_2N_6O_6$ requires: C, 44.5; H, 3.6, N, 10.4%. FTIR (KBr disc), ν_{max}/cm^{-1}: 3438(m), 2928(s), 1611(s), 1552(s), 1470(m), 1371(m), 1212(s), 1190(m), 1155(s), 1095(vs), 1060(vs), 978(m), 897(s), 814(vs), 782(s), 750(vs), 638(w).

4.4.4.2 Synthesis of $[Fe_2(C_{30}H_{27}B_2Br_2N_6O_6)Cl_3]$, (27)



$$2FeCl_3 + 2(p\text{-}BrC_6H_4)B(OH)_2 + 2 \xrightarrow[\text{NaOH}]{\text{MeOH/H}_2\text{O}} [Fe_2(C_{30}H_{27}B_2Br_2N_6O_6)Cl_3] \quad \textbf{(27)}$$

[22]

The procedure was the same as that described in Section 4.4.3.1. The quantities used were: ferric chloride hexahydrate, 0.540g (2.00mmol); 4-bromophenylboronic acid, 0.402g (2.00mmol); 2,6-diacetylpyridinedioxime, 0.386g (2.00mmol); sodium hydroxide, 0.040g (1.00mmol); methanol, 35ml; water, 5ml. The reaction time was 16 hours. The dark-red solid was recrystallised from chloroform to yield a red crystalline solid (0.145g, 15.0%). Found: C, 36.8; H, 2.9; N, 8.4%. $C_{30}H_{27}B_2Br_2Cl_3Fe_2N_6O_6$ requires: C, 37.25; H, 2.8; N, 8.7%. FTIR (KBr disc) ν_{max}/cm^{-1}: 3451(s), 2924(s), 1610(s), 1556(s), 1476(m), 1374(m), 1187(s), 1160(s), 1094(s), 1063(vs), 1009(m), 975(s), 905(vs), 866(s), 810(vs), 781(vs), 753(vs), 641(w).

4.4.3.3 Synthesis of $[Fe_2(C_{32}H_{29}B_2N_6O_8)Cl_3]$, (28)

$$2FeCl_3 + 2(p\text{-}CHOC_6H_4)B(OH)_2 + 2 \xrightarrow[NaOH]{MeOH/H_2O} [Fe_2(C_{32}H_{29}B_2N_6O_8)Cl_3] \quad (28)$$

[23]

The method employed was identical to that described in Section 4.4.3.1 with ferric chloride hexahydrate (0.541g, 2.00mmol), 2,6-diacetylpyridinedioxime (0.386g, 2.00mmol), 4-formylphenylboronic acid (0.299g, 2.00mmol) and sodium hydroxide (0.041g, 1.00mmol) reacted in 40 ml methanol-water (9:1) over 16 hours. Dark crystalline solid was extracted from chloroform solution (0.176g, 20.3%). Found: C, 44.6; H, 3.3; N, 9.5%. $C_{32}H_{29}B_2Cl_3Fe_2N_6O_8$ requires: C, 44.4; H, 3.4; N, 9.7%. FTIR (KBr disc) ν_{max}/cm^{-1}: 3448(vs), 2927(s), 1686(vs), 1608(s), 1560(s), 1458(w), 1376(m), 1216(s), 1149(s), 1097(vs), 1058(vs), 978(m), 899(s), 801(vs), 777(vs), 669(w).

4.4.3.4 Synthesis of $[Fe_2(C_{34}H_{33}B_2N_6O_6)Cl_3]$, (29)

$$2FeCl_3 + 2(p\text{-}C_2H_3C_6H_4)B(OH)_2 + 2 \xrightarrow[NaOH]{MeOH/H_2O} [Fe_2(C_{34}H_{33}B_2N_6O_6)Cl_3] \quad (29)$$

[24]

The procedure follows that exactly as described in Section 4.4.3.1. The quantities used were: ferric chloride hexahydrate, 0.541g (2.00mmol); 4-vinylphenylboronic acid, 0.296g (2.00mmol); 2,6-diacetylpyridinedioxime, 0.387g (2.00mmol); sodium hydroxide, 0.040g (1.00mmol); methanol, 40ml; water, 5ml. The reaction time was 16 hours. Dark red product crystallised from chloroform solution (0.188g, 21.8%). Found: C, 46.9; H, 4.1; N, 9.6%. $C_{34}H_{33}B_2Cl_3Fe_2N_6O_6$ requires: C, 47.4; H, 3.9; N, 9.8%. FTIR (KBr disc) ν_{max}/cm^{-1}: 3446(s), 3076(m), 2924(m), 1608(vs), 1554(s), 1475(m), 1375(m), 1210(s), 1193(m), 1160(s), 1100(vs), 1064(vs), 976(s), 902(vs), 866(s), 784(vs), 753(s), 636(w).

4.4.4 Synthesis of μ-Oxo-bis-[NN'-ethylenebis(salicylideneiminato)iron(III)], [Fe(SALEN)]$_2$O.

The compound was prepared from iron(II) acetate and NN'-ethylenebis(salicylideneimine), $SALENH_2$,[179] as previously reported.[163]

$$2Fe(OAc)_2 + 2SALENH_2 \xrightarrow[O_2]{DMF} [Fe(Salen)]_2O + 2HOAc \qquad [25]$$

The product was confirmed by elemental analyses (C, H and N) and FTIR spectroscopy.

Dark-red block crystals of $[Fe(SALEN)]_2O.CH_2Cl_2$ **(17)** were grown from a dichloromethane-hexane (1:1) solution and the crystallographic data is given below. The structure was solved and refined using SHELXL 97.

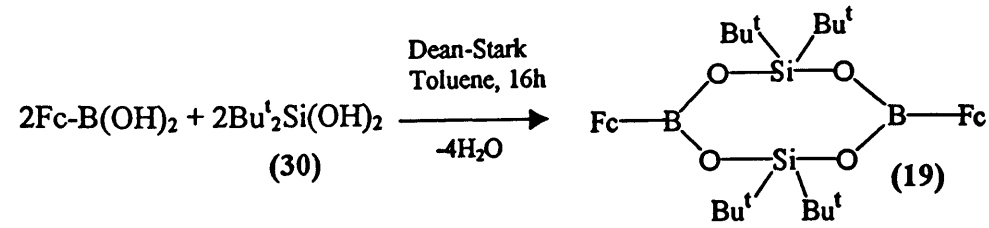
Crystal data for $[Fe(SALEN)]_2O.CH_2Cl_2$ (17): $C_{33}H_{30}Cl_2Fe_2N_4O_5$, F.W. = 745.21, monoclinic, $P2_1/c$, a = 12.29(5)Å, b = 13.99(5)Å, c = 19.29(5)Å, α = 90.0(2)°, β = 106.3(2)°, γ = 90.0(2)°, V = 3184(19)Å^3, Z = 4, D_c = 1.555 g cm-3, λ(Mo-Kα) = 0.70930Å, μ = 1.127 mm^{-1}, F(000) = 1528, T = 150(2) K, R = 0.0727, R_w = 0.1879 for 4737 observed reflections.

4.4.5 *Synthesis of Borosilicate Compounds from Ferrocenylboronic Acid.*

4.4.5.1 *Preparation of di-tert-butylsilanediol, $Bu^t_2Si(OH)_2$ (30)*

Di-*tert*-butyldichlorosilane (5.004g, 23.46mmol) was dissolved in acetone (20ml). A mixture of water (10ml) and acetone (20ml) was added dropwise over 20 minutes. The resulting solution was stirred for 12 hours. A colourless solid was produced on removal of solvent *via* a rotary evaporator. Recrystallisation from ether-cyclohexane (1:3) yielded rectangular colourless crystals (3.645g, 88.1%). M.P., 151-152°C [lit.,[157,158] 152°C]. Found: C, 54.3; H, 11.7%. $C_8H_{20}SiO_2$ requires: C, 54.5; H, 11.4%. FTIR (KBr disc) ν_{max}/cm^{-1}: 3474(br,vs), 2950(m), 2894(vw), 2860(m), 1478(w), 1468(s), 1394(vw), 1364(m), 1013(w), 938(m), 828(vs), 802(s), 668(vw), 655(m), 569(w). MS (EI), m/z: 176 [$(M)^+$]; 161 [$(M)^+ - CH_3$]; 119 [$(M)^+ - Bu^t$]; 56 [$(Bu^t)^+ - H$]; 41 [$(CH_3\text{-}C{=}CH_2)^+$]

4.4.5.2 *Synthesis of $[(FcBO)_2(OSiBu^t_2)_2]$, (19)*



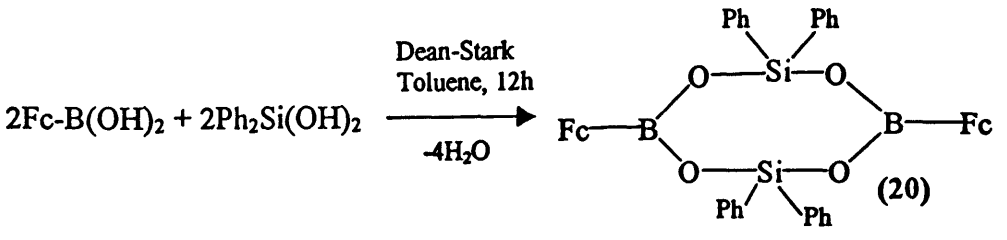
[26]

A mixture of ferrocenylboronic acid (0.230g, 1.00mmol) and di-*tert*-butylsilanediol (0.177g, 1.00mmol) was added to toluene (50ml) and the solution was heated at reflux temperature for 16 hours in a Dean-Stark apparatus. Removal of solvent on a rotary evaporator afforded an orange solid. Thin-layer chromatography of this solid on silica gel plates with dichloromethane-hexane (1:2) as eluent yielded a yellow solid. Recrystallisation from dichloromethane-hexane (1:1) solution gave small rectangular orange crystals (0.052g, 14.1%). M.P., 196-198°C. Found: C, 58.1; H, 7.75%. $C_{36}H_{54}B_2Fe_2O_4Si_2$ requires: C, 58.4; H, 7.35%. FTIR (KBr disc) ν_{max}/cm^{-1}: 3096(m), 2964(s), 2860(s), 1474(s), 1377(vs), 1338(s), 1299(vs), 1261(s), 1227(m), 1172(w), 1106(s), 1025(s), 938(w), 903(m), 818(s), 712(m), 694(m), 659(m), 581(w), 480(m). ^1H NMR ($CDCl_3$, p.p.m.): 4.50-4.12 [m, 9H, $C_5\underline{H}_5FeC_5\underline{H}_4B$]; 1.15 [s, 18H, $C(C\underline{H}_3)_3$].

MS (EI), m/z: 740 [$(M)^+$]; 370 [$(M/2)^+$]; 328 [$(M/2)^+$ - CH_3-CH=CH_2]; 256 [$(M/2)^+$ - 2Bu^t]; 121 [$(CpFe)^+$]; 76 [$(C_5H_4B)^+$].

Crystal data for [$(FcBO)_2(OSiBu^t_2)_2$] **(19):** $C_{36}H_{54}B_2Fe_2O_4Si_2$, F.W. = 740.29, triclinic, P_1, a = 8.1000(15)Å, b = 11.866(2)Å, c = 11.910(2)Å, α = 116.298(13)°, β = 96.43(2)°, γ = 104.817(16)°, V = 958.0(3)Å^3, Z = 1, D_c = 1.283 g cm^{-3}, λ(Mo Kα) = 0.71069Å, μ = .855 mm^{-1}, F(000) = 392, T = 293(2) K, R = 0.0632, R_w = 0.1182 for 1916 reflections. Structure solved and refined by SHELXL 97.

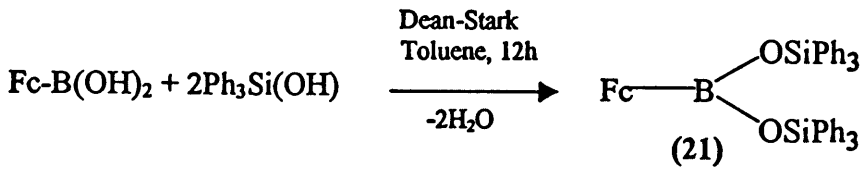
4.4.5.3 Synthesis of [$(FcBO)_2(OSiPh_2)_2$], (20)



[27]

The procedure was the same as that described in **Section 4.4.5.2.** The quantities used were: ferrocenylboronic acid, 0.345g (1.50mmol); diphenylsilanediol, 0.325g (1.50mmol); toluene (50ml). Thin-layer chromatography was not necessary. Orange crystals were formed from dichloromethane-hexane solution (1:1) (0.268g, 43.6%). M.P., 186-188°C. Found: C, 64.0; H, 4.8%. $C_{44}H_{38}B_2Fe_2O_4Si_2$ requires: C, 64.4; H, 4.7%. FTIR (KBr disc) ν_{max}/cm^{-1}: 3070(w), 3023(w), 1592(w), 1457(m), 1430(w), 1392(m), 1375(s), 1349(s), 1295(vs), 1169(m), 1128(m), 1118(m), 1048(w), 1024(w), 999(w), 943(w), 830(m), 742(w), 723(m), 700(s), 589(m), 513(s), 489(m). ^{1}H NMR ($CDCl_3$, p.p.m.): 7.75-7.10 [m, 20H, $C_6\underline{H}_5Si$]; 4.80-3.70 [m, 18H, $C_5\underline{H}_5FeC_5\underline{H}_4B$]. ^{13}C NMR ($CDCl_3$, p.p.m.): 133.28, 129.77, 127.03 [all $\underline{C}_6H_5Si$]; 74.20, 72.44, 68.05 [all $\underline{C}_5H_5Fe\underline{C}_5H_4B$] MS (EI), m/z: 820 [$(M)^+$]; 622 [$(M)^+$ - Ph_2Si=O]; 185 {$(Fc)^+$]; 121 [$(CpFe)^+$].

4.4.5.4 Synthesis of [FcB(OSiPh$_3$)$_2$], (21)



[28]

The method follows that previously described in Section 4.4.5.2. The quantities used were: ferrocenylboronic acid, 0.230g (1.00mmol); triphenylsilanol, 0.553g (2mmol); toluene (50ml). Orange crystals were obtained from dichloromethane-hexane (1:1) solution (0.542g, 72.6%). M.P., 189-190°C. Found: C, 73.7; H, 5.2%. $C_{46}H_{39}BFeO_2Si_2$ requires: C, 74.0; H, 5.3%. FTIR (KBr disc), ν_{max}/cm^{-1}: 3067(w), 1020(w), 1589(w), 1486(w), 1452(m), 1429(m), 1377(m), 1346(m), 1320(vs), 1300(vs), 1290(vs), 1260(m), 1188(w), 1163(m), 1118(vs), 1105(s), 1026(m), 998(m), 937(w), 847(m), 816(m), 746(w), 713(vs), 700(vs), 678(vw), 584(w), 556(s), 510(vs), 476(m). ^{1}H NMR ($CDCl_3$, p.p.m.):7.80-7.15 [m, 30H, $C_6\underline{H}_5Si$]; 4.60-3.70 [m, 9H, $C_5\underline{H}_5FeC_5\underline{H}_4B$]. ^{13}C NMR ($CDCl_3$, p.p.m.): 134.22-133.45, 129.25-128.64, 127.03-126.53 [all $\underline{C}_6H_5Si$]; 73.30, 71.87, 68.03 [all $\underline{C}_5H_5Fe\underline{C}_5H_4B$]. MS (EI), m/z: 747 [$(M)^+$]; 682 [$(M)^+$ - Cp]; 488 [$(M)^+$ - Ph_3Si]; 411 [$(M)^+$ - Ph_4Si]; 121 [$(CpFe)^+$].

CHAPTER 5

MICROWAVE-ASSISTED SYNTHESIS OF INTERCALATION COMPOUNDS DERIVED FROM IRON OXYCHLORIDE

5.1 INTRODUCTION

This chapter describes microwave-assisted synthesis of intercalation compounds derived from iron oxychloride (FeOCl). Ferrocene, ferrocenylboronic acid and $[(FcBO)_2(Bu^t_2SiO)_2]$ (19), one of the borosilicate compounds formed in **Chapter 4**, are amongst the guest species employed in these reactions. The products are characterised chiefly by powder X-ray diffractometry (PXRD) and Mössbauer spectroscopy.

These intercalation reactions were instigated to find new ways to ferrite precursors. However, the chemistry of the FeOCl intercalation compounds is so intriguing and complicated that this chapter can only discuss their preparation and characterisation. A thorough introduction on the intercalation chemistry of FeOCl along with an explanation of the microwave dielectric heating effect is first given.

5.1.1 Definition of Intercalation

The term "intercalation" describes the insertion (usually reversible) of mobile guest species, G, (atoms, molecules or ions) into a host lattice, H, which contains an interconnected system of vacant lattice sites (□). Intercalation can be represented by equation [1].

$$xG + \square_x[H] \rightleftharpoons G_x[H] \qquad [1]$$

The intercalation technique was first discovered by the Chinese around 600-700 A.D.[180] when they formed porcelain from the intercalation of alkali metal ions into common minerals such as quartz and kaolin.[181] The first intercalation process to be reported in Western scientific literature was described by Schafhautl in 1840[182] when he observed the dissolution of graphite in sulphuric acid. Eighty-six years later, Fredenhagen noted the uptake of potassium vapour into graphite.[183] However, it is in the last two decades that intercalation reactions have attracted increased attention leading to over 5000 scientific papers being published on this subject. The main

reason for this interest is the possible design of materials with a variety of applications such as catalysts, solid electrolytes, sensors, electrochromic displays and batteries. Intercalation reactions may be described as topochemical processes as the structure of the host lattice remains the same in the forward and reverse reactions as described in equation [1]. The reactions often occur at ambient temperatures, unlike solid-state processes that need temperatures in excess of 600°C. Host lattices that can undergo intercalation include framework (3-D), layer (2-D) and linear chain (1-D) lattices as schematically represented in **Figure 5.1**. In 3-D lattices, the sizes of the guest species have to be specific in order to enter the empty lattice sites. But in the 2-D host lattices (layered compounds), guest species of different sizes can enter because the host layers have the ability to expand and accommodate the guest species.

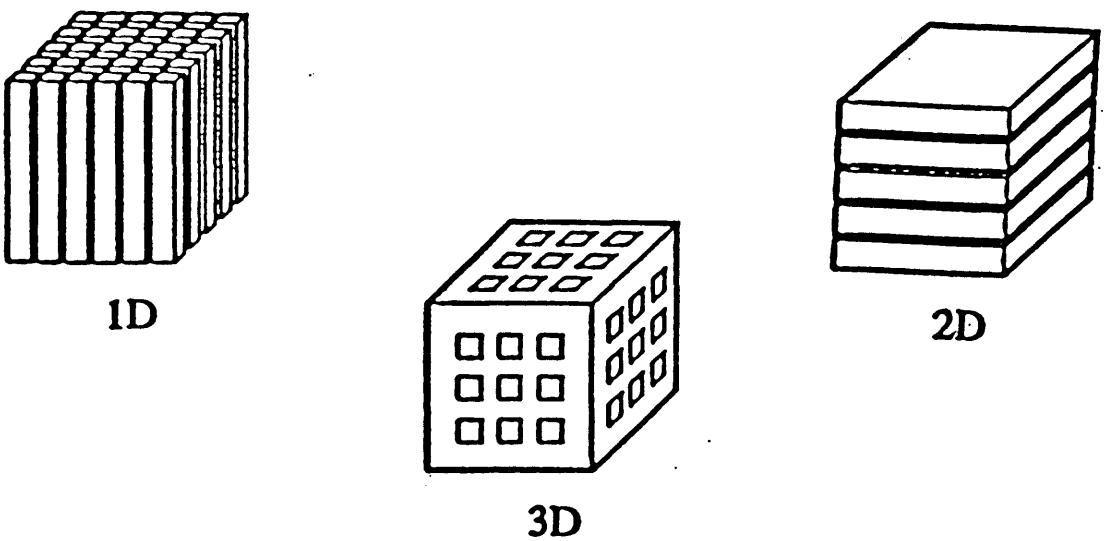


Figure 5.1 A schematic illustration of different host lattice geometries for intercalation.

This flexibility in the layered compounds makes them particularly interesting and useful for research. Examples of host lattices are given in **Table 5.1** and examples of guest species are given in **Table 5.2**. Only the layered host structures will be discussed in detail. Amongst the different types metal, dichalcogenides and metal

oxyhalides have received most attention. The layered host lattices are characterised by strong intralayer interactions and weak interlayer interactions, which are of the van der Waals type for neutral layers and of electrostatic forces for charged layers. The intercalation of a guest species into a layered host lattice often occurs *via* a redox reaction as described by equation [2].

$$xG \longrightarrow (xG^{+} + xe^{-}) \text{ to } [H] \longrightarrow G_x^{+}[H]_x^{-}[H]_{1-x} \qquad [2]$$

Table 5.1 Host Lattices for Intercalation

Three-dimensional structures

Zeolites $M_x^{+}(Al_xSi_{2-x}O_2).nH_2O$[184,185]

β-Alumina[186]

Perovskite related oxides WO_3, ReO_3, V_6O_{13}[187,188,189]

Rutile oxides MO_2 (M = Ti, Mn, Cr, Mo, W, Ir)[189]

h-WO_3[187,190]

Two-dimensional structures

Clays and layered silicates[184,191]

Hydrous oxides[192]

Layered double hydroxides $Zn_2Cr(OH)_6Cl.2H_2O$[193], $Ni(CN)_2$[194]

Graphite[195]

Metal Dichalcogenides MX_2 (M = Ti, Zr, V, Ta, Mo; X = S, Se)[196,197,198]

Metal Oxides MxOy (MoO_3, V_2O_5, $LiNbO_2$)[199,200]

Metal Oxyhalides MOX (M = Ti, V, Cr, Fe; X = Cl, Br[201,202]

One-dimensional structures

MX_3 (M = Ti, Zr, Hf, Nb, Ta; X = S, Se)[203,204]

$AFeS_2$ (A = Na, K, Rb, Cs)[205]

AMo_3X_3 (A = Group 1; X = S, Se)[206]

Table 5.2 Examples of guest species that exhibit intercalation reactions

Guest type	Examples	Host Lattices	Refs.
Atomic Ions	H^+	MO_3	207
	Li^+, Na^+, K^+, Cs^+	MS_2, FeOCl	208, 209
	La^{3+}, Ce^{2+}	TaS_2	210
Molecular Ions	NH_4^+, NR_4^+	MS_2	211, 181
	HSO_4^-	Graphite	212
	$[M(Cp)_2]^+$ (M = Co, Cr)	MS_2	213
	$[Pt(NH_3)_4]^{2+}$	TaS_2	214
	$Co[(PMe_3)_3(C_2H_4)]^-$	Graphite	215
Neutral Molecules	NH_3, NR_3, NR_2H, NRH_2, $H_2N(CH_2)nNH_2$	TaS_2, FeOCl	216, 217
	Py, RNC, R_3PO, $RCONH_2$, RCN, RNO_2	MS_2, MO_3	181, 218
	DMSO, THF, DME, pyrrole	MS_2, FeOCl	219
	Perylene ($C_{20}H_{12}$)	FeOCl	220
	$[M(Cp^a)_2]$ (M = Co, Cr, Fe, Ni)	MS_2, FeOCl	221
	$[Fe(Cp^*)_2]$	FeOCl	221
	TTF, TTN, TTT, TMTTF	FeOCl	222
	$(MeO)_3P$, Et_3P	FeOCl	223
	ET	FeOCl	224
	$[XeOF_4]$, $[XeF_4]$, $[XeF_6]$	Graphite	216
	$[Fe_6S_8(PEt_3)_3]$	TaS_2	225
	$[SnMe_3(NMe_3)]$, $[Sn(NMe_2)_4]$	FeOCl	226

Cp = η^5-C_5H_5, Cp* = η^5-C_5Me_5,
DMSO = dimethyl sulfoxide, THF = tetrahydrofuran, DME = dimethoxyethane,
TTF = tetrathiofulvalene, TTT = tetrathiatetracene,
TMTTF = tetramethyltetraselenafulvalene, TTN = tetrathianaphthalene,
ET = bis(ethylenedithio)tetrathiafulvalene

A very common stipulation for intercalation in layered compounds is that the host and guest can undergo a redox reaction. For example, the host lattice iron(III) oxychloride, on which the present work is based, is a strong oxidising agent. Intercalation of reducing agents into this host lattice is feasible. A brief mention on the mechanism(s) of intercalation, possible synthetic processes for intercalation and different analysis techniques for investigating the structures and properties of intercalation compounds is presented below.

5.1.2 Mechanism of Intercalation[227]

The intercalation process is complicated as it involves the breaking of bonds in the host lattice and the formation of new interactions between the guest and the host. In layered compounds, this leads to an increase in the basal spacing of the unit cell. The expansion of the layers needs a significant amount of energy, which is accommodated in the process of "staging". "Staging" refers to placing guest species in some interlayers while leaving others vacant. The order of staging is given by the number of layers between successive filled or partially filled layers as shown in **Figure 5.2**. **Figure 5.2** also demonstrates the changing in the stacking mode of the layers to give rise to a layer shift.[227]

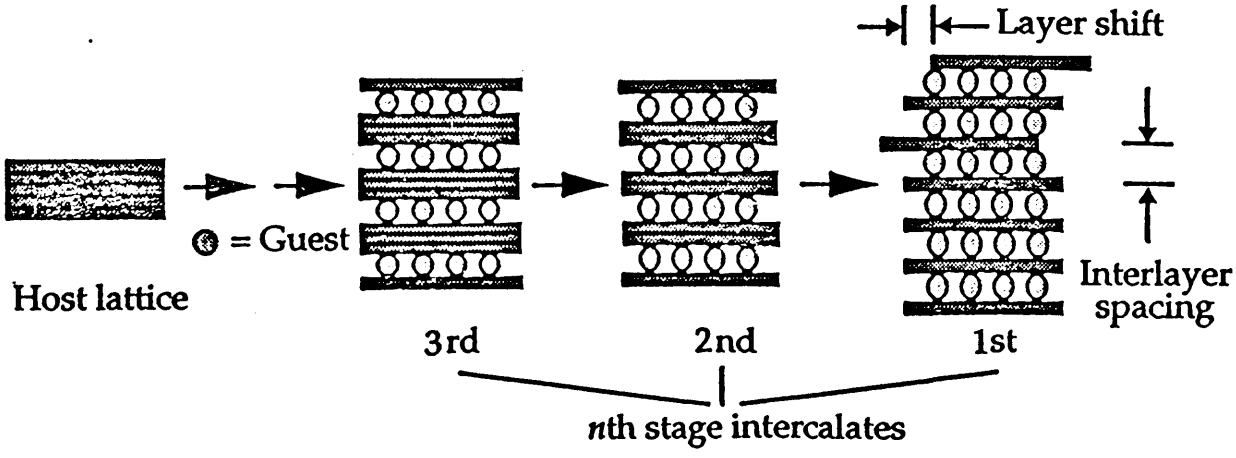


Figure 5.2 Staging process during intercalation of guest species in a layered host lattice leading to (1) change in interlayer spacing and (2) change in stacking mode of layers.[227]

The most widely accepted model for staging has been proposed by Daumas and Herold.[228] The model explains staging in terms of a domain system with all the van der Waals gaps being involved but with local concentrations of the guest species across the basal plane in certain regions as schematically shown in **Figure 5.3.**

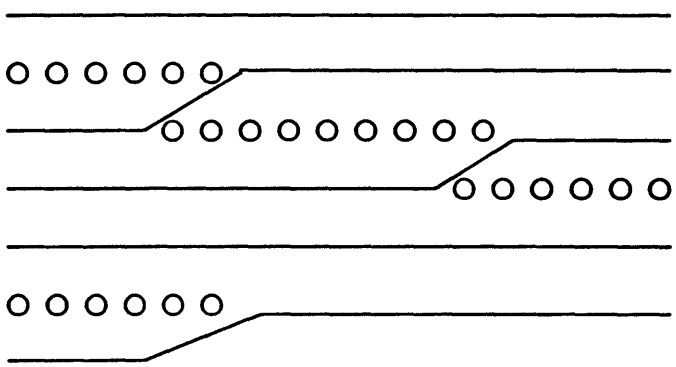


Figure 5.3 Schematic representation of the domain model. The continuous line represents the host layer. The open circles represent a guest layer.

Possible mechanisms of intercalation have been reviewed recently.[229] A study of the time course of intercalation reactions of $VOPO_4.2H_2O$ by *in situ* powder X-ray diffraction suggested three possible mechanisms of intercalation; (see **Figure 5.4**).

(1) Exfoliation of the host layers, addition of the guest molecules and then recombination of guest/host layers.

(2) Formation of an advancing phase boundary,[230] which separates the original host from the intercalation compound along a reaction "front".

(3) Formation of intercalated and unintercalated layers (i.e. stages) in the lattice. The structure may be ordered or disordered (Hendricks-Teller effect[231]).

Figure 5.4 schematically demonstrates the three different mechanisms. Type (1) is quite rare and needs special conditions such as a microwave radiation assistance.[232] Types (2) and (3) are thought to account for most intercalation reactions.

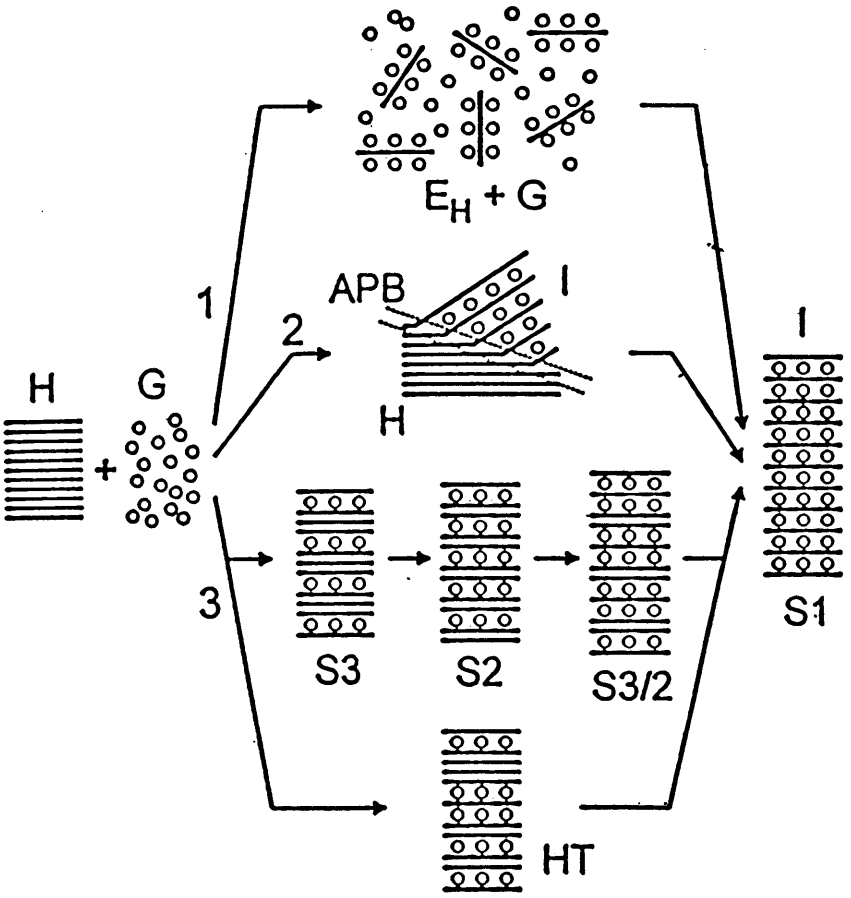


Figure 5.4 Schematic representation of the intercalation mechanisms. H – host, G – guest, I – intercalate, EH – exfoliated host layers, APB – advancing phase boundary, S3, S2, S3/2 and S1 – stages, HT – Hendricks-Teller disordered layer structure.[229]

5.1.3 Synthetic Methods

Preparation of the layered compound FeOCl involves a solid-state reaction between $FeCl_3$ and α-Fe_2O_3. Both solids are held in an evacuated sealed Pyrex tube and reacted at 370°C for *circa* five days. Violet blade-like crystals of FeOCl are afforded in yields of 50-60%.[233]

Guest species can be intercalated into the FeOCl lattice by either direct reaction of the guest with the host, or by treating the host with a solution containing the guest. Reactions have been carried out in sealed, evacuated tubes at temperatures ranging from 60-120°C and for times between minutes and several months. The choice of solvent is critical as increasing the polarity of the solvent increases the rate of

intercalation. However, if the solvent's polarity is too high, it may compete with the guest species for intercalation. Therefore, a careful choice of solvent must be made and usually can only be determined during the course of each specific experiment by trial and error. The direct method, as described above, is used extensively for intercalation in iron(III) oxychloride.

Other synthetic intercalation methods exist with the two most popular being electrochemical intercalation and ion-exchange reaction.[234] Rate enhancement methods such as the use of microwave radiation, extensively discussed in **Section 5.1.7**, are also known. Electrochemical intercalation involves the host lattice serving as the cathode of an electrochemical cell (where reduction of the host layer occurs) and its advantages over the direct technique are (a) ease of control of stoichiometry and (b) enhanced reaction rate at room temperature. An example is the intercalation of Cu^+ ions into TiS_2 layers by electrochemical means,[235] with the formation of Cu_xTiS_2 ($x_{max} = 0.9$) and using $CH_3CN/CuCl$ as the electrolyte. The ion-exchange technique involves the replacement of ions in an intercalated compound with other guest ions and occurs on immersion of the material in a concentrated solution containing the potential guest ion. It is the large excess of the replacement ion which drives the exchange reaction. An example of this type of reaction is the replacement of Na^+ ions by Li^+ ions in TiS_2, as shown in equation **[3]**.

$$Na_xTiS_2 + Li[PF_6] \longrightarrow Li_xTiS_2 + Na[PF_6] \qquad [3]$$

5.1.4 Methods of Analysis

The study of intercalation reactions draws widely from many facets of organic, inorganic, physical and analytical chemistry. Techniques such as X-ray and neutron diffraction, Mössbauer spectroscopy, magnetic measurements, infrared spectroscopy, solid-state NMR and electrical measurements have all been employed in studying intercalation reactions.

The most common analysis methods used to study FeOCl and its intercalated compounds are powder X-ray diffraction (PXRD), ^{57}Fe Mössbauer spectroscopy, infrared spectroscopy and electronic conductivity and magnetic studies. PXRD patterns are used primarily to measure the increase in basal spacing in the FeOCl lattice due to intercalation and any other structural changes in the unit-cell lattice such

as going from primitive to body-centre. Real-time *in situ* PXRD experiments have been used to study mechanisms and kinetics of intercalation reactions.

Mössbauer spectroscopy has become an important analytical technique in the study of FeOCl and its intercalated compounds. ^{57}Fe Mössbauer spectroscopy observes the interaction between the iron nucleus and its electronic environment using gamma radiation as a probe. A typical Mössbauer spectrum of FeOCl (taken at room temperature) is shown in Figure 5.5.[236] The isomer shift, IS, parameter arises from the interaction between the nucleus and the electrons surrounding it and changes in IS correspond with changes of the oxidation state of iron and its spin state. The quadrupole splitting, QS, parameter arises from the interaction between the nuclear quadrupolar moment and the gradient of the electrostatic field at the nucleus. This relates to the charge environment of the nucleus and in particular, whether it is cubic (e.g. in octahedral or tetrahedral symmetry), or non-cubic (such as that found in FeOCl).

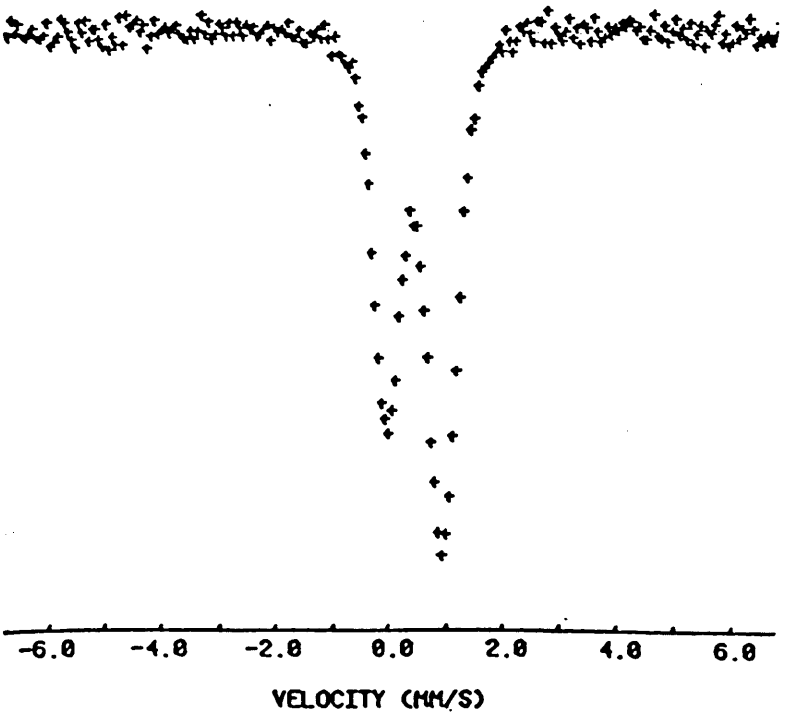


Figure 5.5 Mössbauer spectrum of FeOCl at 298K (IS = 0.39 mms^{-1}, QS = 0.84 mms^{-1}).[236]

As already explained, the intercalation of guest species such as ferrocene into a FeOCl lattice involves a redox reaction and hence Fe^{3+}/Fe^{2+} ions will coexist together within the lattice. The material formed is $FeOCl(ferrocene)_{0.16}$.[201] The two oxidation states of iron can be observed and displayed by Mössbauer spectroscopy. At room temperature, the Fe^{2+}/Fe^{3+} states flip too quickly to be observed by Mössbauer spectroscopy and only a quadrupole doublet is observed for these ions in intercalates of FeOCl. However, at liquid nitrogen temperature (77K), the rate of electron flipping between the two states is decreased to the extent that the ferrous and ferric ions can be observed separately by the Mössbauer technique. One may expect two quadrupole doublets should be observed, one for the Fe^{3+} ions (QS value for Fe^{3+} ions *circa* 1.0 mm s^{-1}), the other for the Fe^{2+} ions (QS value for Fe^{2+} ions *circa* 2.5 mm s^{-1}). In general, these overlap each other and a typical spectrum of the intercalation compound $FeOCl(ferrocene)_{0.16}$ is shown in Figure 5.6.[201] A QS parameter for Fe^{2+} ions of the reduced host can be observed with one peak hidden in the QS of Fe^{3+} and the other appearing at ~2.5 mms^{-1}. A peak representing the oxidised guest (ferrocinium cation) can be distinguished in Figure 5.6. Fe^{3+} types I and II correspond to the different ferric sites on the host lattice. Type I represents Fe^{3+} ions furthest from the ferrocene molecule while type II represents Fe^{3+} ions closest to the ferrocene molecule.

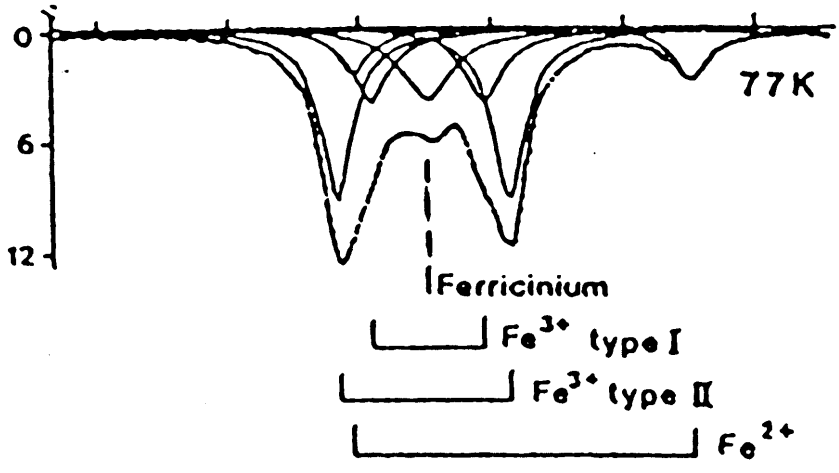


Figure 5.6 Mössbauer spectrum of $FeOCl(ferrocene)_{0.16}$ at 77K.[201]

At this point it should be noted that the Néel temperature (the magnetic ordering temperature that defines the transition from a paramagnetic to a ferromagnetic, or antiferromagnetic state) is observed for FeOCl at *circa* 91K.[217] In the Mössbauer

spectrum, the effect shows a change from a doublet to a sextet. However, a simple sextet-type spectrum is not observed for FeOCl at liquid nitrogen temperature but rather the spectrum is broadened as displayed in Figure 5.7.[236] The broadening has been ascribed to a large distribution of particle sizes in FeOCl some of which may be small enough to exhibit superparamagnetism.[237] Intercalates of FeOCl do not show the magnetic ordering effect and it has been suggested that the Néel temperature is depressed on intercalation (below 77K) and thus no ordering occurs.[237]
Mössbauer spectra can also be used to estimate the amount of reduced (Fe^{2+}) ions present in a sample.

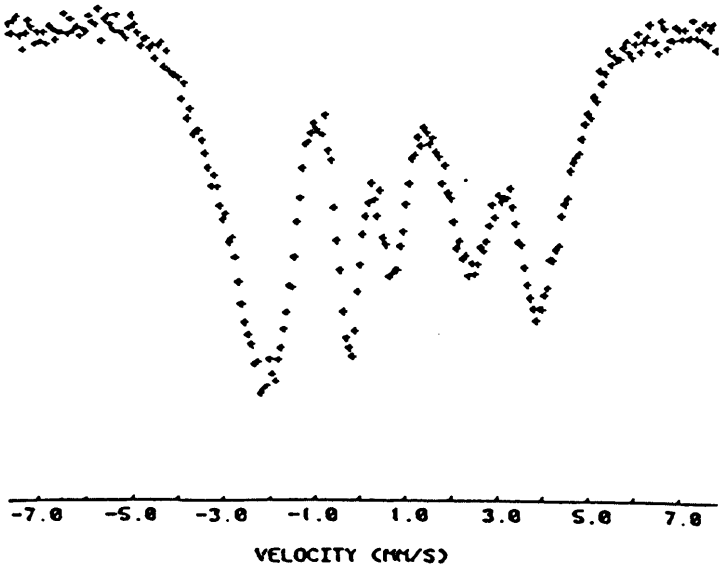


Figure 5.7 Mössbauer spectrum of FeOCl at 77K.[236]

Another important analytical technique for the characterisation of intercalates measures electrical conductivity. Intercalation of FeOCl leads to an increase in conductivity due to the formation of ferrous ions. FeOCl itself is a semiconductor with conductivity in the range of $10^{-7}\Omega^{-1}cm^{-1}$. Intercalation of guest ions into the FeOCl lattice increases this conductivity to around $10^{-2}\Omega^{-1}cm^{-1}$ and this increase in conductivity can easily be measured using pressed pellets of the intercalation compound and the four-probe conductivity method, (see **Appendix E**).

5.1.5 *Iron(III) Oxychloride: Host Structure and Intercalation Properties*

The crystal structure of FeOCl was first described by Goldsztaub[238] and later refined by Lind.[233] It is a layered compound belonging to the orthorhombic space group P*mnm* (D_{2h}^{13}) with two formula units per unit cell. The crystal structure consists of a stack of double sheets of *cis*-$FeCl_2O_4$ octahedra, linked together through oxygen atoms with shared edges along the ac-crystallographic plane. The unit cell dimensions are a = 3.780, b = 7.917 and c = 3.302 Å. The neutral layers of FeOCl are directed perpendicular to the b-direction, with the chlorine atoms forming the outermost atoms of each layer. The bonding across these chlorine atom planes is assumed to be of the van der Waals' type. The van der Waals' interaction is easily disrupted on intercalation and it is the b-cell parameter that is greatest affected. This expansion of the b-plane can be easily interpreted by PXRD studies. **Figure 5.8** displays the layered structure of FeOCl and demonstrates how it changes on intercalation.[201]

Other compounds that adopt the FeOCl structure are VOCl, TiOCl and CrOCl. These metal oxyhalides, however, undergo relatively few intercalation reactions compared to FeOCl. This can be explained by comparison of the M^{3+}/M^{2+} redox potential of each compound. **Table 5.3** gives a list of these values and it shows that FeOCl is the most oxidising. The strong oxidising nature of FeOCl enables the lattice to accept a variety of redox-active guest species. Other species are also accepted including those that are not of a reducing nature. An example of a redox-active guest is ferrocene which intercalates into FeOCl but it isn't reducing enough to intercalate into the other metal oxyhalides (or, the other metal oxyhalides aren't oxidising enough to intercalate ferrocene).

Table 5.3 Reduction Potential ($M^{3+} + e^- \rightarrow M^{2+}$) / V versus standard Hydrogen electrode (SHE) for MOCl hosts.

FeOCl	**0.77V**
VOCl	**-0.25V**
CrOCl	**-0.41V**

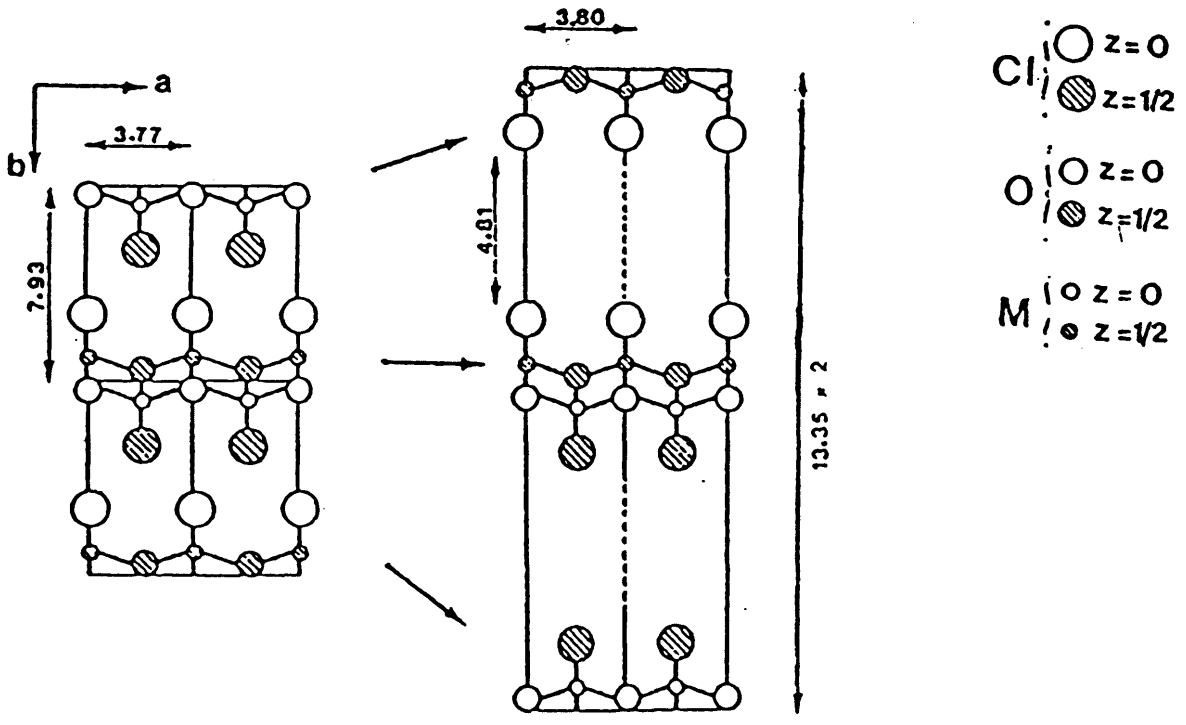


Figure 5.8 Schematic representation of FeOCl layers and their separation during intercalation.

5.1.6 Intercalation Reactions of FeOCl

Attempts to intercalate FeOCl with lithium were first made by treating the host lattice with lithium dissolved in liquid ammonia. However, FeO(NH)Li was produced *via* the formation of $FeO(NH_2)$ on substitution of Cl^- by NH_2^- ion.[201] A lithium intercalate $FeOCl.Li_x$ ($x < 0.50$) has been reported by Palvadeau *et al.*[239] who used Bu^nLi as the reducing agent. In aqueous systems, hydrated alkali intercalation compounds such as $M_{0.14}FeOCl(H_2O)_y$ (M = Li, Na, K and Cs) can be prepared using a chemical reducing agent such as $[Fe(CN)_6]^{4-}$. They exhibit large interlayer spacings that are dependent on the water content which may indicate interactions between solvating water molecules and the chloride layers.

A large number of different amine bases have been successfully intercalated into the FeOCl host lattice. These include ammonia,[217] pyridine and its derivatives,[240] and aliphatic amines such as butylamine and dodecylamine.[217] Herber *et al.*[217] reported a systematic study of ten nitrogen-containing Lewis base intercalates of FeOCl, ranging from ammonia to dodecylamine. The study used PXRD patterns to estimate the

expansion parameter in the b-plane which was observed to range from 3.42Å in $FeOCl(NH_3)_{3/4}$ to 6.89Å in $FeOCl(quinuclidine)_{1/6}$. Mössbauer spectroscopy was used to obtain IS and QS values for each intercalation compound at both room and liquid nitrogen temperatures. However, no Fe^{2+} peaks were detected in the spectra taken at liquid nitrogen temperature and there was no mention of a redox mechanism existing between the amines and the host lattice.[217] Instead, Herber *et al.* explained the structure of the intercalated compounds by suggesting a direct interaction between the lone pairs of the nitrogen atoms and the metal atom of the host matrix. This proposal would place the guest molecules' lone pair electrons parallel to the b-lattice of the host. Later, this model was abandoned, as it became evident that a redox reaction is the important aspect of the mechanism. Recent papers on the intercalation of amine–type systems into FeOCl recognise this fact and Fe^{2+} peaks are usually observed in low-temperature Mössbauer spectra. Current opinion suggests that the amine–type system reduces some of the ferric ions in the host lattice to ferrous ions and an equivalent amount of amine hydrochloride salt is formed.[240] This stays in the expanded layers to balance the charge as shown in equation [4].

$$FeOCl + n\text{Amine} \longrightarrow [(Fe^{2+})_n(Fe^{3+})_{1-n}OCl][\text{AmineH}^+]_n \qquad [4]$$

Pillion *et al.* reported the appearance of Fe^{2+} peaks in the Mössbauer spectrum (taken at low temperatures) of the intercalate formed by the reaction of propargyamine with FeOCl.[241] Although Pillion *et al.* were more interested in the magnetic nature of the intercalate when hydrolysed, they clearly demonstrated the redox nature of the amine-FeOCl compound.

Herber *et al.*[226] later accepted the redox nature of amine intercalation and intercalated organotin compounds (containing amine and pyridine-type functions) into FeOCl. They explained the reduction of ferric ions by oxidation of the tin amines to a positive-charged tin iminium ion. An example of this is shown in equations [5] and [6].[226]

$$2\,(CH_3)_3SnN(CH_3)_2 \rightarrow 2\,(CH_3)_3SnN^{\bullet+}(CH_3)_2 + 2e^- \qquad [5]$$

$$2\,(CH_3)_3SnN^{\bullet+}(CH_3)_2 \rightarrow 2\,(CH_3)_3SnN^{+}(CH_2)=CH_2 + H_2 \qquad [6]$$

This type of intercalation reaction is very similar to that demonstrated for the intercalating of amine bases into metal dichalcogenides.[181] The intercalation of pyridine into a TaS_2 lattice eventually forms the intercalate $TaS_2(py)_{0.5}$.[242] However, the correct formula for this compound is $TaS_2(py)_{0.5-2x}(pyH)_x(bipy)_{x/2}$. This formula accounts for the redox mechanism of intercalation but for convenience sake, the $TaS_2(py)_{0.5}$ formula is often written. This convention is also used for the FeOCl-type systems.

Phosphites and phosphines have also been intercalated into the FeOCl host lattice.[223] Intercalation of trimethylphosphite and triethylphosphines caused an expansion in the b-axis direction by 6.47 and 3.96Å, respectively.[223] Mössbauer and Fourier transform infrared spectra of the intercalates were interpreted as inferring that there is a direct interaction between the lone-pair of electrons of the phosphorus atom and the FeOCl lattice. The Mössbauer spectra didn't give any indication of ferrous ions existing in the lattice. The Mössbauer data exhibited quadrupole doublets for the compounds at 77K with no evidence of the broadening effect by magnetic ordering.[223] A conclusion was that the Néel temperature of FeOCl has been lowered by the intercalation process.

A significant number of organic π-donors compounds have been intercalated into FeOCl. Compounds such as aromatic hydrocarbons,[220] TTF,[222] tetraselenafulvalene (TSF),[243] ET[224] and related molecules[244] have been used as guest species. The intercalation of these compounds occurred with formation of stacks of intercalate-derived cation radicals within the interlayer region.[244] Electrical measurements showed an increase in conductivity for the intercalates but full electron transfer from the guest molecule to the host had prevented the onset of metallic conduction for the above compounds except for the guest molecule ET.[224] In the case of the ET intercalate, structural and electronic studies demonstrated that the material contained stacks that were partially oxidised, with resulted in very high electrical conductivity.[224] Mössbauer spectra indicated the presence of Fe^{2+} ions for all the above intercalation compounds at liquid nitrogen temperature. A representation of the lattice structure of $FeOCl(TTF)_{1/8.5}$ is shown in **Figure 5.9**.[222] The diagram shows two characteristic features in this intercalation process; the expansion of the b-axis layer and the change of the unit cell from primitive to body-centre.

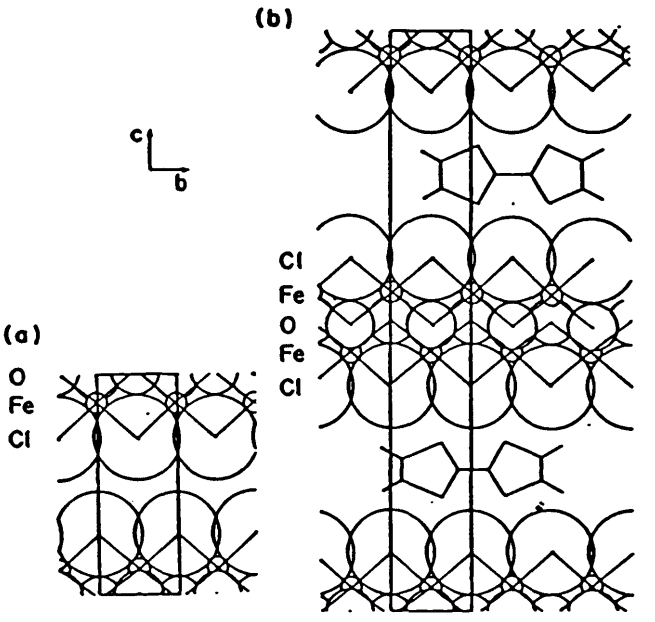


Figure 5.9 Diagram of (a) FeOCl and (b) $FeOCl(TTF)_{1/8.5}$. The unit cell is outlined.[222]

Pyrrole has been intercalated into the FeOCl lattice.[219] It was proposed that polypyrrole (Ppy) and not pyrrole existed in the van der Waals gap, with the suggested formula $FeOCl(Ppy)_{0.34}$.[219] A diagram of the intercalated compound is shown in **Figure 5.10**. The orientation of the polypyrrole was determined by (a) PXRD studies (lattice expansion = 5.23Å) and by (b) further experimentation that showed increased lattice expansion for the intercalative polymerisation of N-methylpyrrole. Four probe pressed-pellet electrical conductivity data showed increased conductivity for $FeOCl(Ppy)_{0.34}$.[219]

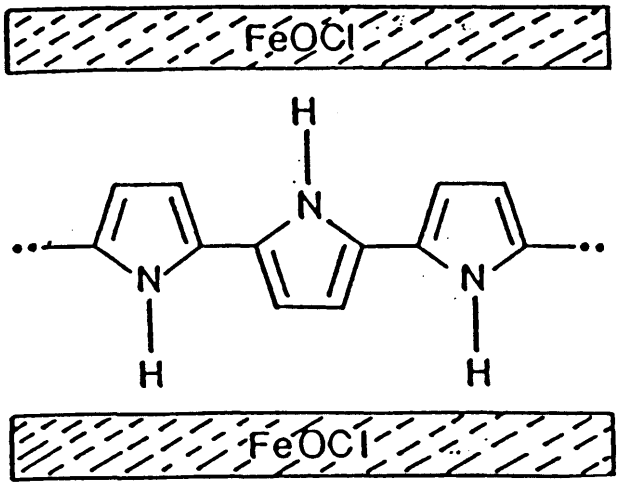


Figure 5.10 Diagram of the intercalation compound $FeOCl(Ppy)_{0.34}$.[219]

FeOCl has been employed as host lattice for the intercalation of aniline.[245] Intercalation resulted in the polymerisation of the aniline in the inorganic framework and hence, the intercalate consisted of alternating monolayers of polyaniline (PANI) and FeOCl monolayers. This material was highly crystalline. **Figure 5.11** shows the proposed structure.[245] The degree of reduction of the FeOCl was 0.1 e^-/mol as suggested from Mössbauer studies.[245] The electrical conductivity of the intercalation compound was 10^{-2} $\Omega^{-1}cm^{-1}$ and it also displayed characteristics of a p-type semiconductor. This suggested that the reduced FeOCl lattice dominated the electronic conduction. The PANI was extracted from its intercalated form by dissolution in acid. The average molecular weight was 3500.[245]

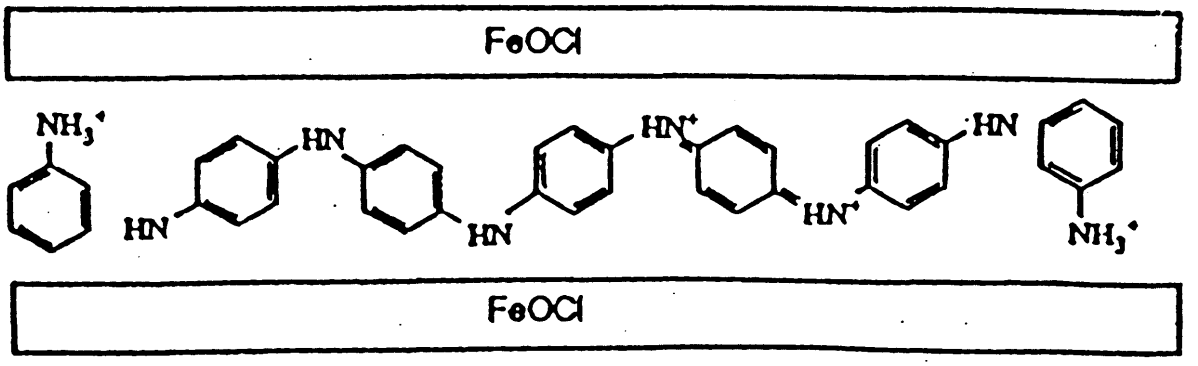


Figure 5.11 Schematic representation of the structure of PANI in FeOCl.[245]

Intercalation of organometallic species such as ferrocene and cobaltocene in FeOCl was first reported by Halbert *et al.*.[221] Structural studies suggested that the metallocenes are accommodated with the η^5-*cyclo*pentadienyl rings perpendicular to the lattice layer as shown in Figure 5.12.[221] The lattice expansion for colbaltocene is 4.94Å and 5.13Å for ferrocene. Mössbauer and magnetic studies suggest complete transfer of the electron from the metallocene guest molecule to the host layer. A review by Rouxel *et al.*[201] also proposed the formation of ferrocenium ions from the oxidation of the ferrocene intercalated in the FeOCl lattice.

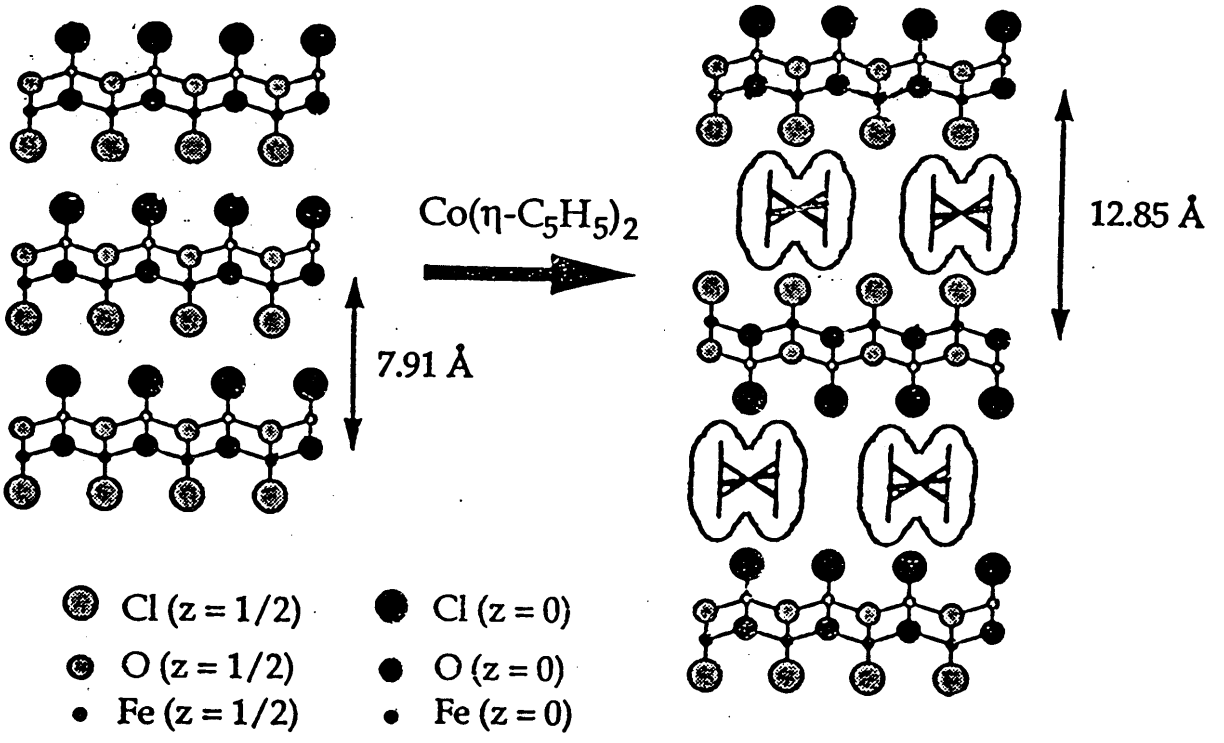


Figure 5.12 Schematic diagram of cobaltocene in FeOCl.[246]

The FeOCl lattice also exhibits a type of interlayer reactivity not found in other systems. Irreversible topochemical substitution reactions are observed where other groups replace the outer halide layers of the FeOCl lattice. For example, the reaction of FeOCl(4-aminopyridine)$_{0.25}$ with methanol at 100°C yielded FeO(OMe).[247] Studies have been performed on reactions of FeOCl with aliphatic and aromatic alkoxides with the resulting products formed as demonstrated in equations [7] and [8].

$$KR + FeOCl \longrightarrow KCl + FeO(R) \qquad [7]$$

$$K_2R + 2FeOCl \longrightarrow 2KCl + (FeO)_2R \qquad [8]$$

As mentioned previously, FeOCl can also be converted to the potential ferrite precursor, γ-FeO(OH), by topotactic hydrolysis. This can be achieved by a number of ways: (1) simple refluxing of FeOCl in water[248], (2) refluxing of FeOCl with 1%

pyridine in water[249] and (3) adding an aqueous solution of NaOH to the layer compound.[250] γ-FeO(OH) can be converted to ferrites by the addition of M^{2+} ions to the material in a 1:2 molar ratio in a basic solution. Subsequent heat treatment affords the product $M^{2+}Fe_2O_4$.[251]

Other recent studies have also investigated the formation of γ-FeO(OH) from intercalation compounds of FeOCl. Sakaebe *et al.* attempted to prepare γ-FeO(OH) from FeOCl previously intercalated with 2,2-bithiophene.[252] The intercalate was stirred in hot water to afford "γ-FeO(OH) including 2,2-bithiophene"[252] rather than just γ-FeO(OH). Sakaebe *et al.* also produced amorphous FeO(OH) including aniline [a_{an}-FeO(OH)] from its corresponding FeOCl analogue.[253] They investigated the compound's charging/discharging characteristics and suggested its use as a cathode material in a rechargeable lithium battery.[253] Pillion *et al.* tried to synthesis γ-FeO(OH) from the intercalate, FeOCl(propargylamine)$_{0.1}$.[241] They used a water:amine (10:90 v/v) medium and a "green rust" was formed instead of the γ-FeO(OH). They concluded that the green rust product was an intercalation compound with some of the chloride ions replaced by hydroxide ions.

5.1.7 Microwave Dielectric Heating and its Application to Intercalation Reactions

Intercalation of guest species into a host lattice is not a simple energetically favourable process as it requires firstly, the expansion of the van der Waals gaps in the interlayers of the host and secondly, the movement of the guest species into these openings. The transport of the guest species from the edges of the layers into the central part of the intercalation host is usually slow. Hence, intercalation reactions frequently require days or months and severe reaction conditions before completion. The long reaction times and severity of the reaction conditions tend to form poorly crystalline products. Since the main structure analysis technique for intercalation compounds is powder X-ray diffractometry (PXRD), reasonable good crystalline products are preferred to avoid broadening the peaks by the amorphous effect. Therefore new preparative techniques have been sought to shorten the time-scale of the intercalation reactions and improve the crystallinity of the products. Rate enhancements have been achieved by the use of ultrasound.[254,255] However, the

microcavitation effects associated with ultrasound have led to poorly crystalline products and hence their structure characterisation was difficult. The microwave dielectric heating effect offers better possibilities for production of intercalation compounds with a high degree of crystallinity. Before discussing reports of intercalation compounds prepared by microwave radiation, a brief comment will be made on the microwave dielectric heating effect and the equipment needed to carry out the experiments.

5.1.8 Interaction of Microwaves with Matter

Microwaves are low-energy electromagnetic radiation with frequencies in between infrared and radio frequencies. They correspond to frequencies of 30 GHz to 300 MHz (wavelengths of 1 cm to 1 m respectively) as shown schematically in **Figure 5.13**. The frequencies between 30 GHz and 1.2 GHz are used for RADAR while the remaining frequencies are used for telecommunications. It was agreed that domestic microwave ovens would operate at 2.45 GHz.

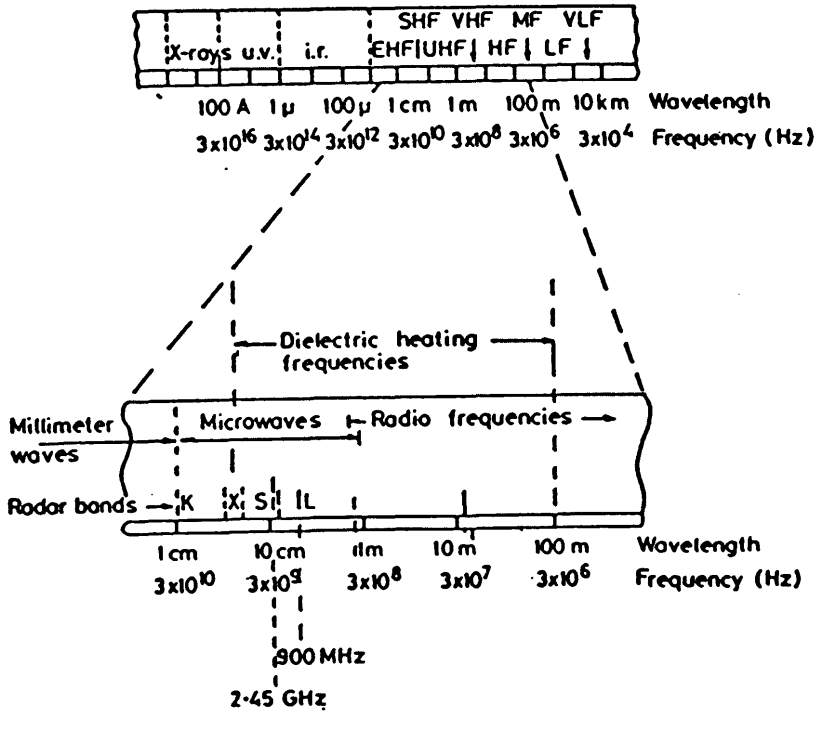


Figure 5.13 The electromagnetic spectrum indicating the microwave frequencies and the frequencies which are used for dielectric heating.

A material is a dielectric if it contains either permanent or induced dipoles that can be polarised in an electric field by rotation of the dipoles. These materials are heated by applying energy in the form of high frequency electromagnetic waves. The origin of the heating effects comes from the ability of an electric field to exert a force on charged particles. Microwave dielectric heating depends on the frequency as well as the power applied. The theory of microwave dielectric heating has been diligently summarised by Mingos *et al.*.[256,257]

A dielectric material can be defined by two parameters, the dielectric constant, ϵ', which describes the ability of the molecule to be polarised by the electric field and the dielectric loss, ϵ'', which measures the efficiency with which the energy of the electromagnetic radiation can be converted into heat. These two parameters can be related by the (dielectric) loss tangent = ϵ''/ϵ'. Loss tangent values of materials are a measure of their efficiency to use microwaves radiation for heating purposes. In general, the larger the loss tangent of a material, the more effective it is in microwave dielectric heating. Table 5.4 lists some common solvents and their loss tangent values at 2.45 GHz.

Table 5.4 Loss tangent values of several common solvents at 2.45 GHz

Type of Solvent	Loss tangent values (unitless)
Water	0.123
Methanol	0.659
Ethanol	0.941
Acetonitrile	0.062
Acetone	0.054
Dichloromethane	0.042
Chloroform	0.091

From the above table one can estimate the efficiency of solvents with respect to microwave heating. For example, acetone should be a more efficient "microwave

solvent" than say dichloromethane and hence should complete microwave reactions in a shorter time.

5.1.9 *Microwave Dielectric Heating at High Pressure Conditions*

The effective coupling between microwaves and polar inorganic and organic solvents raises the temperature and pressure if the reactants are in a closed vessel. Usually, there is an increase in the rate of a reaction. The temperatures and pressures generated in a closed vessel depend on the level of the input microwave power, time of microwave irradiation, the dielectric loss of the reacting solution, the volatility of the solvent, the volume of the container occupied by the solvent and whether gases are generated during the reaction. A typical vessel which can be used for high-pressure microwave synthesis is shown in **Figure 5.14**. The vessel is made of thick walled Pyrex glass and is placed in the microwave cavity through a suitably designed port. Pressure measurement and control can be performed by external circuitry. A photograph of the reaction vessel and the manner in which it is inserted in to the microwave cavity is given in **Figure 5.14**, while the design of the Pyrex reaction system is illustrated in **Figure 5.15**. [258]

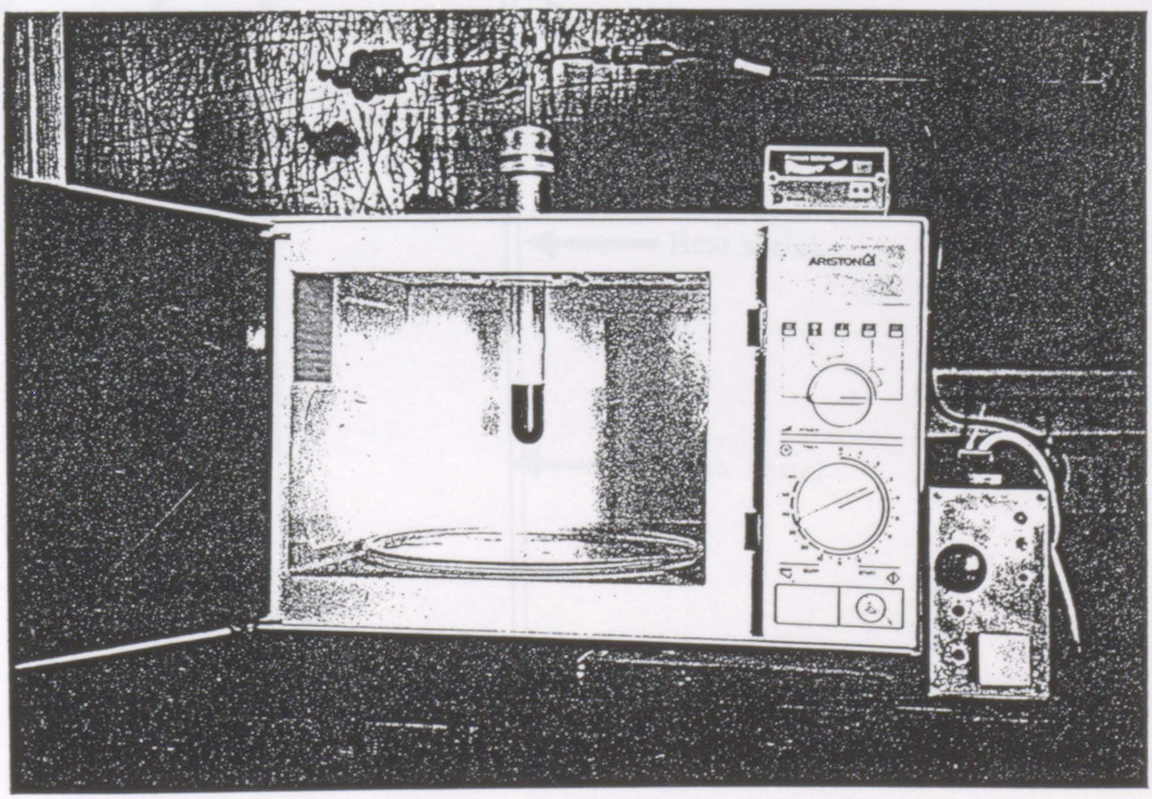


Figure 5.14 The microwave oven with the reaction vessel inserted.[258]

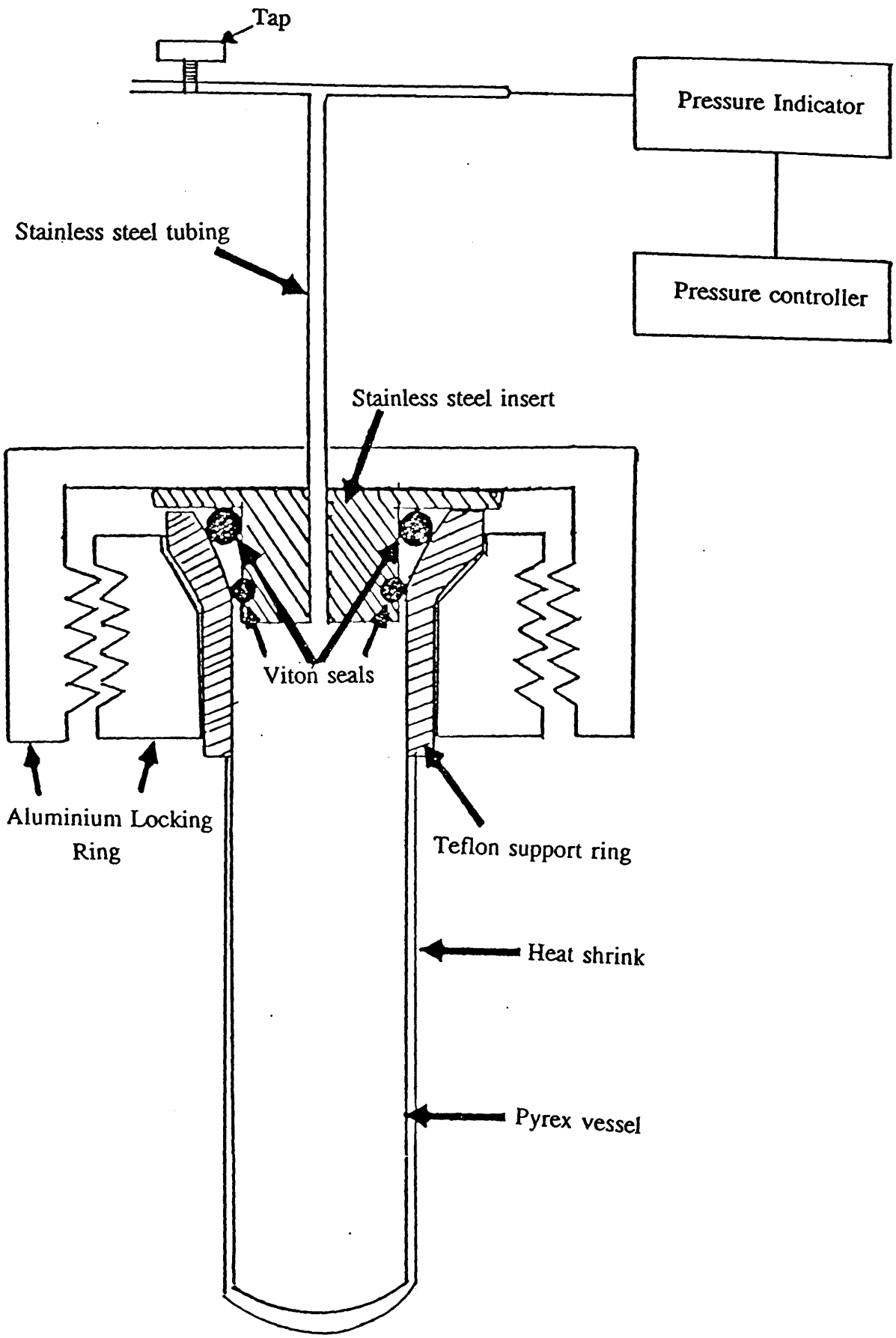


Figure 5.15 Schematic diagram of the high-pressure reaction vessel.

Superheating is known to occur for solvents exposed to microwave radiation in a closed vessel. Superheating means that solvents are heated above their normal boiling points with temperature increases ranging from 40 to 70°C. This occurs by a macroscopic effect similar to that observed in a conventional pressurised cooker. The effect is larger for solvents with low boiling points as high pressures are generated in a short space of time. Table 5.5 gives a list of the temperatures of several common solvents following microwave heating for 10 minutes at a constant pressure of 10 atm along with their boiling points.

Table 5.5 Temperature reached after 10 minutes of microwave heating at a pressure of 10 atm.

Solvent	T / °C	b.p. / °C
Methanol	106	65
Ethanol	117	78
Acetonitrile	142	82
Dimethylformamide	205	153
Dichloromethane	110	40

The superheating effect can be expected to lead directly to acceleration in reaction times compared with conventional reflux conditions.

For organic and inorganic reactions in polar solvents that are accelerated by the microwave dielectric heating effect, the question has been raised: is a specific microwave effect operating or can it be explained by the superheating effect alone. Mingos *et al.*[259] have addressed this question and suggested that the acceleration in reaction rates in a closed vessel (i.e. at high pressures) is due to the superheating effect alone. However, they also postulated that when rate enhancements of 100-1000

fold are observed for microwave reactions at atmospheric pressures, then specific microwave effects might be contributing to the increased rate of reaction.

In summary, microwave dielectric heating can be used to increase the rate of reaction if a suitable polar solvent of a high loss tangent value is used. If a closed vessel is used to generate high pressures, then superheating effects may be solely responsible for accelerating the reaction. Over the last five to ten years, research groups have reported the successful use of microwave dielectric heating in organic,[260,261] organometallic,[262] coordination[263] and solid state chemistry.[264] The microwave technique has also come into use as a preparative technique for intercalation compounds.[265,266]

5.1.10 Microwave Dielectric Heating in Synthesising Intercalation Compounds

As mentioned previously, the intercalation process can be extremely slow with very long reaction times and therefore would be an ideal candidate for rate enhancement *via* the microwave method. Mingos *et al.*[265] have used microwave dielectric heating to intercalate pyridine and substituted pyridines into the layered compound α-$VO(PO_4).2H_2O$. The microwaves caused superheating to temperatures in excess of 200°C at *ca* 50 atm.[265] Under these conditions intercalation was completed within minutes, i.e. an increase of two orders of magnitude over similar reactions by conventional thermal methods. A high degree of crystallinity was observed for the products. Hence the quality of the PXRD data of the products were superior to that for the same products prepared by the conventional thermal technique. In **Figure 5.16** the PXRD pattern clearly shows the presence of two tetragonal phases in the microwave product [**Figure 5.16(a)**] while this is not apparent in the data for the conventional product [**Figure 5.16(b)**].[265]

The microwave method has also been used to prepare layered complexes of vanadyl phosphate with 1-alkanols and 1,ω-alkanediols.[232] Exposure to microwave radiation of $VOPO_4.2H_2O$ in the alcohol solvent formed the product, equation [9]. Evidence for the intermediate $(VOPO_4)_\infty$, which reassembles with the new guest molecules, was found. The exfoliation mechanism of intercalation, which has been mentioned in **Section 5.1.2**, may explain the reaction.

$$VOPO_4.2H_2O(s) + xG(l) \longrightarrow VOPO_4.xG(s) + 2H_2O(l,g) \quad [9]$$

The aliphatic chains of both intercalated alcohol and diol molecules configurations with their axes are perpendicular to the host layers.[232]

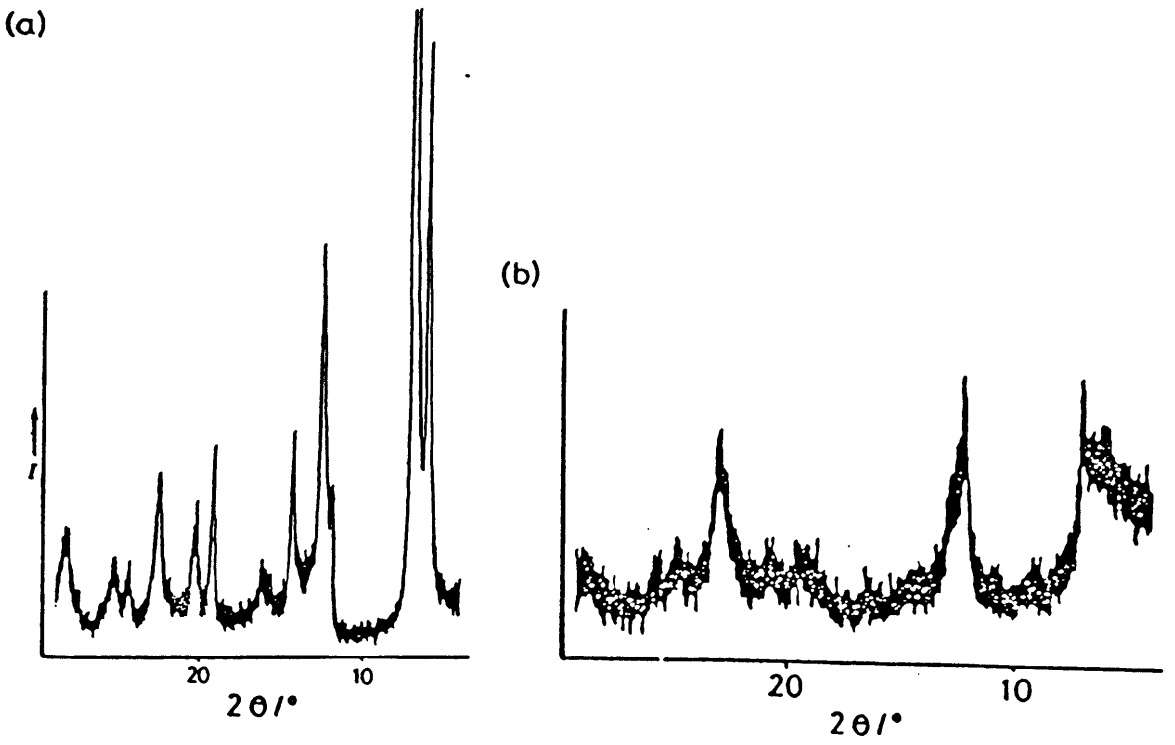


Figure 5.16 A comparison of the PXRD patterns for the intercalation compounds of α-$VO(PO_4)$ with 4-phenylpyridine: (a) microwave product and (b) conventional thermal product.[265]

Benavente and Gonzalez have studied the intercalation of lithium in both titanium and molybdenum disulphides by microwave-assisted processes.[266] Organic and organometallic guest species have also been intercalated by this method into $LiMoS_2$.[266] The reaction is very rapid and about 100 fold faster than that reported using conventional reflux methods.[266] Moreover, the reaction conditions are not very

severe with a temperature of 60°C and pressure of 1 atm. Benevente and Gonzalez concluded that the enhanced rate occurred due to a microwave effect rather than a superheating effect.[266] They also observed different behaviour on intercalating lithium in metal transition dichalcogenides by the conventional and microwave methods and suggested different mechanisms of intercalation staging for the two methods.

5.1.11 Summary

Intercalation reactions are described as the insertion of guest species into a host lattice which contains an interconnected system of vacant lattice sites. The guest species may be atomic ions,[207-210] molecular ions[211-215] or neutral molecules[216-226] while the host lattice may be three-dimensional,[184-190] two-dimensional (layer)[191-202] or one-dimensional[203-206] in structure. The mechanisms of intercalation are usually *via* various staging phenomena[227] but other possible mechanisms such as exfoliation of the host layers have been postualated.[229] Intercalation compounds of the layer host FeOCl are formed by the insertion of molecules or ions into the layer's van der Waals gaps. The reactions are accompanied by electron transfer from the guest molecules to the host lattice and by an increase in the interlayer distance. This has been reported for the intercalation of ferrocene,[221] pyridine[240] and aromatic hydrocarbons.[220] Intercalation compounds are normally prepared by conventional reflux methods but the microwave dielectric heating technique has prepared intercalation compounds of vanadyl phosphate[232] and titanium disulphide.[266] Intercalation compounds *via* the microwave dielectric heating method are formed between 100-1000 times quicker and with a higher degree of crystallinity than the compounds prepared by conventional reflux methods. However, intercalation compounds of FeOCl prepared from microwave dielectric heating techniques have not been reported.

5.2 RESULTS AND DISCUSSION

This section reports the investigation of inclusion compounds prepared from the FeOCl host with ferrocene and derivatives as guest molecules. The conventional thermal method and the microwave dielectric heating method for preparing these compounds are compared. PXRD and Mössbauer spectroscopy were employed as the primary analytical methods.

The microwave-irradiated reactions used the apparatus shown in **Figure 5.14**. Either dichloromethane or acetone was used as medium for these reactions. In the ferrocene intercalation reactions, the medium's colour was blue-green at the end of the reaction. This suggested that the ferrocene had been oxidised to its ferrocenium cation.

5.2.1 Preparation of Intercalation Compounds

The layer host, FeOCl, was prepared according to previous reports.[233] The reaction between α-Fe_2O_3 and $FeCl_3$ in a 1:1.3 molar ratio in a sealed Pyrex glass tube at 370°C for 5 days afforded red-violet blade-like crystals of FeOCl. The product was washed with acetone to remove any excess $FeCl_3$. PXRD and elemental analyses were used to determine that each batch of FeOCl was pure.

Intercalation compounds of FeOCl were synthesised by two methods. The first method employed conventional reflux techniques and was used to synthesis intercalates with ferrocene and 4-aminopyridine (Apy) as the guest species. The reactants were heated at 110°C in a sealed, evacuated, ampoule for 7 days. This technique had been used for all of the intercalation compounds prepared with FeOCl as the host structure.[217,223,226] However, the method can lead to poorly crystalline products and hence, poor structural characterisation. This was the case in the present work with ferrocene and 4-aminopyridine.

The second preparative technique involved microwave dielectric heating. This was used in the formation of intercalates with ferrocene, ferrocenylboronic acid and Apy as the guest species. The reaction times ranged from 3 to 120 minutes and the pressure was never allowed to exceed 10 atmospheres. A high degree of crystallinity was found for the products. Microwave heating was also used in attempts to intercalate $[(FcBO)_2(Bu^t_2SiO)_2]$ (19) into FeOCl.

Either acetone or dichloromethane was used as the medium in the microwave method. These media were employed because (1) both heat quickly when irradiated by microwaves and (2) they did not form intercalation compounds with FeOCl (as determined by elemental analyses and PXRD profiles). As described in **Section 5.1.8,** acetone possesses a higher loss tangent than dichloromethane and therefore, should heat quicker in a microwave field. This should lead to shorter reaction times. This was observed in the microwave reaction of ferrocene with FeOCl. When acetone was employed as solvent, the reaction was completed in three minutes. The reaction was slower in dichloromethane with a reaction times up to two hours. The use of dichloromethane as a microwave solvent may first appear redundant as it slows reaction times but it has two important features:

(1) It reduces the decomposition of the product (decomposition was observed after only five minutes in acetone while no decomposition was seen even after two hours in dichloromethane).

(2) It facilitates a study of the intercalation reaction mechanism.

The second feature may be related to previous experiments which observed *in situ* PXRD of the intercalations of water and ethanol into vanadyl phosphate ($VOPO_4$).[240] The analysis of the products after different reaction times using PXRD data can provide useful information in a study of the reaction mechanism.

Elemental analyses (C, H, Cl and Fe) were used to estimate the stoichiometry of each intercalate. These are given in **Table 5.6** along with the reaction times. The stoichiometries are based on C, Cl and Fe analyses. The rates of reaction of the intercalation materials using the microwave technique are between 100 – 1000 times faster than the rates for intercalation with the conventional thermal technique. However, concentration of ferrocene and Apy in the microwave-produced intercalation compounds never become as high as those previously reported i.e. $FeOCl(ferrocene)_{0.16}$[221] and $FeOCl(Apy)_{0.25}$[247].

Intercalation of ferrocenylboronic acid was apparent after fifteen minutes reaction time in acetone. It should also be noted that intercalation of ferrocenylboronic acid by the conventional reflux method was attempted with a reaction time of several weeks but no product was obtained as determined by elemental analyses and PXRD studies. This suggests that ferrocenylboronic acid is much more difficult to intercalate into

UNIVERSITY COLLEGE Library

FeOCl than ferrocene. As already explained, intercalation occurs *via* a redox mechanism with the guest molecules donating electrons to the host lattice. The electron withdrawing nature of the boronic acid on the ferrocene system makes this compound more difficult to oxidise and therefore, more difficult to intercalate into FeOCl.

Table 5.6 Calculated stoichiometries of prepared intercalation compounds.

Guest Species	Preparative method	Solvent	Reaction Time	Stoichiometry	Intercalate Number
Ferrocene	Conventional	Tol.[a]	7 days	$FeOCl(Fc^{c})_{0.07}$	**(32)**
Apy	Conventional	Me_2CO[b]	7 days	$FeOCl(Apy)_{0.17}$	**(33)**
Ferrocene	Microwave	Me_2CO	3 min.	$FeOCl(Fc)_{0.07}$	**(34)**
Ferrocene	Microwave	Me_2CO	5 min.	$FeOCl(Fc)_{0.07}$	**(35)**
Ferrocene	Microwave	CH_2Cl_2	10 min.	$FeOCl(Fc)_{0.10}$	**(36)**
Ferrocene	Microwave	CH_2Cl_2	20 min.	$FeOCl(Fc)_{0.11}$	**(37)**
Ferrocene	Microwave	CH_2Cl_2	30 min.	$FeOCl(Fc)_{0.12}$	**(38)**
Ferrocene	Microwave	CH_2Cl_2	40 min.	$FeOCl(Fc)_{0.12}$	**(39)**
Ferrocene	Microwave	CH_2Cl_2	120 mins	$FeOCl(Fc)_{0.12}$	**(40)**
$FcB(OH)_2$[d]	Microwave	Me_2CO	10 min.	$FeOCl(FcB(OH)_2)_{0.00}$	**(41)**
$FcB(OH)_2$	Microwave	Me_2CO	15 min.	$FeOCl(FcB(OH)_2)_{0.04}$	**(42)**
$FcB(OH)_2$	Microwave	Me_2CO	20 min.	$FeOCl(FcB(OH)_2)_{0.06}$	**(43)**
$FcB(OH)_2$	Microwave	Me_2CO	30 min.	$FeOCl(FcB(OH)_2)_{0.06}$	**(44)**
$FcB(OH)_2$	Microwave	Me_2CO	40 min.	$FeOCl(FcB(OH)_2)_{0.06}$	**(45)**
Apy	Microwave	Me_2CO	5 min.	$FeOCl(Apy)_{0.10}$	**(46)**

[a] = toluene, [b] = acetone, [c] = ferrocene and [d] = ferrocenylboronic acid.

5.2.2 *Infrared Spectroscopy*

FeOCl has absorption bands at 470, 800, 1095 and 1262 cm^{-1} with the Fe–O–Fe band at 470 cm^{-1} being the strongest. This band is similar to the absorption band (at ~550 cm^{-1}) observed for Fe-O bonding in the glass-ferrites of **Chapter 3** (see **Section 3.2.4**). Many of the organic groups of the guest species were clearly observed in the spectra since there were no overlapping peaks from the inorganic host. **Table 5.7** lists the major features in the intercalation compound's FTIR spectra with assignments to the vibration frequencies of the organic species.

Table 5.7 Significant peaks in typical FTIR spectra of intercalation compounds (acetone as medium).

Intercalate Number	Guest species	Wavenumber (ν/cm^{-1})	Characteristic Bond absorption
(34)	Ferrocene	3093	Ar[a]C-H stretch
3 min.		1408	Ar C-C stretch
		1108	C-H bend (in plane)
		822	C-H bend (out of plane)
(45)	$FcB(OH)_2$	3100	Ar C-H stretch
40 min.		1470	Ar C-C stretch
		1310	B-O stretch
		820	C-H bend (out of plane)
(46)	Apy	3250	N-H stretch
5 min.		3050	Ar C-H stretch
		1648	N-H bend
		1600	Possible NH_3^+ bend
		1523	Ar C-C stretch
		1196	Ar C-N stretch
		817	C-H bend (out of plane)

[a] = aromatic.

5.2.3 *Intercalation of Ferrocene into FeOCl*

5.2.3.1 *PXRD Analysis*

The intercalation of ferrocene into FeOCl has been described before.[221] Intercalation was achieved with conventional reflux methods with either hexane or toluene as solvent. A calculated basal spacing of 13.06Å was obtained from PXRD studies.[221] Thus, the lattice expansion from unintercalated FeOCl was 5.14Å. This reaction was repeated in the current work by both the conventional and microwave techniques. The conventional method formed intercalate (32) after a week reflux in toluene. The microwave method prepared intercalates (34) and (35) in acetone in reaction times of 3 minutes and 5 minutes, respectively. The results, in terms of lattice expansions, are listed in Table 5.8.

Table 5.8 Estimations of basal spacings of intercalated FeOCl calculated from PXRD patterns.

Intercalate Number	Method of Preparation	Guest Species	Interlayer Spacing (Å)	Lattice Expansion (Å)
FeOCl	Conventional	None	7.92	None
(32)	Conventional	Ferrocene	13.13	5.21
(34)	Microwave	Ferrocene	13.01	5.09
(35)	Microwave	Ferrocene	13.00	5.08

5.2.3.1.1 *Reaction in Acetone.*

The results in Table 5.8 compare favourably to those previously reported[221] suggesting that the ferrocene has intercalated in the same way, i.e. with the η^5-*cyclo*pentadienyl rings aligned perpendicular to the lattice layer as demonstrated in Section 5.1.6, Figure 5.12. The essential differences between the two methods used in the present work were reaction times and crystallinity of the products. The microwave method produced the intercalated material in three minutes with acetone as medium and the product was highly crystalline. The conventional method took one

week and the product was not as crystalline. Figure 5.17 shows the difference in crystallinity of the above products as seen in the PXRD profiles. The PXRD pattern of the microwave product is obviously better than its conventional product indicating less amorphous material and better crystallinity. The PXRD pattern of (34) only showed one major peak (010) with the peaks at higher 2θ values (that are seen in the FeOCl pattern) apparently missing. This is a consequence of layer expansion. The ac-crystallographic plane becomes disordered and hence not observable by PXRD. The appearance of a very intense (010) peak relative to peaks at higher 2θ values in an intercalate's PXRD pattern has been reported previously.[221] Observation of relatively intense peaks at high 2θ values in an intercalation compound's pattern generally is interpreted as a sign of incomplete intercalation with either some of the FeOCl layers unfilled or a mixture of FeOCl and unintercalated FeOCl.

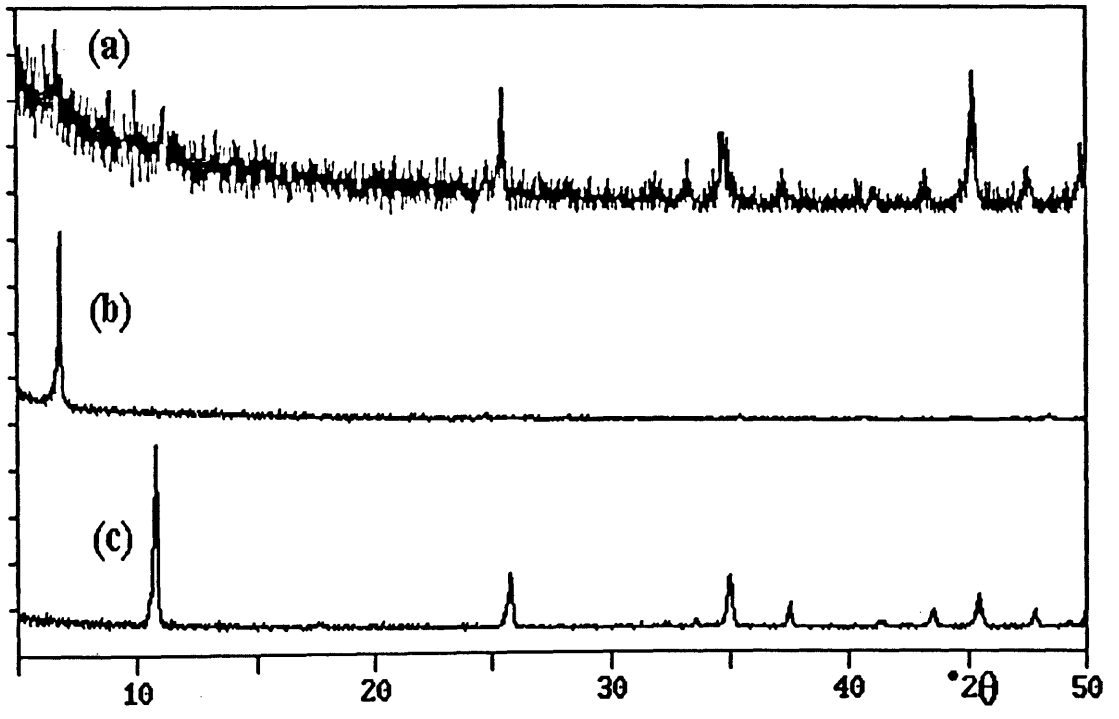


Figure 5.17 PXRD patterns of intercalation compounds prepared by (a) conventional reflux methods (110°C for 1 week in toluene) (32) and by (b) microwave dielectric heating (3 minutes in acetone) (34). (c) PXRD pattern of pristine FeOCl.

The intercalation of ferrocene into FeOCl by microwave dielectric heating has not been reported before. The intercalation reaction was very rapid with acetone as the microwave medium. Moreover, prolonged (i.e. > 5 minutes) exposure to microwave

radiation led to decomposition of the material in this medium. Therefore, intercalation of ferrocene was studied with a medium with a lower loss tangent value, i.e. dichloromethane.

5.2.3.1.2 Reaction in Dichloromethane.

Black, highly crystalline product was obtained with no signs of decomposition even after two hours of microwave heating in dichloromethane. PXRD profiles were taken of the product at different reaction times and the results are schematically shown in **Figure 5.18**.

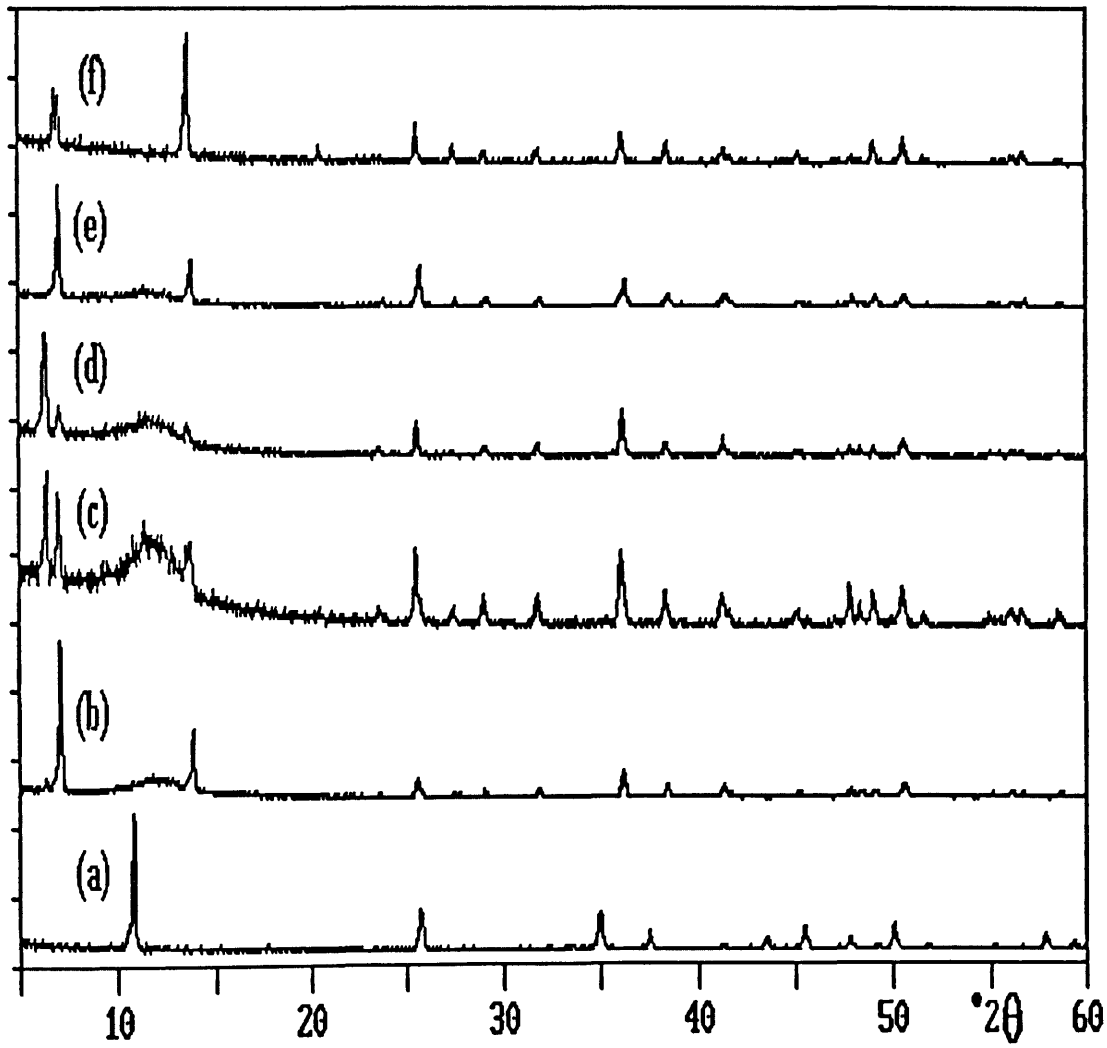


Figure 5.18 Intercalation of ferrocene into FeOCl with dichloromethane as microwave solvent and at different reaction times: (a) zero min., (b) 10 min. (36), (c) 20 min. (37), (d) 30 min. (38), (e) 40 min. (39) and (f) 120 min. (40).

The results are noteworthy in several aspects. Intercalation has occurred in all products with a consequent rearrangement of the FeOCl lattice. However, even after two hours reaction, intercalation still doesn't appear to be complete.

More than one (010) peak is observed (between $2\theta = 6.2$ and 7.1°) for several of the products in **Figure 5.18**, suggesting an expanded lattice with different interlayer distances. This may indicate a two-phase system due to different orientations of the ferrocene guest molecules in the layers. This phenomenon has been reported before for the intercalation of tetramethyltetrathiafulvalene (TMTTF) into FeOCl.[222] Two (010) peaks equivalent to d = 13.59 and 11.94Å were observed in the PXRD data, which could correspond with two orientations of TMTTF within FeOCl. The spacings were consistent with TMTTF lying perpendicular (13.59Å) and parallel (11.94Å) to the FeOCl layers.[222] Unfortunately, the sizes of the two different orientations of ferrocene are very similar (6.60Å lying perpendicular and 6.70Å lying parallel to the FeOCl layers)[267] and therefore, this difference does not explain the two d-spacings in the PXRD data.

The different lattice expansions may be the physical evidence of different mechanisms in the intercalation of FeOCl. Staging has never been directly observed in FeOCl intercalation compounds even though it has always been presumed that the reactions occurred through this mechanism. At one level, different staging may explain the different lattice expansions yet the sequence of the patterns in **Figure 5.18** cannot simply be explained by a single staging mechanism. If the reaction mechanism stuck rigidly to staging, then the highest level of staging would appear first to be replaced eventually by the lower levels of staging. Apparently this is not observed. Rather oscillations of the different lattice spacings are recorded, **Figure 5.18**, in the 2θ range of 6.2 to 7.1°. This may suggest an intercalation model that contains disordered staging, akin to the Hendricks-Teller effect explained in **Section 5.1.2.**[231]

Another curious observation in the patterns is the disappearance of the unintercalated FeOCl lattice spacing. The peak at $2\theta = 11.3^{\circ}$ (representing the (010) layer of FeOCl) becomes broad and apparently amorphous as the reaction evolves, see patterns (b) to (e) in **Figure 5.18**. The reason for this may be the breakdown of the FeOCl crystals to small crystallites as the intercalation reaction proceeds, i.e. some exfoliation takes place.

The peaks at high 2θ values in **Figure 5.18** are relatively intense for each compound. This suggests that intercalation is not complete and may postulate the existence of unintercalated layers within the intercalation compound or a mixture of FeOCl and intercalation compound.

Table 5.9 reports the lattice expansions of the intercalation compounds. The expansions range from 5.92Å to 4.62Å, which can be compared with the lattice expansion of the intercalation compound prepared from ferrocene with acetone as microwave medium of 5.08Å.

Table 5.9 Calculation of lattice expansions of intercalates prepared from ferrocene and FeOCl by the microwave method with dichloromethane as medium.

Intercalate Number	Time of Reaction	Interlayer Spacing (Å)	Lattice Expansion (Å)
(36)	10 min.	12.58	4.66
(37)	20 min.	13.84 / 12.64	5.92 / 4.72
(38)	30 min.	14.19 / 12.59	5.86 / 4.67
(39)	40 min.	12.54	4.62
(40)	120 min.	12.92 / 12.56	5.00 / 4.64

In a separate experiment, FeOCl in dichloromethane was subjected to microwave radiation for an hour to ascertain if the solvent intercalated into the host. FeOCl was recovered with no evidence of intercalation from PXRD analysis and chemical analyses (C, H, Fe and Cl).

Overall, the PXRD patterns in **Figure 5.18** demonstrate some steps in the intercalation process for ferrocene into FeOCl. These occur mainly by staging but the

staging is not simple and there is some evidence for exfoliated species also being present during the reaction. The reaction isn't complete even after two hours in the microwave apparatus. The products from the reaction with dichloromethane medium are not the same as those formed in the reaction with acetone as medium [(34) and (35)]. One principle difference is the FeOCl : ferrocene ratios which were 1:0.07 and 1:0.12 for the reactions in acetone and dichloromethane, respectively. Further evidence for the intercalation mechanism is needed and this may be obtained with data from *in situ* PXRD analysis combined with transmission electron microscopy (TEM).

5.2.3.2 Mössbauer Spectroscopy

As already mentioned, intercalation of guest species into FeOCl creates a disturbance in the antiferromagnetic interaction of the host lattice. This lowers the magnetic ordering temperature (Néel temperature) of the material, which is *circa* 91K for pristine FeOCl.[217] Therefore, a Mössbauer spectrum of an intercalated FeOCl, taken at liquid nitrogen temperature, no longer shows a magnetically ordered sextet of the pristine FeOCl but rather gives a paramagnetic quadrupole doublet. At this temperature, Mössbauer analysis can detect the redox products of intercalation with the observation of extra resonant peaks, assigned to Fe^{2+}, occurring with a quadrupole splitting (QS) value of ~2.5 mm s^{-1} (relative to iron foil). Moreover, quantitative Mössbauer analysis may be used to estimate the degree of reduction in the host lattice and hence, determine whether full or partial electron transfer has occurred between the guest and host. All Mössbauer data reported in this section are relative to iron foil.

5.2.3.2.1 Reaction in Acetone

Mössbauer spectra (room and liquid nitrogen temperatures) were taken of the intercalation compound (34) prepared from the reaction between ferrocene and FeOCl in acetone for 3 minutes by the microwave method. **Table 5.10** lists the relevant data as well as literature values for pristine FeOCl[268] and FeOCl(ferrocene)$_{0.16}$,[217] and **Figure 5.19** illustrates the spectra of sample (34).

Table 5.10 Mössbauer data for intercalated FeOCl with ferrocene.

Name	Iron state	IS (300K) (mm s^{-1})	QS (300K) (mm s^{-1})	IS* (77K) (mm s^{-1})	QS* (77K) (mm s^{-1})
FeOCl	Fe(III)	0.39	0.84	0.42	0.94
(34) (3 minutes in acetone)	Fe(III)	0.41	0.76	0.50	1.17
	Fe(II)	-	-	1.3(1)	2.8(0)
$FeOCl(Fc)_{0.16}$	Fe(III)	0.46	0.65	0.50	1.32
	Fe(II)	-	-	1.2(3)	2.5(8)

* See Section 5.4.1 for calculations of errors in 77K spectra.

The room temperature spectrum of sample (34) [3 minutes in acetone medium] is shown in Figure 5.19 and has a quadrupole splitting consistent with high spin Fe(III). However, in comparison to unintercalated FeOCl[268] (Figure 5.5, Section 5.1.4), the IS value (0.41 mm s^{-1}) is larger while its QS value (0.76 mm s^{-1}) is smaller. The increase in the IS suggests an increase in electron density around the Fe atom in the intercalated FeOCl layer. The decrease in the QS value may correspond to a distortion of the environment of the Fe atom from its octahedral state as a result of the intercalation.

The liquid nitrogen temperature spectrum displays a quadrupole doublet plus as additional resonant absorption peak (marked [x] in Figure 5.19), assigned to the reduced Fe^{2+} ions (i.e. Fe(III) is reduced by the ferrocene which is consequently oxidised to ferrocenium cation). The position of this peak suggests it is one half of a quadrupole doublet with the missing component lying beneath the peak at about 0 mms^{-1}. The IS and QS data for [x] are listed in Table 5.10. They are characteristic of

high spin Fe(II). The peak marked [y] in **Figure 5.19** is characteristic of the ferrocenium cation, see **Figure 5.6, Section 5.1.4.** It is also noted that the liquid nitrogen spectrum of sample (34) does not have the characteristic sextet broadening observed for FeOCl, see **Figure 5.7**[236]. The depression of FeOCl Néel temperature, due to expansion of its layers by intercalation, explains this observation.[217]

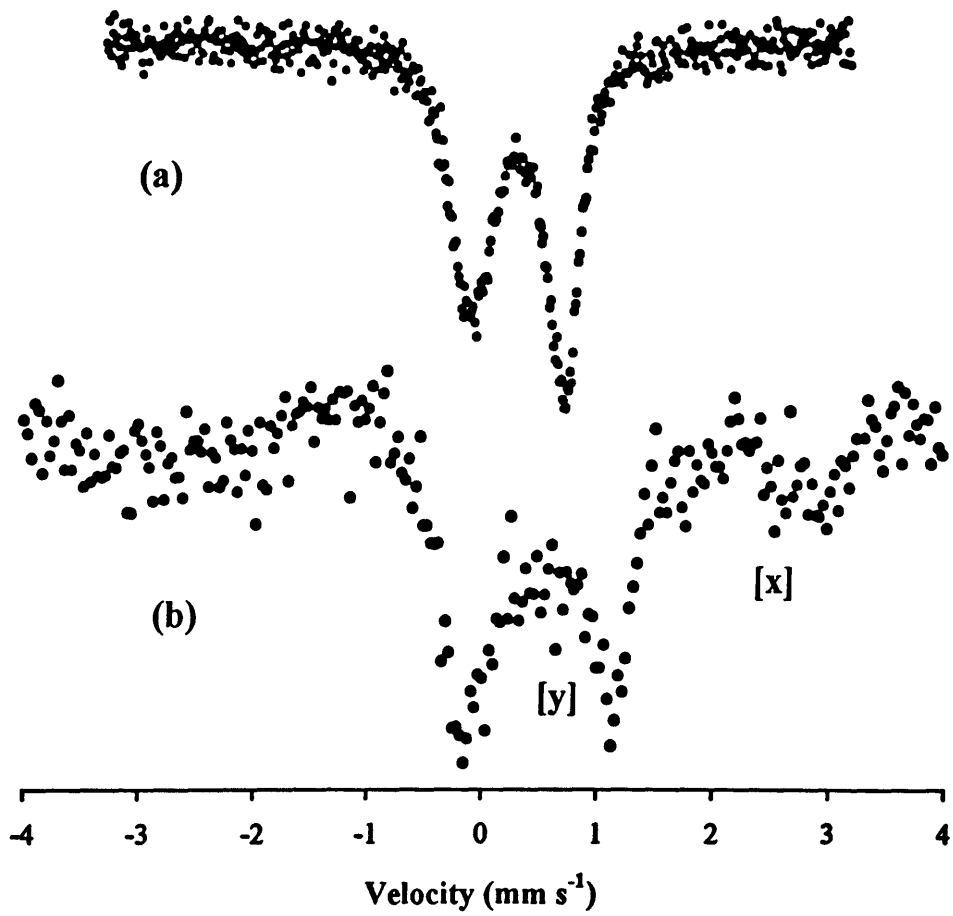


Figure 5.19 Mössbauer spectra of (34) (3 min. in acetone) taken at (a) 300K and (b) 77K.

As seen from **Figure 5.19**, there is a large change in IS and QS values of Fe(III) as one goes from the room temperature spectrum to the liquid nitrogen spectrum. This feature is characteristic of intercalation compounds and has been reported several times before.[215,223,245] **Table 5.10** also lists literature values for FeOCl(ferrocene)$_{0.16}$[217] prepared by conventional reflux methods. The values are slightly different from the

results obtained in the current work but they do follow the same trend in IS and QS values as the temperature is lowered.

The appearance of peaks belonging to Fe(II) ions only at low temperature reflects the conductivity properties of the intercalation compound. At room temperature, Mössbauer spectroscopy cannot detect the Fe(II) ions on its time-scale (10^{-7} s) because of electron-hopping between the iron sites in the inorganic matrix. In other words, the electrons may be considered as delocalised over the system. This leads, in general, to an increase in conductivity of the intercalate and this has been previously studied extensively.[219,245] At 77K, the electron-hopping slows down sufficiently to be localised and hence observed in the Mössbauer spectra. Unfortunately, the amount of Fe(II) to Fe(III) ions in the intercalation compound cannot be estimated from the liquid nitrogen spectrum in **Figure 5.19** as there are relaxation effects, which complicate the calculation.

5.2.3.2.2 Reaction in Dichloromethane

Mössbauer spectra, 300K and 77K, were recorded for the intercalation compounds synthesised from the reaction of ferrocene and FeOCl by the microwave method with dichloromethane as medium for reaction times between 10 and 40 minutes. The results are presented in **Table 5.11**. Each intercalate displayed a quadrupole doublet at room temperature and a quadrupole doublet plus an Fe(II) resonant peak at liquid nitrogen temperature. This is shown in **Figure 5.20** for sample (36) (10 minutes, dichloromethane). The peak detected between the main quadrupole doublet in the 77K spectrum can be assigned to the ferrocenium ions[201] as previously demonstrated in **Figure 5.19**. **Figure 5.20** also shows the increase in IS and QS values on decreasing the temperature, a characteristic feature of intercalation compounds.[215,223,245]

Since Mössbauer spectroscopy is sensitive to changes in environment of the iron atom (both structural and electronic), then the alterations of the intercalate's structure observed by PXRD (**Figure 5.18**) should also be detected by Mössbauer spectroscopy. In **Table 5.15**, the IS and QS values of the intercalation compounds (37) to (39) stay relatively constant for both temperatures. This does not appear to endorse the data from the PXRD profiles of (37) to (39), which showed major structural changes. This result is difficult to explain because Mössbauer spectroscopy

should be able to detect the structural differences between the intercalates. However, the change in IS and QS values between compounds (36) and (37) is significant for both temperatures. There is a large decrease (in general) for both IS and QS values of (37) in comparison to (36). This suggests a significant structural change occurring between these two compounds and supports the PXRD data in which there is a splitting of one lattice expansion into two on progression from (36) to (37).

Table 5.11 Mössbauer results for the intercalation compounds formed from the reaction of ferrocene with FeOCl in dichloromethane by the microwave method.

Name	Iron state	IS (300K) ($mm\ s^{-1}$)	QS (300K) ($mm\ s^{-1}$)	IS* (77K) ($mm\ s^{-1}$)	QS* (77K) ($mm\ s^{-1}$)
(36) (10 min)	Fe(III)	0.43	0.76	0.49	1.24
	Fe(II)	-	-	1.2(8)	2.8(4)
(37) (20 min)	Fe(III)	0.40	0.68	0.51	1.12
	Fe(II)	-	-	1.2(5)	2.6(0)
(38) (30 min)	Fe(III)	0.39	0.65	0.53	1.20
	Fe(II)	-	-	1.2(1)	2.5(8)
(39) (40 min)	Fe(III)	0.38	0.67	0.51	1.17
	Fe(II)	-	-	1.2(1)	2.5(7)

* See Section 5.4.1 for calculations of errors in 77K spectra.

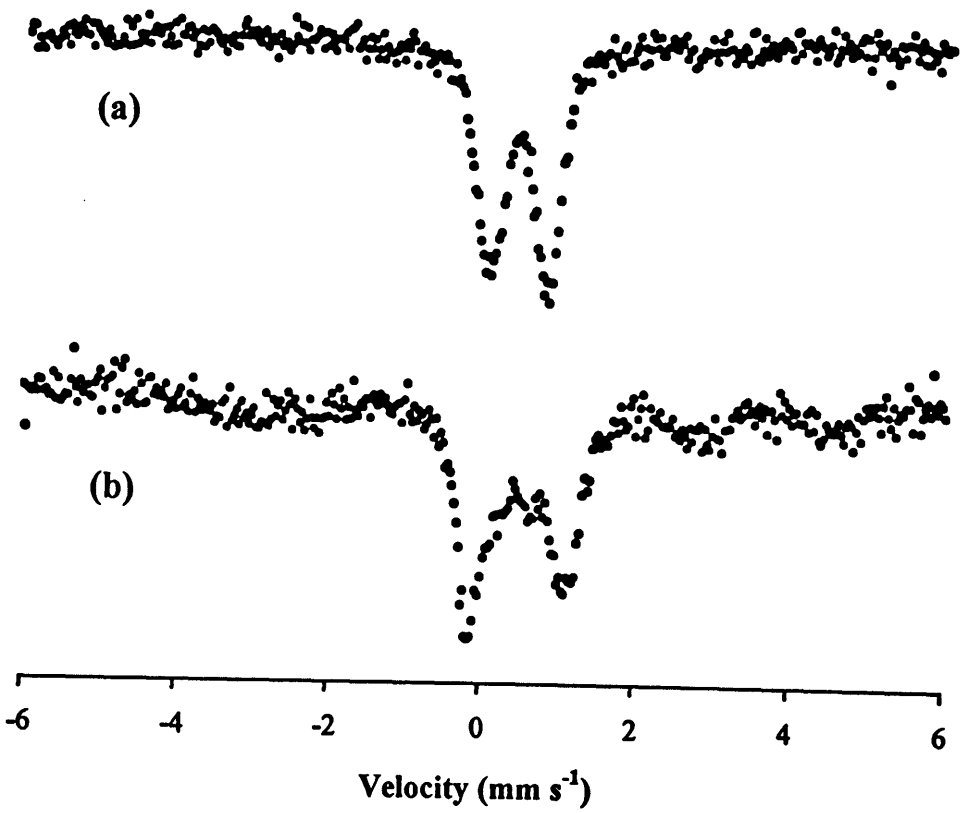


Figure 5.20 Mössbauer spectra of (36) (10 mins. in dichloromethane) taken at (a) 300K and (b) 77K.

5.2.4 Intercalation of Ferrocenylboronic Acid into FeOCl

5.2.4.1 PXRD Analysis

Intercalation of ferrocenylboronic acid, $FcB(OH)_2$, into FeOCl has not been previously reported. Attempts to synthesis the intercalated compound by conventional thermal methods in acetone at 110°C for 2 weeks failed as determined by elemental analyses and PXRD studies. The microwave method with ferrocenylboronic acid was, however, more successful and produced intercalated compounds with acetone. Reaction times varied form 10 to 20 minutes. The PXRD profiles of the products in the reaction are shown in **Figure 5.21**. The results show a trend which was similar to that of the reaction with ferrocene in dichloromethane. After ten minutes, there was very little evidence of intercalation except for an obvious disturbance of the host lattice with a splitting of the basal peak's spacing. Clear

evidence of the intercalation compound appears after fifteen minutes with some of the host lattice still apparent in the profile. In the PXRD patterns of the products after fifteen, twenty, thirty and forty minutes irradiation, the host structure is seen to gradually disappear as the intercalation compound forms. Intercalation is deemed complete at the 40-minute reaction time and the compound has the formula $FeOCl[FcB(OH)_2]_{0.06}$.

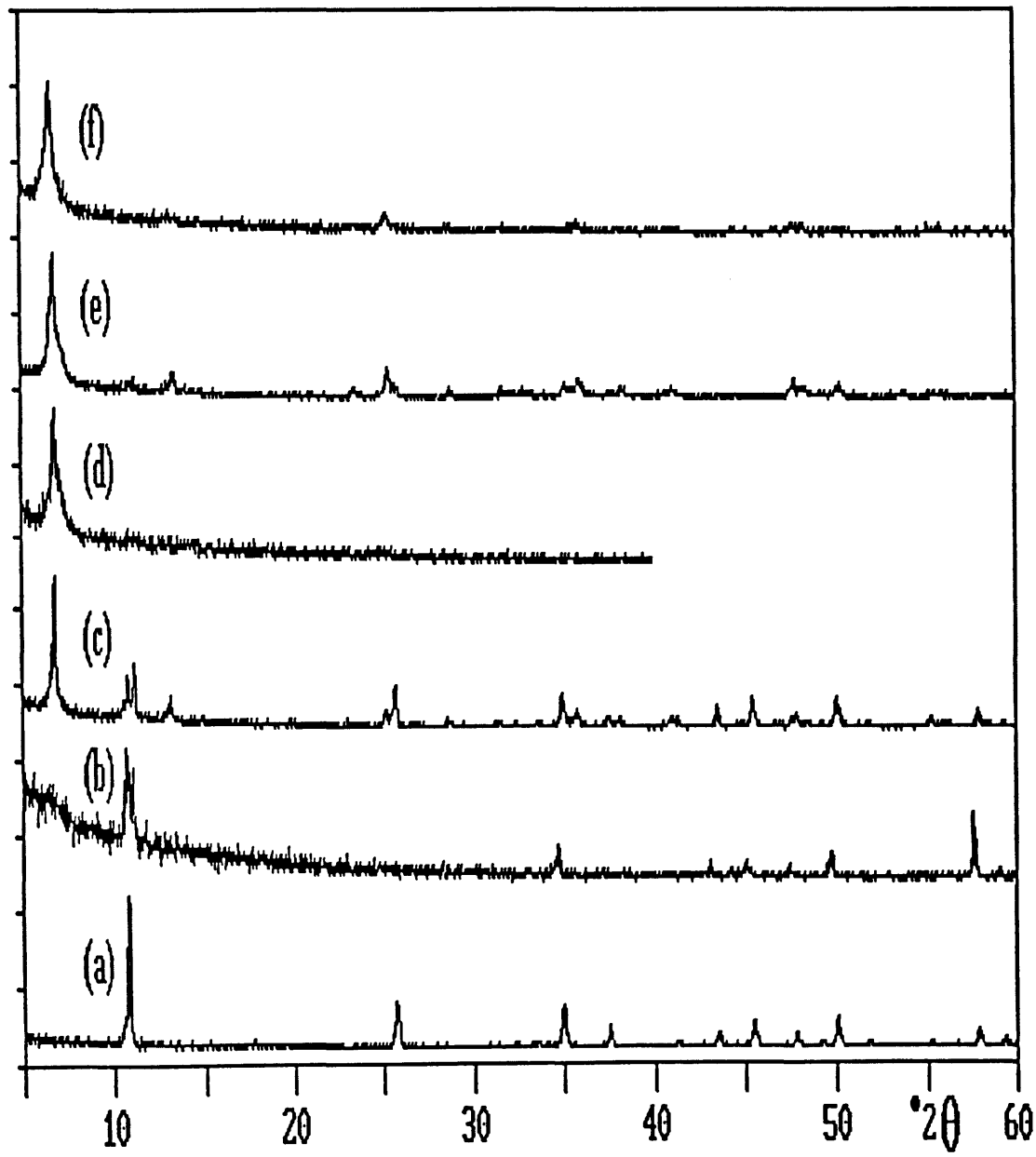


Figure 5.21 PXRD profiles of the reaction of ferrocenylboronic acid with FeOCl by the microwave method in acetone at different reaction times: (a) zero min., (b) 10 min., (41) (c) 15 min., (42) (d) 20 min., (43) (e) 30 min. (44) and (f) 40 min. (45).

Compared to the reaction with ferrocene in dichloromethane, no competitive staging is observed in the PXRD patterns since only one lattice expansion peak was detected in each diffractogram. Neither was there any evidence for exfoliation. The reaction mechanism could be explained by the occurrence of an advancing phase boundary[230] in the host lattice. At reaction time of ten minutes, there begins to be disruption in the host lattice with the appearance of an amorphous phase and, possibly, a very small amount of intercalated compound has formed. The slight increase in relative baseline intensity (at $2\theta = 5°$-$8°$) of the pattern suggests a disordered structure, such as might occur if an advancing phase boundary has formed. As the reaction continues, the advancing phase boundary shifts through the crystal with the formation of the intercalation compound. This type of intercalation mechanism has been described for the intercalation of ethanol into $VOPO_4.2H_2O$.[229]

Table 5.12 lists the lattice expansion of FeOCl due to intercalation of ferrocenylboronic acid.

Table 5.12 Lattice expansions in the products obtained from the reaction of ferrocenylboronic acid in acetone with FeOCl by the microwave method.

Intercalate Number	**Reaction time**	**Interlayer Spacing (Å)**	**Lattice Expansion (Å)**
(41)	10 minutes	7.90	None
(42)	15 minutes	13.02	5.10
(43)	20 minutes	12.95	5.03
(44)	30 minutes	13.00	5.08
(45)	40 minutes	13.42	5.50

The lattice expansions for the reaction are constant at approximately 5.00Å for the reactions with times of fifteen, twenty and thirty minutes. There is a slight increase to 5.50Å for the reaction performed for forty minutes. When the reaction was continued to sixty minutes, a red amorphous powder was formed. Chemical analyses of this powder confirmed decomposition of FeOCl but a fuller characterisation was not possible.

The lattice expansions of these intercalates are very similar to those of the intercalation compounds with ferrocene as the guest species. While this result does not confirm the orientation of the ferrocenylboronic acid guest molecules between the layers, it is quite possible that the molecules are orientated similarly to ferrocene, i.e. with the *cyclo*pentadienyl rings perpendicular to the b-layer spacing, as **in Figure 5.12**.

5.2.4.2 Mössbauer Spectroscopy

Figure 5.22 shows the room and liquid nitrogen temperature Mössbauer spectra of **(45)**, i.e. the reaction continued for 40 minutes in acetone.

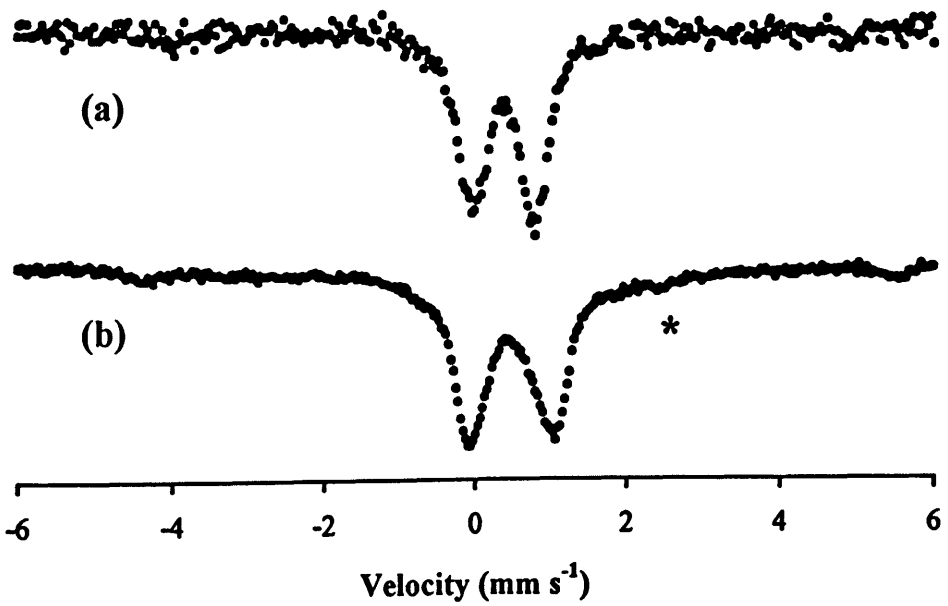


Figure 5.22 Mössbauer spectra of **(45)** (40 min. in acetone) taken at (a) 300K and (b) 77K. * denotes expected position of Fe(II) resonant peak.

The 300K spectrum in **Figure 5.22** shows a quadrupole doublet. This is charateristic of high spin Fe(III) ions in the inorganic matrix. The detection of Fe(II) ions from reduced host was prevented by rapid electron hopping at this temperature. However, the 77K spectrum displays one very weak resonant peak associated with the Fe(II) ions. The characteristic increases in IS and QS values of the intercalation compounds at liquid nitrogen temperature are also exhibited in **Figure 5.22.** Since the spectrum has less relaxation than that observed for the ferrocene reaction **(Figure 5.19),** an estimation of the amount of Fe(II) ions was made (see **Section 5.4.1).** The value is *circa* 7+/-1%, which compares favourably with the stoichiometric value of $FeOCl(FcB(OH)_2)_{0.06}$. This result suggests that there is full electron transfer from the guest to the host and that no unoxidised guest molecules exist within the host layers. **Table 5.13** presents the Mössbauer results of the intercalation compounds **(41)** to **(45).**

Table 5.13 Mössbauer results for the intercalation compounds prepared from the reaction of ferrocenylboronic acid with FeOCl in acetone by the microwave method.

Name	Iron state	IS (300K) ($mm\ s^{-1}$)	QS (300K) ($mm\ s^{-1}$)	IS* (77K) ($mm\ s^{-1}$)	QS* (77K) ($mm\ s^{-1}$)
$FcB(OH)_2$	Fe(II)	-	-	0.51	2.16
FeOCl	Fe(III)	0.37	0.84	0.42	0.94
(41) (10 min)	Fe(III)	0.37	0.83	0.40	0.92
	Fe(II)	-	-	-	-
(42) (15 min)	Fe(III)	0.38	0.80	0.43	1.05
	Fe(II)	-	-	1.2(6)	2.7(3)
(43) (20 min)	Fe(III)	0.38	0.82	0.48	1.01
	Fe(II)	-	-	1.2(5)	2.5(4)
(44) (30 min)	Fe(III)	0.38	0.81	0.46	1.03
	Fe(II)	-	-	1.2(2)	2.5(2)
(45) (40 min)	Fe(III)	0.38	0.79	0.49	1.06
	Fe(II)	-	-	1.1(9)	2.4(7)

* See **Section 5.4.1** for calculations of errors in 77K spectra.

The 77K Mössbauer data for ferrocenylboronic acid are also given in this table for comparison purposes along with the IS and QS values of FeOCl.

The IS and QS values of **(41)** (10 minutes in acetone) are almost identical to the values reported for unintercalated FeOCl and there is no detection of a Fe(II) resonant peak in the 77K spectrum. This is not surprising as the PXRD pattern of **(41)** showed no formation of an intercalation compound and elemental analyses detected no carbon or hydrogen present. The rest of the intercalation compounds give Mössbauer results that are characteristic of intercalation materials,[215,223,245] namely: (1) decrease in QS values from pristine FeOCl at room temperature due to the distortion of the Fe atom's environment by the guest species, (2) a large increase in IS and QS values when the spectrum is recorded at liquid nitrogen temperature, (3) the detection of a Fe(II) resonant peak in the 77K spectrum and (4) a lowering of the Néel temperature for FeOCl.

The Mössbauer results complement the PXRD data of these compounds. The PXRD profiles were interpreted as suggesting an advancing phase boundary mechanism. This led to a gradual disappearance of the FeOCl lattice peaks and the emergence of the intercalation compound's lattice expansion peak. The Mössbauer data also demonstrated a gradual change in the IS and QS values of the Fe(III) ions and the appearance of Fe(II) peak with increasing reaction time. Compound **(45)** (40 minutes in acetone) has the greatest differences between IS and QS values for the different temperatures which suggests that intercalation is most advanced here, which is exactly the interpretation from the PXRD patterns.

5.2.5 *Intercalation of 4-Aminopyridine (Apy) into FeOCl*

5.2.5.1 *PXRD Analysis*

4-Aminopyridine has been reported to intercalate into the FeOCl host structure by the conventional reflux method with acetone as medium for a week.[247] The b-axis layer expanded to 13.57Å. In the present study, the reaction was repeated with the conventional and microwave techniques using acetone as medium. The results are presented in **Table 5.14**. The conventional product was formed after 7 days while the microwave product was prepared after 5 minutes. Both methods synthesised products with similar interspacing distances which are very similar to those previously reported (13.57Å[247]). However, the microwave method not only formed the product in a very short time but also produced a more crystalline product. The differences between the two methods can be clearly observed in their respective PXRD patterns as shown in **Figure 5.23**. The microwave product's PXRD pattern showed sharper and more distinct peaks than the conventional product's profile.

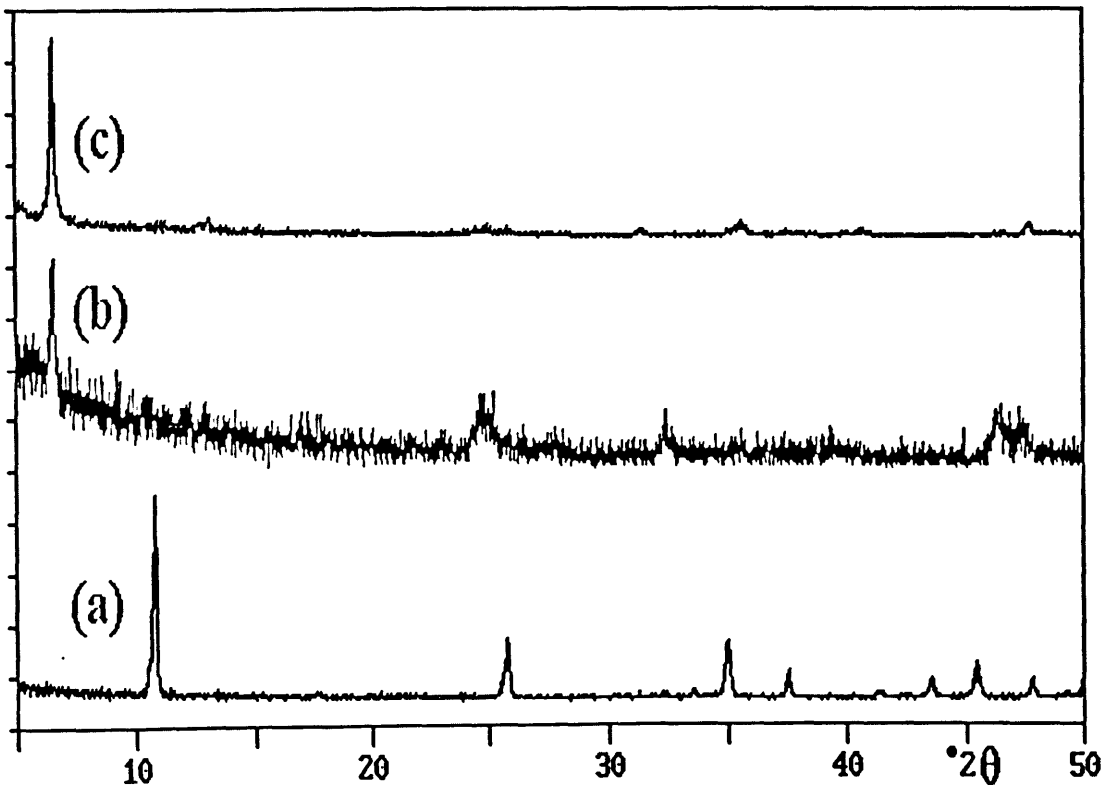


Figure 5.23 PXRD patterns of (a) FeOCl, (b) $FeOCl(Apy)_{0.17}$ **(33)** prepared by the conventional method in 7 days by the present work and (c) $FeOCl(Apy)_{0.10}$ **(46)** prepared by the microwave method in 5 minutes.

Table 5.14 Lattice expansions of the products from the reaction of Apy with FeOCl by the two methods in acetone.

Name	Preparative method	Inter. Spacing (Å)	Inter. Expans. (Å)
(33) – 7 days	Conventional	13.52	5.60
(46) – 5 min	Microwave	13.50	5.58

5.2.5.2 *Mössbauer Spectroscopy*

Mössbauer data on intercalation compounds of FeOCl with amines as guest species have been tabulated elsewhere.[219,245] The results detected the characteristic features of intercalation compounds in Mössbauer spectroscopy including the observation of a reduced host lattice at 77K. There does not appear to be any reported Mössbauer data on intercalation compounds with 4-aminopyridine as the guest species in FeOCl. The IS and QS values of the microwave-prepared intercalation compound **(51)**, prepared in acetone in 5 minutes, is given below in **Table 5.15**. The data is consistent with previous results for amine intercalated compounds.[216,217]

Table 5.15 Mössbauer data on sample **(51)**.

Name	Iron State	IS (300K) ($mm\ s^{-1}$)	QS (300K) ($mm\ s^{-1}$)	IS* (77K) ($mm\ s^{-1}$)	QS* (77K) ($mm\ s^{-1}$)
(46) (5 min)	Fe(III)	0.44	0.79	0.51	1.14
	Fe(II)	-	-	1.2(3)	2.5(6)

*See Section 5.4.1 for calculation of errors in 77K spectrum.

The Mössbauer spectra of (46) are shown in **Figure 5.24**. The 77K spectrum shows very little relaxation and hence, the amount of Fe(II) could be estimated (see **Section 5.4.1**). The value was 11 +/- 1% which is in excellent agreement with its formula

$FeOCl(Apy)_{0.10}$. This suggests total transfer of the electron from the guest to the host. The actual arrangement of the guest in the host cannot be deduced from these results but there is a possibility of polymerisation of the aminopyridine during the reduction stage of intercalation. It should be noted, however, that the literature report made no comments on the polymerisation of aminopyridine.[247] This was reported for aniline in the production of $FeOCl(PANI)_x$, x = 0.16-0.28, compounds.[245]

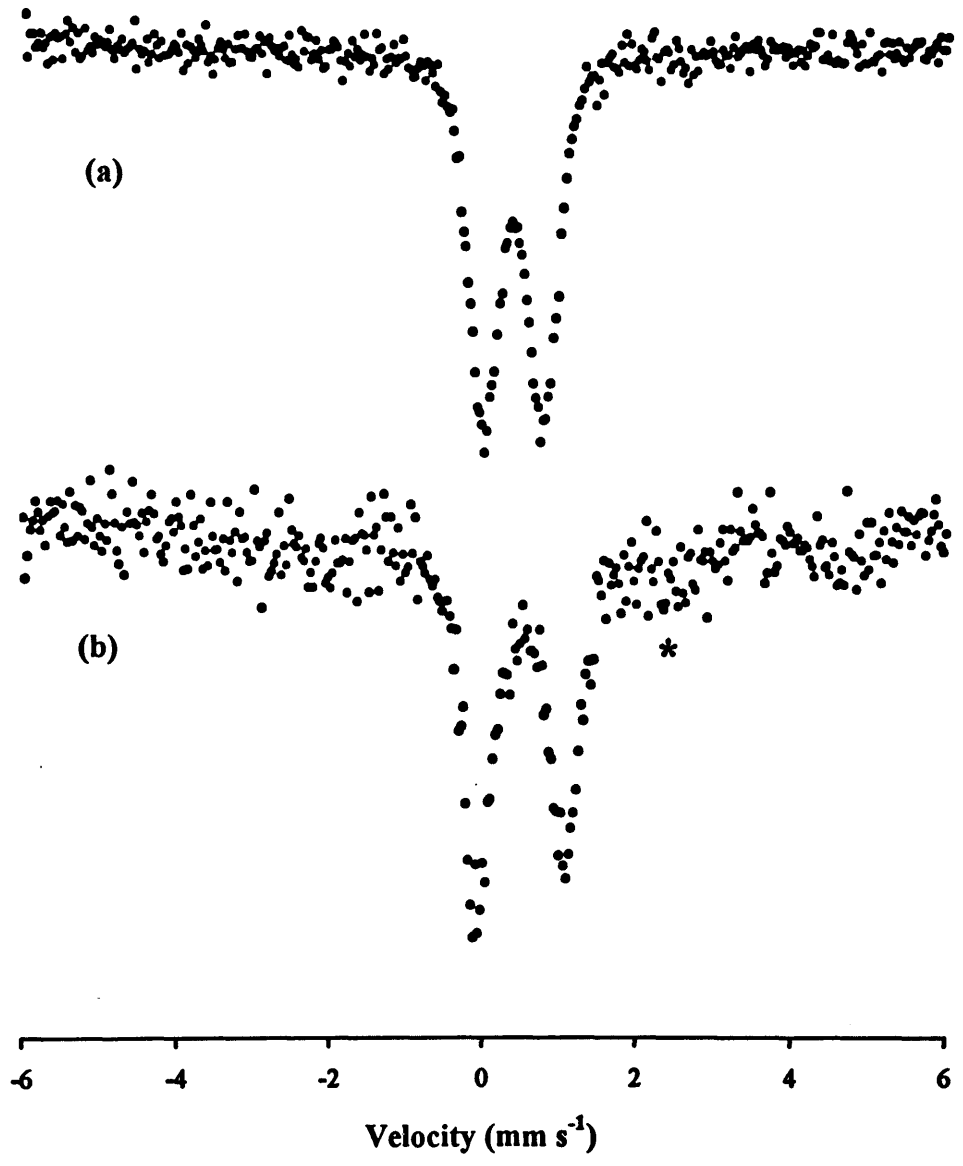


Figure 5.24 Mössbauer spectra of (46) (5 min. in acetone) taken at (a) 300K and (b) 77K. * denotes expected position of Fe(II) resonant peak.

5.2.6 *Attempted Intercalation of [(FcBO)$_2$(Bu$^t_2$SiO)$_2$] (19) into FeOCl*

The synthesis and characterisation of the borosilicate compound (19) was discussed in Section 4.2.5, Chapter 4. The structure may be described as centrosymmetric with a planar $B_2Si_2O_4$- borosilicate ring, see Figure 4.12. If this compound was to intercalate in a similar manner to ferrocene (i.e. ferrocenyl groups oxidised and *cyclo*pentadienyl rings perpendicular to the layers), then the layers would have to expand considerably more to accommodate the large *tert*-butyl groups attached to the silicon atoms (estimated distance is ~13.5Å).

Intercalation was attempted by the microwave technique in acetone medium at different reaction times ranging from 10-60 minutes. Figure 5.25 shows the PXRD pattern obtained for the material after 60 minutes. Clearly, intercalation had not been successful with no sign of a lattice expansion peak. The FeOCl (010) peak can just be detected. The result is disappointing and it raises the question to why intercalation was not achieved. One reason may be the size of the proposed guest molecule. The molecule is bulky (measures approximately 13.5Å from opposite *tert*-butyl groups on each silicon atom) and may be too large to be inserted in between the host layers. However, intercalation of bis(ethylenedithio)tetrathiafulvalene (ET), with the long axis of ET parallel to b-axis, into FeOCl has been reported to occur with a lattice expansion of 14.43Å.[224] Therefore, FeOCl should be capable of accommodating compound (19). Intercalation may not have proceeded because no suitable redox reaction could occur between the host and the borosilicate guest.

Pattern (a) in Figure 5.25 does not have distinct peaks and suggests that the FeOCl has a low crystallinity. The loss of crystallinity of FeOCl to an almost amorphous material is probably due to the harsh reaction conditions (recall that the FeOCl was subjected to superheating in acetone medium in a microwave for 60 minutes).

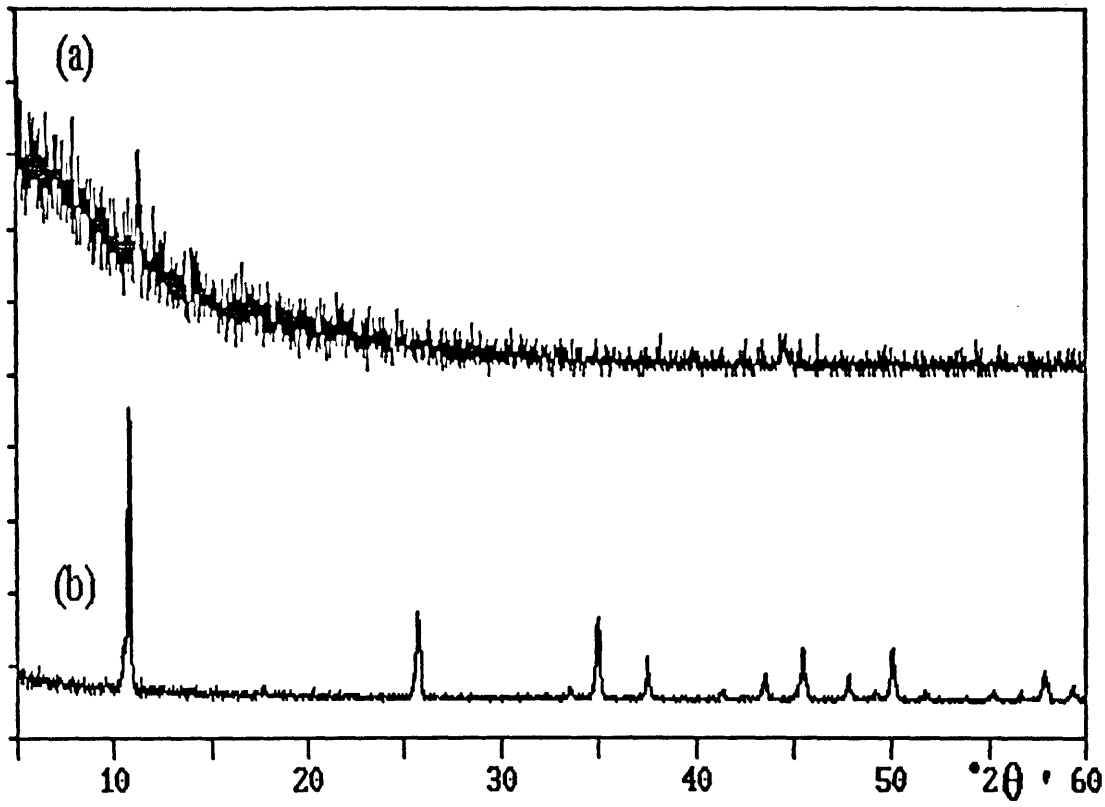


Figure 2.25 PXRD patterns of (a) FeOCl and (19) after 60 minutes in microwave and (b) FeOCl.

5.3 SUMMARY AND CONCLUSIONS

Intercalation compounds of FeOCl have been successfully prepared with the microwave dielectric heating technique. This technique had been employed before to enhance the reaction rate for intercalating materials,[265,266] but no studies have been reported with FeOCl as host lattice. Intercalation reactions of ferrocene or 4-aminopyridine with FeOCl were studied using both thermally and microwave radiation induced reactions. Rate enhancements of over 1000 times were found for both reactions when microwave radiation was used. The products from microwave irradiation showed much higher retention of crystallinity. Novel intercalation compounds were formed with the microwave method with ferrocenylboronic acid as the guest molecule.

All the intercalation compounds were analysed by PXRD and Mössbauer spectroscopy. From the PXRD data the lattice expansion of the host layers due to intercalation was estimated. The Mössbauer results yielded information about the Fe(III) and Fe(II) species present.

Intercalation of ferrocene into FeOCl was achieved by the microwave technique with either acetone or dichloromethane as the liquid medium. In acetone, the product, FeOCl(ferrocene)$_{0.07}$ (35), was formed in 5 minutes and intercalation was deemed complete from its PXRD pattern. For the dichloromethane, the products reaction times were varied between 10 to 120 minutes and the PXRD patterns suggested that complete intercalation was not achieved. The final product was FeOCl(ferrocene)$_{0.12}$ (40). The PXRD profiles of the products from dichloromethane reaction appeared to correspond to some steps in the intercalation process. The steps may have involved a combination of staging and exfoliation-reformation processes.

Intercalation of ferrocenylboronic acid into FeOCl by the microwave technique revealed both intercalated product and reactant coexisting in the early stages of the reaction. After 40 minutes, only the intercalation product, FeOCl[FcB(OH)$_2$]$_{0.06}$ (45), existed. The intercalation process could possibly be described by an advancing phase boundary mechanism. The expansion of the FeOCl layers by intercalation of ferrocenylboronic acid was similar to that found for ferrocene. It is therefore reasonable to assume that the ferrocenylboronic acid molecules existed in the host structure with the *cyclo*pentadienyl rings perpendicular to the b-lattice axis. Mössbauer studies confirmed the formation of the intercalation material and the results suggested full electron transfer from the guest to the host.

Intercalation of 4-aminopyridine (Apy) into FeOCl was accomplished by the microwave method in five minutes [sample (46)] with acetone as the liquid medium. The product exhibited high crystallinity as shown by PXRD studies and Mössbauer spectroscopy suggested that total electron transfer had occurred between the guest molecule and the host lattice.

Overall, the microwave technique for synthesising intercalation compounds has distinct advantages over the normal thermal induction technique particularly rate enhancement and crystallinity retention.

5.4 EXPERIMENTAL DETAILS

5.4.1 Instrumentation

Elemental analyses were performed at the Microanalytical Laboratory, University College, Cork. Infra-red spectra were recorded as KBr discs in the range 4000 – 440 cm^{-1} on a Perkin Elmer FTIR Paragon 1000 spectrometer. Relative intensities are designated as vs, very strong; s, strong; m, medium; w, weak; vw, very weak; sh, shoulder; br, broad. Mössbauer spectra were measured at room and liquid nitrogen (77K) temperature using a commercial constant acceleration drive unit and transducer (Harwell Instruments) in conjunction with a Canberra System 40 multichannel analyser. The source was ^{57}Co in Rh and was of 20mC nominal strength. All data was referred to the spectrum of iron foil as standard. Masses of samples varied between 25 and 35 mg. Data collection times varied from 24 – 48 hours. All spectra were fitted using a non-linear curve-fitting program.[269] Estimations of errors were calculated using this program.[269] Powder X-ray diffraction (PXRD) patterns were collected on a Phillips PW3710 MPD apparatus using $CuK_{\alpha 1}$ (1.5418 Å) radiation with an anode current of 30 mA and accelerating voltage of 40 kV. Data was collected between 5° and 60° 2θ using the standard θ/2θ geometry. In all diffractograms, a step size of 0.03 degrees (2θ) was used with a data collection time of 1.5 seconds per step. All the microwave-initiated reactions were performed in a modified (as described in Section 5.1.9) Ariston model MW 950TW domestic microwave oven, which has a maximum power setting of 650W. The Pyrex vessel used had a 34mm outer diameter, was 25cm long and had a wall thickness of 3.5mm. The Pyrex tube was covered in a protective sheath made from transparent polyolefin heat-shrink. This sheath is to prevent fragmentation of the glass tube in the event of the vessel failing. The glass vessel is attached to a series of Swagelock fittings *via* a "Viton" sealed stainless-steel insert 27mm in diameter. The pressure of the vessel is controlled by a comparator circuit that compares the output pressure with the predetermined reaction hold-pressure and turns off the magnetron on reaching the set pressure. For precautionary measures, pressure is usually limited to 10 atmospheres (atm). The pressure measuring system was based on a Druck Ltd., PDCR 810-0799

0-35 bar pressure transducer. This and the associated pressure indicator were purchased from RS components, England.

5.4.2 Starting Reagents

The following reagents were used as supplied from Aldrich: ferric chloride, iron (III) oxide, 4-aminopyridine, ferrocene and ferrocenylboronic acid. Triply distilled water, 99% dichloromethane (Aldrich), 99% acetone (Aldrich) were used as received and dried toluene was dried over Na/benzophenone.

5.4.3 General Methodology

Iron oxychloride was prepared from $FeCl_3$ and α-Fe_2O_3 in a 1.3:1 ratio as previously described in the literature.[233] Violet blade-like crystals were obtained and stored under an atmosphere of N_2 gas. Each batch of FeOCl was characterised by PXRD and elemental analyses (Fe and Cl).

5.4.4 Intercalation of Ferrocene into FeOCl.

5.4.4.1 Conventional Thermal Method

The procedure followed that described in reference 221.
Iron oxychloride (0.101g, 0.94mmol) and ferrocene (0.029g, 0.16mmol) were placed in a Schlenk tube. Dry toluene (20mls) was syringed into the vessel. The vessel was evacuated, sealed and placed into an oil-bath at 100°C for seven days. Black, slightly crystalline material [(32)] was produced. Found: C, 6.6; H, 0.9; Cl, 29.7%. $FeOCl(ferrocene)_{0.07}$ requires: C, 7.0; H, 0.6; Cl, 29.5%. PXRD data, d(Å), (I/I_o): 13.33, (18); 3.49, (48); 2.58, (46); 2.00, (100); 1.91 (19).

5.4.4.2 Microwave Method

(i) Acetone as Medium

Iron oxychloride (0.050g, 0.47mmol) and ferrocene (0.015g, 0.08mmol) along with acetone (30mls) were introduced into the glass reaction vessel described in **Section 5.1.9**. The pressure control line was attached to the vessel, which was then located in

the microwave oven, as shown in Figure 5.15. A pressure of 10 atm with a 0.5 atm hysteresis was set on the controller. The yellow solution was subjected to microwave irradiation (650W) for different reaction times.

(a) Three minutes (34): Black crystalline solid was filtered from a dark green solution. The change in colour of the solution suggested that oxidation of the ferrocene had occurred. Found: C, 7.3; H, 0.9; Fe, 46.3. $FeOCl(ferrocene)_{0.07}$ requires: C, 7.00; H, 0.6; Fe, 46.4%. PXRD data, d(Å), (I/Io): 13.02, (100); 3.60 (2); 2.53, (2); 1.88, (3); 1.64, (2).

(b) Five minutes (35): A mixture of black crystallites and red-brown powder was extracted from a blue-green solution. Found: C, 7.11; H, 0.80; Fe, 45.94%. $FeOCl(ferrocene)_{0.07}$ requires: C, 6.99; H, 0.59; Fe, 46.42%. PXRD data, d(Å), (I/Io): 13.02, (100); 3.60, (3); 2.36, (4); 2.03, (2).

(c) Ten minutes: A red-brown powder was obtained from a blue-green solution. Found: C, 3.03; H, 1.73; Cl, 12.18; Fe, 46.87%, suggesting a decomposed intercalation product. PXRD data, d(Å), (I/Io): amorphous.

(ii) Dichloromethane as Medium.

Iron oxychloride (0.050g, 0.47mmol) and ferrocene (0.015g, 0.08mmol) along with dichloromethane (30mls) were placed into the microwave glass vessel as described above. The yellow solution was subjected to microwave irradiation for ten minutes. Highly crystalline black material [(36)] was filtered from the yellow solution. Found: C, 9.2; H, 1.2; Cl, 28.0%. $FeOCl(ferrocene)_{0.10}$ requires: C, 9.5; H, 0.8; Cl, 28.2%. PXRD data, d(Å), (I/Io): 12.58, (100); 6.40, (26); 3.48, (43); 2.47, (20); 2.33, (10); 2.04, (10); 1.80, (10).

The above reaction was repeated at different reaction times. Highly crystalline black solid was yielded each time.

(a) Twenty minutes (37): Found: C, 10.2; H, 1.2; Cl, 27.5%. $FeOCl(ferrocene)_{0.11}$ requires: C, 10.3; H, 0.9; Cl, 27.75%. PXRD data, d(Å), (I/Io): 13.84, (100); 12.64, (72); 7.77, (46); 6.40, (38), 3.49, (66); 3.07, (25); 2.81, (23); 2.49, (66); 2.35, (22); 2.19, (29); 1.90, (40); 1.88, (22); 1.86, (35); 1.81, (28).

(b) Thirty minutes (38): Found: C, 11.4; H, 1.1; Cl, 27.6%. $FeOCl(ferrocene)_{0.12}$ requires: C, 11.1; H, 0.9; Cl, 27.35%. PXRD data, d(Å), (I/Io): 14.19, (88);

13.78, (100); 12.58, (28); 7.74, (19); 7.18, (18); 6.47, (14); 3.49, (36); 2.81, (13); 2.48, (48); 2.18, (20); 1.90, (11); 1.80, (17)

(c) Forty minutes (39): Found: C, 11.3; H, 1.2; Cl, 27.5%. $FeOCl(ferrocene)_{0.12}$ requires: C, 11.1; H, 0.9; Cl, 27.35%. PXRD data, d(Å), (I/Io): 12.53, (100); 7.79, (7); 6.38, (38); 3.46, (340; 2.47, (24); 2.33, (8); 2.18, (10); 1.90, (10); 1.80, (8).

(d) 120 minutes (40): Found: C, 11.45; H, 1.2; Cl, 27.7%. $FeOCl(ferrocene)_{0.12}$ requires: C, 11.1; H, 0.9; Cl, 27.35%. PXRD data, d(Å), (I/Io): 12.92, (44), 12.55, (42); 6.47, (100); 4.33, (12); 3.48, (31); 2.81, (10); 2.49, (20); 2.34, (18); 2.18, (10); 1.86, (19); 1.81, (17).

5.4.5 Intercalation of Ferrocenylboronic Acid into FeOCl (Microwave Method)

Iron oxychloride (0.051g, 0.47mmol) and ferrocenylboronic acid (0.018g, 0.08mmol) were placed into acetone (30mls) in the microwave reaction vessel as outlined in Section 5.4.4.2. The orange solution was irradiated with microwaves for ten minutes. A dark crystalline product [(41)] was filtered from an orange solution. Found: C, 0.0; H, 0.0; Cl, 33.0%. PXRD data, d(Å), (I/Io): 8.27, (100); 7.99, (89); 2.58, (41); 2.10, (10); 2.01, (17); 1.92, (12); 1.83, (17); 1.60, (77).

The above reaction was repeated for a number of reaction times. A black crystalline solid was isolated from an orange solution each time.

(a) Fifteen minutes (42): Found: C, 3.9; H, 0.7; Cl, 30.6%. $FeOCl[FcB(OH)_2]_{0.04}$ requires: C, 4.1; H, 0.3; Cl, 30.4%. PXRD data, d(Å), (I/Io): 13.02, (100); 8.17, (30); 7.90, (34); 6.71, (17); 3.53, (11); 3.46, (28); 2.57, (26); 2.50, (11); 2.08, (13); 2.00, (20); 1.82, (23).

(b) Twenty minutes (43): Found: C, 6.2; H, 0.85; Cl 29.1%. $FeOCl[FcB(OH)_2]_{0.06}$ requires: C, 5.95; H, 0.45; Cl, 29.3%. PXRD data, d(Å), (I/Io): 12.99, (100); 7.89, (6.1); 6.59, (13); 3.51, (20); 2.50, (15); 1.90, (12).

(c) Thirty minutes (44): Found: C, 6.25; H, 0.9; Cl 29.35%. $FeOCl[FcB(OH)_2]_{0.06}$ requires: C, 5.95; H, 0.45; Cl, 29.3%. PXRD data, d(Å), (I/Io): 13.00, (100); 6.72, (12); 3.54, (7); 2.50, (6); 1.91, (8).

(d) Forty minutes (45): Found: C, 6.3; H, 1.1; Cl 29.4%. $FeOCl[FcB(OH)_2]_{0.06}$ requires: C, 5.95; H, 0.45; Cl, 29.3%. PXRD data, d(Å), (I/Io): 13.42, (100); 6.70, (8); 3.54, (13); 2.50, (7); 1.91, (6); 1.89, (6).

5.4.6 Intercalation of 4-Aminopyridine (Apy) into FeOCl

5.4.6.1 Conventional Reflux Method

Iron oxychloride (0.101g, 0.93mmol) and 4-aminopyridine (0.022g, 0.23mmol) were placed into acetone (15mls) in an ampoule. The ampoule was evacuated, sealed and heated in an oil-bath at 100°C for seven days. Black crystalline material [(33)] was received from the solution and washed well with acetone. Found: C, 8.3; H, 1.1; N, 3.8%. $FeOCl(Apy)_{0.17}$ requires: C, 8.3; H, 0.8; N, 3.9%. PXRD data, d(Å), (I/Io): 13.52, (100); 7.31, (11); 6.89, (7); 3.63, (38); 2.76, (18); 1.96, (30); 1.91, (19).

5.4.6.2 Microwave Method

Iron oxychloride (0.051g, 0.47mmol) and 4-aminopyridine (0.012g, 0.12mmol) were placed in the microwave tube with acetone (30mls). The mixture was reacted for five minutes and a black crystalline solid [(51)] was filtered from the colourless solution. Found: C, 5.3; H, 1.1; N, 2.1%. $FeOCl(Apy)_{0.10}$ requires: C, 5.15; H, 0.5; N, 2.4%. PXRD data, d(Å), (I/Io): 13.50, (100); 6.92, (4); 6.74, (6); 2.50, (5); 1.90, (6).

5.2.7 Attempted Intercalation of $[(FcBO)_2(Bu^t_2SiO)_2]$ (19) into FeOCl

Iron oxychloride (0.050g, 0.47mmol) and the ferrocenylborosilicate **(19)** (0.058g, 0.08mmol) were mixed into acetone (30mls) in the microwave reaction vessel as described previously. The mixture was irradiated with microwaves for up to 60 minutes. Violet crystals were received back from the red solution. Found: C, 0.0; H, 0.0; Cl, 33.1%. PXRD data, d(Å), (I/Io): 7.94, (100); 2.56, (13); 1.92, (20).

APPENDICES

Appendix A: Powder X-ray Diffraction (PXRD). Technique, Theory and Equipment.

The wavelengths of X-rays are comparable to the lattice spacings of crystals and therefore X-rays may be diffracted when passed through a crystal. The simple diagram in **Figure A.1** demonstrates the scattering of X-rays from crystalline solids. In this diagram, two monochromatic, coherent and parallel X-ray beams of wavelength λ are incident on a set of lattice planes at angle θ. The planes are separated by the interplanar distance d.

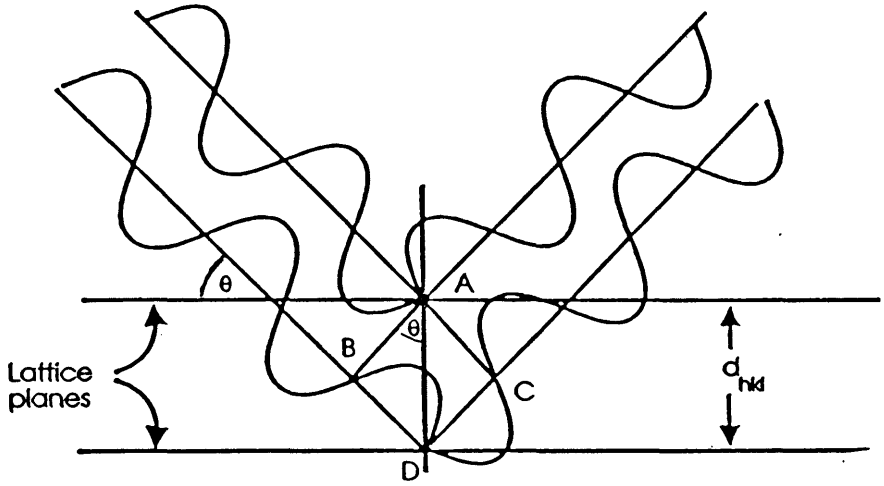


Figure A.1 Diffraction of X-rays by the lattice planes in a crystalline material.

Constructive interference occurs between the two beams if the additional distance travelled by the X-ray beam scattered from D is an integral number of wavelengths, i.e. $BD + DC = n\lambda$. The path difference can easily be related to the interplanar distance, d, to give the following equation, known as Bragg equation.

$$n\lambda = 2d\sin\theta \qquad [1]$$

In the powder technique, a monochromatic beam is passed onto a powdered crystalline sample. In a well ground sample some of the crystallites will always be directed so that the Bragg equation ([1]) will be satisfied. The powder technique has been well known

for the last forty years but has only become commonplace in the last 10-15 years with the advent of inexpensive solid-state detectors, super-accurate goniometers and computer facilities. This has ensured that PXRD profiles can be recorded quickly and, more importantly, quantitatively.

All crystalline solids have in general a unique PXRD pattern in terms of the position and peak intensities of the observed reflections. The position of the peaks in the profile contains information about the unit cell size and geometry, whereas the peak intensity is associated with the different elements situated at their atomic positions within the unit cell. Therefore, PXRD is primarily employed in the determination of the crystal structure properties of polycrystalline, solid inorganic materials.

The particle size of the powder sample may also be estimated by PXRD analysis. In materials with very small crystallites, a broadening of the peaks occurs due to non-total destructive interference. Scherrer's formula[73] ([2]) relates the size of the crystallites to the breadth of the peaks,

$$d = 0.9\lambda/(\beta-\beta_1)\text{Cos}\theta \qquad [2]$$

where **d** is the average grain diameter, β is the half intensity width of the relevant diffraction peak, β_1 is the half intensity width due to instrumental broadening (~0.07°), λ is the X-ray wavelength and θ is the angle of diffraction of the relevant peak.

For the present work, all diffraction patterns were collected on a Phillips PW 3710 MPD diffractometer using CuKα_1 radiation with an anode current of 30mA and an accelerating voltage of 40kV. Data was collected using the standard $\theta/2\theta$ geometry. All samples were subjected to grinding in a mortar and pestle to ensure random orientation. Care was taken to ensure that the surface of the sample was flat to minimise the zero point error of the θ angle.

APPENDIX B The Scanning Electron Microscope (SEM)

The scanning electron microscope (SEM) is used to examine solid surfaces and solid particles and to give images that have a high visual impact. It gives better magnification, depth of field and higher resolution than the normal optical microscope. The instrument is used for surface imaging in medium vacuum environments (pressure of 10^{-5} Torr) and is capable of revealing surface topography down to in-plane resolution of 1nm.

The fundamentals of the instrument are as follows. A beam of electrons from a heated tungsten filament is formed into a very fine electron probe by successive demagnification with two or more condenser lenses so that when the probe strikes the specimen it may only have a diameter of 0.01μm. This probe is caused to move over and back on the surface of the sample specimen in a zigzag raster motion by two pairs of deflecting coils which carry a current from a sawtooth generator. The same sawtooth generator also energises the deflecting coils of the cathode ray tube to produce on the face of this tube an identical but much larger zigzag raster. Finally, secondary electrons leaving the sample are reflected and the resulting current is amplified and used to control the brightness of the cathode ray image. Hence there is a point to point correspondence between the raster on the sample and that on the face of the cathode ray tube. Moreover the brightness of each point of the surface in the latter is controlled by the number of electrons leaving the corresponding point of the surface of the sample. The magnification is determined by the relative size of the two rasters and this can be varied at will by controlling the magnitudes of the currents flowing in the two sets of deflecting coils. Magnifications on the SEM (Hitachi S4000) used in the present work were up to 10^4. SEM is widely used to study surfaces that are not atomically clean and in which the topography is complex.

Sometimes the samples may have to be sputtered with a thin coat of gold to prevent localised electron build-up (charging) on the surface but in the case of the ferrites, this was not necessary as the ferrites were conducting enough to prevent this from happening.

APPENDIX C: Vibrating Sample Magnetometry (VSM)

Vibrating sample magnetometry (VSM) is widely used to characterise ferromagnetic and ferrimagnetic materials with the resulting magnetic hysteresis loop formed.[270] In a VSM, the sample is placed on the end of a rigid rod attached to a mechanical resonator, which oscillates the sample in a vertical direction at a fixed frequency (80Hz). The sample is surrounded by a set of sensing coils to detect changes in the magnetic flux density. As the sample moves, its magnetic field, M, alters the magnetic flux through the coils, which produces an AC current that can be amplified and detected. The external magnetising field is usually provided by a horizontal electromagnet.

Hysteresis loops were collected at room temperature on a Magnetic Solutions magnetometer. The magnetic field was generated using permanent magnets and the maximum applied field was +/-1.1 teslas. A simple diagram of the instrument is given in **Figure C.1**.

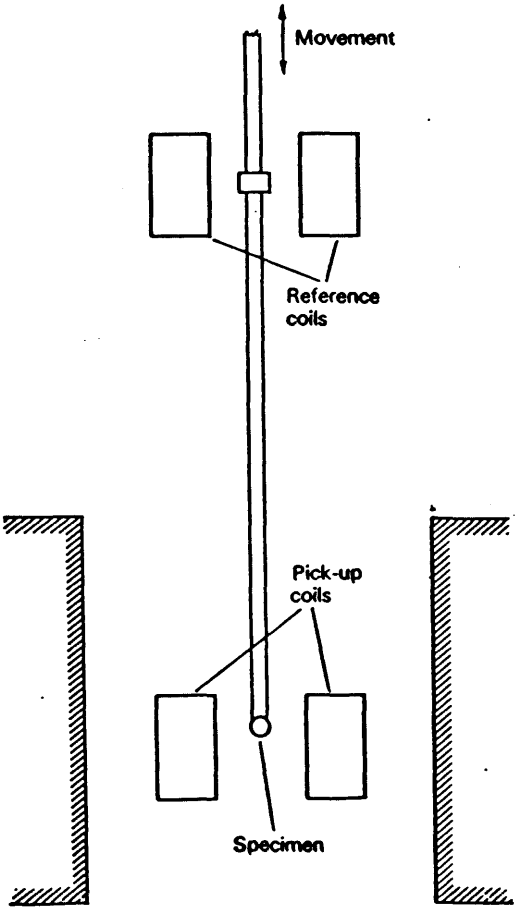


Figure C.1 Schematic diagram of a vibrating sample magnetometer.

APPENDIX D Mössbauer Spectroscopy

Since the late 1950's, ^{57}Fe Mössbauer spectroscopy has enjoyed extensive use as a research tool in iron chemistry.[271(a),271(b)] The experimental method for studying the nuclear processes, which give rise to Mössbauer spectra, was first reported by Rudolf L. Mössbauer in 1958.[272] The Mössbauer experiment can be described in four stages:

(1) A γ-ray is emitted by an atom in a transition from a nuclear excited state to the nuclear ground state. This atom is called the source.
(2) The γ-ray energy is modulated by a small varying amount, δE.
(3) Resonant absorption of the modulated γ-ray takes place by another atom of the same isotope located elsewhere in the instrument. This is called the absorber.
(4) Detection of the γ-ray transmitted through the absorber versus modulation energy gives the Mössbauer spectrum.

In order to observe the resonant absorption, the emitted γ-ray must possess the full transition energy, E_T, between ground and transition states, i.e. the nuclear transitions must occur in a "recoiless" manner. Chemical perturbations are extremely small and therefore only minute energy modulations need be supplied to the primary γ-ray energy to increase these effects. The energy modulations can be conveniently produced using the Doppler effect by imparting small relative velocities, v, between the source and absorber. After γ-ray detection the Mössbauer spectrum is recorded as a plot that shows the intensity of transmitted γ-rays versus Doppler velocity (mm s^{-1}).

The basic Mössbauer[273] equipment is shown in **Figure D.1.** It consists of a drive mechanism to impart a known and controllable velocity to a radioactive source such as ^{57}Co which emits low energy (Mössbauer) gamma rays, a gamma ray detector with associated amplifying and sorting equipment and a data sorting device such as a multichannel analyser.

Mössbauer spectroscopy is a useful analytical technique because the energies of the nuclear states are weakly affected due to the chemical environment. In the absence of a magnetic field in the region of the nucleus, the most important perturbations are of

two types, namely the chemical isomer shift, IS, and the quadrupole nuclear splitting, QS.

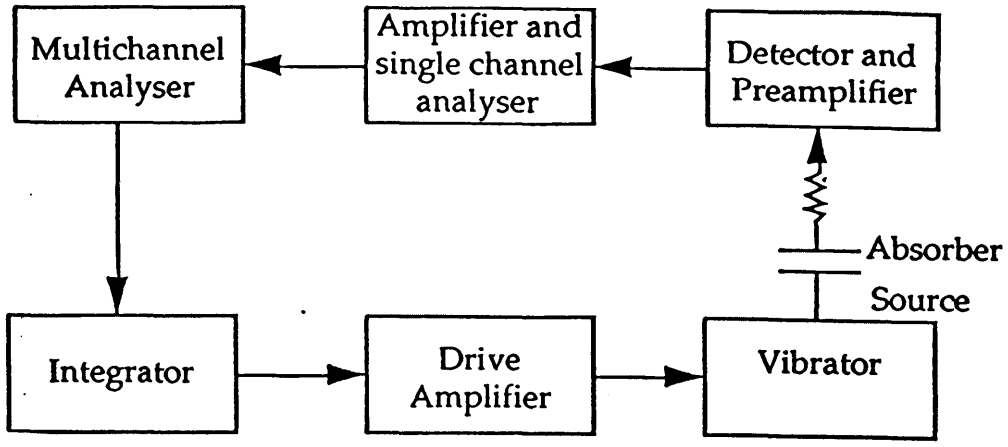


Figure D.1 Basic set-up of a Mössbauer spectrometer.

The isomer shift is due to the interaction between the nuclear charge distribution and those electrons with a finite probability in the region of the nucleus (the iron atom), i.e. the s-electrons. It manifests itself as a shift from the zero velocity of the centroid of the resonance spectrum. An increase in s-electron density around the iron nucleus leads to a decrease in the IS value of that nucleus. The quadrupole splitting is due to the interaction of the quadrupole moment of the iron nucleus with the electric field gradient of the nucleus' environment. This leads to a doublet for the iron atom and the size of the splitting depends on the symmetry of its environment, zero for cubic systems such as octahedral and non-zero for asymmetric systems.

In the presence of a magnetic field in the region of the nucleus, the extreme resolution of the Mössbauer effect can detect the interaction between the magnetic moment of the nucleus with the magnetic field. This is known as magnetic hyperfine splitting and it results in a multiplet line spectrum. In the case of the iron nucleus in ferromagnetics, a sextet is manifested. However, in the case of ferrites, there are two different iron sites, the tetrahedral and octahedral sites. Hence, a doublet of sextets is observed in their Mössbauer spectra.

For this work, Mössbauer spectra were collected using a commercial spectrometer (Harwell Instruments). The source used was 10mCi of ^{57}Co in Rh. Samples were analysed in powder form ranging in weight from 10-150mg.

APPENDIX E Electrical Resistivity Method

The bulk resistivity of pressed sintered ferrite discs were measured using criteria taken from the ASTM D 257-78 standard. For one such disc, circular electrodes are placed onto the sample before any measurement can take place. These electrodes, diameter D1, D2 and D3 (**Figure E.1**) are screen-printed onto the disc using a silver based polmer thickfilm conductor (ESL 1109-5) of emulsion thickness 25μm.

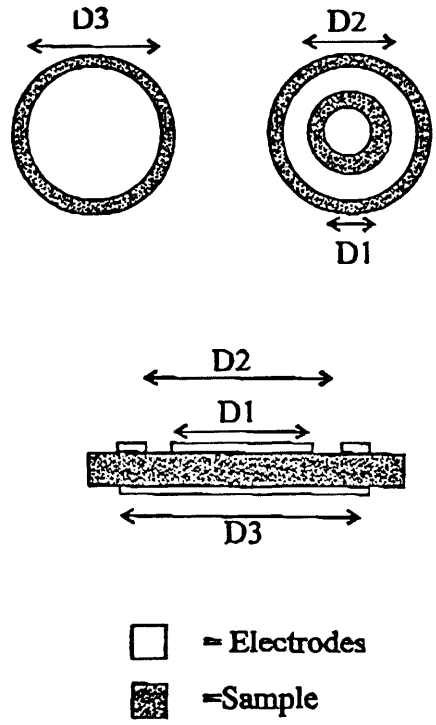
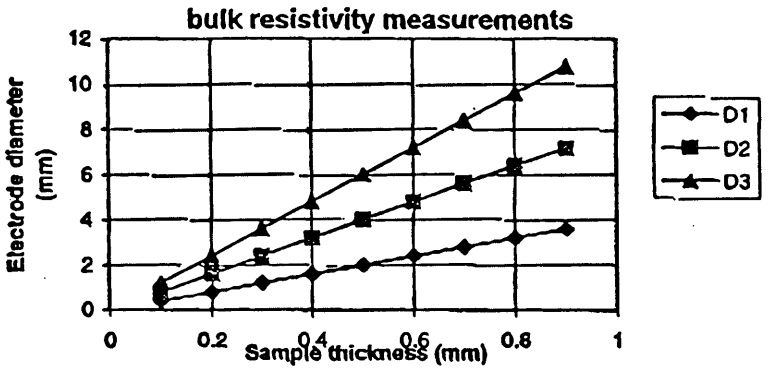


Figure E.1 Electrodes with diameters D1, D2 and D3 screen-printed on a ferrite disc sample.

The dimensions of the electrodes depend on the sample thickness as shown in **Graph E.1**. Once the electrodes are fixed to the sample, some wires are attached for connection to the circuit, using a silver conductor material. The circuit used in the measurement is shown below in **Figure E.2**. The voltage source consists of two 9V PP batteries. The voltage across the source is monitored using a multimeter in parallel and the current is measured using a picometer.



Graph E.1 Plot of suitable electrode diameters for corresponding thickness.

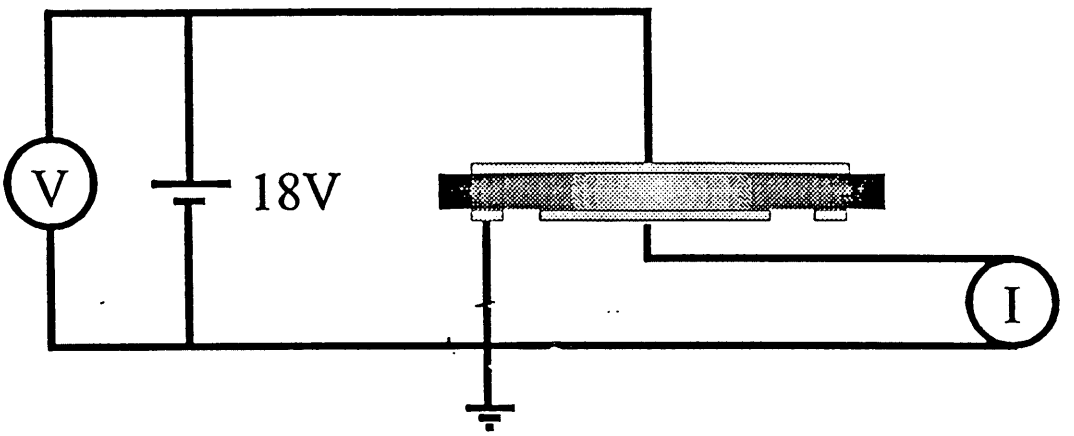


Figure E.2 Measurement circuit.

The bulk resistivity value, ρ, of the ferrite disc is calculated by the equations:

$$\rho = AV/tI \text{ and } A = \pi(D1 + D2)^2/16 \qquad [1]$$

where **A** is the effective area of the electrode, **t** is the thickness of the sample, **V** is the applied voltage and **I** is the current measured.

APPENDIX F Attempted Syntheses of compounds containing Fe-O-B and Fe-O-Si Linkages.

This appendix lists the attempted reactions to form compounds with Fe-O-B and Fe-O-Si bonds. Although none of the reactions succeeded, the expected products are written in the equations. To delve into the reasons why each reaction didn't work as hoped for would take too long but it is sufficient to say that the most common reason for failure would be that the products, if formed, are hydrolysed very quickly on contact in air, making accurate analysis impossible. Infrared spectroscopy usually confirmed this by invariably displaying hydroxyl peaks in the product's spectra. Most of the reactions mentioned below are based on literature accounts. All starting materials were used as purchased from Aldrich. All solvents were dried rigorously before use. All reactions were carried out in inert atmospheres using a Schlenk line. All starting materials that were prepared in the laboratory were fully characterised by infrared spectroscopy and elemental analyses.

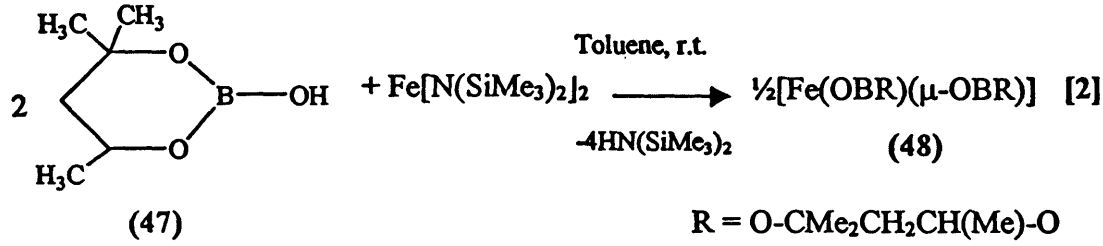
F.1 Compounds with Fe-O-B Linkages.

There have been several compounds with Fe-O-B linkages reported in the literature[113-116] (see Section 4.1.1) but the compound of interest here formed from the direct reaction of a boronous acid with an iron(II) amide to form compound (3).[115]

$$2Mes_2BOH + Fe[N(SiMe_3)_2] \xrightarrow[-4HN(SiMe_3)_2]{\text{Toluene, r.t.}} \tfrac{1}{2}[Fe(OBMes_2)(\mu\text{-}OBMes_2)]_2 \quad [1]$$

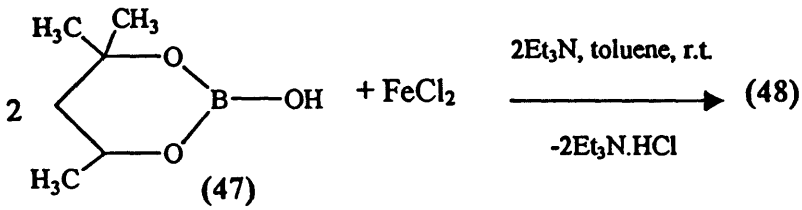
(3)

$Fe[N(SiMe_3)_2]_2$ was prepared from the reaction of $LiN(SiMe_3)_2$ with $FeBr_2$ in THF-diethylether solution in a 2:1 ratio as reported in the literature.[274] The product was vacuum distilled and was very sensitive to aerial hydrolysis. Hence, it was used directly. Reaction [2] was attempted with 4,4,6-trimethyl-1,3,2-dioxaborinan-2-ol (47) instead of dimesitylboronous acid. The starting reagent (47) was prepared by the reaction of boric acid and the organic diol in a 1:1 ratio in water in according to the literature.[275]

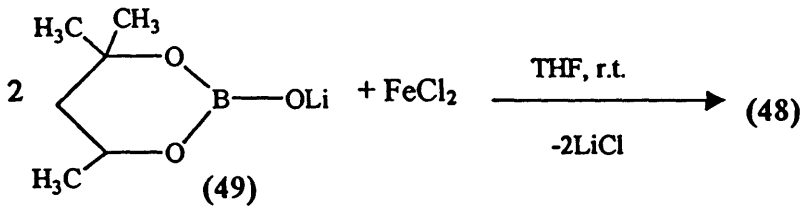


[2]

Other variations of reaction [2] were tried by either elimination of HCl by an amine or removal of a salt (LiCl) in order to prepare (48). These are shown below.



[3]

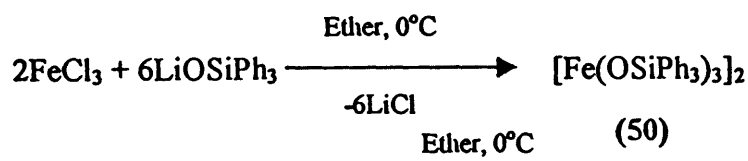


[4]

The lithium form of (47) was prepared by the reaction of (47) with *n*-butyllithium in ether.

F.2 *Compounds with Fe-O-Si Linkages.*

Schmidbauer *et al.* claimed in the early sixties to have prepared dimeric iron siloxane compounds by the reaction of ferric chloride with group one metal silanolates in a 1:3 molar ratio (see reaction [10], Section 4.1.2).[142,143] These reactions were repeated exactly according to the published experimental details but no iron siloxane product was ever obtained. Bulkier silanolates starting materials were also used in an attempt to form an iron siloxane which was relatively stable to aerial hydrolysis as shown below.



[5]

$$2FeCl_3 + 6LiOSi(OSiMe_3)_3 \xrightarrow[-6LiCl]{} [Fe\{OSi(OSiMe_3)_3\}_2]_2 \quad (51) \qquad [6]$$

$$dppeFeCl_2 + 2LiOSiPh_3 \xrightarrow[-2LiCl]{\text{Ether, 0°C}} dppeFe(OSiPh_3)_2 \quad (52) \qquad [7]$$

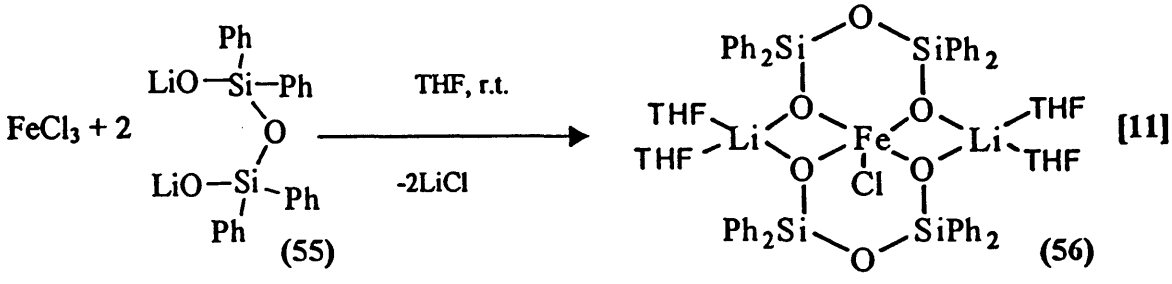
$$dppeFeCl_2 + 2KOSiMe_3 \xrightarrow[-2KCl]{\text{Ether, 0°C}} dppeFe(OSiMe_3)_2 \quad (53) \qquad [8]$$

The last two reactions involved the reagent $dppeFeCl_2$ (dppe = 1,2-bis(diphenylphosphino)-ethane). It was envisaged that the dppe ligand would retard the aerial decomposition of the final product. Syntheses of similar products of the above reactions were also attempted as shown below.

$$2FeCl_3 + 6Ph_3SiOH \xrightarrow[-6PhNH_2.HCl]{6PhNH_2, \text{ ether}} [Fe(OSiPh_3)_3]_2 \quad (50) \qquad [9]$$

$$dppeFeCl_2 + 2Ph_3SiOH \xrightarrow[-2Et_3N.HCl]{2Et_3N, \text{ ether}} dppeFe(OSiPh_3)_2 \quad (52) \qquad [10]$$

Recently, Roesky reviewed the chemistry of metallosiloxanes derived from silanediols, disilanols and trisilanols.[136] The review mainly described the preparation of these compounds by reactions involving either elimination of HX (X = Cl or Br) or loss of MCl (M = Group 1 metal). Similar reactions were tried for iron and they are described below. It should be noted that the products are only speculative. The structure of compound (56), reaction [11], is based on the literature structure for $[Cr\{(OSiPh_2OSiPh_2)\text{-}\mu\text{-}Na(THF)_2\}_2]$.[276] The starting reagent 1,1,3,3-tetraphenyldisiloxane-1,3-diol $[(HOSiPh_2)_2O]$ (54) was prepared from its dichloro-analogue in an acetone-water mixture according to the literature method.[277] Its melting point of 112-114°C compared well to the literature value of 115°C.[277] The lithium form of (54) was formed from the simple reaction of (54) with *n*-butyllithium in ether.

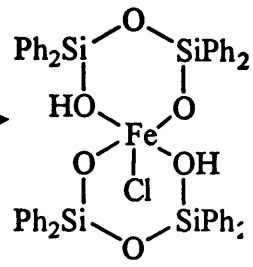


[11]

$$FeCl_3 + 2Bu^t_2Si(OLi)_2 \xrightarrow[-2LiCl]{THF,\ r.t.} [Li_2Fe(O_2SiBu^t_2)_2].4THF \quad (57) \qquad [12]$$

$$FeCl_3 + 2(HOSiPh_2)_2O \xrightarrow[-2Et_3N.HCl]{THF,\ r.t,.\ 2Et_3N} \quad (58) \qquad [13]$$

(54)



$$FeCl_3 + 2Bu^t_2Si(OH)_2 \xrightarrow[-2Et_3N.HCl]{THF,\ r.t.,\ 2Et_3N} Fe[OSi(OH)Bu^t_2]_2Cl \quad (59) \qquad [14]$$

$$dppeFeCl_2 + LiOSiPh_2OSiPh_2OLi \xrightarrow[-2LiCl]{THF,\ r.t.} dppeFe[(OSiPh_2)_2O] \quad (60) \qquad [15]$$

$$dppeFeCl_2 + (LiO)_2SiBu^t_2 \xrightarrow[-2LiCl]{THF,\ r.t.} dppeFe(O_2SiBu^t_2) \quad (61) \qquad [16]$$

The last type of reaction attempted was a repeat of the reaction that prepared the only structurally characterised compound with a Fe-O-Si linkage, i.e. $[Fe(SALEN)]OSi(CH_3)_3$, **(15)**, as mentioned in **Section 4.1.2.**[146] The reaction is given below with reaction of $[Fe(SALEN)]_2O$ (SALEN is the condensation product of salicylaldehyde and ethylenediamine) with excess hexamethyldisilazane in toluene under anaerobic conditions. The product was reported to crystallise upon addition of petroleum ether.[146] However, in the present work only the starting reagent $[Fe(SALEN)]_2O$ was ever isolated. Attempts to incorporate 1,3-diphenyl-1,1,3,3-tetramethyldisilazane instead of hexamethyldisilazane failed. The reactions are given below with their expected products.

$$[Fe(SALEN)]_2O + HN(SiMe_3)_2 \xrightarrow[Pet.\ ether]{Toluene,\ reflux} [Fe(SALEN)]OSiMe_3 \quad (15) \qquad [17]$$

$$[Fe(SALEN)]_2O + HN(SiMe_2Ph)_2 \xrightarrow[Pet.\ ether]{Toluene,\ reflux} [Fe(SALEN)]OSiMe_2Ph \quad (62) \qquad [18]$$

REFERENCES

(1) "The International Electrotechnical Vocabulary", 1988, 50, chap. 221, item 221-01-17.

(2) S. Hilpert, *Ber. dtsch. chem.*, 1909, 42, 2248.

(3) H. Forestier, *Ann. Chim.*, 1928, IX, 316.

(4) J.L. Snoek, "New Developments in Ferromagnetic Materials", Elsevier Publishing Co., New York-Amsterdam, 1948.

(5) H.P.J. Wijn, *Ferrites Proc. Int. Conf.*, 1970, 1, 19.

(6) J. J. Thompson, *Phil. Mag.*, 1903, 5, 346.

(7) N. Bohr, *Phil. Mag.*, 1913, 5, 476.

(8) S. Goudsmit and G.E. Uhlenbeck, *Nature*, 1926, 117, 264.

(9) W. Heisenberg, *Z. Physik*, 1928, 49, 619.

(10) P. Curie, *Ann. Chim. Phys.*, 1895, 5, 289.

(11) J. Smit and H.P.J. Wijn, "Ferrites", New York, John Wiley & Sons, 1959.

(12) P. Weiss, *J. Phys.*, 1907, [4] 6, 661-690.

(13) L. Neel, *Ann. de Phys.*, 1932, 17, 61.

(14) S. Chikazumi, "Physics of Magnetism", New York, John Wiley & Sons, 1964.

(15) L. Neel, *Ann. de Phys.*, 1948, 3, 137.

(16) E.W. Gorter, *Philips Res. Rep.*, 1954, 9, 321.

(17) A. Goldman, "Electronic Ceramics", New York, Marcel Dehker, 1988.

(18) J. Smit, *Solid State Commun.*, 1968, 6, 745.

(19) G.E. Bacon, "Neutron Diffraction", London, Clarendon Press, 1955.

(20) C. Guillard, *J. Phys. Rad.*, 1951, 12, 239.

(21) F. Bertaut and Forrant, *Comptes Rendue*, 1956, 247, 382.

(22) S. Geller, and M.A. Gilleo, *Acta Cryst.*, 1957, 10, 239.

(23) F. Bloch, *Physik Z.*, 1932, 24, 295.

(24) W.D. Kingery, H.K. Bowen and D.R. Uhlmann, "Introduction to Ceramics", New York, John Wiley & Sons, 1976.

(25) K.M. Ralls, T.H. Courtney and J. Wulff, "Introduction to Materials Science & Engineering", New York, John Wiley & Sons, 1976.

(26) T. Ochiai and K. Okatani, *Advances in Ceramics*, 1985, 16, 447.

(27) F.J. Schnettler, and D.W. Johnson, *Ferrites Proc. Int. Conf.*, 1971, 1, 75.

(28) S. Hirano, J. Watanabe and S. Naka, *Advances in Ceramics*, 1985, 1, 65.

(29) A.W. Apblett, L.A. Cubano, G.D. Georgieva and J.T. Mague, *Chem. Mater.*, 1996, 8, 650.

(30) N. Feltin and M.P. Pileni, *Langmuir*, 1997, **13**, 3927.

(31) N.S. Kammareddi, M. Tata, V.T. John, G.L. McPherson, M.F. Heman, Y.-S Lee, C.J. O' Connor, J.A. Ahhara and D.L. Kaplan, *Chem. Mater.*, 1996, **8**, 801.

(32) E.H. Walker, Jr., M.L. Breen and A.W. Apblett, *Chem. Mater.*, 1998, **10**, 1265.

(33) T. Akashi, Y. Kenmoku, Y. Shinma and T. Tsuji, *Ferrites Proc. Int. Conf.*, 1971, **1**, 183.

(34) T. Takada and M. Kiyama, *Ferrites Proc. Int. Conf.*, 1971, **1**, 69.

(35) A. Goldman and A.M. Laing, *J. de Phys.*, 1977, **38**, C1, 297.

(36) B.B. Yu and A. Goldman, *Ferrites Proc. Int. Conf.*, 1985, **3**, 606.

(37) G. Economos, *J. Am. Ceram. Soc.*, 1959, **42**, 628.

(38) S.P. Chaudhuri and I. Roy, *British Ceram. Trans.*, 1995, **94**, 250.

(39) D.G. Wickham, E.R. Whipple and E.G. Larson, *J. Inorg. and Nuc. Chem.*, 1960, **14**, 217.

(40) P. Sainamthip and V.R.W. Amarakoon, *J. Am. Ceram. Soc.*, 1988, **71**, C-92-L-95.

(41) E.L. Uzunova, I.G. Mitov and D.G. Klissurski, *J. Mater. Chem.*, 1996, **6**, 1035.

(42) I.J. McColm and N.J. Clark, "Forming, Shaping and Working of High Performance Ceramics", Blackie, Glasgow, 1988, p. 1.

(43) A. Chatterjee, D. Das, S.K. Pradhan and D. Chakravorty, *J. Mag. and Magn. Mater.*, 1993, **127**, 214.

(44) J.L. Woodhead et al, *Br. Patent*, **1266494**, 1972.

(45) S. Komarneni, E. Fregeau, E. Breval and R. Roy, *J. Am. Ceram. Soc.*, 1988, **71**, C-26.

(46) Y. Konishi, T. Kawamura and S. Asai, *Ind. Eng. Chem. Res.*, 1993, **32**, 2888.

(47) D. Chen, and R. Xu, *Mat. Res. Bull.*, 1998, **33**, 1015.

(48) Y. Konishi, T. Kawamura and S. Asai, *Ind. Eng. Chem. Res.*, 1996, **35**, 320.

(49) N. Takahashi, N. Kakuta, A. Ueno, K. Yamaguchi, T. Fujii, T. Mizushima and Y. Udagawa, *J. Mater. Sci.*, 1991, **26**, 497.

(50) K. Tanaka, T. Yoko, M. Atarashi and K. Kamiya, *J. Mater. Sci. Lett.*, 1989, **8**, 83.

(51) G.K. Brooks and V.R.W. Amarakoon, *J. Am. Ceram. Soc.*, 1991, **74**, 851.

(52) S. Strijbos, P.J. Rankin, R.J. Klein Wassink, J. Bunnink and G.J. Oudemans, *Powder Technology*, 1977, **18**, 187.

(53) A.L. Stuijts, *Ferrites Proc. Int. Conf.*, 1970, **1**,180.

(54) S-J.L. Kang, K-H. Kim and D.N. Yoon, *J. Am. Ceram. Soc.*, 1991, **74**, 7.

(55) C. Guillard and M. Paulus, *Comptes Rendues*, 1956, **242**, 2525.

(56) E. Roess, *Electronic Component Bull.*, 1966, **1**, 138.

(57) C. Guillard, G. Villers, A. Marais and D.N. Yoon, "Solid State Physics in Electronics and Telecommunications", London, Academic Press, 1960, **3**, 71.

(58) V.T. Gol'danskii, V.F. Belov, M.N. Devisheva and V.A. Trukhtanov, *Sov. Phys. JETP*, 1966, **22**, 1149.

(59) J.M. Daniels and A. Rosencwaig, *Can. J. Phys.*, 1970, **48**, 381.

(60) L.K. Leung, B.J. Evans and A.H. Morrish, *Phys. Rev.*, 1973, **B8**, 29.

(61) D.C. Khan, R.C. Srivastava and A.R. Das, *J. Phys.: Condensed Matter*, 1992, **4**, 1379.

(62) R.C. Srivastava, D.C. Khan and A.R. Das, *Phys. Rev.*, 1990, **B41**, 12514.

(63) Y. Yafet and C. Kittel, *Phys. Rev.*, 1952, **87**, 290.

(64) M.A. Gilleo, *Phys. Chem. Solids*, 1960, **13**, 33.

(65) (a) V.C. Wilson and J.S. Kasper, *Phys. Rev.*, 1954, **95**, 1408. (b) N.S. Satya Murthy, M.G. Natera, S.I. Yousef, R.J. Begum and C.M. Srivastava, *Phys. Rev.*, 1969, **181**, 969.

(66) Y. Ishikawa, *J. Phys. Soc. Japan*, 1962, **17**, 1877.

(67) M. Arshed, M. Siddique, M. Anwar-ul-Islam and N.M. Butt, *Solid State Commun.*, 1995, **93**, 599-602.

(68) T.C. Gibb, *J. Chem. Soc. Dalton Trans.*, 1983, 2031.

(69) A.-F. Lehlooh and S.H. Mahmood, *J. Mag. Magn. Mater.*, 1995, **151**, 163.

(70) A-F Lehlooh, S. Mahmood and I.J. Abu-Aljarayesh, *J. Mag. Magn. Mater.*, 1994, **136**, 143-148.

(71) R.D. Shannon, *Acta Cryst. A*, 1976, **A32**, 751-754.

(72) A. Globus, H. Pascard and V. Cagan, *J. de Phys. Collogue C1*, 1977, **C1-38**, C1-163-8.

(73) B.E. Warren, "X-ray Diffraction", Addison-Wesley, Reading, MA, 1990, p. 253.

(74) J. Smit and H.P.J. Wijn, "Ferrites", New York, John Wiley & Son, 1959, p. 159.

(75) H. Igaraski and K. Okazuki, *J. Am. Ceram. Soc.*, 1972, **60** [1-2], 51.

(76) T. Sano, A. Monta and A. Matsakawa, *Proc. of 3rd HFPC*, 1988, 85.

(77) A. Goldman, "Modern Ferrite Technology", Van Nostrand Reinhold, New York, 1990

(78) L.G. Van Uitert, *J. Chem. Phys.*, 1955, **23**, 1883.

(79) T. Alaski, *Trans. Jap. Inst. Met.*, 1961, **2**, 171.

(80) T.G.W. Stijntjes, J. Klerk and A. Broese van Groenou, *Philips Res. Reps.*, 1970, **25**, 95.

(81) J.C. Baclar and E.M. Jones, *Inorg. Synth.*, 1939, **1**, 37.

(82) C. Mathoniere, C.J. Nutall, S.G. Carling and P. Day, *Inorg. Chem.*, 1996, **35**, 1201-1206.

(83) G. Ferguson, T.R. Spalding and E.A. Herlihy, *Acta Cryst. C*, 1997, 658.

(84) H. Raivson, "Inorganic Glass Forming Systems", 1967, Academic Press, London.

(85) W.H. Zachariasen, *J. Am. Chem. Soc.*, 1933, **54**, 3841.

(86) W.D. Kingery, H.K. Bowen and D.R. Uhimann, "Introduction to Ceramics", 1976, Wiley, New York.

(87) J.D. MacKenzie, *J. Non-Cryst. Sol.*, 1988, **100**, 51.

(88) P.F. James, *J. Non-Cryst. Sol.*, 1988, **100**, 93.

(89) G.M. Vest, V.P. Cone, C.J. Herzfeld and A.K. Bhansali, *Mat. Res. Soc. Symp. Proc.*, 1986, **72**, 47.

(90) R.W. Vest, "Thick Film Glasses", Nov. 1987, Purdue Univ. Lafagette, Turner Lab. Report No. 0173-77-C-0142.

(91) H. Dislich and P. Hinz, *J. Non-Cryst. Sol.*, 1982, **48**, 11.

(92) M. Prassas and L.L. Hench, "Ultrastructure Processing of Ceramics, Glasses and Composites", 1984, Wiley, New York, p. 100.

(93) M. Yamane and T. Kojima, *J. Non-Cryst. Sol.*, 1980, **44**, 191.

(94) F. Pancrazi, J. Phallipou, F. Sorrentino and J. Zarzycki, *J. Non-Cryst. Sol.*, 1984, **63**, 81.

(95) J. Phallipou, M. Prassas and J. Zarzycki, *J. Non-Cryst. Sol.*, 1982, **48**, 17.

(96) C. P. Scherer and C.G.Pantano, *J. Non-Cryst. Sol.*, 1986, **82**, 246.

(97) M. Yamane, J.B. Caldwell and D.T. Moore, "Better Ceramics Through Chemistry II", 1986, Materials Research Soc., 765.

(98) P.E.C. Franken and W.T. Stacy, *J. Am. Ceram. Soc.*, 1980, **63**, 315.

(99) C. Akita, M. Fujimoto, H. Haneda and J. Tanake, *Bunseki Kayaka*, 1991, **40**, 867.

(100) T. Akaski, *J. Appl. Phys. Jpn*, 1961, **30**, 708.

(101) T. Ochiai and K. Okutani, *Advances in Ceramics*, 1985, **16**, 447.

(102) T. Mochizuki, *Advances in Ceramics*, 1985, **16**, 487.

(103) T. Sano, A. Morita and A. Matsukawa, *Proceedings of ICF5*, 1989, 595.

(104) A. Nitta, H. Nakamura, T. Komatsu and K. Matusita, *J. Appl. Phys.*, 1992, **71**, 1992.

(105) A. Nitta, H. Nakamura, T. Ono, T. Komatsu and K. Matusita, *J. Ceram. Soc. Jpn*, 1997, **105**, 731.

(106) A. Nitta, H. Nakamura, T. Komatsu and K. Matusita, *J. Mater. Sci.*, 1990, **25**, 2857.

(107) F. Muller, H.P. Steier and J.S. Moya, *J. Europ. Ceram. Soc.*, 1996, **16**, 985.

(108) D.W. Stukler and R. Roy, *Mater. Sci.*, 1971, **6**, 200.

(109) J.-H. Jean and T.K. Gupta, *J. Am. Ceram. Soc.*, 1993, **76**, 2010.

(110) J.-H. Jean and T.K. Gupta, *J. Am. Ceram. Soc.*, 1993, **76**, 751.

(111) M.E. Ehwanife, M.U. Nwachuku, F.P. Rinchart and S.J. Sime, *J. Chem. Soc., Faraday Trans.*, 1975, **71**, 1432.

(112) J.B. Farmer, *Adv. Inorg. Chem. Radiochem.*, 1982, **25**, 187.

(113) R.P. Micciche, J.L. Briguglio and L.G. Sneddon, *Inorg. Chem.*, 1984, **23**, 3992.

(114) H. Braunschweig, T.P. Spaniol and P. Paetzold, *Chem. Ber.*, 1994, **127**, 91.

(115) H. Chen, P.P. Power and S.C. Shoner, *Inorg. Chem.*, 1991, **30**, 2884.

(116) I. Vasilevsky, N.J. Rose and R.E. Stenkamp, *Acta Cryst.*, 1992, **B48**, 444.

(117) G. Spoul and G.D. Stucky, *Inorg. Chem.*, 1973, **12**, 2898.

(118) K.A. Abboud, R.C. Palenik and G.J. Palenik, *Acta Cryst.*, 1994, **C50**, 525.

(119) G.A. Nicholson, J.L. Petersen and B.J. McCormick, *Inorg. Chem.*, 1980, **19**, 195.

(120) G.A. Nicholson, C.R. Lazarus and B.J. McCormick, *Inorg. Chem.*, 1980, **19**, 192.

(121) A. Chakravorty, Coord. *Chem. Rev.*, 1974, **13**, 1.

(122) T. Totani, H. Nakai, M. Shiro, and T.J. Nakagawa, *J. Chem. Soc., Dalton Trans.*, 1975, 1938.

(123) T.K. Hilty, D.A. Thompson, W.M. Butler and R.W. Rudolph, *Inorg. Chem.*, 1979, **18**, 2642.

(124) G. Ferguson, J.F. Gallagher, D. Murphy, J.P. Sheehan and T.R. Spalding, *Polyhedron*, 1993, **12**, 859.

(125) R.C. Mehrotra, *Adv. Inorg. Chem.*, 1983, **26**, 269.

(126) H.P. Weber, *Acta Cryst. C*, 1983, **39**, 508.

(127) A. Modaressi, *J. Solid State Chem.*, 1985, **60**, 107.

(128) D.H. Lindsley, *Science*, 1970, **168**, 364.

(129) D.J. Drysdale, *Am. Mineral.*, 1975, **60**, 105.

(130) M. Cameron, *Am. Mineral.*, 1973, **58**, 594.

(131) J.A. Speer, *Rev. Mineral.*, 1982, **5**, 412.

(132) M.D. Dorfman, *Am. Mineral.*, 1960, **45**, 252.

(133) O. Johnsen, *Z. Crystallogr.*, 1978, **147**, 297.

(134) M.E. Fleet, *Am. Mineral.*, 1977, **62**, 990.

(135) M.D. Dyar, *Am. Mineral.*, 1984, **69**, 1127.

(136) R. Murugavel, A. Voigt, M.G. Walawalkar and H.W. Roesky, *Chem. Rev.*, 1996, **96**, 2205.

(137) F.-Q. Liu, I. Uison and H.W. Roesky, *J. Chem. Soc., Dalton Trans.*, 1995, 2453.

(138) H.-G. Gosink, H.W. Roesky, M. Noltemeyer, H.-G. Schmidt, C. Freire-Erdbrugger and G.M. Sheldrich, *Chem. Ber.*, 1993, **126**, 279.

(139) M.B. Hursthouse and M.A. Hossain, *Polyhedron*, 1984, **3**, 95.

(140) H.W. Roesky, A. Mazzah, D. Hesse and M. Noltemeyer, *Chem. Ber.*, 1991, **124**, 519.

(141) H.-G. Gosink, H.W. Roesky, H.-G. Schmidt, M. Noltemeyer, E. Irmer and R. Herbst-Irmer, *Organometallics*, 1994, **13**, 3420.

(142) H. Schmidbauer and M. Schmidt, *J. Am. Chem. Soc.*, 1962, **84**, 3600.

(143) H. Schmidbauer, *Chem. Ber.*, 1964, **97**, 842.

(144) H. Schmidbauer, *Chem. Ber.*, 1964, **97**, 836.

(145) F. Schindler and H. Schmidbauer, *Angew. Chem. Int. Edit.*, 1967, **6**, 683.#

(146) S.J. Dzugan and V.L. Goedken, *Inorg. Chimica Acta*, 1986, **119**, 43.

(147) Von A.F. Shikada, *Z. Anorg. Allg. Chem.*, 1974, **408**, 9.

(148) K.S. Murray, *Coord. Chem. Rev.*, 1974, **12**, 1 (*and refs. therein*).

(149) P. Coggon, A.T. McPhail, F.E. Mabbs and V.N. McLachlan, *J. Chem. Soc. (A)*, 1971, 1014.

(150) E. Wiberg and U. Kruerke, *Z. Naturforsch B*, 1953, **8**, 609; *Chem. Abstr.*, 1954, **48**, 4346.

(151) V.F. Gridina, A.L. Klepanslsii, B.A. Bartashev, L.P. Dorofeinko, N.V. Kozlova and L.E. Krupova, *Zh. Obshch. Khim.*, 1966, **36**, 1283; *Chem. Abstr.*, 1966, **65**, 15415.

(152) J.P. Sheehan, M.Sc. Thesis, University College, Cork, Ireland, 1989.

(153) P.N. Bhardwaj and G. Srivastava, *J. Indian Chem. Soc.*, 1982, **59**, 300.

(154) D. Murphy, J.P. Sheehan, T.R. Spalding, G. Ferguson, A.J. Lough and J.P. Gallagher, *J. Mater. Chem.*, 1993, **3**, 1275.

(155) D.F. Murphy, M.Sc. Thesis, University College, Cork, Ireland, 1991.

(156) K.A. Andrianov, T.V. Vasil'eva and R.A. Romanova, *Dokl. Akad. Nauk. S.S.S.R.*, 1966, **168**, 1057; *Chem. Abstr.*, 1966, **65**, 12227

(157) K.A. Andrianov and T.V. Vasil'eva, *Kremniiorg. Soedin, Tr. Soveshch (U.S.S.R.)*, 1967, **3**, 51; *Chem. Abstr.*, 1968, **69**, 87069.

(158) B.J. Brisdon, M.F. Mahon, K.C. Molloy and P.J. Schofield, *J. Organomet. Chem.*, 1992, **436**, 11 (*and refs. therein*).

(159) A. Mazzah, A. Huaudi-Mazzah, M. Noltemeyer and H.W. Roesky, *Z. Anorg. Allg. Chem.*, 1991, **604**, 93.

(160) H.G. Schafer and A. Linser, *Chem. Tech. (Berlin)*, 1950, **7**, 181.

(161) R.M. Silverstein, G.C. Bassler and T.C. Morrill, "Spectrometric Identification of Organic Compounds", Fifth Edition, Wiley & Sons, New York, 1991.

(162) N.B. Culthup, L.H. Daly and S.E. Wibberby, "Introduction to Infrared and Raman Spectroscopy", Second Edition, Academic, New York, 1975.

(163) F. Calderazzo, C. Floriani, R. Henzi and F.l'Eplattenier, *J. Chem. Soc. (A)*, 1969, 1378.

(164) M. Gerloch and F.E. Mabbs, *J. Chem. Soc. (A)*, 1967, 1598.

(165) W.P. Schaefer and R.E. Marsh, *Acta Cryst.*, 1969, **25B**, 1675.

(166) S. Bruchner, M. Calligaris, G. Nardin and L. Randaccio, *Acta Cryst.*, 1969, **25B**, 1671.

(167) F.H. Allen, O. Kennard, D.G. Watson, L. Brammer, A.G. Orpen and R. Taylor, *J. Chem. Soc., Perkin Trans. II*, 1987 S1.

(168) N.H. Buttrus, C. Eaborn, P.B. Hitchcock and A.K. Saxena, *J. Organomet. Chem.*, 1985, **284**, 291.

(169) M. Weidenbruch, H. Pesel and D. Van Hieu, *Z. Naturforsch. B*, 1980, **59**, 300.

(170) P.N. Bhardwaj and G. Srivastava, *J. Indian Chem. Soc.*, 1982, **59**, 300.

(171) E.W. Abel and A. Singh, *J. Chem. Soc.*, 1959, 690.

(172) A.B. Goel and V.D. Gupta, *J. Organomet. Chem.*, 1974, **77**, 183.

(173) A.D. Irwin, J.S. Holmgren, T.W. Zerda and J. Jonas, *J. Non. Cryst. Sol.*, 1987, **89**, 191 (*and refs. therein*).

(174) T. Raftery, M.Sc. Thesis, University College, Cork, Ireland, 1989.

(175) L.J. Bellamy, "The Infrared Spectra of Complex Molecules", Wiley & Sons, Inc., New York, 1954 (*and refs. therein*).

(176) Y.Z. Voloshin, T.E. Kron, V.K. Belsky, V.E. Zavodnik, Y.A. Maletin and S.G. Kozackhov, *J. of Organomet. Chem.*, 1997, **536**, 207.

(177) D.D. Penn, W.L.F. Formarego and D.R. Perrin, "Purification of Laboratory Chemicals", Pergamon Press, Oxford, 1966.

(178) E.I. Baucom and R.S. Drago, *J. Am. Chem. Soc.*, 1971, **93**, 6469.

(179) N.S. Biradar and V.H. Kulkarni, *J. Inorg. Nucl. Chem.*, 1971, **33**, 3847.

(180) B. Laufer, "Beginnings of Porcelain in China", ARC Press, 1917.

(181) A. Weiss and A. Weiss, *Angew. Chem.*, 1960, **72**, 413.

(182) C.Schafhautl, *J. Prakt. Chem.*, 1840, **3**, 129.

(183) K. Fredenhagen and G. Cadenbach, *Z. Anorg. Allg. Chem.*, 1926, **158**, 249.

(184) R.M. Barrer, "Zeolites and Clay Minerals", Eds., A.K. Cheetham and P. Day, Academic Press, New York, 1978.

(185) J.M. Dewsam, "Solid State Chemistry", Oxford University Press, Oxford, 1992, p. 234.

(186) B.C. Tofield, "Intercalation Chemistry", Eds., M.S. Whittingham and A.J. Jacobson, Academic Press, New York, 1982, p 181.

(187) M. Figlarz, Prog. *Solid State Chem.*, 1989, **19**, 1.

(188) D.W. Murphy and P.A. Christian, *Science*, 1979, **205**, 651.

(189) D.W. Murphy, F.J. DiSalvo, J.N. Carides and J.V. Wasczzak, *Mater. Res. Bull.*, 1978, **13**, 1395.

(190) K.H. Cheng, A.J. Jacobson and M.S. Whitiingham, *Solid State Ionics*, 1981, **5**, 355.

(191) F. Liebau, "Structural Chemistry of Silicates", Springer-Verlag, Berlin, 1985.

(192) R. Schollhorn, "Inclusion Compounds", Eds., J.L. Atwood, J.E.D. Davies and D.D. MacNicol, Academic Press, New York, 1984, p. 191.

(193) R. Allman, *Chimia*, 1970, **24**, 99.

(194) T. Iwamoto, "Inclusion Compounds", Eds., J.L. Atwood, J.E.D. Davies and D.D. MacNicol, Academic Press, New York, 1984, p. 29.

(195) F. Levy, "Physics and Chemistry of Materials with Layer Structures", Reidel, Holland, 1976, Vol. 2.

(196) M.S. Whittingham and A.J. Jacobson, "Intercalation Chemistry", Academic Press, New York, 1982, p. 230.

(197) R. Schollhorn, *Angew. Chem., Int. Ed. Engl.*, 1980, **19**,983

(198) J. Rouxel, *Rev. Inorg. Chem.*, 1979, **1**, 245.

(199) R. Schollhorn, R. Kichlmann and J.C. Besenhard, *Mat. Res. Bull.*, 1976, **11**, 83.

(200) D.W. Murphy, P.A. Christian, F.J. DiSalvo and J.V. Wasczzak, *Inorg. Chem.*, 1979, **18**, 2800.

(201) J. Rouxel and P. Palvadeau, *Rev. Chim. Miner.*, 1982, **19**, 317.

(202) T. Bein, "Supramolecular Architecture", ACS Symposium Series 499, American Chemistry Society, Washinton, 1992.

(203) J. Rouxel, "Physics and Chemistry of Materials with Layer Structures", Ed., F. Levy, Riedal, Holland, 1976, Vol.6, 201.

(204) J. Rouxel and R. Brec., *Annu. Rev. Mater. Sci.*, 1986, **16**, 137.

(205) A.J. Jacobson, M.S. Whittingham and S.M. Rich, *J. Electrochem. Soc.*, 1979, **126**, 887.

(206) M. Potel, P. Gougeon, R. Chevrel and M. Sregent, *Rev. Chim. Miner.*, 1984, **21**, 34.

(207) B. Schlsche and R. Schollhorn, *Rev. Chim. Miner.*, 1982, **19**, 534.

(208) J.A. Maquire and J.J. Banewicz, *Mater. Res. Bull.*, 1984, **19**, 1573.

(209) R. Schollhorn and H. Meyer, *Mater. Res. Bull.*, 1974, **9**, 1237.

(210) K. Suzuki, N. Kojima, T. Ban and I. Tsujikama, *Synth. Met.*, 1987, **19**, 893.

(211) G. Lagaly, *Solid State Ionics*, 1986, **22**, 43.

(212) H. Selig and L.B. Ebert, *Adv. Inorg. and Radiochem.*, 1980, **23**, 281.

(213) R. Clement, *J. Chem. Soc., Chem. Commun.*, 1980, 647.

(214) C. Riekel, H.G. Reznik and R. Schollhorn, *J. Solid State Chem.*, 1980, **84**, 253.

(215) J.O. Besenhard, I. Kain, H.F. Klein and H. Witty, *Mater. Res. Soc. Symp. Proc.*, 1983, **20**, 221.

(216) P.J.S. Foot and N.G. Shaker, *Mat. Res. Bull.*, 1983, **18**, 173.

(217) R.H. Herber and Y. Maeda, *Inorg. Chem.*, 1981, **20**, 1409.

(218) J.W. Johnson, A.J. Jacobson, S.M. Rich and J.F. Brody, *J. Am. Chem. Soc.*, 1981, **103**, 5246.

(219) M.G. Kanatzidis, L.M. Tonge, T.J. Marks, H.O. Marcy and C.R. Kannewurf, *J. Am. Chem. Soc.*, 1987, **109**, 3797.

(220) J.F. Bringley and B.A. Averill, *J. Chem. Soc., Chem. Commun.*, 1987, 399.

(221) T.R. Halbert, D.C. Johnston, L.E. McCandlish, A.H. Thompson, J.C. Scanlon and J.A. Dumesic, *Physica B*, 1980, **99**, 128.

(222) S.M. Kauzlarich, J.F. Ellena, P.D. Stupik, W.M. Reiff and B.A. Averill, *J. Am. Chem. Soc.*, 1987, **109**, 4561.

(223) R.H. Herber and Y. Maeda, *Inorg. Chem.*, 1980, **19**, 3411.

(224) J.F. Bringley, J.-M. Fabre and B.A. Averill, *J. Am. Chem. Soc.*, 1990, **112**, 4577.

(225) L.F. Nazar and A.J. Jacobson, *J. Chem. Soc., Chem. Commun.*, 1986, 570.

(226) J.E. Phillips and R.H. Herber, *Inorg. Chem.*, 1986, **25**, 3081.

(227) R. Schollhorn, *NATO ASI SER, Ser B*, 1987, **172**, 149.

(228) A. Herold, " Intercalated Layered Materials", Reidal, Dordrecht, 1979,321.

(229) L. Benes, K. Melanova, V. Zima, J. Kalousova and J. Votinsky, *J. Incl. Phenom.*, 1998, **31**, 275.

(230) G. Alberti, *Acc. Chem. Res.*, 1978, **11**, 163.

(231) D.C. Johnston and S.P. Flysinger, *Phys. Rev. B*, 1984, **30**, 980.

(232) L. Benes, K. Melanova, V. Zima, J. Kalousova and J. Votinsky, *Inorg. Chem.*, 1997, **36**, 2850.

(233) M.D. Lind, *Acta. Cryst.*, 1970, **B26**, 1058.

(234) R. Clement, *J. Am. Chem. Soc.*, 1981, **103**, 6998.

(235) R. Schollhorn, "Physics of Intercalation Compounds", Spinger-Verlag, Berlin, 1981, 33.

(236) R.H. Herber, *Z. Phys. Chim. Neu Fol. B*, 1987, **151**, 69.

(237) R.H. Herber, *Acc. Chem. Res.*, 1982, **15**, 216.

(238) S. Goldsztaub, *Bull. Soc. Fr. Mineral Crystallogr.*, 1935, **58**, 6.

(239) P. Palvadeau, L. Coic, J. Rouxel and J. Portier, *Mater. Res. Bull.*, 1978, **13**,

221.

(240) S. Kikkawa, F. Kanamaru and M. Koiszumi, *Bull. Chem. Soc. Jpn.*, 1979, **52**, 963.

(241) J.E. Pillion, H.D. Gafney, M.H. Rafailovich, J. Sokolov, D. Sunil, C.J. O'Connor and M.E. Thompson, *J. Solid. State Chem.*, 1994, **113**, 261.

(242) C. Riekel, D. Hohlwein and R. Schollhorn, *J. Chem. Soc.,Chem. Commun.*, 1976, 863.

(243) J.F. Bringley, B.A. Averill and J.-M. Fabre, *Mol. Cryst. Liq. Cryst.*, 1988, **170**, 215.

(244) S.M. Kauzlarich, B.K. Teo and B.A. Averill, *Inorg. Chem.*, 1986, **25**, 1209.

(245) C.G.Wu, D.G. DeGroot, H.O. Marcy, J.L. Schindler, C.R. Kannewurf, T. Bakas, V. Papaefthymiou, W. Hirpo, J.P. Yesinowski, Y.-J. Liu and M.G. Kanatzidis, *J. Am. Chem. Soc.*, 1995, **117**, 9229.

(246) T.R. Halbert, "Intercalation Chemistry", Eds., M.S. Whittingham and A.J. Jacobson, Academic Press, New York, 1982, Chapter 12, p. 375.

(247) S. Kikkawa, F. Kanamaru and M. Koizumi, *Inorg. Chem.*, 1976, **15**, 2195.

(248) J. Portier, *Rev. Chim. Mater.*, 1966, **3**, 483.

(249) K. Kananura, C. Zhen, H. Sakaebe and Z. Takehara, *J. Electrochem. Soc.*, 1991, **138**, 331.

(250) R.S. Hilpert, K.H. Maeir and A. Hoffman, *Ber.*, 1938, **71B**, 2676.

(251) Y. Tamanura, K. Ito and T. Katsura, *J. Chem. Soc. Dalton Trans.*, 1983, 189.

(252) H. Sakaebe, S. Higuchi, K. Kanamura, H. Fujimoto and Z. Takehara, *Solid State Ionics*, 1995, **79**, 234.

(253) H. Sakaebe, S. Higuchi, K. Kanamura, H. Fujimoto and Z. Takehara, *J. Electrochem. Soc.*, 1995, **142**, 360.

(254) M.S. Whittingham and A.J. Jacobson (Eds.), "Intercalation Chemistry", 1982, Academic Press, New York, p. 340.

(255) K. Chatakondu, M.L.H. Green, M.E. Thompson and K.S. Suslich, *J. Chem. Soc. Chem. Comm.*, 1987, 900.

(256) D.M.P. Mingos and D.R. Baghurst, *Chem. Soc. Rev.*, 1991, **20**, 1.

(257) C. Gabriel, S. Gabriel, E.H. Grant, B.S.J. Halstead and D.M.P. Mingos, *Chem. Soc. Rev.*, 1998, **27**, 213.

(258) D. O'Connell, Ph.D. Thesis, University College, Cork, 1994.

(259) D.M.P. Mingos, *Res. Chem. Intermed.*, 1994, **20**(1), 85.

(260) R. Gedye, F. Smith, K. Westaway, H. Ali, L. Balderisa, L. Laberge and J. Roussell, *Tetrahedron Lett.*, 1986, 27, 279.

(261) R.I. Giguerre, T.L. Bray, S.N. Duncan and G. Majetich, *Tetrahedron Lett.*, 1986, 28, 4945.

(262) D.R. Baghurst, D.M.P. Mingos and M.J. Watson, *J. Organometallic Chemistry*, 1989, 368, C43.

(263) D.R. Baghurst, S.R. Cooper, D.L. Greene, D.M.P. Mingos and S. M. Reynolds, *Polyhedron*, 1990, 9, 893.

(264) D.R. Baghurst and D.M.P. Mingos, *J. Chem. Soc. Chem. Comm.*, 1988, 829.

(265) K. Chatakondu, M.L.H. Green, D.M.P. Mingos and S.M. Reynolds, *J. Chem. Soc. Chem. Comm.*, 1989, 1515.

(266) E. Benavente and G. Gonzalez, *Mater. Res. Bull.*, 1997, 32(6), 709.

(267) H. Stahl, *Inorg. Nucl. Chem. Letters*, 1980, 16, 271.

(268) S.M. Medeiros, J.C.P. de Oliveira, J. Mendes Filho, R.R. dos Reis, F.M.S. Garrido and O.L. Alves, *Hyperfine Interactions*, 1991, 66, 279.

(269) G. Groake, private communication.

(270) D. Jiles, "Introduction to Magnetism and Magnetic Materials", Chapman & Hall Ltd., London, 1991.

(271) (a) T.C. Gibb, "Principles of Mössbauer Spectroscopy", Chapman & Hall Ltd., London, 1976. (b) N.N. Greenwood and T.C. Gibb, "Mössbauer Spectroscopy", Chapman & Hall, London, 1971. (c) J.J. Spijkerman, L.H. Hall and J.L. Lambert, *J. Am. Chem. Soc.*, 1968, 90, 2039. (d) W.M. Reiff, W.A. Baker, Jr., and N.E. Erickson, *J. Am. Chem. Soc.*, 1968, 90, 4794. (e) G.K. Wertheim and R.H. Herber, *J. Chem. Phys.*, 1963, 38, 2106.

(272) R.L. Mössbauer, *Z. Physik*, 1958, 151, 124.

(273) S.J. Clark, J.D. Donaldson and S.M. Grimes, *Roy. Soc. Chem. Annual Reports*, 1981, 78C, 93.

(274) R.A. Andersen, K. Faegri, J.C. Green, A. Haaland, M.F. Lappert, W.-P. Leung, K. Rypdal, *Inorg. Chem.*, 1988, 27, 1782.

(275) H. Steinberg (Ed.), "Organoboron Chemistry", Interscience, New York, Vol. 1, 1964 (*and refs. therein*).

(276) M. Motevalli, M. Sanganee, P.D. Savage, S. Shak and A.C. Sullivan, *J. Chem. Soc., Chem. Commun.*, 1993, 1132.

(277) G.I. Harris, *J. Chem. Soc.*, 1963, 5978.

(278) A. Norman, Ph.D. Thesis, University College, Cork, 1998.

(279) S. Music, S. Popovic and S. Daipi, *J. Mater. Sci.*, 1993, **28**, 1793.